

# **Improved Characterization of Primary and Secondary Carbonaceous Particles**

Report to the  
California Air Resources Board  
Contract 09-328

Prepared by:  
Lynn M. Russell

Scripps Institution of Oceanography  
University of California at San Diego  
9500 Gilman Drive, La Jolla CA 92093-0221

15 June 2013

## DISCLAIMER

This report was prepared by the University of California, San Diego (Contractor) as an account of work sponsored by the California Air Resources Board (CARB), under contract 09-328. The statements and conclusions in this report are those of the contractor, and not necessarily of CARB. The mention of any commercial products, their use in conjunction with material reported here, or their source is not to be construed as an actual or implied endorsement of such products.



## Table of Contents

<b>List of Tables</b>	<b>vi</b>
<b>List of Figures</b>	<b>viii</b>
<b>List of Acronyms</b>	<b>xiv</b>
<b>Abstract</b>	<b>1</b>
<b>Executive Summary</b>	<b>2</b>
<b>1.0 Introduction</b>	<b>6</b>
1.1 Background and Motivation	6
1.2 Research Objectives	7
1.3 Structure of Report	8
<b>2.0 Field Measurements at Bakersfield</b>	<b>10</b>
2.1 Sampling Site and Meteorological Conditions	10
2.2 Collection and Analysis of Fine Particles	11
2.2.1 Bulk Particle Organic Functional Groups	11
2.2.2 Single-particle Microscopy of Organic Functional Groups	12
2.2.3 Size-resolved Organic and Inorganic Mass Fragments for Bulk and Single Particles	12
2.2.4 Elemental Concentrations	13
2.3 Organic and Inorganic Compositions of Fine Particles	14
2.4 Conclusions	18
<b>3.0 Factor Analysis of Carbonaceous Particles at Bakersfield during CalNex</b>	<b>19</b>
3.1 Introduction	19
3.2 Factor Extraction of FTIR PM <sub>1</sub> and PM <sub>2.5</sub> Samples	19
3.3 Factor Extraction of AMS Measurements	22
3.4 Summary	26
<b>4.0 Identification and Comparison of Factors from the FTIR and AMS Measurements</b>	<b>26</b>
4.1 Factors Identified from FTIR PM <sub>1</sub> and PM <sub>2.5</sub> Measurements	26
4.2 Factors Identified from AMS Measurements	31
4.3 Comparison of FTIR (PM <sub>1</sub> and PM <sub>2.5</sub> ) and AMS Factors	34
4.4 Conclusions	36
<b>5.0 Cluster Analyses of Ensemble and Single-particle Spectra</b>	<b>37</b>
5.1 Cluster Analysis of FTIR Spectra	37
5.2 Cluster Analysis of Single-particle NEXAFS Spectra	38
5.3 Cluster Analysis of Single-particle Mass Spectra	39
5.4 Comparison of Particle Cluster Types with Source Types	40
5.5 Conclusions	40
<b>6.0 Organic Particle Types by Single-particle Measurements using LS-ToF-AMS</b>	<b>41</b>
6.1 Introduction	41

6.2 Measurements	43
6.3 Results and Discussion	45
6.3.1 Classification of Single Particles into Vaporization Types	45
6.3.2 Organic Particle Types Identified from Cluster Analysis	51
6.3.3 Comparison of Single-particle Types with Ensemble Components	57
6.4 Concluding Remarks	58
6.5 Appendix	59
6.5.1 Comparison of number concentration measured by LS-ToF-AMS and SMPS	59
6.5.2 Comparison of ions generated by single particles of different vaporization types	59
6.5.3 Duty cycle versus particle number concentration	60
6.5.4 Comparison of mass-based and number-based collection efficiency	61
6.5.5 Selecting particles for cluster analysis	61
<b>7.0 Implications of Secondary Organic Aerosol Formation</b>	<b>65</b>
7.1 Contrasting Formation of Alkane and Aromatic Secondary Organic Aerosol Components	65
7.2 Nighttime Formation of Biogenic Secondary Organic Aerosols	68
7.3 Insights of SOA Formation from Factor Size Distribution	71
7.4 Conclusions	73
<b>8.0 Formation and Growth of Ultrafine Particles from Secondary Sources in Bakersfield during CalNex</b>	<b>74</b>
8.1 Introduction	74
8.2 Site and Methods	75
8.2.1 Field Site and Meteorology	75
8.2.2 Experimental	77
8.3 Results and Discussion	80
8.3.1 Ultrafine Particle Growth Events	80
8.3.2 Classification of Growth Events and Chemical Composition of Growing Particles	83
8.3.3 Diurnal Cycles of Tracers for Primary and Secondary Aerosols	83
8.3.4 Sulfuric Acid versus Organics in Contributing to Condensational Growth	87
8.3.5 Parameters Affecting Condensational Growth and Particle Number Concentration	88
8.4 Summary and Conclusion	92
<b>9.0 Primary and Secondary Organic Aerosols in the CalNex and Cal-Mex Regions and their Fossil Fuel Sources</b>	<b>95</b>
9.1 Introduction	95
9.2 Methods	96
9.2.1 OM and CO Measurements	96
9.3 Results and Discussion	98
9.3.1 Comparison of CalNex and Cal-Mex OC with Monitoring Sites	98
9.3.2 Factor Analysis of FTIR Spectra at CalNex and Cal-Mex Sites	100

9.3.3 Comparison of Fuel and Fossil Fuel Factor Organic Functional Groups	104
9.3.4 Contributions of POA and SOA	106
9.4 Conclusions	107
9.5 Appendix	108
9.5.1 Factor extraction for FTIR PM <sub>1</sub> samples onboard R/V Atlantis	108
9.5.2 Factor extraction for FTIR PM <sub>2.5</sub> samples at Pasadena	109
<b>10.0 Summary of Contributions to Other Completed Papers</b>	<b>114</b>
10.1 NO <sub>x</sub> control of nighttime SOA formation	114
10.2 SOA formation from diesel and gasoline vehicles	114
10.3 Sources of OA using speciated organic compounds as tracers	114
10.4 Nanospray desorption/electrospray ionization mass spectrometry to characterize OA	114
10.5 Molecular associations with field and lab-generated SOA	115
<b>11.0 Conclusions and Findings</b>	<b>116</b>
11.1 Primary Conclusions	116
11.2 Research highlights	117
<b>References</b>	<b>119</b>

## List of Tables

Table 2.1: Campaign average OM (measured by FTIR and AMS) and organic functional group (measured by FTIR) concentrations ( $\mu\text{g m}^{-3}$ ) in  $\text{PM}_{10}$  and  $\text{PM}_{2.5}$ . Functional group mass fractions are shown in parentheses.

Table 3.1: Correlations of FTIR factors in  $\text{PM}_{2.5}$  to source markers.

Table 4.1: Correlations of FTIR factors in  $\text{PM}_{10}$  to source markers.

Table 4.2: Correlations of AMS Group I factors to source markers.

Table 4.3: Summary of O/C values for primary or HOA components from previous studies and O/C of SOA components in this study.

Table 4.4: Source inventory of  $\text{PM}_{2.5}$  for Kern County in the San Joaquin Valley in 2008 (downloaded from <http://www.arb.ca.gov/ei/emissiondata.htm>) (shown as percentage of  $\text{PM}_{2.5}$ ) and sources identified in this study (shown as percentage of  $\text{OM}_{2.5}$ ).

Table 6.1: Comparison of single-particle measurement techniques and their detection limits.

Table 6.2: Particle number and number fraction for the three vaporization types.

Table S6.1: Cross correlation of the mass fraction time series for the three single-particle clusters (Clusters I, II, and III) and the ensemble-derived factors. Pearson's correlation coefficients are shown.

Table 7.1: Summary of concentration, OM fraction (in parentheses), oxidant, peak time, O/C, organic functional group (OFG) composition, size range, and source of FTIR and the AMS factors.

Table 7.2: Mean concentration, variability, and fraction of variability explained by the AMS factors for the OM sections.

Table 9.1: Distances, less than 200km, for each pair of short-term (CalNex/CalMex) and long-term (IMPROVE and CARB) sites. Distances shown for R/V *Atlantis* correspond to the mean value of each sub-region. Minimum and maximum values are also shown in brackets.

Table 9.2: Common peak locations in fossil fuel spectra and their peak heights relative to the highest peak ( $2923\text{ cm}^{-1}$ ).

Table 9.3: Summary of the alkane peak locations for the fossil fuel combustion factors.

Table S9.1: Concentration, mass fraction, and composition of PMF factors identified from the FTIR measurements. Colors in pie charts indicate alcohol (pink), alkane (blue), carboxylic acid (green), non-acid carbonyl (teal), and primary amine (orange) organic functional groups. Concentrations and mass fractions listed in parentheses indicate short filters only (3-6 hr resolution). Values not in parentheses were calculated for both long and short filters.

Table S9.2: Correlations ( $r$  values) of FTIR PMF components with gas phase and aerosol tracers measured at the Pasadena ground site during CalNex. The highest correlation for each tracer is underlined. Correlations in parentheses indicate those for short samples only.



## List of Figures

Figure 2.1: (a) Comparison of DMA-measured  $PM_{500nm}$  ( $d_m$ ) with the sum of concentrations for AMS-measured  $PM_{700nm}$  ( $d_{va}$ ) and EC. Correlation coefficient and slope are 0.88 and 0.97, respectively. Hourly-averaged concentrations were used to match the 1-hr time resolution of EC measurements; (b) comparison of DMA-measured  $PM_{700nm}$  ( $d_m$ ) with the sum of concentrations for AMS-measured  $PM_1$  ( $d_{va}$ ), EC, and dusts. Correlation coefficient and slope are 0.90 and 0.98, respectively. Averaged concentrations of 3 or 6 hr (time resolution for FTIR measurements) were used for comparison. Dust was assumed to be a mixture of metal oxides and salts, including  $SiO_2$ ,  $Al_2O_3$ ,  $Fe_2O_3$ ,  $Na_2O$ ,  $K_2O$ ,  $TiO_2$ ,  $BaO$ ,  $MnO$ ,  $CaCO_3$ , and  $MgCO_3$  [Usher *et al.*, 2003]; their concentrations were calculated from corresponding elemental concentrations quantified by XRF. In both figures, a CE of 0.8 was used for AMS measurements. The red line in each panel shows the best linear fit for the data points.

Figure 2.2: Campaign average composition of (a)  $PM_1$ , (b)  $PM_{2.5}$ , and (c)  $PM_{150nm}$  [Ahlm *et al.*, 2012].

Figure 2.3: Time series of FTIR-measured organic functional group concentrations (stacked bars) in  $PM_1$  and AMS-measured OM (green line). The pie chart shows campaign average functional group composition in  $PM_1$ .

Figure 2.4: Van Krevelen diagram (H/C versus O/C) from the AMS measurements. The orange line represents the linear fit (slope = -1.2 and intercept = 1.9). The AMS factors are shown as squares.

Figure 3.1: Dependence of  $Q/Q_{expected}$  on FPEAK values for FTIR  $PM_1$  (blue), FTIR  $PM_{2.5}$  (green), and AMS (red) PMF analyses.

Figure 3.2: Dependence of  $Q/Q_{expected}$  on number of factors for FTIR  $PM_1$  (blue), FTIR  $PM_{2.5}$  (green; right axis), and AMS (red) PMF analyses. Solid circles indicate selected solutions.

Figure 3.3: Time series for (a) normalized (by total infrared absorptions) sum of total residuals of FTIR  $PM_1$  5-factor solution, (b) normalized sum of total residuals of FTIR  $PM_{2.5}$  6-factor solution, and (c) sum of total residuals of the AMS 7-factor solution.

Figure 3.4: Box plots of scaled residuals for (a) FTIR  $PM_1$  5-factor solution, (b) FTIR  $PM_{2.5}$  6-factor solution, and (c) AMS 7-factor solution. Upper and lower bounds of the boxes represent 25<sup>th</sup> and 75<sup>th</sup> percentiles, and whiskers extend to 5<sup>th</sup> and 95<sup>th</sup> percentiles.

Figure 4.1: (a) FTIR factor spectra derived from  $PM_1$  (solid line) and  $PM_{2.5}$  (dashed line) measurements. The pie charts show factor compositions, with

functional groups as follows: alkane (blue), hydroxyl (hot pink), carboxylic acid (green), non-acid carbonyl (teal), and organonitrate (beige) functional groups. (b) Campaign average mass fractions of FTIR PM<sub>1</sub> and AMS factors. Colors indicate aromatic SOA (red) (red and dark red for the AMS low and high O/C aromatic SOA factors, respectively), alkane SOA (blue) (light blue and dark blue for the AMS low and high O/C alkane SOA factors, respectively), NOA (green), PO SOA (black), and vegetative detritus (orange), and COA (purple) factors. (c) Mass spectra of AMS factors.

Figure 4.2: Diurnal cycles for (a) aromatic SOA<sub>FTIR</sub> (red), low O/C aromatic SOA<sub>AMS</sub> (red), and high O/C aromatic SOA<sub>AMS</sub> (dark red), (b) alkane SOA<sub>FTIR</sub> (blue), low O/C alkane SOA<sub>AMS</sub> (light blue), and high O/C alkane SOA<sub>AMS</sub> (dark blue), (c) NOA<sub>FTIR</sub> (green) and NOA<sub>AMS</sub> (green), (d) PO SOA<sub>FTIR</sub> (black) and PO SOA<sub>AMS</sub> (black), (e) vegetative detritus (orange), and (f) COA (purple) factors. In each panel, horizontal bars represent FTIR factors (PM<sub>1</sub> samples), with bar lengths indicating sampling duration; lines with markers represent AMS factors.

Figure 4.3: Mass concentration comparison of FTIR PM<sub>1</sub> and PM<sub>2.5</sub> factors. Striped and solid bars indicate PM<sub>1</sub> and PM<sub>2.5</sub> factors, respectively. Color assignments for functional groups are the same as in Figure 2.3.

Figure 5.1: FTIR spectra during CalNex for (a) cluster 1 (143 spectra), (b) cluster 2 (69 spectra), (c) cluster 3 (11 spectra), and (d) cluster 4 (5 spectra). Horizontal bars represent functional group absorbance ranges: hydroxyl (pink), carboxylic acid (green), alkane (blue), non-acid carbonyl (teal), amine (orange), organonitrate (beige). Pie chart shows the average functional group composition in each cluster. Vertical bar represents the average relative contributions of the FTIR factors in each clusters, with colors indicating alkane SOA (blue), aromatic SOA (red), NOA (green), PO SOA (black), and vegetative detritus (orange).

Figure 5.2: Normalized single-particle X-ray spectra for particle types: a) Group I (35 particles), b) Group II (24 particles), and c) Group III (21 particles). Other identifiers include individual particle spectra (gray) and group averages (blue). For comparison, note type “a”, “h”, and “k” particles (red), as identified by Takahama et al. [2007], respectively, in panels a), b), and c). Vertical lines (orange) in each panel represent absorptions at energies 285.0, 288.7, 297.4, and 299.9 eV.

Figure 6.1: Time-integrated light scattering signals of prompt and delayed particles as a function of  $d_{va}$  ( $d_g$ ). In (a), each particle is colored by its organic mass fraction with colors shown in the color bar. In (b), particles are colored by particle clusters derived cluster analysis in Section 3.2. Colors indicate Cluster I (dark blue), Cluster II (light blue), Cluster III (green), and unknown (grey).

Figure 6.2: (a) Particle number size distributions measured by SMPS (red) and LS-ToF-AMS (solid blue). A density of 1.4 g cm<sup>-3</sup> was used to convert SMPS

mobility diameter to  $d_{va}$  [Ahlm *et al.*, 2012]. Dashed blue line represents number size distribution for sum of prompt and delayed particles. The inset shows number fractions for Cluster I (dark blue), Cluster II (light blue), Cluster III (green), and unknown (grey) particles. Particle size is binned logarithmically. For each size bin, logarithmic ratio of upper size to lower size is 0.03. (b) Comparison of campaign-average mass distribution as a function of particle time-of-flight of ensemble (dotted black line; PToF mode) and single-particle measurements (LSSP mode). The total (red) represents the sum of the prompt (blue), delayed (green), and null (black) particle signals measured by the LSSP mode.

Figure 6.3: Collection efficiency versus particle size. Point colors indicate number of particles measured in the corresponding size, with color scale shown by the vertical bar.

Figure 6.4: Spectrum similarity to Cluster I centroid (dark blue), Cluster II centroid (light blue), and Cluster III centroid (green) for (a) Cluster I spectra, (b) Cluster II spectra, and (c) Cluster III spectra. The horizontal bar in each box represents the median value. Each box's upper and lower bounds represent the 25<sup>th</sup> and the 75<sup>th</sup> percentiles, respectively, with the whiskers extending 1.5 interquartile ranges.

Figure 6.5: (a) Example single-particle spectra for i) Cluster I, ii) Cluster II, and iii) Cluster III. The particles in i), ii), and iii) were collected on 16 May ( $d_{va} = 507$  nm,  $d_g = 362$  nm), 31 May ( $d_{va} = 402$  nm,  $d_g = 287$  nm), and 16 May ( $d_{va} = 492$  nm,  $d_g = 351$  nm), respectively. (b) Variability of normalized single particle spectra for each cluster for this study (15 May to 29 June 2010). In each panel, the black sticks show the average spectrum for the cluster, and the whiskers represent standard deviations (variability) at each  $m/z$ . Colors indicate organic (green), nitrate (blue), and sulfate (red) fragments.

Figure 6.6: (a) Cluster centroid (group-average mass spectrum) for i) Cluster I, ii) Cluster II, and iii) Cluster III particles. (b) Mass spectrum for i) the high O/C alkane SOA factor, ii) the low O/C alkane SOA factor, and iii) mass-weighted average for the COA, PO SOA, and nighttime OA factors identified from the ensemble measurements using PMF analysis. (c) The difference between spectra in (a) and (b).

Figure 6.7: Time series of the number fraction for i) Cluster I (dark blue), ii) Cluster II (light blue), and Cluster III (green) particles. Time series of odd oxygen (Ox, shown in panel i) and temperature (panel ii and iii) are shown for comparison.

Figure 6.8: Solid lines show time series of the mass fraction for (a) Cluster I (dark blue), (b) Cluster II (light blue), and (c) Cluster III (green) particles. Dashed lines represent time series of the mass fraction for (a) the sum of high O/C alkane and aromatic SOA (dark blue), (b) the low O/C alkane SOA (light blue), and (c) the

sum of COA, PO SOA, and nighttime OA factors (green) identified from ensemble measurements using PMF analysis [S Liu et al., 2012a]. Measurements were averaged to 4-hour intervals.

Figure S6.1: Time series of SMPS-measured (red) and LS-ToF-AMS-derived (blue) number concentration for particles in 560- to 1000-nm  $d_{va}$  (400- to 715-nm  $d_g$ ) size range.

Figure S6.2: Comparison of number of ions associated with prompt and delayed, null, and non-particle events by using (a) the major ions including  $m/z$  15, 27, 30, 41, 43, 44, 46, 48, 55, 57, and 64 and (b) using all ions ( $m/z$  1 to  $m/z$  111). Horizontal lines indicate the threshold of 6 ions.

Figure S6.3: Data saving duty cycle (number of particles saved using LSSP over total number of LS-circuit counted particles) versus SMPS measured particle total number concentration (130 to 715 nm  $d_m$ ). The line represents the linear fit of the points with a slope of  $-5.6 \times 10^{-6}$ .

Figure S6.4: Columns C1-C5 represent cluster centroids for the clusters identified using thresholds of 6, 12, 18, 30, 40, 50, 60, 80, 100, and 120 ions. Column C14 represents number-weighted combination of clusters C1 and C4, and column C35 represents number-weighted combination of clusters C3 and C5. The percentage in the panel represents the number fraction of the cluster.

Figure S6.5: Number size distribution for (a) particles with 6-40 ions and (b) particles with more than 40 ions.

Figure 7.1: (a) Diurnal variations of mass fraction for the high O/C alkane  $SOA_{AMS}$  factor (blue boxes), mass fraction for the high O/C aromatic  $SOA_{AMS}$  factor (dashed red line), odd oxygen (pink), and OH (purple). (OH radical was measured by William Brune's research group [Ahlm et al., 2012].) The horizontal bar and the circle in each box represent median and mean values, respectively. Upper and lower bounds of the boxes represent 25<sup>th</sup> and 75<sup>th</sup> percentiles, with whiskers extending to 5<sup>th</sup> and 95<sup>th</sup> percentiles. (b) Correlation of mass fraction of the high O/C alkane  $SOA_{AMS}$  (blue) and high O/C aromatic  $SOA_{AMS}$  (red) factors to odd oxygen. Darker colors indicate higher temperatures as the vertical color bars show.

Figure 7.2: (a) Diurnal cycle of  $NOA_{FTIR}$  with inner charts showing frequency of daytime and nighttime wind directions. (b) Correlation of  $NOA_{FTIR}$  with  $NO_x$  for nighttime samples. The inner box plot shows dependence of factor concentration on RH, which included at least 10 points (45 points total) per bin. For each box in (a) and (b), upper and lower bounds represent 25<sup>th</sup> and 75<sup>th</sup> percentiles, and whiskers extend to 5<sup>th</sup> and 95<sup>th</sup> percentiles.

Figure 7.3: Size distributions of  $r^2$  (fraction of variability explained) for FTIR and AMS factors (left axes) and mass size distributions of (a)  $m/z$  44, (b)  $m/z$  57, (c)  $m/z$  43, and (d) sulfate and nitrate (right axes) for daytime (I) and nighttime (II) measurements. Legends for the factors and AMS-measured components are displayed on the left and right sides, respectively.

Figure 8.1: HYSPLIT back trajectory (72 hours) analysis for trajectories initiated at Bakersfield (left). The color scale indicates  $\log_{10}$  of the number of trajectories that have passed (through a certain grid cell). The grid cells are 0.2 degrees wide in both latitudinal and longitudinal direction. For every day 12 back trajectories have been calculated with an interval of two hours between each trajectory. The map to the right (from Google) shows the location of the Calnex Supersite in Bakersfield. The red arrow indicates the most frequent wind direction at the site.

Figure 8.2: Time series of the particle number size distribution for the whole campaign. The color scale represents  $dN/d\log D_p$  ( $\text{cm}^{-3}$ ) and the vertical black grid lines indicate midnight. The red curve represents mass of particles with a diameter lower than 150 nm derived from the SMPS size distributions with an assumed particle density of  $1.4 \text{ g cm}^{-3}$  (Sec. 8.2.2).

Figure 8.3: Temporal evolution of aerosol size distributions between 07:00 and 21:00, averaged over two-hour intervals, on three different days. a), e) and i) show scanning DMA particle number size distributions on 20 May (a), 22 May (e) and 4 June (i). b), f) and j) show calculated mass size distributions (using the number size distributions) for the same days with an assumed particle density of  $1.4 \text{ g cm}^{-3}$ . c), g) and k) show AMS organic mass size distributions and d), h) and l) show AMS sulfate mass size distributions for the same days.

Figure 8.4: Aerosol chemical composition of the growing mode during ten different days. The AMS mass size distributions have been cut at 150 nm. The black curves represent the diameter associated with the center of the growing mode.

Figure 8.5: Median diurnal cycles of EC (black),  $\text{C}_4\text{H}_9^+$  (red),  $\text{CO}_2^+$  (blue), organic mass (green), particle number concentration (brown) and condensation sink (grey). In a-c, only high growth (HG) days have been included. In d-f, only low growth (LG) days have been included. In the diurnal cycles of  $\text{C}_4\text{H}_9^+$ ,  $\text{CO}_2^+$  and organic mass, only particles with a diameter lower than 150 nm have been included.

Figure 8.6:  $\text{SO}_2$ , EC and wind directions on 25 May (a), 1 June (b) and 11 June (c).

Figure 8.7: Correlations between aerosol mass of particles smaller than 150 nm and some gas-phase compounds for the time period 09:00 to 14:00.

Figure 9.1: Locations of short-term and long-term sites. R/V *Atlantis* sampling points were divided into five off-coast regions according to proximity to urban locations.

Figure 9.2: Organic carbon concentrations at rural and urban locations close to the ground and ship platforms of CalNex and Cal-Mex field projects. Intensive organic carbon measurements during summer 2010 (black) are shown in a 24 hrs basis for comparison purposes. Rural and urban continuous monitoring sites belong to IMPROVE (blue) and CARB (pink) networks, respectively. Organic Carbon was measured in fine particles (less than 2.5  $\mu\text{m}$ ) at permanent locations and submicron particles (less than 1.0  $\mu\text{m}$ ) at CalNex and Cal-Mex sites, except for Pasadena where fine particles were collected.

Figure 9.3: Reconstruction of PMF spectra and organic composition for Bakersfield (teal), Pasadena (red), R/V *Atlantis* (black), and Tijuana (purple). Source factors are categorized into five main groups: a) LO fossil fuel combustion, b) MO fossil fuel combustion, c) marine, d) vegetative detritus, and e) biomass burning/polluted biogenic SOA

Figure 9.4: Distribution of oxygenated functional groups in ambient samples and PMF factors for each site: Bakersfield (teal), Pasadena (red), R/V *Atlantis* (black), and Tijuana (purple). Sources, according to PMF solutions, are categorized into five classes, LO fossil fuel combustion (squares), MO fossil fuel combustion (triangles), marine (diamonds), vegetative detritus (wedges), and biomass burning/polluted biogenic (crosses).

Figure 9.5: Most left panel show four common peaks of fossil fuel standard spectra in gasoline (black), diesel (blue), ship diesel (green), and oil (purple). Contiguous panels show (red) the only-alkane spectra of the more oxygenated (MO) and less oxygenated (LO) of fossil fuel ambient factors for each campaign with the fuel spectra as reference. Nine out of eleven FFC presented a characteristic peak at  $\sim 2923\text{ cm}^{-1}$ .

Figure 9.6: Upper and lower limits of  $\Delta\text{POA}/\Delta\text{CO}$  ratios from combustions sources. Carbon monoxide were collected by CARB monitoring sites at Fresno, La Mesa-Tijuana, and Los Angeles during the same period than measurements at Bakersfield, Tijuana and Pasadena.

## List of Acronyms

AIM-IC	Ambient Ion Monitor Ion Chromatograph
AMS	Aerosol Mass Spectrometer
BFSP	Brute Force Single Particle
C-ToF-AMS	Compact Time of Flight AMS
CARB	California Air Resources Board
CCN	Cloud Condensation Nuclei
CE	Collection Efficiency
CFCs	ChloroFluoro Carbons
CMB	Chemistry Mass Balance
COA	Cooking OA
DAQ	Data AcQuisition
DMA	Differential Mobility Analyzer
$d_g$	Geometric Diameter
$d_{va}$	Vacuum Aerodynamic Diameter
EC	Elemental Carbon
EDAS40	Eta Data Assimilation System
FTIR	Fourier Transform Infrared
GC-MS	Gas Chromatography Mass Spectrometry
	Ground-based Tropospheric Hydrogen Oxides Sensor
GTHOS	
GZIP	Gnu Zip
HG	High Growth
HOA	Hydrocarbon-like organic aerosol
HR-ToF-AMS	High Resolution Time of Flight AMS
	Hybrid Single Particle Lagrangian Integrated Trajectory
HYSPLIT	Interagency Monitoring of Protected Visual Environments
IMPROVE	
LA	Los Angeles
LG	Low Growth
LO	Less Oxygenated
LS-TOF-AMS	Light Scattering Time of Flight AMS
LSSP	Light Scattering Single Particle
LV-OOA	Low Volatility OOA
	Megacity Initiative Local and Global Research Observations
MILAGRO	
MO	More Oxygenated
MS	Mass Spectrum
NEXAFS	Near-Edge X-ray Absorption Fine Structure
NOA	Nighttime OA
NR-PM <sub>1</sub>	Non-refractory PM <sub>1</sub>
OA	Organic Aerosol

OC	Organic Carbon
OFG	Organic Functional Group
OM	Organic Mass
OOA	Oxygenated Organic Aerosol
PAH	Polycyclic Aromatic Hydrocarbon
PM <sub>1</sub>	Submicron Particle Mass
PM <sub>2.5</sub>	Sub 2.5 micron Particle Mass
PMF	Positive Matrix Factorization
PO SOA	Petroleum Operation SOA
POA	Primary Organic Aerosol
PSL	Polystyrene Latex sphere
PToF	Particle Time of Flight
Q-AMS	Quadrupole AMS
RH	Relative Humidity
SJV	San Joaquin Valley
SMPS	Scanning Mobility Particle Analyzer
SOA	Secondary Organic Aerosol
STXM	Scanning Transmission X-ray Microscopy
SV-OOA	SemiVolatile OOA
TAG	Thermal desorption Aerosol GC-MS
TLS	Timing of optical Signal
TMS	Timing of chemical Signal
TMS ION	Ion time of flight
TMS P	Predicted Timing of chemical Signal
UPLC/ESI-HR-Q-TOFMS	Ultra Pure Liquid Chromatography Electrospray Ionization HR-ToF-AMS
VOC	Volatile Organic Compound
XRF	Xray Fluorescence



## Abstract

Secondary organic aerosols (SOA), known to form in the atmosphere from oxidation of volatile organic compounds (VOCs) emitted by anthropogenic and biogenic sources, are a poorly understood but substantial component of atmospheric particles. In this report, we examined the chemical and physical properties of SOA in summer 2010 at Bakersfield, California, a site influenced by anthropogenic and terrestrial biogenic emissions.

This study is composed of the following sections: (i) collection and measurement of ambient fine particles during the intensive field campaign, (ii) factor analysis for source apportionment, (iii) identifying particle clusters using cluster analysis, and (iv) studying formation mechanisms of the SOA components. We measured chemical composition of submicron particle mass ( $PM_{1}$ ) and sub 2.5 micron particle mass ( $PM_{2.5}$ ) using a set of complementary, ensemble, and single particle analysis techniques, including Fourier transform infrared (FTIR) spectroscopy, Aerosol Mass Spectrometry (AMS), and scanning transmission X-ray microscopy with near edge absorption fine structure (STXM-NEXAFS). Positive matrix factorization (PMF) was used to extract major components that contributed to the organic mass. Cluster analysis applied to the ensemble infrared spectra, the single-particle mass, and NEXAFS spectra separated particles into several groups, each of which has characteristics of distinct sources or atmospheric processes. By showing the consistency of particle source types (from factor analysis) and clusters, we indicate that SOA accounts for a major fraction of fine particle mass. Based on the composition and diurnal cycle of the SOA components and their relationships with potential atmospheric oxidants, formation mechanisms of the SOA components were estimated.

We found that OM accounted for 56% of  $PM_{1}$  in summer at Bakersfield, California, with SOA components contributing 80% to 90% of OM from 15 May to 29 June 2010. SOA formed from alkane and aromatic compounds, the two major classes of vehicle-emitted hydrocarbons, accounted for 65% OM (72% SOA) in the summertime San Joaquin Valley. The alkane and aromatic SOA components were associated with 200- to 500-nm-accumulation-mode particles, likely from condensation of daytime photochemical products of VOCs. In contrast, biogenic SOA likely formed from condensation of secondary organic vapors, produced from  $NO_3$  radical oxidation reactions during nighttime hours, on 400- to 700-nm-sized primary particles, and accounted for less than 10% OM. Emissions from local petroleum operations contributed 13% to the OM. Vegetative detritus (10%) and cooking activities (7%) accounted for other small yet nonnegligible sources. While the mass spectra of several linearly-independent SOA components were nearly identical and external source markers were needed to separate them, each component had distinct infrared spectrum, likely associated with the source-specific VOCs from which they formed.

## Executive Summary

**Introduction:** It is well known that atmospheric aerosols can affect the radiative balance of the Earth, reduce air quality, and adversely impact human health. However, quantitative evaluation of these effects is associated with large uncertainties. It is therefore critical to improve our understanding of the properties of aerosols, including their chemical composition, origin, and formation and transformation mechanisms. While the inorganic fraction of aerosols mainly consists of sulfate, nitrate, and ammonium, composition of the organic fraction of aerosols is poorly characterized. To date, only 20% of the organic mass of fine particles has been characterized at the molecular level using the gas chromatography-mass spectrometry (GC-MS) method. This limitation is due to the variety of the sources and complex atmospheric processes that lead to the formation of organic aerosols. Organic aerosols are either emitted at the source (primary organic aerosol, POA) or formed in the atmosphere (secondary organic aerosol, SOA) by oxidation of volatile organic compounds (VOCs). Only a limited number of VOC reactions have been studied in the laboratory. As a result, the formation mechanism of SOA is not well known. The sources of the organic aerosols are not well quantified. For example, the fraction of anthropogenic and biogenic sources and the fraction of POA and SOA are both difficult to separate, resulting in significant underestimates of the mass of SOA, using current models. Therefore, more field measurements are needed to quantify sources of aerosols and examine which mechanisms proposed in laboratory studies are most consistent with observations. This will improve our understanding of organic aerosols.

**Background:** Organic source apportionment of organic carbon (OC) and mass (OM) has been carried out using organic molecular markers to identify sources. An example is provided by *Minguillon et al.* [2008], who used chemical mass balance (CMB) modeling to estimate 70-83% contributions to OC from vehicle traffic in Long Beach. At Riverside on the other end of the Los Angeles Basin, 45-90% of the OM was identified as SOA but was not attributed to specific sources. These recent findings illustrate the need to improve the chemical characterization of SOA in California so that its sources can be identified (as was done for Houston by *Russell et al.* [2009]).

In addition, aerosol particles play an important role in the radiative balance of the atmosphere, with their organic fraction representing one of the largest uncertainties in our ability to quantify climate cooling and feedback effects. The organic fraction of particles constitutes a significant fraction of particles transported in the troposphere across North America and the Arctic, making important contributions to light scattering and health impacts. After sulfates, organic compounds are the most abundant component of fine aerosol globally [*Heintzenberg*, 1989] and are thought to comprise 10-70% of the mass of fine aerosol [*Middlebrook et al.*, 1998; *Turpin et al.*, 2000]. The Earth's radiative

forcing can be directly affected by anthropogenically-produced particles [*National Research Council (NRC)*, 1996], but the quantity and composition of the man-made contribution to atmospheric organic particles are not well characterized.

Since organic aerosol is the largest contributor to both aerosol air quality and radiative forcing in many parts of the Earth, assessing their atmospheric role requires observations of organic functional groups. Measurements are also needed to increase our knowledge of organic aerosol in regions where there are currently only sparse data. Identifying organic functional groups helps us to understand how these particles will behave in the atmosphere in terms of their thermodynamic, microphysical, and optical properties. One example is that these properties determine the underlying processes that control particle-cloud interactions. Preliminary calculations show that this indirect effect may be significant [*IPCC*, 2007; *Lohmann and Feichter*, 2005; *Ramanathan et al.*, 2001].

Because of the overlapping importance of organic aerosols for both climate and air quality, this project was carried out at Bakersfield in the context of the CalNex campaign, a short-term atmospheric sampling program through which the combined issues of climate change and air quality could be studied to develop new integrated policies are to effectively and efficiently address both environmental issues. Separate programs are in place to regulate air quality and climate change impacts, even though decisions pertaining to one can greatly affect the outcomes of the other. During the CalNex campaign, many types of atmospheric measurements were used to study constituents contributing to both climate change and poor air quality. Ground-based measurements were located in a measurement super-site located in the southern San Joaquin Valley (SJV), which is a part of the Central Valley of California, at Bakersfield.

The Bakersfield super-site allowed for comparison of complementary collocated measurements and will be able to extend the comparisons to measurements available from the other platforms. The SJV contains many regions in which the average hourly ozone and PM<sub>2.5</sub> levels were above the California state standards put forth by the Environmental Protection Agency (EPA) for a significant fraction of the year during 2004, 2005, and 2006 [CARB, <http://www.arb.ca.gov/adam/cgi-bin/db2www/adamtop4b.d2w/Branch>]. The San Joaquin valley is also a major agricultural center in California. With its combination of meteorology, geography, and local and transported sources, the Bakersfield site in the southern SJV was an ideal location for the CalNex super-site, where the causes and effects of pollution could both be studied. Ground-based measurements focused specifically on the intensive study of particulate mass and ozone.

**Methods:** A set of techniques was used to measure the chemical composition of aerosols. These techniques include: 1) FTIR spectroscopy analysis to quantify mass concentrations of organic functional groups, including alkane, hydroxyl, carboxylic acid, amine, carbonyl, organonitrate, alkene, aromatic, and organosulfate groups; 2) STXM-NEXAFS measurements of single-particle

organic functional groups, including alkane, hydroxyl, ketone, alkene, and carboxylic acid groups; 3) AMS measurements of non-refractory inorganic and organic components and their size distributions.

## **Conclusions:**

### Chemical composition of organic aerosols

OM was the major component in fine particles, contributing to about 55% and 40% of the PM<sub>1</sub> and PM<sub>2.5</sub>, respectively, in summer 2010 at Bakersfield, California. On average, 75% of the OM in PM<sub>2.5</sub> was from submicron particles. Consequently, the OM<sub>2.5</sub> and OM<sub>1</sub> were chemically similar, with the alkane, carboxylic acid, and hydroxyl functional groups respectively accounting for about 35%, 20%, and 25% of the masses.

### Source and formation of organic aerosols

A majority (80-90%) of the OM was composed of oxidized components, among which the vehicular emission oxidation products accounted for 65% of the OM in summer 2010 at Bakersfield, California. Specifically, the alkane SOA and aromatic SOA components, which were the oxidation products of the two major vehicular exhaust constituents (alkane and aromatic compounds), were consistently identified from the FTIR and the AMS measurements. The FTIR alkane SOA factor was characterized by large fractions of alkane and carboxylic acid groups, consistent with ozone-driven mechanism proposed by *Russell et al.* [2011]. The aromatic SOA factor was largely composed of the non-acid carbonyl groups, consistent with that of the aromatic oxidation products by OH radicals, indicating that this factor was likely formed via the OH oxidation processes. The alkane and aromatic SOA components were mainly associated with 200-500 nm particles, suggesting that they were formed by condensation of gas-phase oxidation products.

Compared to the vehicular emission SOA, the biogenic SOA was relatively small, accounting for 10% of the OM. However, this factor was high during the night and its mass fraction reached up to 50% at night and contained the largest mass fraction of organonitrate groups (8%). The downslope winds from the mountains to the east and south of the sampling site likely brought biogenic VOCs, typically terpenes emitted from the coniferous trees from the forests, providing nighttime precursors. The correlation of this factor to NO<sub>x</sub>, the NO<sub>3</sub> radical precursor, suggested that this factor was likely formed from NO<sub>3</sub> oxidation processes. The biogenic SOA was mainly associated with 400-700 nm particles, likely caused by condensation of biogenic SOA on large, primary particles.

We also identified aerosols likely emitted from local petroleum operations and cooking activities, which were mainly in particles smaller than 200 nm. Though these sources were negligible in the inventory of primary emissions for the Bakersfield site, they accounted for 13% and 7% of the PM<sub>1</sub> organic mass, respectively.

In summary, our work indicates that vehicular emission is the main source of OM, pointing out the need for enhancing regulation of vehicular emissions in the summertime San Joaquin Valley (SJV).

## 1.0 Introduction

### 1.1 Background and Motivation

The organic fraction of atmospheric particles is comprised of a complex mixture of hundreds or thousands of individual compounds [Hamilton *et al.*, 2004], which originate from a variety of sources and processes. In urban areas, the major source is fossil fuel combustion from gasoline- and diesel-powered vehicles and other industrial activities (e.g., oil burning). Emissions from these sources are largely composed of alkane and aromatic hydrocarbons, with a minor fraction of alkene compounds [Kirchstetter *et al.*, 1999; Schauer *et al.*, 1999]. Another important source, biogenic emissions, accounts for 90% of total volatile organic compounds (VOCs) globally [Goldstein and Galbally, 2007] and is key to particle formation in some regions (e.g., the southeastern US) [Goldstein *et al.*, 2009]. After emission, VOCs are transported from their sources during which time they are oxidized in the atmosphere, forming low-volatility products that can condense into the particle phase. The organic aerosols formed in the atmosphere are categorized as “SOA” (secondary organic aerosol) as opposed to “POA” (primary organic aerosol), organic aerosols directly emitted at their sources.

Formation of SOA is a dynamic process that involves complex chemical reactions and physical transformations. Despite significant progress in the past years, quantitative measurement of SOA mass and its mass fraction in organic aerosols remains challenging. The elemental carbon (EC)-tracer analysis has been used to identify non-SOA components since the 1980s [Grosjean, 1984]: The organic carbon (OC)-to-EC ratio (OC/EC) that exceeds the average OC/EC from source measurements is assumed to be SOA [Turpin *et al.*, 1991]. Using this method, field measurements conducted at Los Angeles suggested that production of SOA could be 3 to 4 times more than that of POA during smog events [Grosjean, 1984; Turpin *et al.*, 1991]. Supporting the argument that SOA could be the major OM component were reaction chamber studies carried out during this time, which showed high mass yields of precursor compounds [Hatakeyama *et al.*, 1985; Hatakeyama *et al.*, 1987]. However, the EC-tracer approach suffers from large uncertainties, since the ratio of OC/EC of emission sources is highly variable and is substantially affected by meteorological conditions (e.g., air mixing) [Gray *et al.*, 1986]. Another approach, the organic tracer-based chemical mass balance (CMB) model [Cass, 1998; Schauer *et al.*, 1996], has been applied to identify sources of atmospheric fine particles since the 1990s. In this method, the mass that cannot be predicted by the model is assigned to SOA [Schauer *et al.*, 2002a; Zheng *et al.*, 2002]. Therefore, the CMB model does not directly predict SOA but provides an upper limit of SOA mass based on limited source markers (source types) [Cass, 1998]. Over the last 10 years, the development of aerosol mass spectrometer (AMS) and Fourier transform infrared (FTIR) spectroscopy has provided new insights for SOA quantification [Jayne *et al.*, 2000; Maria *et al.*,

2002]. Positive matrix factor (PMF) analysis applied to the AMS and FTIR measurements during field experiments carried out worldwide consistently showed that 65% to 95% of OM is oxygenated organic aerosols (OOA), having higher OM/OC and oxygen-to-carbon molar ratio (O/C) composition than expected for primary organic components [Jimenez *et al.*, 2009; Lanz *et al.*, 2007; Liu *et al.*, 2011; Russell, 2003; Russell *et al.*, 2011; Turpin *et al.*, 2000; Zhang *et al.*, 2007].

However, there is a lack of direct evidence that OOA equates to SOA because some primary OM includes oxidized functional groups (e.g. natural sources such as polysaccharides in sea spray and cellulose in vegetative detritus, in addition to vehicular emissions that can have carbonyl group contributions of less than 3% in the semivolatile fraction [Jakober *et al.*, 2008]). Consequently, there is a need to directly compare OOA to laboratory-produced SOA. Russell *et al.* [2011] compared OOA to SOA generated in smog chamber. In this case, OOA was derived by factor analysis of FTIR measurements, a technique that provides more molecular functional group specificity than mass spectra methods that employ electron impact ionization. Results of this comparison suggested that functional group compositions of OOA and SOA are comparable and precursor (and sometimes oxidant) dependent, making it possible to separate out SOA and, so, help address the controversy of POA and SOA mass fractions. In addition, Russell *et al.* [2011] proposed that atmospheric alkanes are important SOA precursors—oxidation of alkanes produces multi-generation SOA products, which is supported by a recent model simulation study [Yee *et al.*, 2012] that suggests more than two-thirds of alkane SOA are fourth or higher generation products after reaction for 10 hrs. Despite the improvements in laboratory and model studies, more field measurements are needed to separate SOA formed from different precursors and identify which mechanisms best explain the chemical properties of SOA formed in the complex atmosphere.

## 1.2 Research Objectives

The objective of this proposed study was to quantify the mass fraction of OM functional groups (including those formed as SOA) to emissions from combustion and biological processes using trace metal and organic molecular signatures from VOCs. The organic aerosol sampling was carried out at a designated sampling location southwest of Bakersfield in the southern San Joaquin Valley (i.e., CalNex-SJV), in coordination with CalNex 2010 measurements. Time series will be used to report the organic contribution to fine particle mass concentrations. The measurements will be analyzed using cluster and factorization techniques in coordination with VOC and elemental tracers in order to apportion the organic mass to its major sources. Ultimately the UCSD measurements will also contribute to the CalNex overall objectives, in which the synthesis of the results of several collaborating groups will result in the improved characterization of organic particles impacting climate and air quality in the SJV of California.

### 1.3 Structure of Report

The objectives of the work were achieved by fulfilling the specific research tasks detailed as follows:

**Task 1:** Field Measurements for CalNex-SJV (San Joaquin Valley).

This task was completed by conducting a 6-week field campaign in May and June 2010 in Bakersfield, CA, which is part of the SJV. Descriptions of the field site and measurements from this campaign are presented in Section 2.0.

**Task 2:** Data Reduction, Clustering and Factor Analysis.

This task was completed and is presented here and in multiple peer-reviewed papers. Section 3.0 presents work from the factor analysis of measurements from both FTIR spectroscopy and AMS taken at Bakersfield. Section 4.0 expands the discussion of this task by comparing the results from the factor analysis of the two techniques. Section 5.0 addresses this task using cluster analysis of ensemble and single particle spectra collected at Bakersfield. Section 6.0 describes the data reduction of the light scattering time of flight AMS (LS-ToF-AMS) measurements and the resulting determination of organic particle types.

**Task 3:** Comparison of Organic Concentrations and PMF Factors to Gas-phase Organic, Nitrogen Oxide, and Oxidant Tracers.

This task was completed and is presented in Section 7.0, which outlines the formation of alkane and aromatic secondary organic aerosol using gas-phase and oxidant tracers and PMF factors. Section 8.0 discusses new particle formation from secondary sources identified using gas-phase tracers.

**Task 4:** Completion of Manuscripts for Publication and Preparation of Final Report.

Task 4 has been completed with three peer-reviewed manuscripts, which are listed below.

The main findings of this work have been summarized in the following published and submitted manuscripts:

1. Secondary organic aerosol formation from fossil fuel sources contribute majority of summertime organic mass at Bakersfield [*Liu et al.*, 2012a].
2. Organic particle types by single-particle measurements using a time-of-flight aerosol mass spectrometer coupled with a light scattering module [*Liu et al.*, 2012b].
3. Formation and growth of ultrafine particles from secondary sources in Bakersfield, California [*Ahlm et al.*, 2012].

In addition, this study contributed to a regional comparison that will be included in a manuscript currently in preparation:

Primary and Secondary Organic Aerosols in the CalNex and Cal-Mex Regions and their Fossil Fuel Sources [*Guzman Morales et al.*, in prep.].



Additional findings from Tasks 1-3 have contributed to papers submitted by other research groups, including:

1. Evidence for NO<sub>x</sub> Control over Nighttime SOA Formation [*Rollins et al.*, 2012]
2. Elucidating secondary organic aerosol from diesel and gasoline vehicles through detailed characterization of organic carbon emissions [*Gentner et al.*, 2012]
3. Sources of organic aerosol investigated using organic compounds as tracers measured during CalNex in Bakersfield [*Zhao et al.*, submitted]
4. Molecular Characterization of Organic Aerosol Using Nanospray Desorption/Electrospray Ionization Mass Spectrometry: CalNex 2010 field study [*O'Brien et al.*, 2012]
5. Probing Molecular Associations of Field-Collected and Laboratory-Generated SOA with Nano-DESI High-Resolution Mass Spectrometry [*O'Brien et al.*, Accepted 2012]

## 2.0 Field Measurements at Bakersfield<sup>1</sup>

### 2.1 Sampling Site and Meteorological Conditions

SJV is surrounded by coastal mountain ranges to the west, the Sierra Nevada range to the east, and the Tehachapi Mountains to the south [Chow *et al.*, 2006a], topography that regularly limits air ventilation. The basin's air pollution levels are especially high during wintertime [Chow *et al.*, 2006a; Chow *et al.*, 2006b]. Bakersfield, located in SJV's southern region and one of its biggest cities, has a wintertime PM<sub>2.5</sub> concentration often exceeding 50 µg m<sup>-3</sup>, with OM typically accounting for more than 50% of the PM<sub>2.5</sub> mass [Chow *et al.*, 2006a]. Since 2000, annual mean PM<sub>2.5</sub> concentrations in Bakersfield have at times worsened (e.g. 2002, 2005-2008), despite an overall decrease in mean PM<sub>2.5</sub> concentrations for the state of California and the United States (<http://www.usa.com/bakersfield-ca-air-quality.htm>). In addition, Bakersfield PM<sub>2.5</sub> concentrations are roughly twice as high as state of California and the United States (<http://www.usa.com/bakersfield-ca-air-quality.htm>). Such trends in PM<sub>2.5</sub> concentrations caused Bakersfield to have the worst year-round and short-term particle pollution in the United States for 2011, confirming the need for further studies in this region [American Lung Association, 2011]. Previous studies conducted at other sites in Bakersfield showed that gasoline- and diesel-powered vehicles, wood combustion, and meat cooking comprise the site's major air pollution sources [Kleeman *et al.*, 2009; Schauer and Cass, 2000]; wood combustion occurs primarily in winter [Chow *et al.*, 2006a]. In addition, biogenic hydrocarbons emitted from trees in the foothills are likely significant contributors to summertime VOCs [Tanner and Zielinska, 1994], providing potential biogenic precursors to form biogenic SOA. Thus, the high concentration of air pollution and the variety of its sources make Bakersfield an ideal site for studying ambient particles. Measurements were conducted from 15 May to 29 June 2010 at Bakersfield (35.35° N, 118.97° W). The sampling site, located in an open urban area at the southeast edge of the city near Freeway 99 (7 km to the west) and Highway 58 (0.8 km to the north), had no nearby obstructions (e.g., tall trees or buildings). In addition to vehicular traffic, nearby sources also include oil extraction and refinery operations north and northwest of Bakersfield.

Instruments were deployed in temperature-controlled (20°C) containers with sampling heights of 3 to 5 m and 18 to 20 m above ground level, respectively, for particle-phase and gas-phase measurements. The sampling period was characterized by a series of clear, dry days with consistent diurnal cycles of temperature and relative humidity (RH), except for 15 to 17 May when intermittent rainfall occurred. The average temperature for the campaign, 24°C, included a 7°C standard deviation, with lows typically occurring at ~0500 hr and maximums often observed at ~1500 hr (lagged peak solar radiation by 3 hr). RH was anti-correlated with temperature, with an average of 38% and a standard

---

<sup>1</sup> Work presented in this section has been previously published by Liu *et al.* [2012a].

deviation of 17%. The observed diurnal cycle of wind direction was consistent with the pattern described by [Zhong *et al.*, 2004]: Northwesterly winds prevailed during daytime (0800 to 2100 hr); between midnight and early morning, easterly and southeasterly winds prevailed for 34 (of 45) days. Easterly and southeasterly winds typically represented downslope flows [Zhong *et al.*, 2004] that were likely associated with biogenic VOCs emitted from the mountains' coniferous trees (e.g., Sequoia National Forest), the chemistry of which being distinct from anthropogenic pollutants (e.g., aromatic and alkane hydrocarbons).

## 2.2 Collection and Analysis of Fine Particles

### 2.2.1 Bulk Particle Organic Functional Groups

PM<sub>1</sub> and PM<sub>2.5</sub> filter (Pall Inc., 37mm diameter Teflon filters, 1.0 μm pore size) samples were collected for FTIR analysis downstream of 1 μm and 2.5 μm sharp cut cyclones (BGI Inc). The study did not follow the federal method procedure because it would make the collection efficiency of particles vary with relative humidity, which would have led to inconsistencies between different days. The submicron particles were dried (Silica gel, Sigma-Aldrich) prior to the cyclone. Back filters were collected to quantify VOC absorption and artifacts; however absorbance on all back filters was below detection limit. Five PM<sub>1</sub> samples were collected daily, representing morning (0600-1200 hr), early afternoon (1200-1500 hr), late afternoon (1500-1800 hr), evening (1800-2300 hr), and nighttime (0000-0600 hr) periods (local Pacific Standard Time is used throughout the text). Improved time resolution of FTIR PM<sub>1</sub> samples (compared to previously reported 12- or 24-hr samples in Russell *et al.*, [2011]) allows analysis of diurnal variations of organic functional groups. Shorter sampling times also greatly enhanced statistical significance of data analysis (e.g., correlation analysis) and reduced uncertainties caused by loss of semivolatile compounds. The single PM<sub>2.5</sub> sample collected each day (0000-2300 hr) that overlapped the multiple PM<sub>1</sub> sample collection times represented daily average PM<sub>2.5</sub> concentrations. To reduce evaporative losses, samples were stored and transported at 0°C prior to analysis in La Jolla, California, by a Bruker Tensor 27 FTIR spectrometer equipped with a DTGS detector (Bruker, Waltham, MA). Organic functional groups were quantified from FTIR absorbance spectra from the linear response of peak area to the number of moles of organic bonds [Gilardoni *et al.*, 2007; Maria *et al.*, 2002; Maria *et al.*, 2003]. An automated algorithm [Russell *et al.*, 2009; Takahama *et al.*, 2012] was used to conduct background subtraction, spectrum baselining, peak fitting, and peak integration procedures, in order to quantify organic functional groups, including alkane, hydroxyl, carboxylic acid, amine, carbonyl, organonitrate, alkene, aromatic, and organosulfate groups. We excluded alkene and aromatic groups from this study because they were below the detection limit of the FTIR measurements for all samples. Additional procedural details are outlined by Gilardoni *et al.* [2009] and Liu *et al.* [2009].

### **2.2.2 Single-particle Microscopy of Organic Functional Groups**

Single particles were impacted on Si<sub>3</sub>N<sub>4</sub> windows on 18, 20, 22 May and 13 June. One morning and one afternoon sample were collected on each collection day. Stored samples were frozen below 0°C. Sample analysis was performed at the Advanced Light Source (Lawrence Berkeley National Laboratory, CA) on beamline 5.3.2. Single-particle X-ray absorption spectra were acquired using a combination of scanning transmission X-ray microscopy (STXM) and near-edge X-ray absorption fine structure (NEXAFS) spectroscopy [Russell *et al.*, 2002], which provided relative quantification of single-particle organic functional groups, including alkane, hydroxyl, ketone, alkene, and carboxylic acid groups. Functional group abundance was quantified using an automated algorithm developed by Takahama *et al.* [2010].

### **2.2.3 Size-resolved Organic and Inorganic Mass Fragments for Bulk and Single Particles**

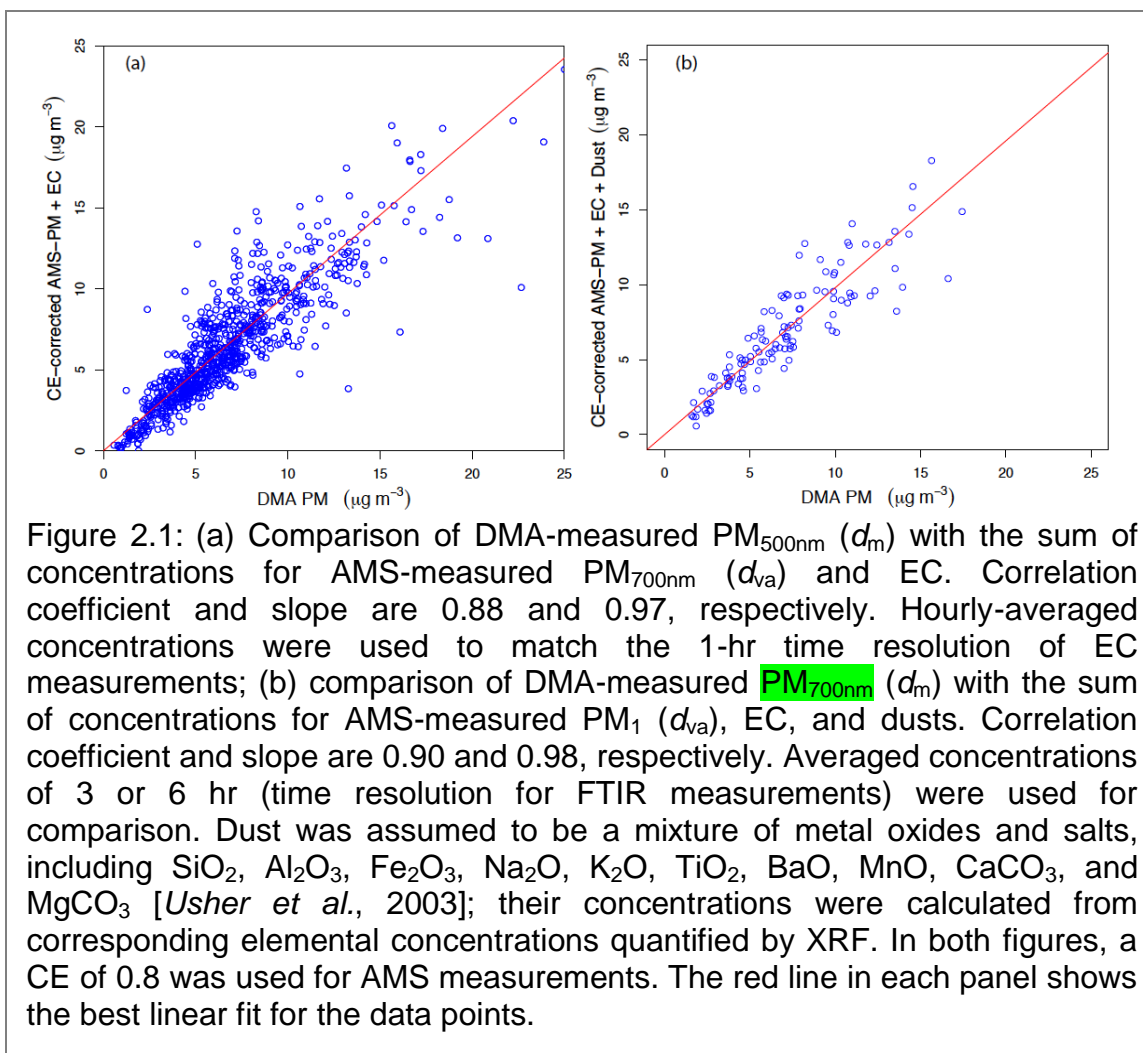
A high resolution time-of-flight aerosol mass spectrometer (HR-ToF-AMS; Aerodyne, Billerica, MA) was deployed to provide high time-resolution measurements of nonrefractory components, including OM, sulfate, nitrate, ammonium, and chloride. Particles passing through a 100- $\mu$ m pinhole are focused and accelerated by an aerodynamic lens. The accelerated particles impact a heated surface (600°C), and the nonrefractory components flash vaporize and ionize. The ionized vapor fragments are subsequently analyzed by a time-of-flight mass spectrometer [Canagaratna *et al.*, 2007]. The resulting high mass resolution allows the HR-ToF-AMS to separate ions that would otherwise overlap in a relatively low-mass resolution quadrupole detector (in a Quadrupole-AMS). As a result, the detector provides detailed quantitative elemental compositions from which the O/C, an indicator of the oxidation state of ambient aerosols [Jimenez *et al.*, 2009], can be calculated. Particle sizes, measured by the time-of-flight between a rotating chopper and the vaporizer [Jayne *et al.*, 2000], provide size-resolved chemical composition measurements of submicron particles. A light-scattering (LS) module, coupled with the HR-ToF-AMS, optically detects single particles from a 405-nm laser before particles reach the vaporizer. Light pulses scattered by the particles trigger acquisition of single-particle mass spectra [Cross *et al.*, 2007], enabling real-time measurements of single-particle chemical compositions. The path through the time-of-flight chamber was altered between high signal to noise “V” mode and high mass resolution “W” mode (both of which are mass spectrum (MS) modes) every 120 s, followed by 60 s “LS” mode to produce a 5-min time resolution for each measurement cycle. Particle size distributions were generated every V-mode by running the AMS in particle time-of-flight (PToF) mode.

The collection efficiency (CE) of the AMS measurements was evaluated by comparing AMS-measured particle mass to the mass derived from a scanning differential mobility analyzer (DMA). Comparisons were made for particles of vacuum aerodynamic diameters ( $d_{va}$ ) smaller than 700 nm and  $d_{va}$  smaller than 1

$\mu\text{m}$  (Figure 2.1). The 700-nm size cut was selected (in addition to 1  $\mu\text{m}$ ) because smaller particle sizes ( $\text{PM}_{700\text{nm}}$ ), having nearly 100% transmission efficiency [Jayne *et al.*, 2000], likely compare better with the DMA measurements in the same size range. AMS-measured  $\text{PM}_{700\text{nm}}$  and  $\text{PM}_1$  were calculated by summing the concentrations of the individual components, each of which was derived by integrating their mass size distributions measured in TOF mode. A factor of 2 was applied to the integrated concentrations (i.e., multiply by 2) to scale the integrated concentration (from the TOF-mode measurements) to the concentration measured from the MS-V mode. To account for the missing refractory components, elemental carbon (EC) and the sum of EC and dust were added to  $\text{PM}_{700\text{nm}}$  and  $\text{PM}_1$ , respectively, assuming that dust mainly existed in the larger particles (700 nm–1  $\mu\text{m}$   $d_{\text{va}}$ ). A density ( $\rho$ ) of 1.4  $\text{g cm}^{-3}$  was applied to convert the DMA-measured number concentration to mass concentration, assuming spherical particles [Ahlm *et al.*, 2012]. Concentrations were calculated by integrating the DMA-derived mass size distributions for particles smaller than 500 nm and 700 nm in mobility diameter ( $d_{\text{m}}$ ), which corresponded to 700 nm and 1  $\mu\text{m}$  in  $d_{\text{va}}$  ( $d_{\text{m}} = d_{\text{va}}/\rho$ ), respectively. A set of CE (0.5–1) values was tested, and a CE of 0.80 resulted in the best comparison of the AMS- and DMA-derived masses (slopes are close to 1) for both  $\text{PM}_{700\text{nm}}$  and  $\text{PM}_1$  (Figure 2.1). Therefore, a CE of 0.8 was assigned to each of the 5-min AMS measurements throughout the campaign.

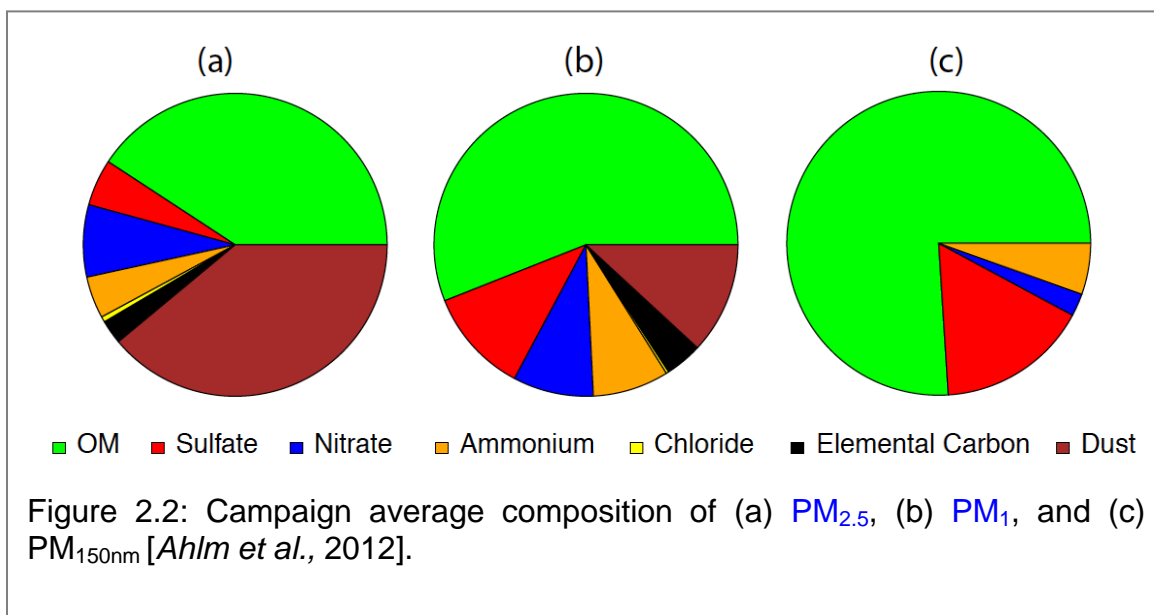
#### **2.2.4 Elemental Concentrations**

A total of 150  $\text{PM}_1$  and 46  $\text{PM}_{2.5}$  filter samples used for FTIR analysis (65% and 100% of  $\text{PM}_1$  and  $\text{PM}_{2.5}$  samples, respectively) were selectively analyzed using X-ray fluorescence (XRF) at Chester Laboratories (Chester LabNet, Tigard, Oregon). Concentrations of 38 elements (heavier than Ne) were quantified. Elements Al, Si, S, K, Ca, Fe, Co, Zn, and Br were above detection limit in 80% of the samples.



### 2.3 Organic and Inorganic Compositions of Fine Particles

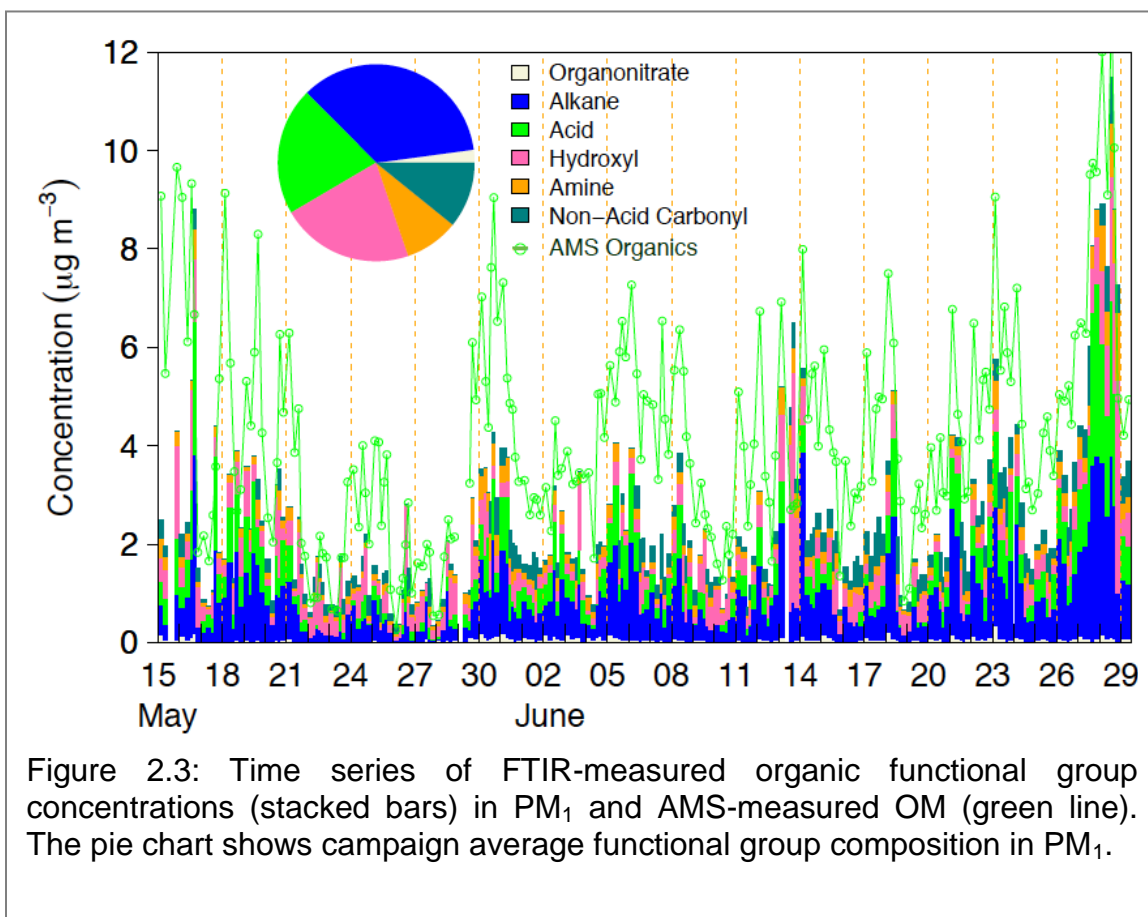
OM was the major component in submicron particle mass (56%), followed by dust (12%), sulfate (11%), nitrate (9%), ammonium (8%), and EC (4%) (Figure 2.2). The submicron OM ( $OM_1$ ) concentration measured by FTIR varied from 0.4 to 11.5  $\mu g m^{-3}$ , averaging 2.4  $\mu g m^{-3}$  for the entire campaign (Table 2.1). AMS- and FTIR-measured OM closely tracked each other (Figure 2.3) with a correlation coefficient ( $r$ ) of 0.77. Linear regression of the two quantities (intercept forced to zero) suggested that the FTIR-measured OM was on average nearly 70% of the CE-corrected AMS-measured OM. Given the measurement uncertainties (25%–30% for the FTIR and AMS measurements), the differences lie within the expected range for the two independent measurements. However, the possibility of desorption of semivolatile components from the 3- or 6-hr filter samples could not be ruled out, although the comparability of the AMS-FTIR mass differences for both the 3-hr and 6-hr samples suggests that volatile losses did not increase with sampling time as is usually expected [Mader *et al.*, 2001].



Major functional groups contributing to  $OM_1$  included alkane (35%), hydroxyl (22%), and carboxylic acid (21%) groups, among which carboxylic acid and alkane groups correlated with an  $r$  of 0.90. Similar correlation between these two groups was observed previously [Liu *et al.*, 2011], suggesting that carboxylic acid and alkane groups formed from the same source and likely via the same mechanism, likely by photooxidation of gas-phase alkane molecules [Russell *et al.*, 2009]. Non-acid carbonyl groups, typically associated with oxidation products of aromatic compounds [Lee and Lane, 2010], accounted for 11% of the OM. Amine groups (9% OM) were likely associated with bovine emissions in the region, as animal husbandry operations are major sources of atmospheric ammonia and amines [Schade and Crutzen, 1995]. Organosulfate groups were below detection limit for all submicron particles and identified as 1% of  $OM_{2.5}$  (Table 2.1), which is consistent with the low mass of organosulfate molecules ( $\sim 0.2\%$  OM) measured by UPLC/ESI-HR-Q-TOFMS at the same site.

Table 2.1: Campaign average OM (measured by FTIR and AMS) and organic functional group (measured by FTIR) concentrations ( $\mu\text{g m}^{-3}$ ) in  $\text{PM}_{10}$  and  $\text{PM}_{2.5}$ . Functional group mass fractions are shown in parentheses.

	FTIR <sub>PM<sub>10</sub></sub>	FTIR <sub>PM<sub>2.5</sub></sub>	AMS
OM	2.42±1.68	3.24±1.42	4.23±2.75
Alkane	0.85±0.73 (35%)	1.09±0.45 (34%)	-
Hydroxyl	0.53±0.58 (22%)	0.98±1.00 (30%)	-
Carboxylic acid	0.51±0.58 (21%)	0.61±0.29 (19%)	-
Nonacid carbonyl	0.26±0.24 (11%)	0.14±0.20 (4%)	-
Amine	0.22±0.18 (9%)	0.33±0.15 (10%)	-
Organonitrate	0.05±0.05 (2%)	0.07±0.06 (2%)	-
Organosulfate	BDL	0.02±0.04 (1%)	-



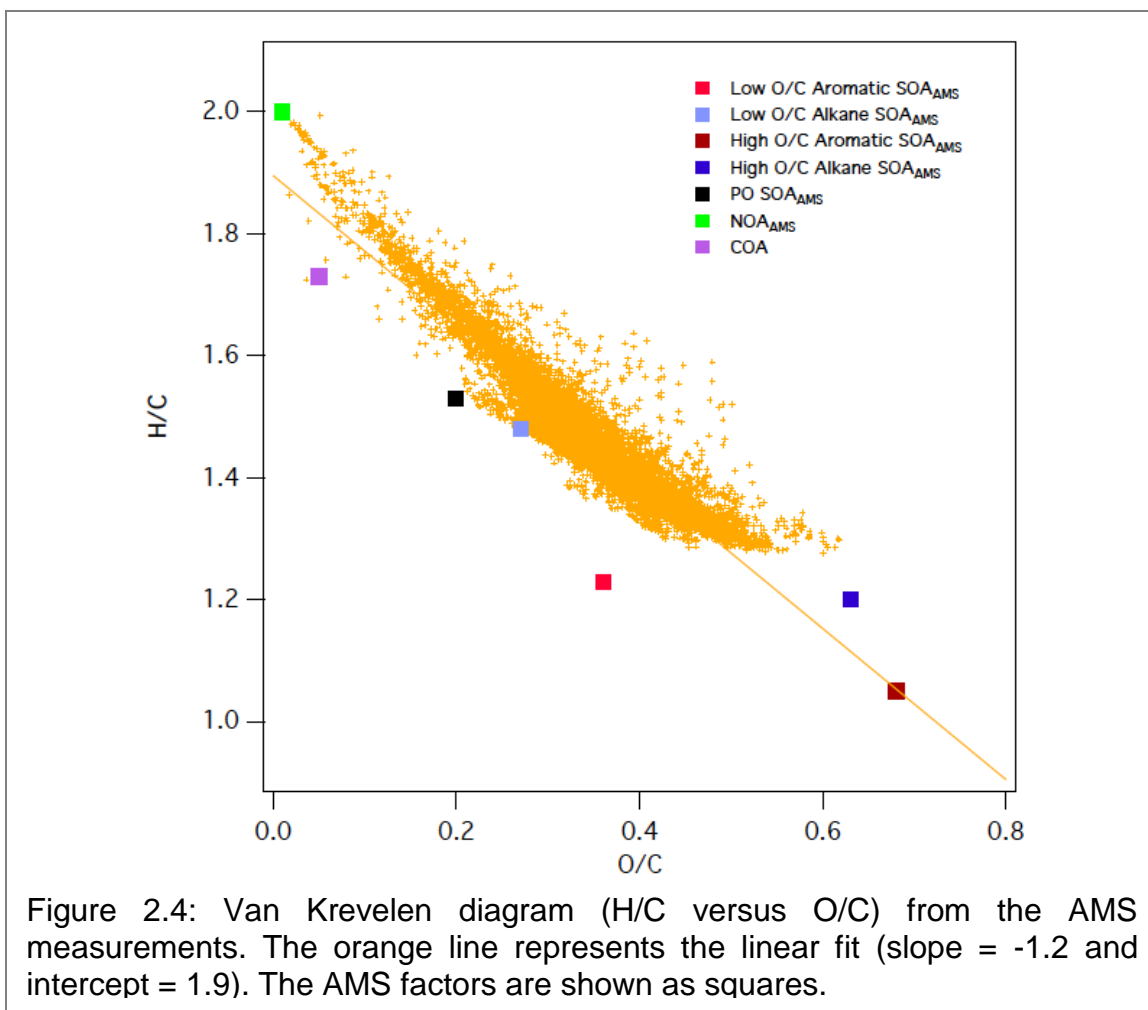
We found  $m/z$  44 ( $\text{CO}_2^+$ ) accounted for 10% of AMS-measured OM. AMS-measured sulfate, nitrate, and ammonium contributed almost equally to  $\text{PM}_{10}$ , the mass fraction ranging from 8% to 11% on average. Using these three components in an ion balance calculation revealed that the  $\text{PM}_{10}$  positive ions (ammonium) were 20% higher than that of the negative ions ( $2 \times \text{sulfate} + \text{nitrate}$ ).



The time series of the positive and negative ions correlated with an  $r$  of 0.99, indicating that these ions likely formed and condensed simultaneously (sulfuric acid and nitric acid interact with ammonia to form ammonium sulfate and ammonium nitrate, respectively). High ammonium levels in Bakersfield aerosols are consistent with large ammonia emissions in the SJV [Sorooshian *et al.*, 2008]. Because the excess ammonium (relative to inorganic sulfate and nitrate) was ~50% less (in molar concentration) than the FTIR-measured carboxylic acid groups, the aerosol might be slightly acidic.

Elemental ratios (H/C and O/C) measured by the HR-ToF-AMS are illustrated in the Van Krevelen diagram space (Figure 2.4). The Van Krevelen diagram, displayed as H/C versus O/C, has proven to be useful for describing evolution of atmospheric organic aerosols [Heald *et al.*, 2010; Ng *et al.*, 2011]. For example, conversion of alkane groups ( $-\text{CH}_2-$ ) to carbonyl groups ( $-\text{C}(=\text{O})-$ ) results in a slope of -2 (addition of 1 oxygen and loss of 2 hydrogen atoms), whereas replacement of alkane groups with hydroxyl groups ( $-\text{OH}$ ) does not change the slope in the Van Krevelen diagram. Consequently, formation of hydroxycarbonyl or carboxylic acid groups yields a slope of -1. The O/C in this study ranged from ~0 to ~0.6. The measured O/C and H/C strongly anticorrelated ( $r = 0.94$ , slope = -1.2), suggesting the atmospheric processes, including oxidation, condensation, and volatilization moved along a straight line. The tight anticorrelation of O/C and H/C also suggested that reactions such as hydration, dehydration, and oligomerization, which involve addition or loss of water molecules (i.e., O/C and H/C increase or decrease simultaneously), were likely not the major reaction mechanisms during the measurement period. The slope of -1.2 of the linear fit was similar to the slope of -1.1 observed during the SOAR-1 (Study of Organic Aerosol at Riverside) measurements at Riverside [Heald *et al.*, 2010], indicating formation of hydroxycarbonyl and carboxylic acid groups, which proved to be major functional groups (measured by FTIR) and contributed 54% to the OM at Bakersfield. The linear fit originated at H/C of 1.9 and O/C of 0.0—an indication of cycloalkanes and long-chain alkanes being major precursors for SOA (will be discussed in detail in chapters 3 and 4), which is supported by the observation of unreacted, particle-phase cyclic terpenoid (e.g., 17A(H)-21B(H)-hopane) and long-chain alkane (e.g., nonacosane) molecules with concentration of  $\sim 0.1 \text{ ng m}^{-3}$  and  $\sim 1 \text{ ng m}^{-3}$ , respectively, from the GC-MS analysis.

Compared to  $\text{PM}_{10}$ ,  $\text{PM}_{2.5}$  was comprised of a larger fraction of dust components (39%) and a lower fraction of OM (41%) (Figure 2.2). Dust components were mainly composed of elements Ca, Si, Al, and Fe (more likely by their oxides and salts). OM in  $\text{PM}_{2.5}$  ( $\text{OM}_{2.5}$ ) was largely (75%) in submicron particles. The mass difference between  $\text{OM}_1$  and  $\text{OM}_{2.5}$  (55% of  $\text{OM}_1$ ) can be explained by the hydroxyl groups, suggesting that they were associated with larger particles such as dust components (details in following section). Scaling the AMS-measured  $\text{OM}_1$  by the  $\text{OM}_{2.5}$ -to- $\text{OM}_1$  ratio measured by FTIR, the calculated AMS  $\text{OM}_{2.5}$  was  $5.6 \mu\text{g m}^{-3}$ , which is comparable to the  $\text{OM}_{2.5}$  ( $\sim 6\text{--}7 \mu\text{g m}^{-3}$ ) measured during May-June 1999-2001 at Bakersfield [Chow *et al.*, 2006b].



## 2.4 Conclusions

We have successfully measured chemical composition of  $PM_1$  and  $PM_{2.5}$  at Bakersfield during 15 May – 29 June 2010. On average, 75% of  $PM_{2.5}$  was in submicron particles;  $PM_1$  consisted of OM (56%), followed by dust (12%), sulfate (11%), nitrate (9%), and ammonium (8%). The OM was largely composed of alkane (35%), carboxylic acid (21%), and hydroxyl (22%) functional groups. Elemental analysis of OM showed that the O/C ranged from 0 to 0.6, strongly anticorrelating to H/C with a slope of -1.2, which suggests that cycloalkane or long-chain alkane hydrocarbons were likely the major VOC precursors. The complementary and consistent measurements using FTIR and AMS techniques provided the basis for the subsequent factor and cluster analyses, which were used to identify sources and atmospheric processes that contributed to OM and are presented in the following chapters.

## 3.0 Factor Analysis of Carbonaceous Particles at Bakersfield during CalNex<sup>2</sup>

### 3.1 Introduction

Because the measured infrared and mass spectra (FTIR and AMS, respectively) are sums of mass-weighted spectra for individual components that vary with time, multivariate factor analysis can be applied to the spectra to extract these components, which are commonly termed as factors. Therefore, the measured data set (typically a matrix with the columns representing the time series of variables) can be decomposed into several factors, significantly reducing the complexity of the measurements.

The most commonly used factor analysis tool in atmospheric sciences is positive matrix factorization (PMF) that was developed by *Paatero and Tapper* [1994]. The PMF model is described by the matrix equation presented in Equation (3.1):

$$X_{i,j} = \sum_p G_{i,p} F_{p,j} + E_{i,j} \quad (3.1)$$

where  $X_{i,j}$  is the data matrix, G and F refer to factor time series and factor profile, respectively,  $E_{i,j}$  represents the residuals of the PMF fitting, i and j index the rows and columns of the matrix, respectively, and p is an index for the factors in the solution. In the PMF analysis procedure, G and F are iteratively fit to the matrix ( $X_{i,j}$ ) by minimizing a parameter Q defined as

$$Q = \sum \sum \left( \frac{E_{i,j}}{\sigma_{i,j}} \right)^2 \quad (3.2)$$

where  $\sigma_{i,j}$  represents the measurement errors. In this chapter, factor extraction procedures of the FTIR and AMS measurements are described, and the optimal solutions were determined.

### 3.2 Factor Extraction of FTIR PM<sub>1</sub> and PM<sub>2.5</sub> Samples

PMF was separately applied to PM<sub>1</sub> (228 samples) and PM<sub>2.5</sub> (46 samples) mass-weighted FTIR spectra. Data matrices were composed of infrared absorptions, and scaling factor matrices were calculated from baselining<sup>3</sup> errors using an automated algorithm described in *Russell et al.* [2009]. The PMF was applied in robust mode (i.e., outliers were downweighted during fitting processes). “FPEAKs” (rotational values) of ±1, ±0.8, ±0.6, ±0.4, ±0.2, and 0

---

<sup>2</sup> Work presented in this section can be found in the Supporting Information of *Liu et al.* [2012a].

<sup>3</sup> Baselining of the FTIR spectra was completed by fitting curves between points with no absorption in order to create a zero absorption line as the starting point of the absorption peaks.

were tested, resulting in nearly identical factors. Minimum  $Q/Q_{\text{expected}}$ , a mathematical diagnostic for PMF fitting [Paatero et al., 2002], corresponded to FPEAK of 0 in PM<sub>1</sub> and PM<sub>2.5</sub> factor analysis results (Figure 3.1). Therefore, factors with FPEAK of 0 were selected to represent solutions. To investigate consistency of the solutions, seed values of 0 to 100 (varied by 10) were tested. For each of the PM<sub>1</sub> and PM<sub>2.5</sub> measurements, factor spectra and strengths derived using different seed values correlated with  $r$  values of 0.99 or better, demonstrating the robustness of the factors.

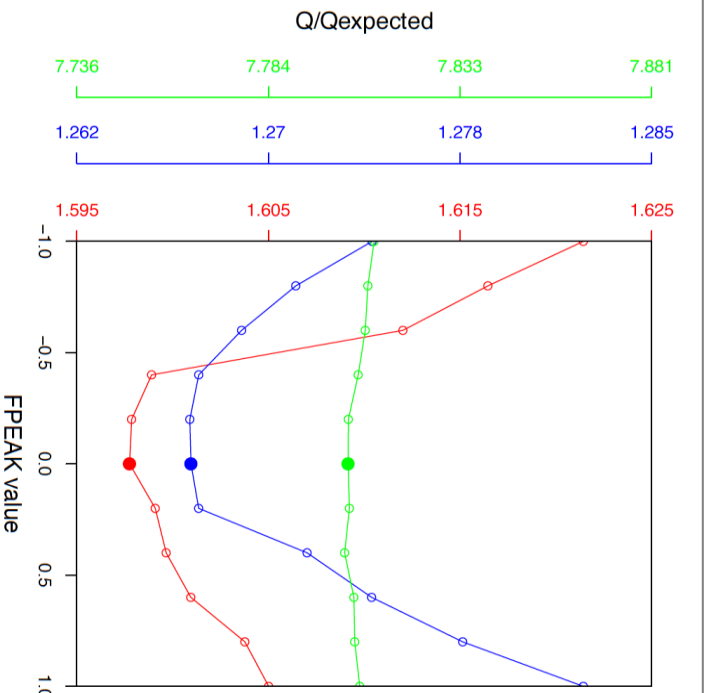
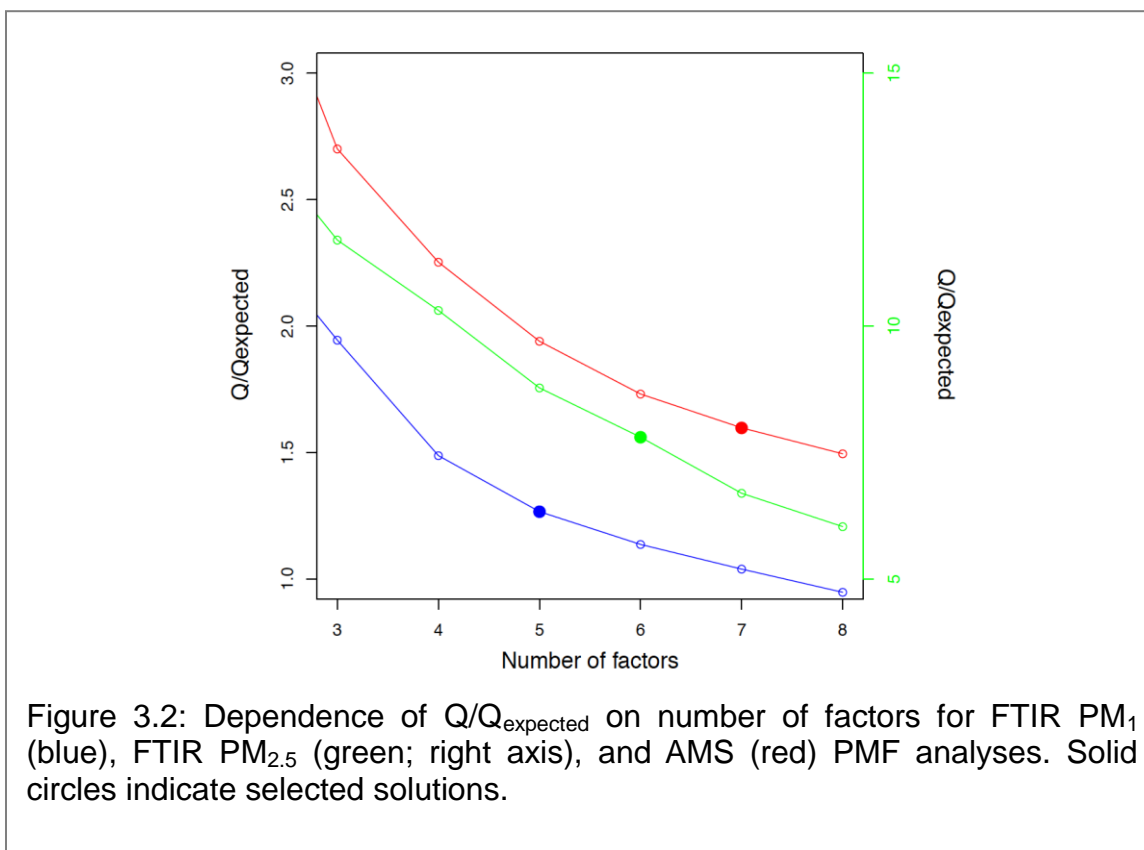


Figure 3.1: Dependence of  $Q/Q_{\text{expected}}$  on FPEAK values for FTIR PM<sub>1</sub> (blue), FTIR PM<sub>2.5</sub> (green), and AMS (red) PMF analyses.

When exploring 2- to 8-factor solutions,  $Q/Q_{\text{expected}}$  decreased with increasing factor numbers (Figure 3.2), indicating that the measured spectra were a better fit with more factors. However, too many factors may result in “factor splitting” [Ulbrich et al., 2009], and the “correct” number of factors should be evaluated on the basis of the physical meaning of the solutions. Therefore, solutions with  $Q/Q_{\text{expected}}$  close to 1 (theoretical value of ideal solution) are not necessarily the best solutions. The 5-factor solution was chosen for PM<sub>1</sub> factor analysis because one or more factors ( $\geq 12\%$  OM) with specific source signatures were not identified from the 2-, 3-, and 4-factor solutions, and small ( $\leq 7\%$  OM) factors (i.e., unidentified factors) that did not correlate to any source markers were generated when 6 or more factors were applied. For PM<sub>2.5</sub> factor analysis, a unique factor with 15% (mass fraction) organonitrate groups was not identified in solutions with less than 6 factors, and factors with unrealistic infrared spectra

were found in solutions with more than 6 factors. Therefore, the 6-factor solution was selected for PM<sub>2.5</sub> measurements. In this solution, 2 factors had similar chemical compositions and correlated in time with an  $r$  of 0.60, indicating they were likely split from one source [Ulbrich *et al.*, 2009]. The 2 correlated factors were combined into 1 factor (mass of the combined factor equals sum of factor masses used in combination), resulting in 5 linearly-independent factors, which explained the same degree of OM variability as the 6 factors prior to factor recombination.



The normalized sum of residuals (sum of infrared absorptions for each sample) fluctuated around 0, with amplitude less than 7% for the PM<sub>1</sub> and PM<sub>2.5</sub> solutions (Figures 3.3a and 3.3b). No correlation was observed for the normalized sum of residuals and OM. Scaled residuals showed no evidence of characteristic functional group absorptions (Figures 3.4a and 3.4b). Random patterns of the normalized sum of residuals and scaled residuals suggested that residuals represented fitting noises and input matrices were well fit. The correlations of these factors to components known to be good source tracers are summarized in Table 3.1.

### 3.3 Factor Extraction of AMS Measurements

PMF was applied to high-resolution mass spectra (V mode) measured by the HR-ToF-AMS. Data and error matrices were prepared using standard AMS data processing procedures (PIKA version 1.09) with Igor Pro 6 (Wavemetrics, Inc.). To appropriately weigh the data points, variables (time series of  $m/z$ ) with S/N smaller than 0.2 were omitted from the analysis. Weak points (S/N between 0.2 and 2) and  $\text{CO}_2^+$ -related ions ( $m/z$  16, 17, 18, 28, and 44) were downweighted by a factor of two [Paatero and Hopke, 2003; Ulbrich et al., 2009]. Robust mode was used in the fitting procedure. FPEAKs of  $\pm 1$ ,  $\pm 0.8$ ,  $\pm 0.6$ ,  $\pm 0.4$ ,  $\pm 0.2$ , and 0 were investigated, and no rotational effects were identified. Factors with an FPEAK of 0 corresponded to the minimum  $Q/Q_{\text{expected}}$  (Figure 3.1), so they were selected to represent the solutions. Seeds of 0 to 100 (varied by 10) were tested, resulting in two groups of solutions: Group I was composed of solutions with seeds 10, 20, 30, 50, 70, 80, and 100, and Group II comprised solutions with seeds 0, 40, 60, 90. Within each group, the factors had nearly identical mass spectra and strengths (with  $r \geq 0.94$  and  $r \geq 0.99$  for Group I and Group II factors, respectively). Comparing Group I with Group II, factors had similar factor mass spectra ( $r \geq 0.90$ ) but different factor strengths, resulting in different factor time series. The two groups of factors were investigated separately to find the best solution.

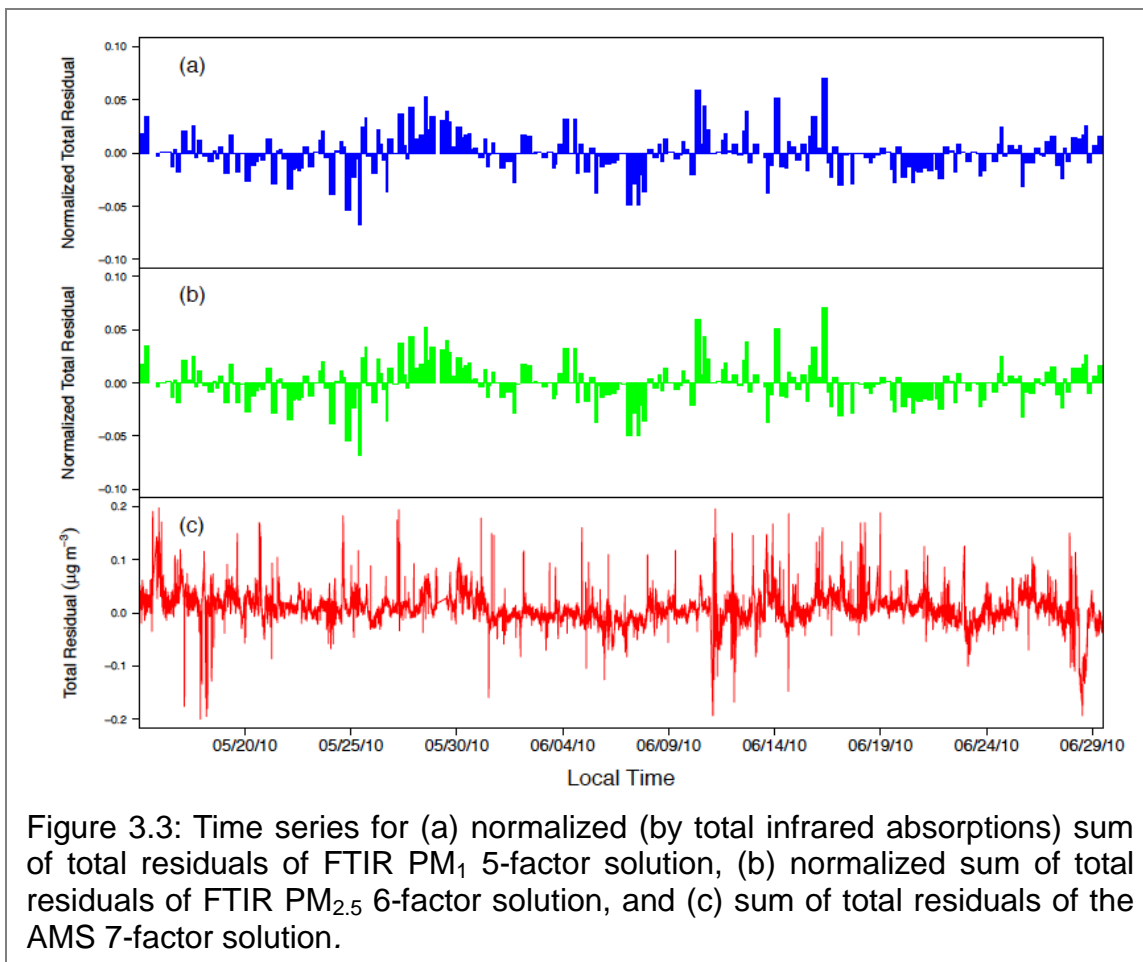
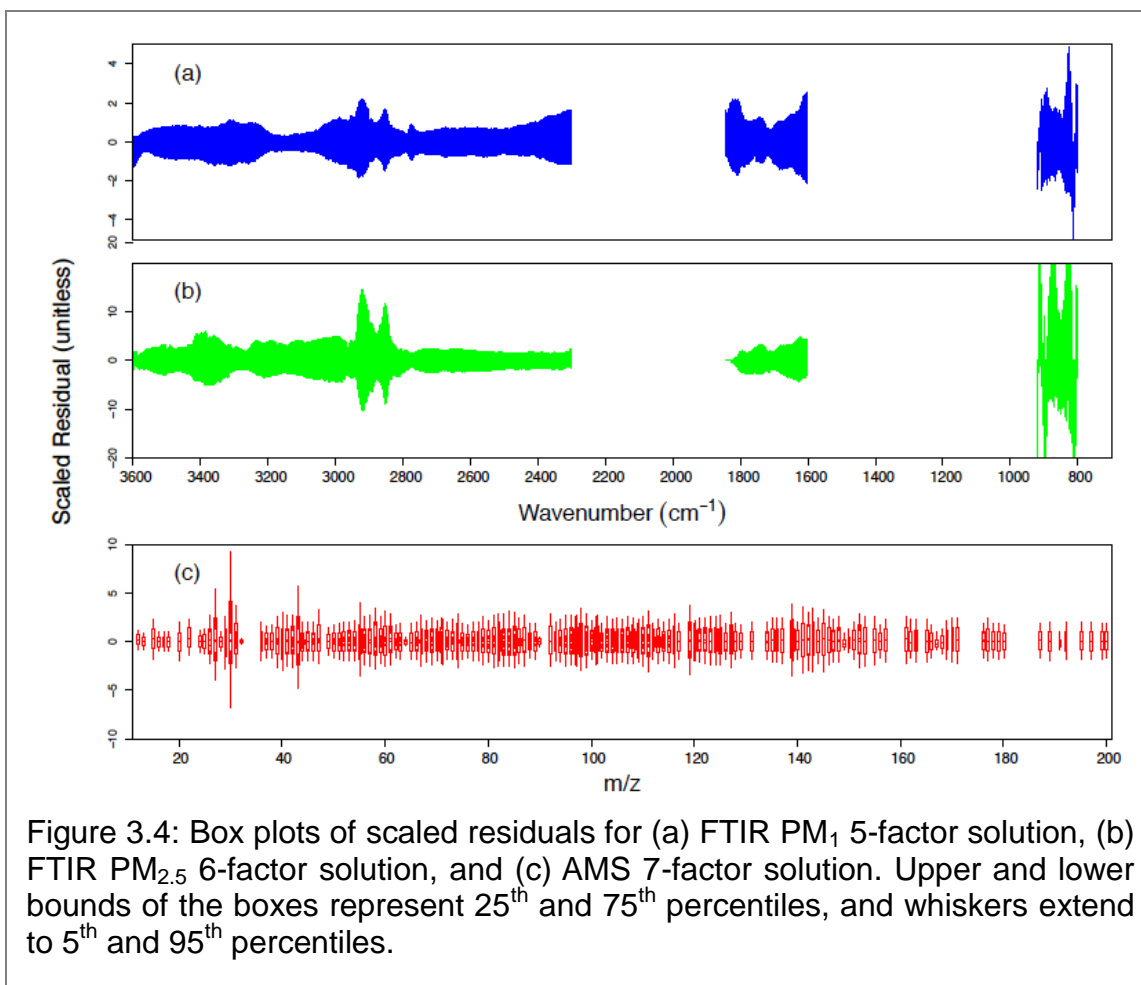


Table 3.1: Correlations of FTIR factors in PM<sub>2.5</sub> to source markers.

Source Type	Source Markers	Aromatic SOA					Alkane SOA					NOA		PO SOA		Vegetative detritus										
PAH	Methylanthracene	0.59	0.67	0.67	0.56	0.18	0.66	0.74	0.74	0.65	0.49	0.45	0.41	0.41	0.26	0.59	-0.20	-0.14	-0.14	0.00	0.07	-0.30	-0.33	-0.33	-0.34	-0.24
	Methylphenanthracene-1	0.73	0.61	0.68	0.63	0.67	0.66	0.67	0.53	0.68	0.58	0.56	0.47	0.49	0.53	0.90	0.65	0.85	0.58	0.53	-0.52	-0.52	-0.03	-0.53	-0.56	
	Methylphenanthracene	0.45	0.41	0.41	0.26	0.59	-0.18	0.06	0.24	-0.09	-0.04	0.16	0.02	-0.05	0.29	-0.16	0.07	0.07	0.04	0.67	0.74	0.47	0.73	0.78		
	Naphthalene-2-phenyl	0.02	0.05	0.29	-0.16	0.07	0.07	0.04	0.67	0.74	0.47	0.73	0.78	-	-	-	-	-	-	-	-	-	-	-	-	
	1, 2-Benzanthracene	0.01	0.01	-0.19	-0.14	0.07	-0.32	-0.04	-0.31	-0.26	-0.10	-0.25	-0.25	-	-	-	-	-	-	-	-	-	-	-	-	
PAH SOA	2H-1-benzopyran-2-one	-0.27	-0.29	-0.34	-0.30	-0.25	-0.12	-0.24	-0.24	0.03	-0.50	-0.35	-0.34	-0.18	0.78	0.81	0.81	0.57	0.04	-0.03	-0.34	-0.04	-0.13	-		
	Dibenzofuran	0.73	0.61	0.68	0.63	0.67	0.66	0.67	0.53	0.68	0.58	0.56	0.47	0.49	0.53	0.90	0.65	0.85	0.58	0.53	-0.52	-0.52	-0.03	-0.53	-0.56	
	1,8-Naphthalic acid/Naphthalic anhydride	0.45	0.41	0.41	0.26	0.59	-0.18	0.06	0.24	-0.09	-0.04	0.16	0.02	-0.05	0.29	-0.16	0.07	0.07	0.04	0.67	0.74	0.47	0.73	0.78		
	Benzophenone	0.02	0.05	0.29	-0.16	0.07	0.07	0.04	0.67	0.74	0.47	0.73	0.78	-	-	-	-	-	-	-	-	-	-	-	-	
	4-hydroxy-9-fluorenone	0.01	0.01	-0.19	-0.14	0.07	-0.32	-0.04	-0.31	-0.26	-0.10	-0.25	-0.25	-	-	-	-	-	-	-	-	-	-	-	-	
Phthalic acid/Phthalic anhydride	-0.27	-0.29	-0.34	-0.30	-0.25	-0.12	-0.24	-0.24	0.03	-0.50	-0.35	-0.34	-0.18	0.78	0.81	0.81	0.57	0.04	-0.03	-0.34	-0.04	-0.13	-			
Alkane	Heptadecane	0.45	0.41	0.41	0.26	0.59	-0.18	0.06	0.24	-0.09	-0.04	0.16	0.02	-0.05	0.29	-0.16	0.07	0.07	0.04	0.67	0.74	0.47	0.73	0.78		
	Octadecane	0.02	0.05	0.29	-0.16	0.07	0.07	0.04	0.67	0.74	0.47	0.73	0.78	-	-	-	-	-	-	-	-	-	-	-	-	
Alkane SOA	Undecanone	0.01	0.01	-0.19	-0.14	0.07	-0.32	-0.04	-0.31	-0.26	-0.10	-0.25	-0.25	-	-	-	-	-	-	-	-	-	-	-	-	
	Dodecanone	-0.27	-0.29	-0.34	-0.30	-0.25	-0.12	-0.24	-0.24	0.03	-0.50	-0.35	-0.34	-0.18	0.78	0.81	0.81	0.57	0.04	-0.03	-0.34	-0.04	-0.13	-		
	Tridecanone	0.45	0.41	0.41	0.26	0.59	-0.18	0.06	0.24	-0.09	-0.04	0.16	0.02	-0.05	0.29	-0.16	0.07	0.07	0.04	0.67	0.74	0.47	0.73	0.78		
	Tetradecanone	0.02	0.05	0.29	-0.16	0.07	0.07	0.04	0.67	0.74	0.47	0.73	0.78	-	-	-	-	-	-	-	-	-	-	-	-	
Biogenic SOA	pinonaldehyde	0.01	0.01	-0.19	-0.14	0.07	-0.32	-0.04	-0.31	-0.26	-0.10	-0.25	-0.25	-	-	-	-	-	-	-	-	-	-	-	-	
	V	-0.27	-0.29	-0.34	-0.30	-0.25	-0.12	-0.24	-0.24	0.03	-0.50	-0.35	-0.34	-0.18	0.78	0.81	0.81	0.57	0.04	-0.03	-0.34	-0.04	-0.13	-		
Petroleum operation	Si	0.45	0.41	0.41	0.26	0.59	-0.18	0.06	0.24	-0.09	-0.04	0.16	0.02	-0.05	0.29	-0.16	0.07	0.07	0.04	0.67	0.74	0.47	0.73	0.78		
	Ca	0.02	0.05	0.29	-0.16	0.07	0.07	0.04	0.67	0.74	0.47	0.73	0.78	-	-	-	-	-	-	-	-	-	-	-	-	
	Al	0.01	0.01	-0.19	-0.14	0.07	-0.32	-0.04	-0.31	-0.26	-0.10	-0.25	-0.25	-	-	-	-	-	-	-	-	-	-	-	-	
	Mg	-0.27	-0.29	-0.34	-0.30	-0.25	-0.12	-0.24	-0.24	0.03	-0.50	-0.35	-0.34	-0.18	0.78	0.81	0.81	0.57	0.04	-0.03	-0.34	-0.04	-0.13	-		
Dust	Hexadecanoic acid <sup>a</sup>	0.45	0.41	0.41	0.26	0.59	-0.18	0.06	0.24	-0.09	-0.04	0.16	0.02	-0.05	0.29	-0.16	0.07	0.07	0.04	0.67	0.74	0.47	0.73	0.78		
		0.02	0.05	0.29	-0.16	0.07	0.07	0.04	0.67	0.74	0.47	0.73	0.78	-	-	-	-	-	-	-	-	-	-	-	-	
Cooking		0.01	0.01	-0.19	-0.14	0.07	-0.32	-0.04	-0.31	-0.26	-0.10	-0.25	-0.25	-	-	-	-	-	-	-	-	-	-	-	-	
		-0.27	-0.29	-0.34	-0.30	-0.25	-0.12	-0.24	-0.24	0.03	-0.50	-0.35	-0.34	-0.18	0.78	0.81	0.81	0.57	0.04	-0.03	-0.34	-0.04	-0.13	-		

<sup>a</sup> Correlations are not reported for the cooking marker since less than 10 data points remained after averaging-to-filter sampling times





Solutions with 2 to 8 factors were investigated to determine the optimal number of factors. In Group I, the input matrix was best interpreted by a 7-factor solution, because one or more physically meaningful factors with significant masses (> 15% OM) were missing for solutions with 6 or fewer factors; when 8 factors were applied, small (< 6% OM) and highly correlated ( $r$  of 0.80) factors were generated, indicating that some factors split into smaller factors that correlated in time, which could not be identified. In Group II, solutions with 7 or more factors contained highly correlated factors (e.g.,  $F_1$  and  $F_7$  correlated with an  $r$  of 0.82 in the 7-factor solution). Compared to Group I solutions, some of Group II's factors had weaker correlations to the source markers, and more than one factor correlated to the same source markers, which resulted in indistinguishable factors. For example,  $F_1$  and  $F_7$  did not significantly correlate to any group of source markers;  $F_4$  and  $F_5$  correlated to cooking organic aerosol marker hexadecanoic acid (Table 3.1). The solutions with less than 7 factors in Group II were not preferred since our goal is to maximize sources. Therefore, the 7-factor solution in Group I was selected. The summed residual of this solution fluctuated around 0, with an absolute amplitude smaller than  $0.2 \mu\text{g m}^{-3}$  (Figure 3.3c)—much smaller than OM variability of  $2.2 \mu\text{g m}^{-3}$ . The pattern of scaled residuals

resembled random noise (Figure 3.4c), indicating the measurement was well fit by the factors.

### **3.4 Summary**

We have applied the PMF analysis to the independent FTIR (including PM<sub>1</sub> and PM<sub>2.5</sub>) and AMS measurements. Solutions were grouped by number of factors, rotational values, and seed values. Mathematical criteria were used to evaluate PMF model fitting and facilitate the solution selection. The extracted factors, by comparing their time series with the time series of source markers, can be linked to emission sources or atmospheric processes, which will be discussed in the next chapter.

## 4.0 Identification and Comparison of Factors from the FTIR and AMS Measurements<sup>4</sup>

The main factors contributing to the OM were identified separately from FTIR (PM<sub>1</sub> and PM<sub>2.5</sub>) and AMS measurements using positive matrix factorization (PMF) method (PMF2) [Paatero and Tapper, 1994] described in the previous chapter. The factors were identified primarily by their correlations with particle-phase source markers, facilitated by comparisons of factor composition and spectra to factors identified from past studies. Subscripts “FTIR,” “FTIR2.5,” and “AMS” denote the factors commonly identified from FTIR PM<sub>1</sub>, FTIR PM<sub>2.5</sub>, and AMS measurements. Detailed factor identification procedures are presented below.

### 4.1 Factors Identified from FTIR PM<sub>1</sub> and PM<sub>2.5</sub> Measurements

Five factors were identified from FTIR PM<sub>1</sub> and PM<sub>2.5</sub> measurements (described in Section 3.0). The PM<sub>1</sub> and PM<sub>2.5</sub> factors were similar in factor spectra and compositions (Figure 4.1a), indicating nearly the same factors were found for OM<sub>1</sub> and OM<sub>2.5</sub> (consistent with the fact that 75% of OM<sub>2.5</sub> was in OM<sub>1</sub>).

The first factor covaried in time with polycyclic aromatic hydrocarbon (PAH) oxidation products 2H-1-benzopyran-2-one, dibenzofuran, 1,8-naphthalic acid/anhydride, benzophenone, 4-hydroxy-9-fluorenone, and phthalic acid/anhydride [Kautzman *et al.*, 2010; Lee and Lane, 2009; 2010; Webb *et al.*, 2006] measured by thermal desorption aerosol GC-MS (TAG) (Table 4.1) and phthalic acid ( $r = 0.7$ ) measured by GC-MS. The factor composition, largely composed of non-acid carbonyl groups (59%), was consistent with oxidation products for aromatic hydrocarbons [Chan *et al.*, 2009; Jaoui *et al.*, 2008; Russell *et al.*, 2011], including PAH and light aromatic compounds. Therefore, this factor was identified as an aromatic SOA factor, representing SOA formed from aromatic hydrocarbons (PAHs and light aromatic compounds) that were likely emitted from gasoline- and diesel-powered vehicles [Schauer *et al.*, 1999; 2002b].

---

<sup>4</sup> Work presented in this section is published by Liu *et al.* [2012a].

The time series of the second factor correlated most strongly to the time series of C<sub>11</sub>-C<sub>14</sub> ketones (undecanone, dodecanone, tridecanone, and tetradecanone) with *r* of 0.63 to 0.77 for the PM<sub>1</sub> factor and 0.58 to 0.90 for the PM<sub>2.5</sub> factor (Table 4.1 and Table 3.1). (Enhanced correlations for the PM<sub>2.5</sub> factor were likely caused by longer averaging time intervals.) Long-chain (C<sub>11</sub>-C<sub>14</sub>) ketones have been previously suggested to be first-generation alkane oxidation products [Lim and Ziemann, 2005; 2009], indicating that this factor was likely formed from alkane oxidation processes. The factor spectra and functional group compositions were nearly identical to the fossil fuel combustion factors identified from the shipboard measurements near Houston and the ground-based measurements in Southern California, which were suggested to originate from alkane oxidation processes [Hawkins and Russell, 2010; Liu et al., 2011; Russell et al., 2009]. Thus this factor was denoted as alkane SOA factor.

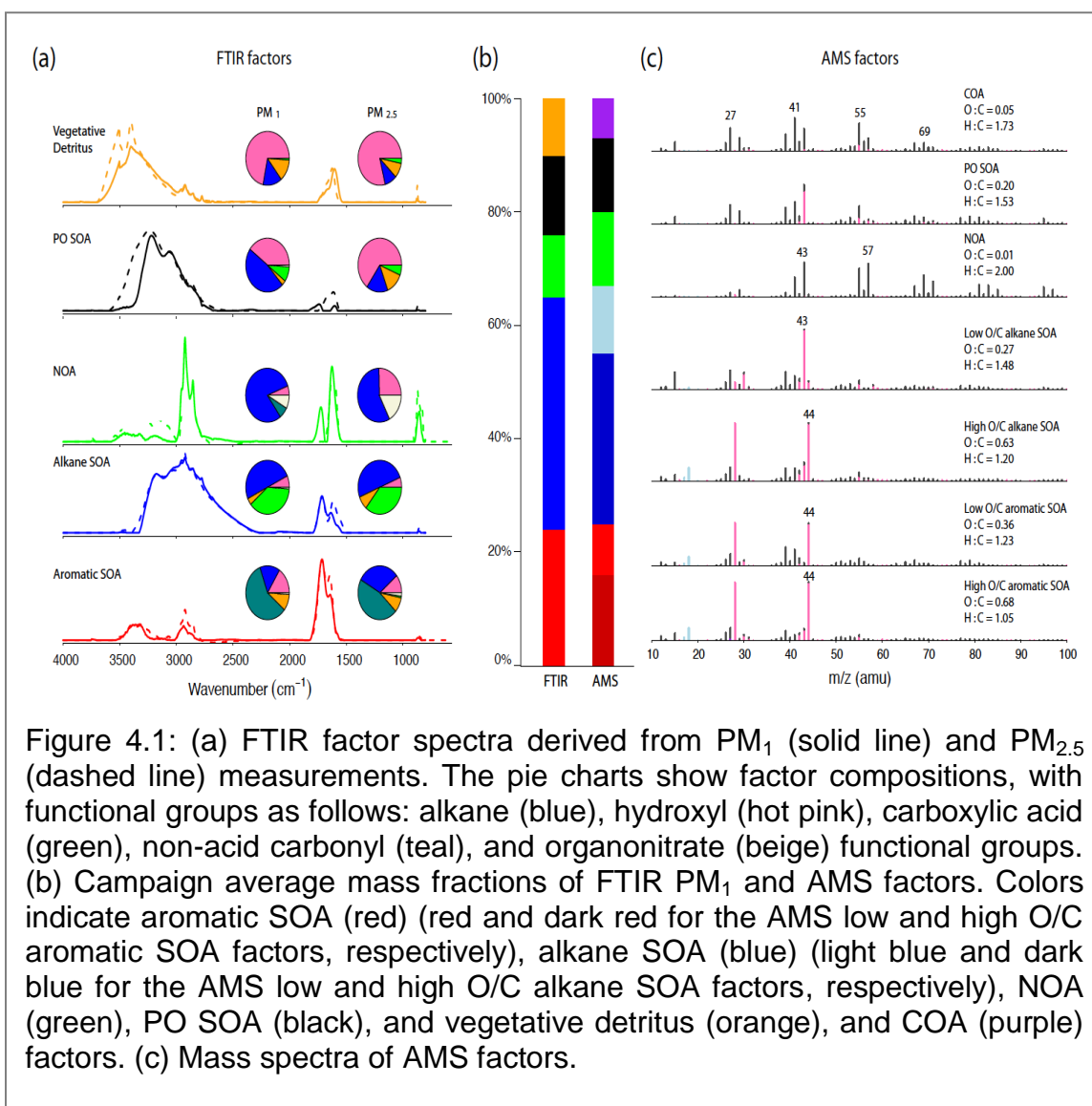


Figure 4.1: (a) FTIR factor spectra derived from PM<sub>1</sub> (solid line) and PM<sub>2.5</sub> (dashed line) measurements. The pie charts show factor compositions, with functional groups as follows: alkane (blue), hydroxyl (hot pink), carboxylic acid (green), non-acid carbonyl (teal), and organonitrate (beige) functional groups. (b) Campaign average mass fractions of FTIR PM<sub>1</sub> and AMS factors. Colors indicate aromatic SOA (red) (red and dark red for the AMS low and high O/C aromatic SOA factors, respectively), alkane SOA (blue) (light blue and dark blue for the AMS low and high O/C alkane SOA factors, respectively), NOA (green), PO SOA (black), and vegetative detritus (orange), and COA (purple) factors. (c) Mass spectra of AMS factors.

The third factor from the PM<sub>1</sub> factor analysis correlated ( $r$  of 0.65) with pinonaldehyde measured by TAG and 3-Hydroxyglutaric acid ( $r$  of 0.5) measured by GC-MS, which are markers for biogenic SOA formed from oxidation of  $\alpha$ -pinene [Claeys *et al.*, 2007; Hallquist *et al.*, 1999]. This factor, observed in high concentrations at night, was largely composed of alkane groups (79%) and had the largest mass fraction (8%) of organonitrate groups of all the factors; its composition was consistent with products from  $\alpha$ -pinene and  $\beta$ -pinene oxidation by NO<sub>3</sub> radicals [Hallquist *et al.*, 1999; Wangberg *et al.*, 1997]. However, the factor showed a weaker correlation ( $r \leq 0.50$ ) with PAH compounds, suggesting a contribution of primary anthropogenic sources to this factor. Thus, this factor was determined to be the nighttime biogenic SOA factor mixed with less oxygenated hydrocarbon-like anthropogenic emissions and denoted as NOA. The PM<sub>2.5</sub> nighttime OA (NOA) factor had similar composition to the PM<sub>1</sub> NOA factor, being dominated by alkane (57%) and organonitrate (17%) groups, but also contained a larger hydroxyl group mass and enhanced correlations to dust elements. Thus, the PM<sub>2.5</sub> NOA factor likely included a small fraction of dust-related organic components.

The fourth factor (of PM<sub>1</sub>) correlated ( $r$  of 0.6) with the crude oil marker V (vanadium) [Khalaf *et al.*, 1982]. Its IR spectrum was comparable to the “oil combustion/refining” factor spectrum identified from the shipboard measurements near Houston [Russell *et al.*, 2009]. High mass fraction (40% to 65%) of hydroxyl groups indicates that this factor was likely secondarily formed in the atmosphere. The factor was identified as a petroleum operation SOA (PO SOA) factor, representing the oil extraction and refinery operations north and northwest of Bakersfield. The most commonly used method for oil extraction, steam injection, heats crude oil using high-temperature steams. The heated crude oil has reduced viscosity thereby it is easier to flow [Fatemi and Jamaloei, 2011]. The high-temperature steam comes from steam generators, which usually burns crude oil and likely emits vanadium-rich pollutants (in addition to NO<sub>x</sub>, CO, and hydrocarbons) [Myers, 1986]. The corresponding PM<sub>2.5</sub> factor spectrum was comparable to that of the PM<sub>1</sub> factor (Figure 4.1), suggesting that they are the same factors. It is worth noting that V in PM<sub>2.5</sub> correlated well with dust elements, such as V correlating to Si with an  $r$  of 0.96 in PM<sub>2.5</sub> (in contrast, the correlation coefficient of V and Si in PM<sub>1</sub> was 0.35), indicating that V in PM<sub>2.5</sub> was largely from dust sources [Chow *et al.*, 2003], resulting in a weakly negative correlation of the PO SOA factor and V in PM<sub>2.5</sub>.

The fifth factor of the PM<sub>1</sub> and PM<sub>2.5</sub> solutions correlated to the dust elements Si, Al, Ca, and Mg, suggesting that the factor represented organic components associated with dust particles. Double peaks at 2850 cm<sup>-1</sup> and 2920 cm<sup>-1</sup>, along with a strong spectral absorption at 3500 cm<sup>-1</sup>, indicated the existence of methylene and phenol groups, which likely originated from plant wax [Hawkins and Russell, 2010] and plant lignin compounds [Cass, 1998], respectively. The large fraction of hydroxyl groups (71% to 79%) in this factor was consistent with saccharide-type compounds in plant materials [Bianchi *et al.*, 1993]. Association

of the factor with dust and plant components suggests that this factor was likely from vegetative detritus that resuspended with dust particles.

Table 4.1: Correlations of FTIR factors in PM<sub>1</sub> to source markers.

	PAH					PAH SOA					Alkane		Alkane SOA				Biogenic SOA Petroleum operation		Dust				Cooking	
	Source Markers					Source Markers					Source Markers		Source Markers				Source Markers		Source Markers				Source Markers	
	Methylanthracene	Methylphenanthracene-1	Methylphenanthracene	Naphthalene-2-phenyl	1, 2-Benzanthracene	2H-1-benzopyran-2-one	Dibenzofuran	1,8-Naphthalic acid/Naphthalic anhydride	Benzophenone	4-hydroxy-9-fluorenone	Phthalic acid/Phthalic anhydride	Heptadecane	Octadecane	Undecanone	Dodecanone	Tridecanone	Tetradecanone	Pinonaldehyde	V	Si	Ca	Al	Mg	Hexadecanoic acid <sup>a</sup>
Vegetative detritus	-0.01	-0.07	-0.07	-0.03	0.15	-0.22	-0.05	-0.03	-0.07	-0.05	-0.08	-0.09	-0.14	0.42	0.18	0.13	0.04	-0.08	0.04	0.82	0.74	0.90	0.94	-
PO SOA	0.11	0.11	0.05	0.12	-0.07	0.36	0.37	-0.09	0.39	0.21	0.28	-0.04	-0.10	0.42	0.03	0.32	0.26	0.12	0.60	0.02	-0.06	-0.01	-0.06	-
NOA	0.50	0.47	0.47	0.40	0.37	-0.16	-0.17	0.04	-0.31	-0.20	0.01	0.50	0.53	0.2	-0.10	0.47	-0.07	0.65	-0.06	-0.01	0.07	-0.01	-0.03	-
Alkane SOA	0.56	0.50	0.50	0.54	0.13	0.72	0.35	0.63	0.43	0.58	0.58	0.38	0.46	0.71	0.65	0.63	0.77	0.28	-0.01	0.19	0.22	0.15	0.06	-
Aromatic SOA	0.49	0.54	0.54	0.47	0.17	0.75	0.73	0.69	0.67	0.67	0.62	0.21	0.16	0.65	0.39	0.60	0.56	0.24	0.15	0.28	0.16	0.25	0.12	-

<sup>a</sup>Correlations are not reported for the cooking marker since less than 10 data points remained after averaging-to-filter sampling times.

Table 4.2: Correlations of AMS Group I factors to source markers.

	PAH					PAH SOA					Alkane		Alkane SOA				Biogenic SOA	Petroleum Operation	Dust					Cooking
	Source Markers					Source Markers					Source Markers		Source Markers				Source Markers	Source Markers	Source Markers					Source Markers
	Methylanthracene	Methylphenanthracene-1	Methylphenanthracene	Naphthalene-2-phenyl	1, 2-Benzanthracene	2H-1-benzopyran-2-one	Dibenzofuran	1,8-Naphthalic acid/Naphthalic anhydride	Benzophenone	4-hydroxy-9-fluorenone	Phthalic acid/Phthalic anhydride	Heptadecane	Octadecane	Undecanone	Dodecanone	Tridecanone	Tetradecanone	pinonaldehyde	V	Si	Ca	Al	Mg	Hexadecanoic acid
Low O/C aromatic SOA	0.90	0.84	0.84	0.82	0.81	0.43	0.32	0.69	0.26	0.39	0.38	0.56	0.60	0.58	0.49	0.66	0.62	0.35	0.00	0.35	0.38	0.31	0.22	0.43
Low O/C alkane SOA	0.72	0.78	0.78	0.73	0.57	0.29	0.07	0.67	-0.02	0.32	0.17	0.66	0.66	0.59	0.73	0.81	0.68	0.69	-0.09	0.08	0.12	0.08	-0.05	0.25
High O/C aromatic SOA	0.42	0.46	0.42	0.45	0.38	0.64	0.37	0.65	0.44	0.62	0.49	0.25	0.27	0.28	0.52	0.71	0.66	0.15	-0.03	0.32	0.29	0.29	0.14	0.62
High O/C alkane SOA	0.55	0.61	0.60	0.56	0.43	0.78	0.61	0.68	0.70	0.66	0.60	0.37	0.38	0.52	0.38	0.54	0.50	0.44	0.02	0.38	0.36	0.34	0.22	0.27
NOA	0.32	0.25	0.26	0.31	0.36	-0.07	-0.18	0.04	-0.27	-0.13	-0.07	0.21	0.22	0.00	0.49	0.29	0.27	0.00	-0.17	-0.10	0.00	-0.11	-0.10	0.15
PO SOA	-0.12	-0.12	-0.10	-0.04	-0.32	0.38	0.17	-0.13	0.24	0.31	0.28	0.01	0.08	0.21	0.22	0.10	0.07	0.16	0.40	0.07	0.10	0.03	0.01	0.19
COA	-0.19	-0.22	-0.21	-0.13	-0.09	0.07	-0.13	-0.27	-0.11	0.05	-0.14	-0.10	-0.03	-0.25	0.33	0.14	0.15	-0.13	-0.03	-0.18	-0.17	-0.18	-0.16	0.68

## 4.2 Factors Identified from AMS Measurements

Seven factors were identified from the AMS measurements. The factor m/z spectra, O/C, and H/C are shown in Figure 4.1c.

The first factor correlated strongly ( $r$  of 0.81 to 0.90) to particle-phase PAH marker compounds (Table 4.2), which are usually coemitted with light aromatic compounds in vehicular exhausts. This factor was characterized by a strong peak at m/z 44 and had an O/C of 0.36, which was higher than the typical O/C of hydrocarbon-like organic aerosol (HOA) components ( $\sim$ 0.10) observed in laboratory and field studies (Table 4.3) but in the O/C range of 0.20 to 0.60 for SV-OOA (semivolatile OOA) identified from a number of AMS measurements [Ng *et al.*, 2010]. Thus, it suggests that this factor was oxidized but associated with a low oxidation state and, so, was termed low O/C aromatic SOA factor.

Compared to the low O/C aromatic SOA factor, the second factor more closely correlated with long-chain alkanes and alkane SOA components but showed a weaker correlation to PAH hydrocarbons (Table 4.2), suggesting that this factor likely originated from alkane-related sources. The H/C of this factor was 21% higher than the H/C of the low O/C aromatic SOA factor (Figure 4.1c). This result is consistent with the expectation of a higher H/C for alkane SOA (compared to aromatic SOA) because their precursors (alkanes) are more saturated than aromatics. As the factor O/C (0.27) was higher than expected for primary OM ( $\sim$ 0.10) (Table 4.3), it was identified as a low O/C alkane SOA factor.

Table 4.3: Summary of O/C values for primary or HOA components from previous studies and O/C of SOA components in this study.

Source type	O/C <sup>a</sup>	References
Primary OA	< 0.1	This study
HOA (New York City)	0.06	<i>Sun et al.</i> , [2011]
HOA (Mexico City aircraft)	0.06	<i>DeCarlo et al.</i> , [2010]
Diesel exhaust	0.03	<i>Aiken et al.</i> , [2008]
Gasoline exhaust	0.05	<i>Nakao et al.</i> , [2011]
NOA	0.04	<i>Aiken et al.</i> , [2008]
COA	0.01	This study
	0.05	This study
Secondary OA	0.20–0.68	<i>Liu et al.</i> , [2011] (and references therein)
Alkane OA	0.27–0.63	
Aromatic OA	0.36–0.68	This study
PO SOA	0.20	

<sup>a</sup>AMS-measured O/C excludes organonitrate and organosulfate contributions to O as the nitrate and sulfate components were not distinguishable from inorganic.



The third and fourth factors had the highest O/C (~0.65) of all the factors, suggesting they were also secondary but more oxidized than the first two factors—possibly because they formed in later generations [Jimenez *et al.*, 2009]. Both factor spectra were nearly identical and resembled those of LV-OOA (low-volatility OOA) [Ulbrich *et al.*, 2009]. The time series of the two factors correlated to PAH SOA and alkane SOA marker compounds. While the similarity of the factor spectra and their correlations make it difficult to trace their sources, their diurnal cycles were different (Figure 4.2a and 4.2b). The third factor peaked at noon and in the evening (2000 hr), while the fourth factor had a broad peak centered at 1500 hr. Distinct diurnal cycles suggested different formation pathways. The third and fourth factors correlated weakly to long-chain alkane compounds (e.g., heptadecane and octadecane in Table 4.2), with the latter having stronger correlations ( $r$  of 0.25 to 0.27 for the third factor and  $r$  of 0.37 to 0.38 for the fourth factor). Furthermore, enhanced correlations (to alkane compounds) of 0.63 to 0.72 resulted from daily-averaged concentration of the fourth factor, but such a large enhancement was not observed under the same conditions for the third factor ( $r$  of 0.37 to 0.46). This suggests that the fourth factor was likely largely linked to alkane-related sources (although contribution of aromatic SOA to this factor cannot be entirely ruled out), while the third factor likely formed from aromatic-related processes. Accordingly, the third and fourth factors were defined as high O/C aromatic SOA and high O/C alkane SOA, respectively. The high O/C alkane SOA accounted for 71% of total alkane SOA (including high and low O/C alkane SOA components), consistent with mechanism simulation that suggests more than 67% of alkane SOA was fourth and higher generation products after 10 hrs of reactions [Yee *et al.*, 2012].

Concentrations of the fifth factor peaked at night (Figure 4.2c), having been associated with nighttime easterly and southeasterly winds. This pattern compares to that of monoterpenes and their oxidation products (e.g., pinonaldehyde), which suggests contributions from biogenic sources to this factor. The very low O/C (<0.1) also indicates a contribution from primary OM. The mass spectrum was similar to spectrum of HOA [Ulbrich *et al.*, 2007; Ulbrich *et al.*, 2009], indicating unoxidized primary anthropogenic sources. As such, this factor was identified as nighttime OA (NOA).

The sixth factor had a stronger correlation to V than any other source markers. In addition, the factor's diurnal cycle matched the diurnal cycle of V, suggesting organic components from petroleum operations. The factor was characterized by  $m/z$  43 (87%  $C_2H_3O^+$  and 13%  $C_3H_7^+$ ) with an O/C of 0.20, which is larger than 0.10 that is typical for HOA (Table 4.2). For this reason, this factor is considered secondary rather than primary and termed petroleum operation SOA (PO SOA).

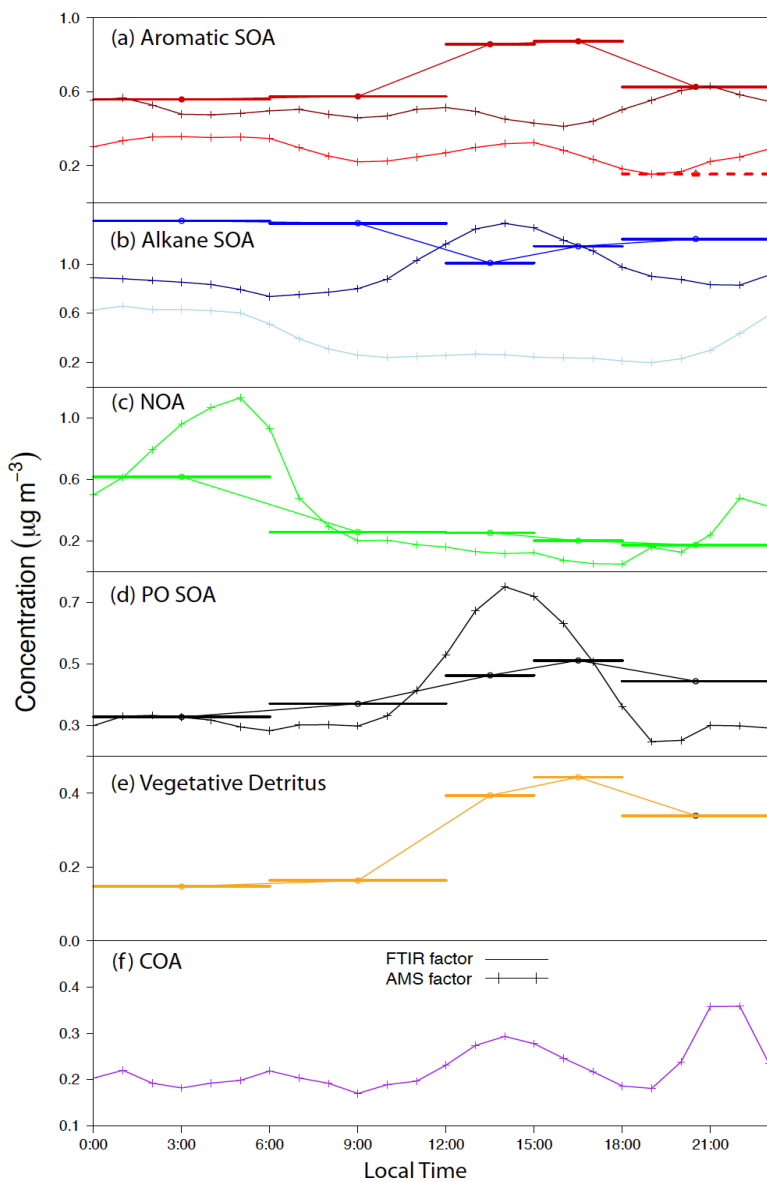


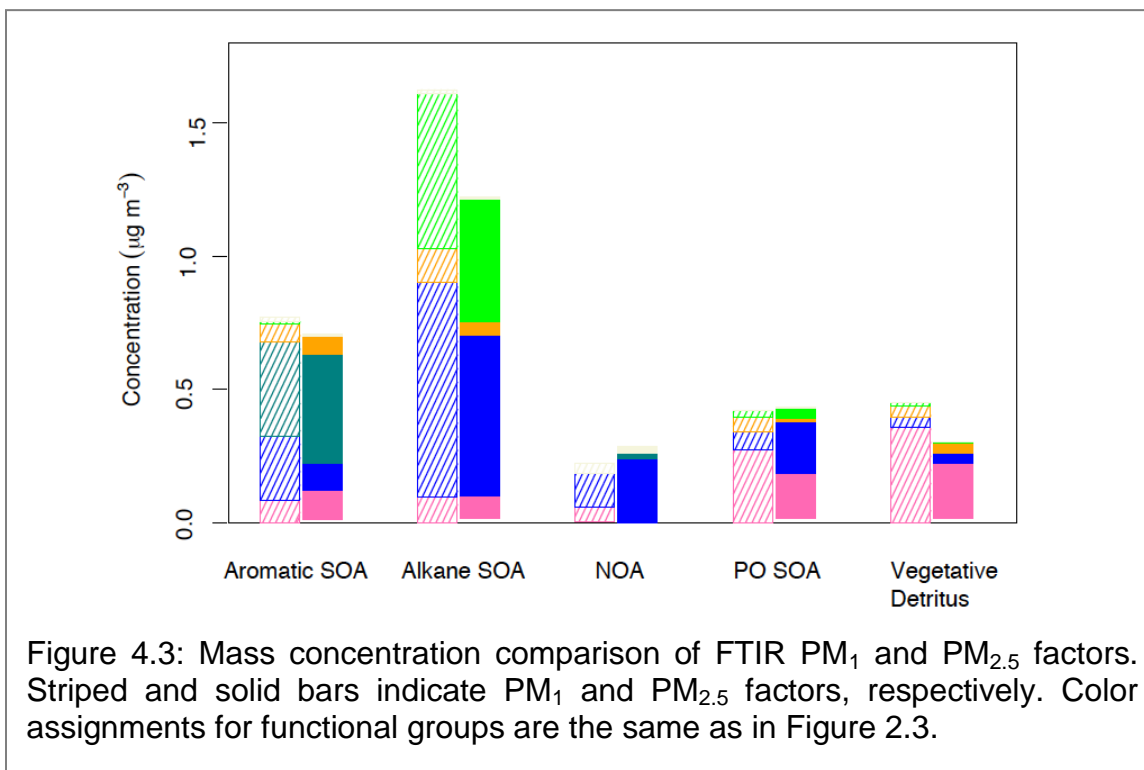
Figure 4.2: Diurnal cycles for (a) aromatic SOA<sub>FTIR</sub> (red), low O/C aromatic SOA<sub>AMS</sub> (red), and high O/C aromatic SOA<sub>AMS</sub> (dark red), (b) alkane SOA<sub>FTIR</sub> (blue), low O/C alkane SOA<sub>AMS</sub> (light blue), and high O/C alkane SOA<sub>AMS</sub> (dark blue), (c) NOA<sub>FTIR</sub> (green) and NOA<sub>AMS</sub> (green), (d) PO SOA<sub>FTIR</sub> (black) and PO SOA<sub>AMS</sub> (black), (e) vegetative detritus (orange), and (f) COA (purple) factors. In each panel, horizontal bars represent FTIR factors (PM<sub>1</sub> samples), with bar lengths indicating sampling duration; lines with markers represent AMS factors.

The seventh factor was identified as a cooking organic aerosol (COA) factor for two reasons: The factor spectrum was characterized by m/z 27, 41, 55, and 69 (with  $\Delta m/z$  of 14), fragments specific for unsaturated fatty acids emitted from cooking activities [He *et al.*, 2010]; and the factor correlated to the food cooking

marker hexadecanoic acid (Table 4.2) [Allan *et al.*, 2010; He *et al.*, 2004]. Further, a low O/C (0.05) suggests that this factor was simply recondensed cooking oils from local sources that had undergone little or no oxidation in the atmosphere.

### 4.3 Comparison of FTIR (PM<sub>1</sub> and PM<sub>2.5</sub>) and AMS Factors

The FTIR PM<sub>1</sub> and PM<sub>2.5</sub> factors were similar in compositions but differed in mass. Overall, the reconstructed ratio of OM<sub>1</sub> (the sum of PM<sub>1</sub> factors) to OM<sub>2.5</sub> (the sum of PM<sub>2.5</sub> factors) was 0.85, 9% higher than the actual measured OM<sub>1</sub>/OM<sub>2.5</sub> of 0.75. The greatest difference between PM<sub>1</sub> and PM<sub>2.5</sub> factors was observed in the vegetative detritus factor, the OM being 55% higher in PM<sub>2.5</sub>. This difference was largely (92%) attributed to hydroxyl groups (Figure 4.3), which likely originated from plant materials and then mixed with dusts to result in a larger fraction with bigger particles. The aromatic SOA and alkane SOA factors were 12% and 33% higher, respectively, in PM<sub>2.5</sub>, with the alkane groups accounting for the largest difference in each pair of factors. As aforementioned, the NOA<sub>FTIR2.5</sub> likely had some dust fractions, indicating incomplete separation of this factor from PM<sub>2.5</sub> samples, so NOA<sub>FTIR2.5</sub> was slightly smaller than NOA<sub>FTIR</sub>. The PO SOA<sub>FTIR</sub> was higher in the alkane group mass and lower in the hydroxyl group mass compared to the PO SOA<sub>FTIR2.5</sub>, resulting in comparable total OM between the two factors.



The factors identified from AMS measurements show consistencies and differences to the factors derived from FTIR measurements. The low O/C and high O/C aromatic SOA<sub>AMS</sub> factors, taken together, correlated to aromatic SOA<sub>FTIR</sub> with an  $r$  of 0.73. The sum of the low and high O/C aromatic SOA<sub>AMS</sub> factors accounted for 25% of OM, consistent with the OM fraction (24%) of the aromatic SOA<sub>FTIR</sub> factor (Figure 4.1b). Similarly, good correlation ( $r = 0.74$ ) was observed for the alkane SOA<sub>AMS</sub> factor (the sum of low and high O/C alkane SOA<sub>AMS</sub> factors) and the alkane SOA<sub>FTIR</sub> factor, each of which accounted for 41% to 42% of the OM. The PO SOA<sub>AMS</sub> and PO SOA<sub>FTIR</sub> (correlated with an  $r$  of 0.52) contributed 13% to 14% of OM. The campaign-average mass fractions of NOA<sub>FTIR</sub> and NOA<sub>AMS</sub> factors were 10% to 13%, with higher fractions (21% to 24%) during 0000–0600 hr. These factors correlated with an  $r$  of 0.52. The vegetative detritus factor (10% OM) was identified only from FTIR measurements, likely because this component was mixed with dust in particles of 500 nm and larger, which could not be vaporized, making them unlikely to be detected by the AMS. The COA<sub>AMS</sub> (7% OM) was not found in the FTIR measurements. This difference between the AMS and FTIR factors may be due to COA components mainly existing as small particles (100–200 nm, as discussed in Section 4.3), where the 50% collection efficiency of 1- $\mu$ m Teflon filters [Liu and Lee, 1976] and the small mass in this size range made the FTIR less sensitive.

Table 4.4: Source inventory of primary PM<sub>2.5</sub> for Kern County in the San Joaquin Valley in 2008 (downloaded from <http://www.arb.ca.gov/ei/emissiondata.htm> and shown as percentage of PM<sub>2.5</sub>) and sources of OM identified in this study (shown as percentage of OM<sub>2.5</sub>).

Source type	Inventory (%)	This study (%)
Mobile motor sources	31 (80) <sup>a</sup>	65
Petroleum production and refining	0 (1)	14
Miscellaneous processes		
Dust	16 (14)	10
Cooking	2 (4)	7
Residential fuel combustion	7	ND <sup>b</sup>
Farming operations	9	ND
Construction and demolition	1	ND
Managed burning and disposal	6	ND
Fuel (mainly natural gas) combustion	14	ND
Industrial processes	13	ND
Solvent evaporation	0	ND
Waste disposal	0	ND
Cleaning and surface coatings	0	ND

<sup>a</sup>The numbers in the parentheses represent percentage out of the four sources (mobile motor sources, petroleum production and refining, dust, and cooking) that are commonly identified in the emission source inventory and from this study.

<sup>b</sup>ND represents sources that were not detected from this study.

#### 4.4 Conclusions

In summary, factors identified from FTIR ( $PM_{10}$  and  $PM_{2.5}$ ) and AMS measurements showed good agreement in source type, mass fraction, and time series. While the PMF factors of the two measurement types were complementary and similar, the solutions had minor differences in the COA and vegetative detritus sources. The missing vegetative detritus factor (for the AMS measurements) and COA factor (for the FTIR measurements) contributed 10% of OM in  $PM_{10}$ , and both were within the expected uncertainties for each technique. The high O/C aromatic and alkane SOA factors were mathematically independent ( $r < 0.7$ ) but their mass spectra were chemically similar (cosine similarity was 0.99) (cosine similarity is defined as cosine of the angle between two vectors [Stein and Scott, 1994], values ranging from 0 to 1, with higher values indicating higher similarity), thus source markers are needed to justify separation of these factors; in contrast, the FTIR aromatic and alkane SOA factors were mathematically independent ( $r < 0.5$ ) and their IR spectra were chemically different (e.g., cosine similarity was 0.3), thus source markers are not needed to justify separation of the FTIR factors but provide a link to their precursors.

The FTIR and AMS factors suggested that 80% to 90% of OM was secondary, even those measurements conducted near emission sources. Of these SOA components, aromatic and alkane SOA factors accounted for 65% of OM. Based on their compositions and correlations with tracers these factors were identified as being from fossil fuel combustion, likely from motor vehicles, and represent the largest source at Bakersfield (Table 4.4). This finding is consistent with previous source apportionment studies at Bakersfield [Hamilton *et al.*, 2004; Kleeman *et al.*, 1999; Schauer and Cass, 2000]. Also from these studies, wood combustion was identified as a significant source only in winter, likely because residential heating (the main source of wood burning) was not in use during the early summer period [Chow *et al.*, 2006a]. A recent source inventory in the southern SJV (Table 4.5) listed petroleum operations as having near-zero primary  $PM_{2.5}$  emissions. If secondary organic aerosol is also included, as measured in this study, the petroleum operation should be categorized as contributing 14% to OM, based on the PO SOA factor.

## 5.0 Cluster Analyses of Ensemble and Single-particle Spectra<sup>5</sup>

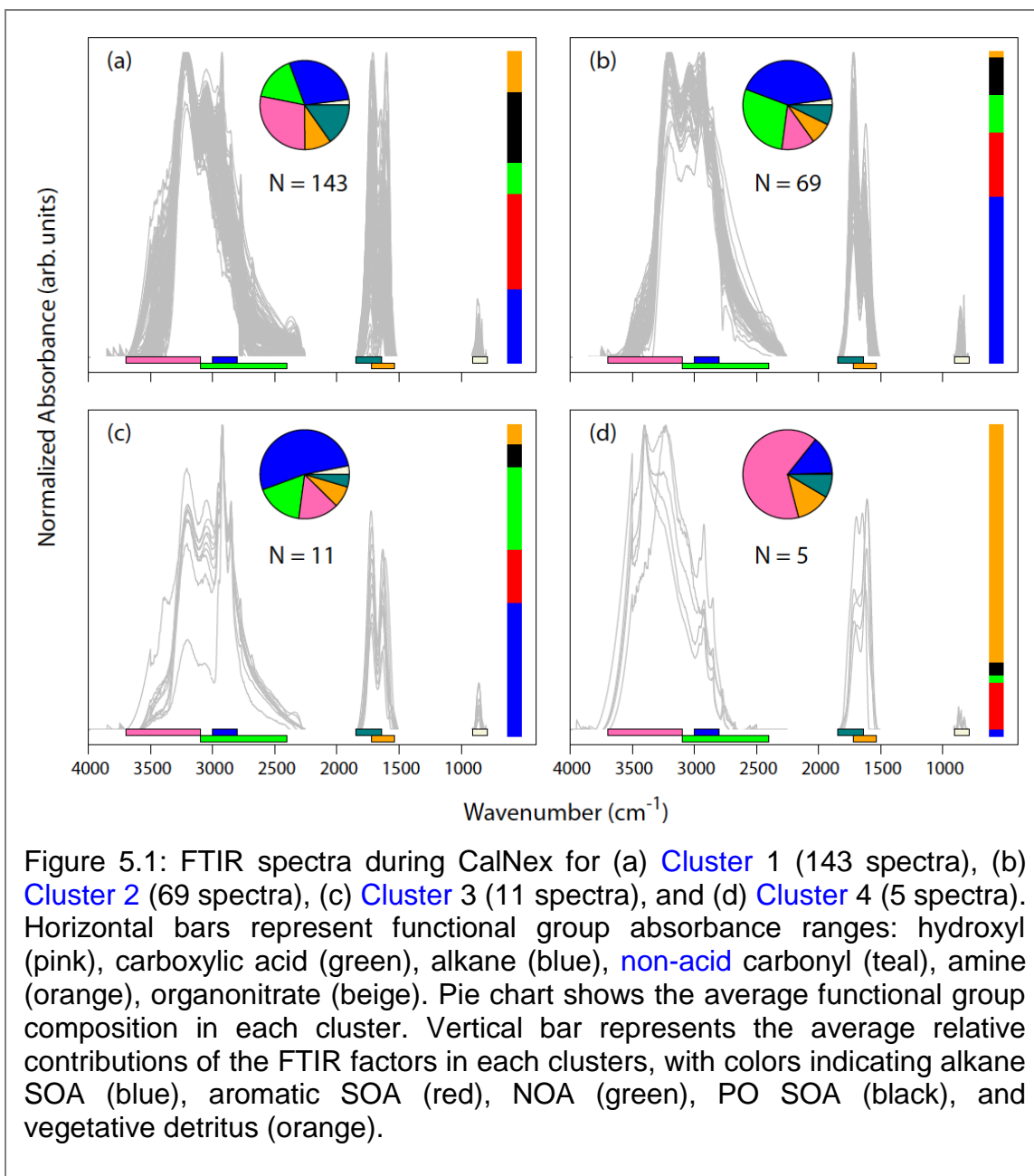
Cluster analysis was used to categorize particles that have similar chemical compositions into groups, each of which has distinct characteristics that likely result from a specific source or atmospheric process. Commonly used cluster analyses include the hierarchical cluster technique (e.g., the Ward algorithm) and K-means clustering algorithm. In the Ward algorithm, each spectrum is initially considered as a separate group. By progressively merging the spectra with the least-square criterion for each merging step, a dendrogram is generated from the spectra and ultimately all spectra are merged into one single group. The dendrogram can be “cut” at different levels of branching (similarity) to create a number of clusters [Hopke and Kaufman, 1990]. The Ward clustering algorithm has the advantage to display the relationship of each pair of spectra. However, the clustering process is quite slow and, therefore, it is not practical for large data sets such as high-resolution single-particle measurements. The K-means clustering algorithm has proven effective and accurate in dividing single particles into meaningful clusters. In this algorithm, the single-particle spectra are divided into K clusters such that the sum of squares of the distances between the spectra and their corresponding cluster centroid is minimized [Hartigan and Wong, 1979]. In addition, cluster analysis is used as another classification technique for the FTIR measurements and can be compared to the results from factor analysis (PMF) in the previous chapter. While PMF can separate individual sources that contribute to a single sample, cluster analysis groups individual samples together to determine the general aerosol types. In this chapter, the FTIR and single-particle NEXAFS spectra are clustered using the Ward clustering algorithm, and the single-particle mass spectra are categorized using the K-means algorithm. Detailed clustering procedures and the results are presented.

### 5.1 Cluster Analysis of FTIR Spectra

Normalized FTIR (PM<sub>1</sub>) spectra were grouped using the Ward algorithm [Liu *et al.*, 2009; Russell *et al.*, 2009; Ward, 1963], which resulted in four clusters (Figure 5.1). Particles in Cluster 1 had the largest fraction of non-acid carbonyl groups (15%) among the four clusters, with alkane, hydroxyl, and carboxylic acid groups contributing 29%, 28%, and 16% to the OM, respectively. Cluster 2 particles were mainly composed of alkane (42%) and carboxylic acid (29%) groups. Together, Cluster 1 and Cluster 2 accounted for 93% of the submicron FTIR spectra. Spectra in Cluster 3 were characterized by sharp alkane group peaks and had the largest fraction of alkane groups (52%) among the four clusters. Cluster 4 represented particles that were mainly composed of hydroxyl groups (65%). The distinct chemical composition of the four clusters indicated differing contributions from various sources and processes throughout the study.

---

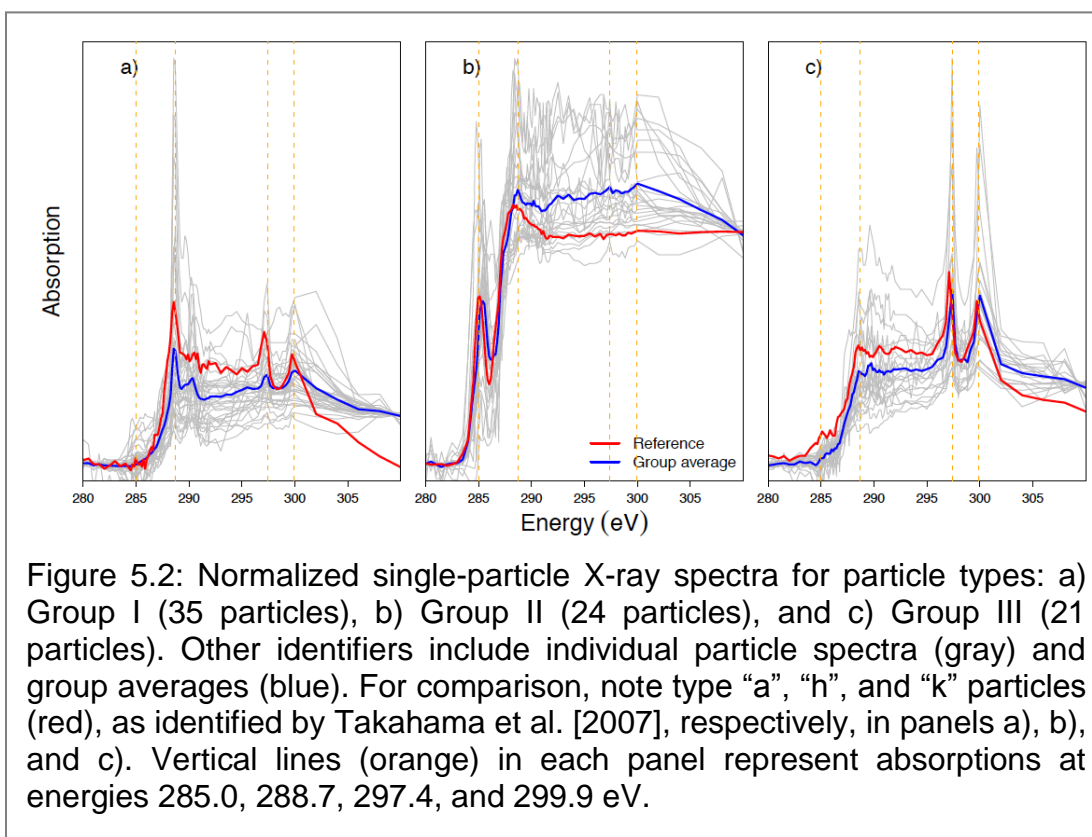
<sup>5</sup> Work in this section has been published by Liu *et al.* [2012a].



## 5.2 Cluster Analysis of Single-particle NEXAFS Spectra

Single-particle X-ray spectra (80 particles) were categorized into three major groups based on their spectroscopic similarities (Figure 5.2). To gain further insight into their source types, each group was compared to single-particle X-ray spectra for each of the 14 types of particles identified by *Takahama et al.* [2007]: Group I particles showed strong carboxylic acid group absorption at 288.7 eV. Their particle spectra were comparable to type “a” particles, likely formed from atmospheric processing, which suggests the group's secondary origins. Group I will be referred to as “secondary” particles. Group II spectra were characterized

by strong absorption at 285.0 eV due to  $sp^2$ -bonding of soot or black carbon. Since these particles resembled Takahama's "strongly aromatic aerosols" (e.g., type "h" particles) (Figure 5.2b), diesel exhaust was the likely origin, and this group will be referred to as "diesel exhaust" particles. Group III particles showed no significant peaks for organic functional groups. The lack of a C=C peak at 285.0 eV and a C-OH peak at  $\sim 287.0$  eV, which are characteristic for biomass-burning type particles (although the C=C peak for such particles is relatively smaller compared to that of diesel soot particles), essentially excluded the possibility of Group III having a biomass burning source [Braun, 2005; Tivanski et al., 2007]. Furthermore, high absorbance seen in the K region (at 297.4 and 299.9 eV) was consistent with dust sources, the likely origin of Group III's particles, and Group III will be referred to as "dust" particles.



### 5.3 Cluster Analysis of Single-particle Mass Spectra

Single-particle mass spectra for 147,357 particles were clustered (detailed in the next chapter) to reveal three single-particle clusters: Cluster I mass spectra were characterized by  $m/z$  44 and were comparable to LV-OOA spectra in the AMS database [Ulbrich et al., 2009]. Cluster II particles had strong  $m/z$  43 signals, and their spectra resembled those of SV-OOA components. Cluster III spectra were characterized by  $m/z$  27, 29, 41, 55, 57, and 69, which were typical for hydrocarbon type aerosols ( $m/z$  29, 57) or cooking organic aerosols ( $m/z$  27, 41,



55, 69). This suggested that Cluster III particles likely originated from mixed local primary sources.

#### **5.4 Comparison of Particle Cluster Types with Source Types**

The “secondary” (Group I), “diesel exhaust” (Group II), and “dust” (Group III) particle types resulting from single-particle X-ray spectra broadly matched the major source types identified from bulk particle functional group factor analysis. Secondary particles accounted for 44% of total measured particles, which was consistent with bulk particle analysis that suggested SOA was the major component of OM. Similarly, the “high m/z 44” (Cluster I), “high m/z 43” (Cluster II), and “mixed” (Cluster III) particle types derived from single-particle mass spectra analysis matched the major source types from the bulk particle mass spectra factor analysis (PMF, described in the previous chapter). Taken together, the high m/z 44 and m/z 43 types accounted for 56% of identified particles, both by number and mass. Specifically, the group-average high m/z 44 single-particle spectrum correlated to the mass spectra for the high O/C alkane and aromatic SOA components with an  $r$  of 0.96 and 0.92, respectively. High spectral correlations were also observed for the high m/z 43 type particles (correlated to the low O/C alkane SOA with  $r = 0.96$ ) and the mixed-type particles (correlated to COA, PO SOA, and NOA with  $r = 0.86$ , 0.76, and 0.70, respectively).

#### **5.5 Conclusions**

We have identified particle clusters from the FTIR, STXM-NEXAFS, and LS-ToF-AMS measurements using the Ward and K-means algorithms. The cluster that is likely associated with atmospheric processes contributed the majority of the particle number and mass. The single-particle clusters agreed with the bulk particle types identified from the PMF analysis, suggesting the ubiquity of SOA in fine OM at Bakersfield.

## 6.0 Organic Particle Types by Single-particle Measurements using LS-ToF-AMS<sup>6</sup>

### 6.1 Introduction

Rapid measurements are needed to accurately quantify atmospheric particle sources and compositions and to study their transformations. The Aerosol Mass Spectrometer (AMS) is one fast-developing and widely-used technique used for monitoring size and composition of submicron particles in real time [Jayne *et al.*, 2000]. Quantified species include nonrefractory organic mass (OM), sulfate, nitrate, ammonium, and chloride. Recent developments enable separation of ions that are slightly different in mass and overlap in unit-mass spectrum by replacing the quadrupole mass spectrometer (in Q-AMS) with a compact time-of-flight mass spectrometer (C-ToF-AMS), as described in *Drewnick et al.* [2005], and a high resolution time-of-flight mass spectrometer (HR-ToF-AMS), described in *DeCarlo et al.* [2006]. The ToF-AMS collects signals from the composition of ensembles of particles in each chopper cycle. In the brute force single particle (BFSP) mode of the ToF-AMS operation, mass spectrum extractions within a chopper cycle are saved, enabling acquisition of single-particle mass spectra. However, the BFSP mode is typically turned off during field measurements to conserve data storage and processing time. The only published analysis utilizing this mode came from field measurements made by *Drewnick et al.* [2005], whereby single-particle mass spectra were acquired several times, each for a few minutes. These single-particle spectra were used to investigate internal and external mixing properties of submicron particles. *Cross et al.* [2009] advanced the AMS by coupling a light scattering module (LS-ToF-AMS) in which particles are optically detected by a laser before they reach the vaporizer. In LS-ToF-AMS, single-particle mass spectra are recorded during the operation of the light scattering single particle (LSSP) mode. The LSSP mode is similar to the BFSP mode, except that particle light scattering signals trigger the saving of single-particle mass spectra, which considerably enhances the data transfer and saving efficiency compared to the BFSP mode operation, during which mass spectra in each chopper cycle are saved individually regardless of the existence of particles. The LS-ToF-AMS was successfully deployed during the MILAGRO (Megacity Initiative: Local and Global Research Observations) 2006 field campaign for a 75-h sampling period [*Cross et al.*, 2009], demonstrating its unique ability to provide insights into the atmospheric transformations of ambient particles.

Compared to other single-particle measurement techniques (Table 6.1), the LS-ToF-AMS has the advantage of providing simultaneously quantified single- and ensemble-particle mass spectra, although the single-particle detection limit of the LS-ToF-AMS is higher than most of the online single-particle mass spectrometers (using laser ablation) and refractory components are not measured by LS-ToF-

---

<sup>6</sup> Work in this section is published online and is in review in *Liu et al.* [2012b, AMTD].

MS. Single-particle measurement statistics of LS-ToF-AMS are comparable to other online single-particle mass spectrometers and much greater than offline electron microscopy techniques, although the latter provide additional information about particle morphology and elemental composition.

Table 6.1: Comparison of single-particle measurement techniques and their detection limits.

	Technique	Measured components	Size DL (nm)		Size resolution	Method for DL determination	Reference
			$d_{va}$	$d_g$			
Laser ablation	LAMMA		-	500	-	Not specified	Wieser et al., 1980
	ATOFMS		200	-	25-40 <sup>a</sup> nm	Smallest laboratory-calibrated particles	Noble and Prather 1996; Gard et al., 1997
	UF-ATOFMS		100	-	-	Smallest particles that have non-zero detection efficiency	Su et al., 2004
	PALMS	Refractory and nonrefractory components, including organics, salts, metals, and dusts in single particles	-	200	-	Not specified	Murphy and Thomson, 1995; Thomason et al., 2000
	RSMS-III		50	-	5-20 <sup>b</sup> nm	Smallest particles that have non-zero detection efficiency	Lake et al., 2003; Johnston and Wexler, 1995; Phares et al., 2002
	SPLAT-II		50	-	-	Smallest particles that have non-zero detection efficiency	Zelenyuk et al., 2009
Electron microscopy	SEM-EDX or ESEM	Single-particle elemental compositions and morphology	-	100	-	Smallest particles tested in the laboratory	Laskin et al., 2001
	STXM	Organic functional groups, potassium, carbonate in single particles	-	100	-	Smallest particles analyzed	Takahama et al., 2007
Thermal volatilization	LS-Q-AMS		-	180	5-10 <sup>c</sup>	Smallest particles that have non-zero detection efficiency	Cross et al., 2007
	LS-ToF-AMS	Nonrefractory organics, sulfate, nitrate, ammonium, chloride of single and ensemble particles	180	130	5-10 <sup>c</sup>	Smallest particles that produce significant optical (S/N $\geq$ 5) and chemical signals (> 6 ions)	This study
	LS-ToF-AMS		430	307	5-10 <sup>c</sup>	Size at which 50% of particle number are detected (compared to DMA)	This study

<sup>a</sup> Calculated as the standard deviation of the size-calibration curve fitting.

<sup>b</sup> Inferred from reported size distributions.

<sup>c</sup> Calculated as  $d/\Delta d$  at FWHM (full width at half maximum).

This study expands previous work [2007; Cross et al., 2009] (to identify three chemically-distinguishable classes of particles with a 46-day field measurement using the LS-ToF-AMS at a polluted urban site. We used the modified standard

light scattering and single-particle mass spectra processing algorithm Sparrow and describe single-particle post-processing procedures. To interpret the organic composition of the individual particles, we grouped single particle mass spectra to reduce the large dataset into a few clusters, each with distinct characteristics.

## 6.2 Measurements

The LS-ToF-AMS (Aerodyne, Billerica, MA) was deployed from 15 May to 29 June 2010 at Bakersfield during the CalNex (California Research at the Nexus of Air Quality and Climate Change) field campaign. The instrument combines the well-characterized HR-ToF-AMS and a light scattering module specifically developed for ToF-AMS applications. The ToF-AMS has been widely used in laboratory and field studies and is described in detail previously [DeCarlo *et al.*, 2006; Drewnack *et al.*, 2005; Jayne *et al.*, 2000]. The use of the LS-ToF-AMS for single-particle detection was first reported by Cross *et al.* [2009] with a compact ToF-AMS system. The work reported here is the first time the LS module has been used to acquire single-particle data with a high resolution ToF system (HR-ToF-AMS). Adding the light scattering module does not influence ToF-AMS performance but rather physically identifies all particles (both nonrefractory and refractory) that reach the vaporizer and are larger than its detection limit, thereby providing substantially more information about single particles. During the entire campaign, the LS-ToF-AMS was operated in the MS mode (measures ensemble average chemical composition), PToF mode (particle time-of-flight, provides size-resolved chemical composition for ensemble average), and LSSP mode (acquires single-particle mass spectrum) for 120, 120 and 80 seconds of approximately every 5 minutes.

Briefly, the LS-ToF-AMS has five major components: aerosol sampling inlet, particle time-of-flight chamber, light scattering module for single-particle detection, particle vaporization and ionization chamber, and in this case, a high resolution time-of-flight mass spectrometer. Aerosols sampled through a 100- $\mu\text{m}$  critical orifice are focused by an aerodynamic lens system, forming a narrow ( $\sim 1$  mm diameter) and highly collimated particle beam. Focused particles are transmitted under high vacuum ( $\sim 10^5$  Pa) through a laser beam for optical detection to the vaporization and ionization chamber, where they impact a heated surface ( $\sim 600$  °C). The nonrefractory fractions of the particles are flash vaporized and ionized by electron impact. Orthogonally extracted ions are subsequently analyzed by a time-of-flight mass spectrometer, which generates a complete mass spectrum at each extraction. A rotating chopper placed at the front of the particle-sizing chamber chops the particle beam and sets the starting time of particle flight. By measuring particle flight time between the mechanical chopper and the thermal vaporizer, particle vacuum aerodynamic diameter ( $d_{va}$ ) can be determined from a calibration curve, which relates particle velocity (calculated using the known distance between the chopper and the vaporizer and the measured flight time) to particle size. The calibration curve was derived using polystyrene spheres (PSL of diameter 200 nm, 350 nm, 500 nm, and 600 nm)

and ammonium nitrate particles that were size-selected by a differential mobility analyzer (DMA). Comparison of nominal PSL size and mobility-selected size showed good agreement. In this study, geometric diameter ( $d_g$ ) is calculated using  $d_{va}$  and particle density ( $d_g = d_{va}/\rho$ ), assuming spherical particles. The density ( $1.4 \text{ g cm}^{-3}$ ) was derived by comparing AMS-measured mass size distribution with SMPS (scanning mobility particle sizer)-measured volume size distributions detailed in *Ahlm et al.* [2012].

The laser used for optical detection was a 405 nm continuous wave 50 mW laser (Crysta-Laser, LC BCL-050-405). In order to maximize the overlap of the laser and the particle beams, the laser beam was not focused [*Cross et al.*, 2007]. Light scattered by sampled particles are collected using an ellipsoidal mirror and detected with a photomultiplier tube. The current system differs from the LS-ToF-AMS used by *Cross et al.* [2009] in the mechanism used for detecting single particles and saving the optical and chemical information for each detected particle. The key technical improvements include (1) adding the detected light scattering signal to the chopper frequency signal for unambiguous correlation in time, where the chopper frequency is the fundamental clock for the PToF and LSSP mode ToF-AMS data acquisition, and (2) using an external comparator circuit to test for the presence of a single particle in the scattered light signal, using a user set threshold level. This test is performed without transferring data to the computer for software evaluation, a process that takes longer time than an individual chopper cycle. The comparator circuit triggers the saving of the mass spectral data. Once triggered, the DAQ reports individual mass spectra for the entire chopper period in which the LS event occurred (mass spectra obtained as a function of particle time-of-flight). This approach dramatically reduces the overhead associated with any data transfer for events where there are no particles and eliminates the need to transfer the data from the DAQ board to the computer for software detection of particles. The light scattering particle counter, which is part of the comparator circuit, counts all of the threshold crossers observed by the external comparator circuit in the LSSP, PToF, and MS modes. This includes LS pulses for which single-particle mass spectral data were not recorded due to the transfer and saving times. This counter provides a measure of the particle number concentration for all optically detected particles and allows for the accurate evaluation of the true duty cycle obtained by the LSSP mode and direct comparisons with independent aerosol instruments that measure particle number concentrations. In addition, the (GNU zip) GZIP compression algorithm is applied to the single-particle files, thereby reducing the data transfer time and enhancing the sampling efficiency of the LS-ToF-AMS.

The LSSP mode records full mass spectra as a function of time during each chopper cycle. In the current configuration, there are 319 mass spectra obtained per chopper cycle. Each mass spectrum is baseline corrected to account for background signal at each  $m/z$ , using the average of two user selected “DC” regions at the start and end of the chopper cycle. Single-particle spectra are obtained by adding together a subset (~5 spectra) of the total number of baseline

corrected mass spectra collected during a single chopper cycle.

The chopper used during this study had a 0.02 duty cycle (percent of time active out of the total time, i.e. 2% of the time in the open position during one cycle) and operated at 125 to 160 Hz frequency (set to 143 Hz) during the measurement. With this frequency, there is typically ~1 particle or less per chopper cycle on average [DeCarlo *et al.*, 2006], allowing correlated measurements of single-particle light scattering and chemical compositions. Potential particle coincidence events were investigated by examining the light scattering profile (i.e., light scattering intensity as a function of particle time-of-flight) for each LS event. Particle coincidence is identified as multiple crossing of thresholds, which are defined as 5 times the standard deviation of the baseline of the light scattering profile. Using this criterion, the number of particle coincidence events was 0.3% of the total particle events, suggesting that particle coincidence events are negligible. Particles in the coincidence events were excluded in the analysis.

The limiting issues with the LSSP mode include the typically low duty cycles of the chopper and the overhead associated with transferring and saving the mass spectral data for single particles [Kimmel *et al.*, 2011]. During the transferring and saving of mass spectral data for a single chopper cycle, data from the following 6 chopper cycles were not recorded. The resulting duty cycle due to data storage processes ranged from 0.14 (i.e., 1/7 chopper cycles) to 1.0, depending upon the sampled particle number concentration, with an average of ~0.62 for this study. An additional duty cycle of 0.45 was present during this study due to an unusual noise spike (characterized by near-zero light scattering signals and were filtered out in single-particle analysis) in the LS channel that triggered saves. Taken together, the LSSP mode data rates obtained during this study represent a single-particle detection efficiency improvement of greater than a factor of five from the Cross *et al.* [2009] study.

## **6.3 Results and Discussion**

We began by classifying single particles into vaporization types based on timing of optically and chemically detected signals. We then clustered individual particles' organic mass spectra with significant signals into groups, each of which is associated with distinct chemical signatures. Finally, we compared these single-particle groups with components extracted from ensemble measurements.

### **6.3.1 Classification of Single Particles into Vaporization Types**

Light scattering and single-particle measurements were processed using an updated version of the standard AMS light scattering data processing software Sparrow 1.04A (written by D. Sueper, Aerodyne Research Inc. and University of Colorado-Boulder; downloadable at [http://cires.colorado.edu/jimenez\\_group/ToFAMSResources/ToFSoftware/index.html# Analysis4](http://cires.colorado.edu/jimenez_group/ToFAMSResources/ToFSoftware/index.html#Analysis4)), which classifies the particles by their vaporization types and generates the physical (particle size

in  $d_{va}$ , light scattering intensity) and chemical (unit-mass spectrum and mass of organics, sulfate, nitrate, and ammonium) data of single particles. A total of 271,641 particles were measured during the 46-day campaign. Figure 6.1a shows the time-integrated light scattering signals plotted versus  $d_{va}$  and  $d_g$  for all of the saved particles. The optical detection limit, defined as the size at which particles produce detectable optical signals ( $S/N > 5$ ), was 180 nm  $d_{va}$  (130 nm  $d_g$ ). The optical detection efficiency, defined as the ratio of optically detected particle number concentrations to SMPS-measured number concentrations (Figure 6.2a), dropped below 100% at 550 nm  $d_{va}$  (393 nm  $d_g$ ) and below 50% at 430 nm  $d_{va}$  (307 nm  $d_g$ ). In comparison, the size that corresponds to 50% optical detection efficiency, derived from LS-coupled Q-AMS system in the laboratory by Cross *et al.* [2007], was 240 nm  $d_g$ —22% lower than 307 nm  $d_g$ , suggesting that the alignment of LS-ToF-AMS used in this study was less optimized than that of the Cross *et al.* laboratory study. A group of particles with relatively high organic mass fractions ( $\sim 1$ ) are distinct from the majority of the particles (Figure 6.1a). This subset of particles are dominated by hydrocarbon-like organic aerosol (HOA) signals, have lower  $d_{va}$ 's and higher integrated scattering signals compared to the rest of the particles. As these particles are classified in Cluster III that may consist of substantial primary OM (Figure 6.1b and Section 6.3.2), these particles may contain black carbon or other primary refractory components that modified the shape, density, or the combined real refractive index of the particles. A similar externally mixed, HOA-dominated particle type was observed in Mexico City and reported in Cross *et al.* [2009]. However, more work needs to be done to fully characterize these particle types.

Total saved particles were scaled by overall duty cycle to derive average particle number size distribution for this study. The overall duty cycle accounted for the 0.02 chopper duty cycle, data transfer and saving duty cycle (ranged from 0.2-1.0 with an average of 0.62), and noise spike duty cycle (0.45). Figure 6.2a represents the first direct in situ measure of the particle number-based sampling efficiency of an AMS and comparison with simultaneous SMPS number-based measurements. The light scattering signals indicate that particle sampling efficiency for particle sizes greater than 550 nm  $d_{va}$  (393 nm  $d_g$ ) is similar to the laboratory measurements for the aerodynamic inlet lens system, with decreasing transmission efficiency at larger particle sizes [Liu *et al.*, 2007]. Figure 6.2b shows the comparison of campaign-average ion signals measured by the LSSP and PToF modes of the LS-ToF-AMS operation. Particles with time-of-flight greater than 0.0035 s, corresponding to 600 nm  $d_{va}$ , showed good agreement between the LSSP mode and PToF mode measurements, consistent with the agreement of number concentrations for particles larger than 550 nm  $d_{va}$  (Figure 6.2a). Cross *et al.* [2009] demonstrated that the LSSP mode and PToF mode measured ion signals agreed for particles larger than 350 nm  $d_{va}$ , indicating that the LS system in that work was more optimized.

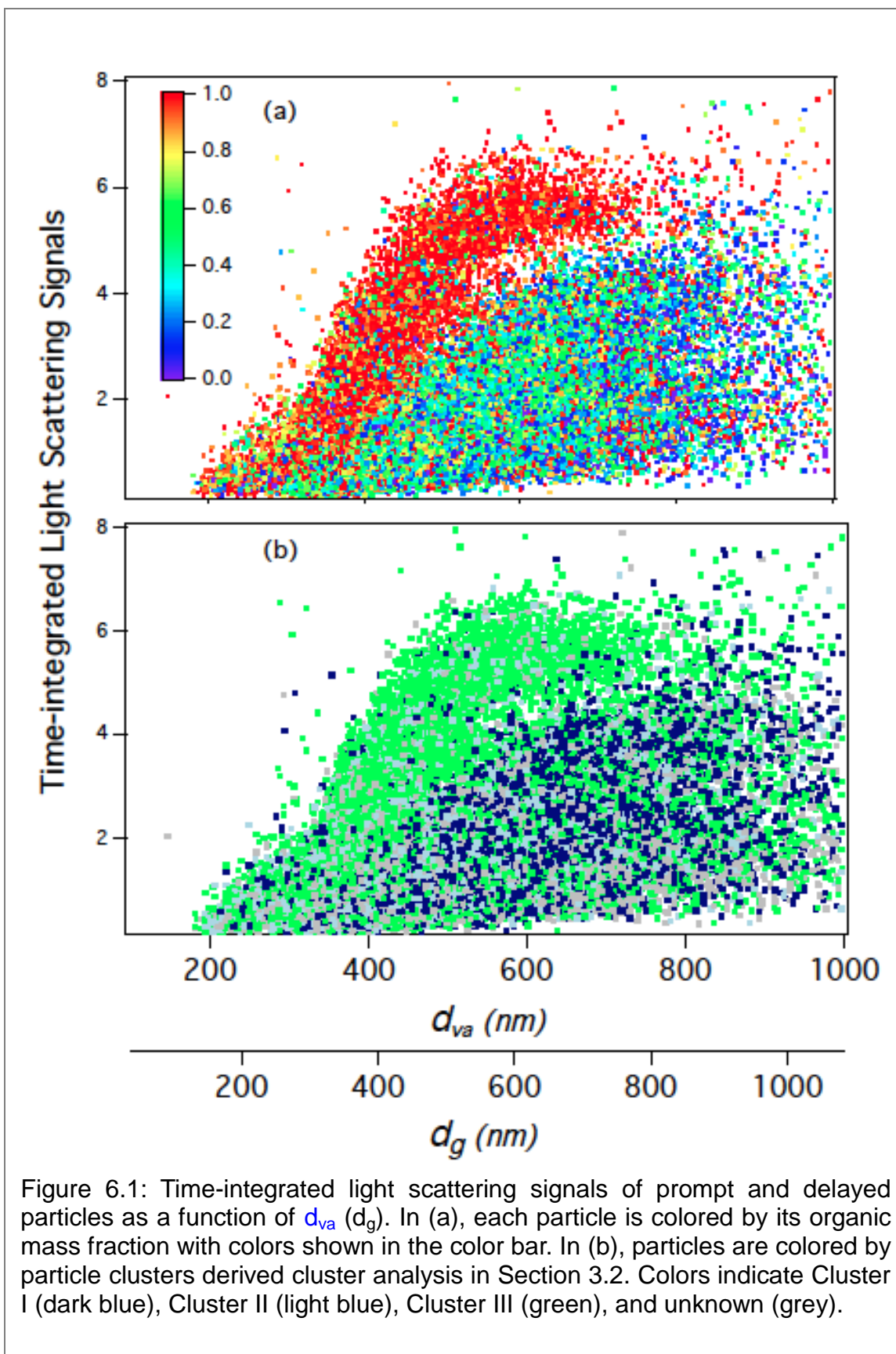


Figure 6.1: Time-integrated light scattering signals of prompt and delayed particles as a function of  $d_{va}$  ( $d_g$ ). In (a), each particle is colored by its organic mass fraction with colors shown in the color bar. In (b), particles are colored by particle clusters derived cluster analysis in Section 3.2. Colors indicate Cluster I (dark blue), Cluster II (light blue), Cluster III (green), and unknown (grey).



Low detection efficiency for small particles likely resulted from (i) widening of particle beam beyond the region of overlap of the particle and laser beams or low detection efficiency for small particles passing through the edges of the laser beam and (ii) size detection limit of small particles by the laser. Comparison of LS-ToF-AMS- and SMPS-measured total particle number concentration showed similar time series, i.e., total number concentration of 560- to 1000-nm  $d_{va}$  (400- to 715-nm  $d_g$ ) particles agreed reasonably well (Figure S6.1)—the linear fit has a slope of 0.89 (the SMPS-measured concentration was 11% higher) and an intercept of 6.25, and the number concentrations correlated with an  $r$  of 0.7, while the total concentration of 200- to 560-nm  $d_{va}$  (140- to 400-nm  $d_g$ ) particles measured by LS-ToF-AMS was much lower.

In order to determine the timing of the measured chemical signals, a mass intensity profile (i.e., mass intensity quantified by the ToF-MS mass spectrometer as a function of particle time-of-flight) is needed for each particle. The profile is the sum of profiles for all detected ion fragments (including organic and inorganic fragments) for each particle. Since the acquisition rate is faster than the particle vaporization time, several mass spectra are obtained during the ( $\sim 100$   $\mu$ s) particle vaporization event. These individual spectra are co-added to accumulate the total measured ion intensity for the single particle. However, adding fragments with low intensities can significantly lower the contrast between real and background signals. Additionally, background-related fragments  $m/z$  18 ( $H_2O^+$ ), 28 ( $N_2^+$ ), 32 ( $O_2^+$ ), and 39 ( $K^+$ ) can greatly mask real signals. Therefore, only the profiles of non-background high-intensity fragments were summed to construct a mass intensity profile for each particle.

Ensemble average concentrations (from the MS mode measurement) were used to estimate ion fragment abundance of single particles. Ten high-intensity ion fragments were selected for this campaign, including  $m/z$  15, 27, 30, 41, 43, 44, 46, 48, 55, 57, and 64. This list combined organic- and inorganic- (nitrate, sulfate, and ammonium) dominated fragments. Additionally, selected organic fragments were characteristics of specific particle types; for example,  $m/z$  44 is a tracer for oxygenated organic aerosols (OOA), and  $m/z$  57 typically represents HOA [Zhang *et al.*, 2005b].

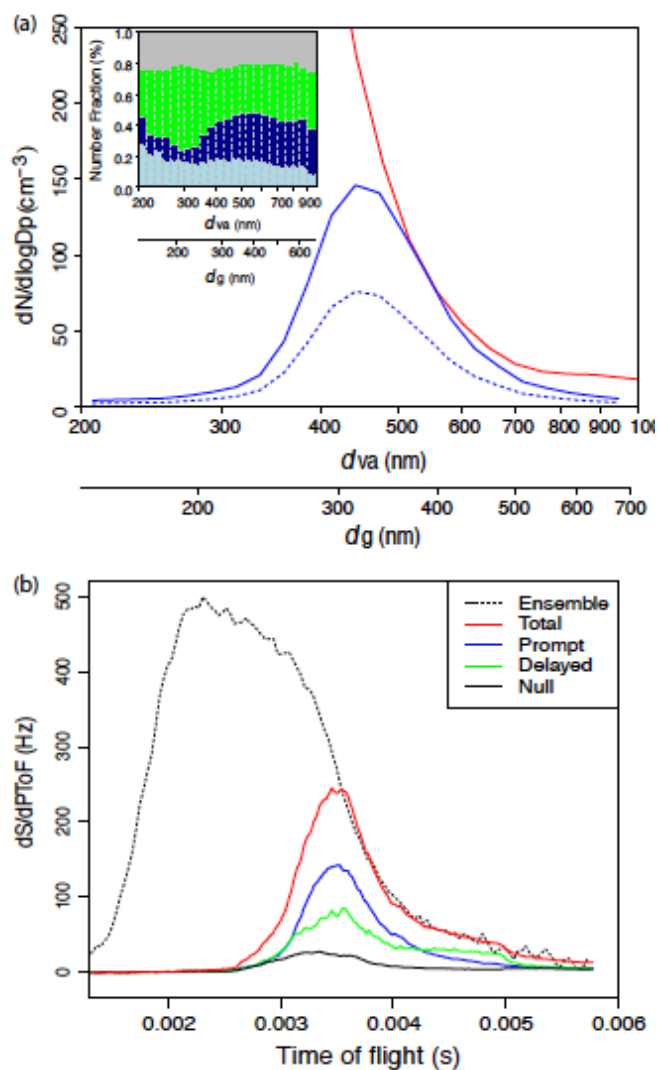


Figure 6.2: (a) Particle number size distributions measured by SMPS (red) and LS-ToF-AMS (solid blue). A density of  $1.4 \text{ g cm}^{-3}$  was used to convert SMPS mobility diameter to  $d_{va}$  [Ahlm *et al.*, 2012]. Dashed blue line represents number size distribution for sum of prompt and delayed particles. The inset shows number fractions for Cluster I (dark blue), Cluster II (light blue), Cluster III (green), and unknown (grey) particles. Particle size is binned logarithmically. For each size bin, logarithmic ratio of upper size to lower size is 0.03. (b) Comparison of campaign-average mass distribution as a function of particle [time-of-flight](#) of ensemble (dotted black line; PToF mode) and single-particle measurements (LSSP mode). The total (red) represents the sum of the prompt (blue), delayed (green), and null (black) particle signals measured by the LSSP mode.

Timing of the optical signals (TLS) and chemical signals (TMS) was retrieved by locating the maximum light scattering intensity and mass intensity from the light scattering (i.e., light scattering intensity as a function of particle time-of-flight) and mass intensity profiles, respectively. TLS and TMS, respectively, represent the particle flight time from the midpoint of chopper opening to the laser and to the mass spectrometer (including the vaporization and ion transit time from the vaporizer to the time-of-flight mass spectrometer). Using the particle velocity (calculated from TLS and the chopper-to-laser distance) and the chopper-to-vaporizer distance, the timing of particle chemical signals can be predicted (TMS P). By comparing timing of the predicted particle chemical signals (TMS P) with the timing of the measured chemical signals (TMS), the vaporization and ion flight time (TMS ION) can be estimated by the y-axis offset of the TMS P versus TMS (scatter) plot. Using TMS and the sum of TMS P +TMS ION, each single particle was classified as one of three discrete particle types: (1) “prompt,” for which the deviation of TMS/(TMS P +TMS ION) from 1 was less than 20% (i.e., particles optically and chemically detected at the expected time offset); (2) “delayed,” for which the deviation of TMS/(TMS P +TMS ION) from 1 was greater than 20% (i.e., TMS significantly lagged TMS P +TMS ION); and (3) “null,” for which optical signals were detected, but no significant chemical signals were observed. The criterion of insignificant chemical signals is a minimum sum of chemical signals for the mass intensity profile of 6 ions. Using this criterion, the null particles had typically 2-4 ions (Figure S6.2) that are comparable to the number of ions generated in the non-particle events (chopper cycles that have no particles).

Particle statistics associated with the three vaporization types (Table 6.2) show that prompt and null particles dominated, accounting for 46% and 48%, respectively, of the saved particles, while delayed particles accounted for a 6% fraction. The null particle fraction was comparable to that of the 51% fraction identified from the Mexico City measurement [Cross *et al.*, 2009], suggesting that the AMS vaporization-ionization may typically miss about 50% of sampled particles (for particle diameters larger than 180 nm  $d_{va}$  or 130 nm  $d_g$ ), based on particle number. The mass-based collection efficiency (CE) of the AMS is dependent on particle composition and is higher for low-sulfate particles [Matthew *et al.*, 2008; Middlebrook *et al.*, 2012; Quinn *et al.*, 2006]. While the prompt particle (46%) group points to a number-based CE of ~0.5 for particles larger than 180 nm  $d_{va}$  (130 nm  $d_g$ ), smaller particles (<180 nm  $d_{va}$ ), which accounted for 35% of submicron particle mass, may have had higher CE due to their low sulfate (15% of non-refractory (NR)-PM<sub>1</sub>) and high organic contents (75% of NR- PM<sub>1</sub>) [Ahlm *et al.*, 2012]. Therefore, the number-based CE of 0.5 was lower compared to the average mass-based CE of 0.8, which was determined by scaling the AMS mass to the SMPS-derived mass for particles of all sizes smaller than 1000 nm (excluded masses of elemental carbon and dusts) [Ahlm *et al.*, 2012]. CE values ranged from 0.43 to 0.52 for particles larger than 180 nm  $d_{va}$ , with peak values associated with 500-600 nm  $d_{va}$  particles (Figure 6.3). Particles in 800- to 1000-nm  $d_{va}$  had the lowest CE values, likely due to

enriched dust components in this size range [Silva and Prather, 2000] that were not vaporized by the AMS or because of the enhanced mass fraction of sulfate and decreased mass fraction of the organics (Figure 6.1a).

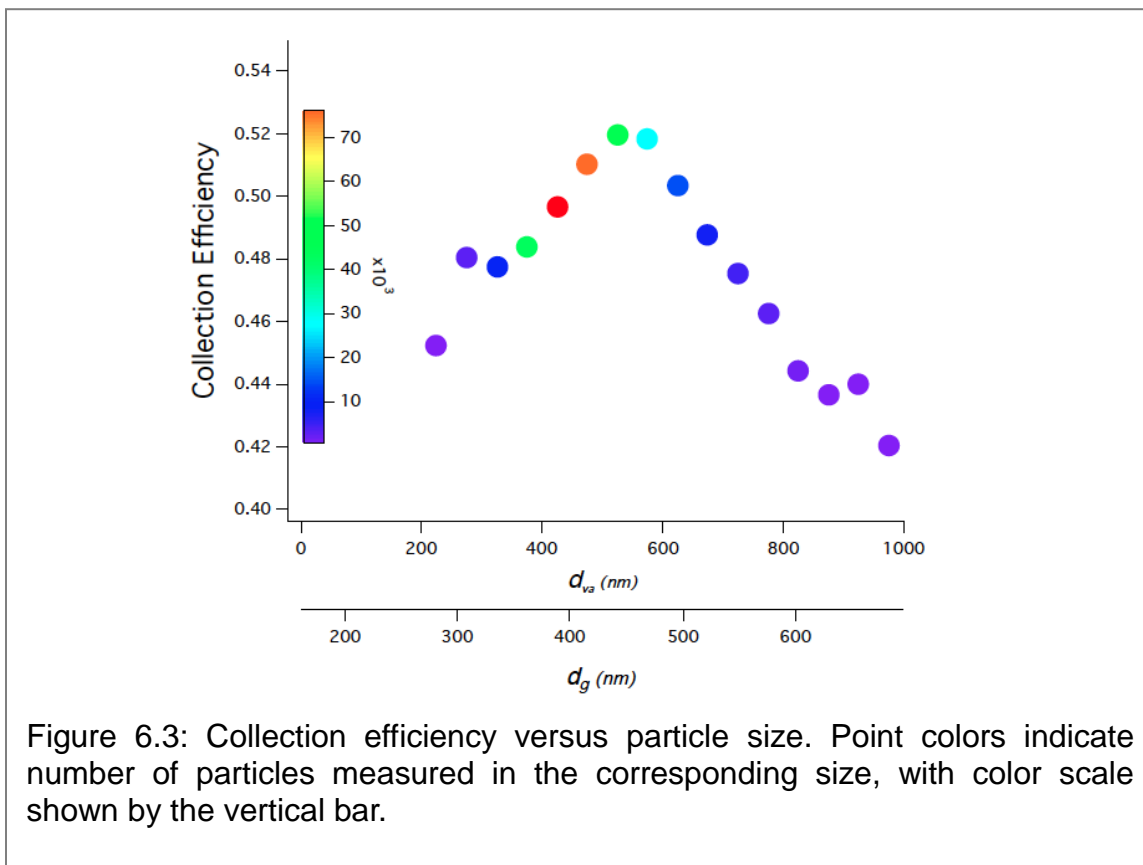


Table 6.2: Particle number and number fraction for the three vaporization types.

Particle vaporization type	Particle Number	Number fraction (%)
Prompt	130361	46
Delayed	16996	6
Null	124284	48

### 6.3.2 Organic Particle Types Identified from Cluster Analysis

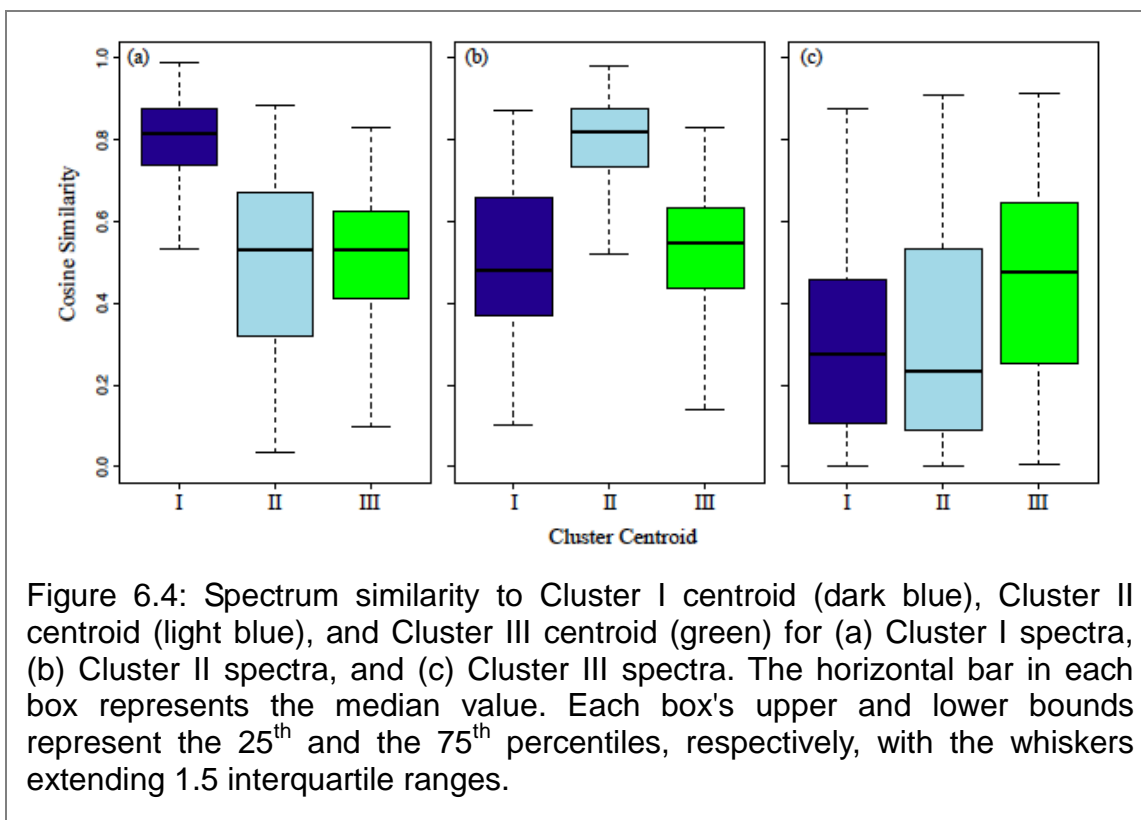
Prompt and delayed particles that had significant mass spectrum signals were used for cluster analysis. The K-means clustering algorithm, applied to the 147,357 single-particle organic mass spectra, divides spectra into K clusters such that the sum of squares of the distances between the spectra and their corresponding cluster centroid is minimized [Hartigan and Wong, 1979]. Spectra

were normalized before clustering so that the sum of intensities for each mass spectrum was 1. In order to identify organic particle types, only organic fragments were included in the cluster analysis. K values of 2 to 12 (varying by 1) were tested. For each run, 10 sets of random 5 cluster centroids were iterated. Using  $K < 6$  resulted in one dominating cluster (containing ~75% of particles used for clustering) with an average spectrum characterized by mixed types of marker fragments (e.g.,  $m/z$  44 for OOA and  $m/z$  57 for HOA), which indicated that particles in this cluster were not well separated; thus,  $K < 6$  solutions were not preferred. However, three major clusters were consistently identified from the  $K > 6$  clustering solutions, with each cluster associated to a distinct mass spectrum. Taken together, these particles accounted for ~80% of the particles. Each of the remaining clusters typically contained less than 5% of the particles.

Cosine similarity is a useful tool for estimating mass spectrum similarity [Stein and Scott, 1994] and was therefore used here as a metric to measure the within-cluster and cross-cluster similarity of single-particle spectra. In brief, cosine similarity is the cosine of the angle between two vectors (where each vector represents a mass spectrum) and is calculated using the following equation:

$$\cos \theta = \frac{\mathbf{A} \cdot \mathbf{B}}{\|\mathbf{A}\| \cdot \|\mathbf{B}\|} = \frac{\sum_i^n A_i \times B_i}{\sqrt{\sum_i^n (A_i)^2} \times \sqrt{\sum_i^n (B_i)^2}} \quad (6.1)$$

where  $\|\mathbf{A}\|$  and  $\|\mathbf{B}\|$ , respectively, represent the magnitudes of vectors A and B, and  $\mathbf{A} \cdot \mathbf{B}$  denotes the dot product of A and B. Cosine similarity ranges from 0 to 1, with higher values representing smaller angles and higher similarity. The cosine similarity between each single particle spectrum and the three major cluster centroids (the average spectra) was calculated (Figure 6.4). Spectra in Cluster I had significantly higher similarity (median value is  $> 0.8$ ) to Cluster I centroid than Cluster II and III centroids (Figure 6.4a). In other words, the within-cluster similarity was far higher than the cross-cluster similarity for Cluster I spectra. In addition, the variability of the within-cluster similarity was lower than that of the cross-cluster similarity, suggesting good separation of Cluster I spectra. Similar results were found for Cluster II spectra (Figure 6.4b). Compared to Cluster I and Cluster II, the within-cluster similarity for Cluster III spectra had lower values (median value of 0.5) and greater variability (Figure 6.4c). However, the within-cluster similarity was significantly higher than the cross-cluster similarity at 99% confidence level for Cluster III spectra. The cosine similarity analysis also suggests that each cluster may have limited chemical properties of other clusters, indicating that particles were likely internally mixed but dominated by one type so they can be grouped by the dominant signatures.



The effects of single-particle size and organic mass fraction on the derived single-particle clusters were examined. The number of organic ions detected for each single-particle is a function of the organic mass fraction (for a given threshold of 6 ions described in Section 6.3.1) and particle size (larger particles produce more ions). Sulfate and nitrate, the major inorganic ions, were found to be independent of organic cluster types (Figure 6.5), i.e., sulfate and nitrate, respectively, accounted for 16% and 4% of single-particle mass for each cluster (on average). To test the effects of organic mass fractions on the derived clusters, a K-means algorithm was applied to four subsets of the total 147,357 particles, which were composed of particles with organic mass fractions greater than 10%, 20%, 30%, and 40% of the total particle mass, respectively. Three major clusters were identified in each case. The cluster centroids were identical to the centroids of Clusters I to III, and the relative cluster sizes (number of particles in the cluster) were comparable to the relative sizes of Clusters I to III, indicating that the same single-particle clusters were identified. The effects of particle size on clustering results were tested by applying a K-means analysis to three subsets of the total particles, which were composed of particles larger than 300 nm, 400 nm, and 500 nm  $d_{va}$ , respectively. The same clusters (as Clusters I to III) were identified. That the inorganic-to-organic mass ratio and particle size did not affect the results of cluster analysis indicated that the single-particle organic mass ions were sufficient for cluster analysis and the identified clusters were robust.

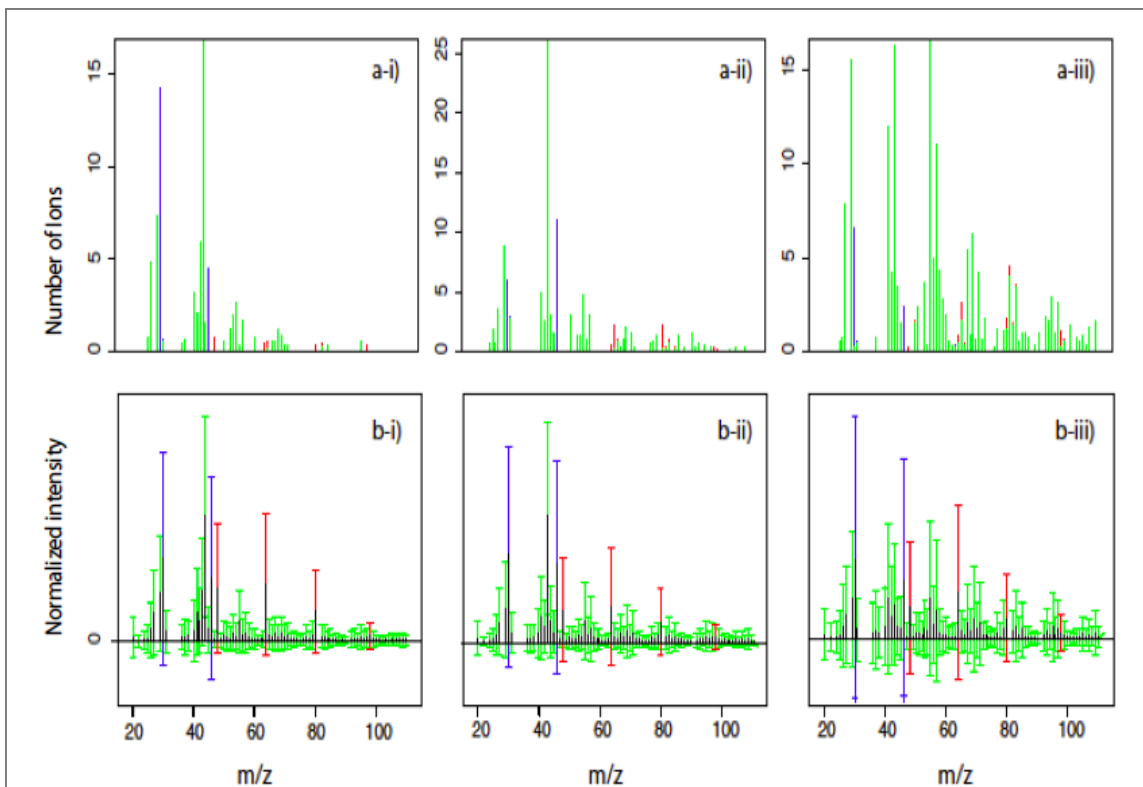
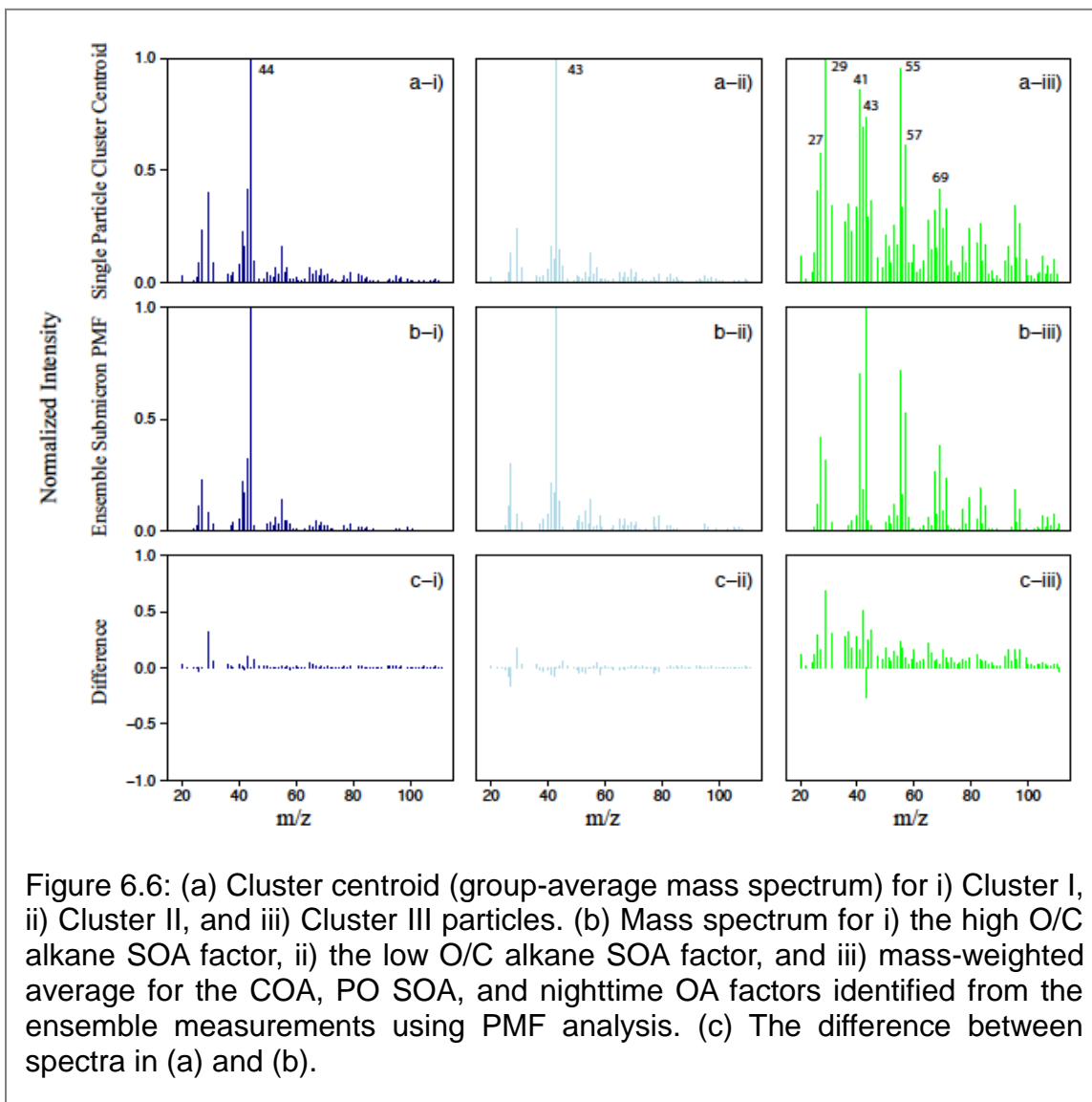


Figure 6.5: (a) Example single-particle spectra for i) Cluster I, ii) Cluster II (y-axis 0-25), and iii) Cluster III. The particles in i), ii), and iii) were collected on 16 May ( $d_{va} = 507$  nm,  $d_g = 362$  nm), 31 May ( $d_{va} = 402$  nm,  $d_g = 287$  nm), and 16 May ( $d_{va} = 492$  nm,  $d_g = 351$  nm), respectively. (b) Variability of normalized single particle spectra for each cluster for this study (15 May to 29 June 2010). In each panel, the black sticks show the average spectrum for the cluster, and the whiskers represent standard deviations (variability) at each  $m/z$ . Colors indicate organic (green), nitrate (blue), and sulfate (red) fragments.

Examples of single-particle spectra for the three major clusters are shown in Figure 6.5a. (The cluster centroids and time series of the minor clusters are shown in Figure S6.3 and S6.4, respectively, in the Section 6.5.) While the single-particle spectra exhibit large variability (Figure 6.5b), the centroids for the three particle types (Figure 6.6a) show that the Cluster I spectrum was characterized by a dominant peak at  $m/z$  44, comparable to that of LV-OOA (low-volatility OOA) components extracted from the positive matrix factorization (PMF) analysis in a number of field measurements [Ulbrich *et al.*, 2009]. This indicates that particles in this cluster were highly oxidized and associated with high O/C, which is consistent with the correlation of the number fraction of Cluster I particles with odd oxygen (Figure 6.7a). It is suggested that Cluster II particles, which had strong  $m/z$  43 signals and mass spectra resembling those of SV-OOA (semivolatile OOA) components identified by Lanz *et al.* [2007], Ng *et al.* [2010], and Ulbrich *et al.* [2009], were relatively less oxidized SOA and, so, were likely

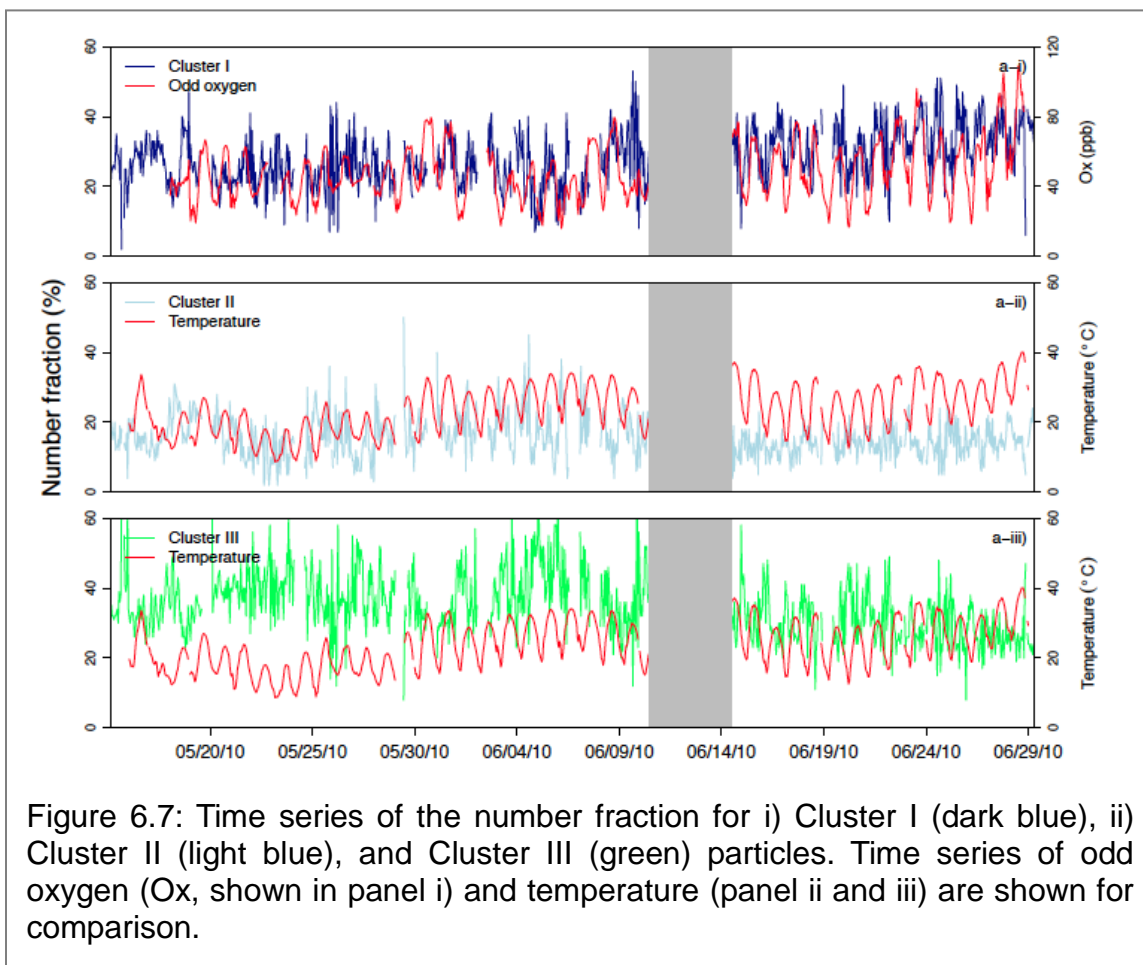
associated with lower O/C than Cluster I particles. The number fraction of Cluster II particles increased at night and showed the opposite diurnal cycle to temperature (Figure 6.7b), which is consistent with the previous findings that the less processed component accumulated and condensed onto preexisting particles during nighttime hours [Lanz *et al.*, 2007].



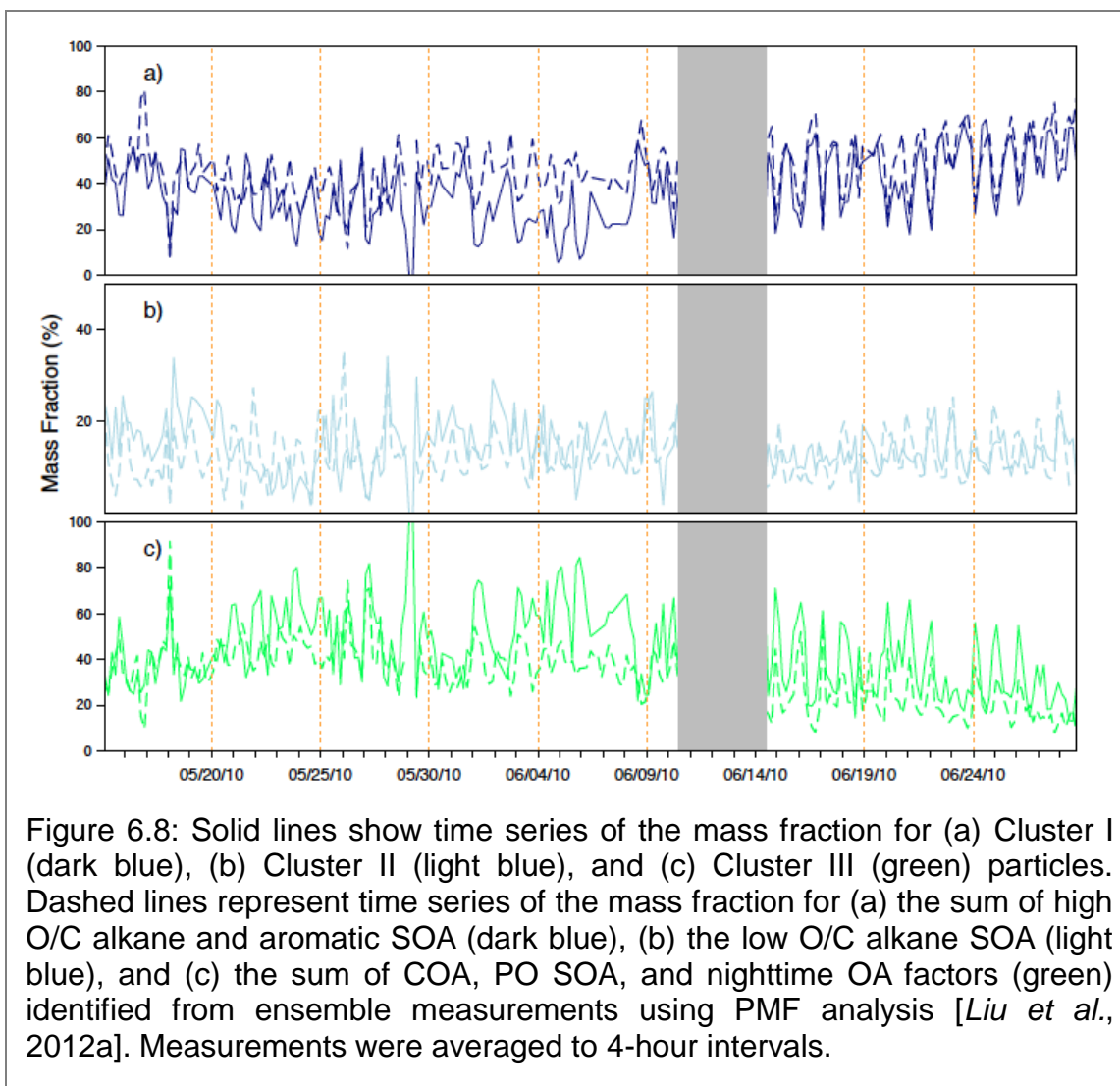
However, the correlation of Cluster II particle number fraction with particle-phase nitrate, whose formation is strongly dependent on temperature, was not found, suggesting that there might be other factors that affected the formation of Cluster II particles. The average spectrum for Cluster III particles was characterized by  $m/z$  27, 29, 15 41, 43, 55, 57, and 69, which are characteristic of both HOA and cooking organic aerosol (COA) components [He *et al.*, 2010; Mohr *et al.*, 2009]. However, the HOA and COA components are not distinguishable due to the high similarity of their unit-mass spectra [Mohr *et al.*, 2009; Mohr *et al.*, 2012],



although both the HOA-influenced component (the nighttime OA factor) and the COA component were identified from the PMF analysis of the high-resolution ensemble mass spectra measured by the same LS-ToF-AMS during the CalNex campaign [Liu *et al.*, 2012a]. The number fraction of Cluster III particles peaked at night, anti-correlating with temperature (Figure 6.7c). Thus particles in Cluster III may be produced by a mixture of different sources, possibly including cooking oils and local unoxidized vehicular emissions at night.



Size distributions of particle types (Figure 6.2a) show an increased number fraction of Cluster I type for particles larger than 300 nm  $d_{va}$  (215 nm  $d_g$ ). In contrast, Cluster III type dominated particles smaller than 400 nm  $d_{va}$  (285 nm  $d_g$ ). Compared to Cluster I and Cluster III particle types, Cluster II type was more evenly distributed across particle size. A likely explanation of size dependence of particle types is that oxidized particles (in Cluster I) formed by condensation of secondary vapors onto preexisting particles so that they grew bigger, whereas Cluster III particles were associated with fresh emissions in which particles were smaller.



### 6.3.3 Comparison of Single-particle Types with Ensemble Components

Cluster I, Cluster II, and Cluster III particle types broadly matched the OM components identified from ensemble factor analysis using PMF (Liu et al., submitted). Ensemble-based OM spectra were categorized into three groups according to their O/C values (calculated from the high resolution mass spectra using the method described by Aiken et al. [2007]): Group I consisted of high O/C alkane and aromatic SOA components (O/C = 0.63-0.68); Group II consisted of low O/C alkane and aromatic SOA components (O/C = 0.27-0.36); and Group III was likely a mixture of COA, petroleum operation (PO) SOA, and local traffic and biogenic nighttime OA components (O/C = 0.00-0.20). The mass fractions of  $m/z$  44 (f44; an indicator of O/C [Aiken et al., 2008]) for Cluster I (23.1%), Cluster II (4.1%), and Cluster III (2%) reasonably agreed with the f44 for the ensemble-based Group I (19.6%), Group II (2.4%), and Group III (0.5%), respectively. Specifically, the Cluster I centroid correlated to the mass spectra for high O/C alkane and aromatic SOA components with an  $r$  of 0.96 and 0.92, respectively

(Figure 6.6). The mass fraction of Cluster I particles had similar magnitude and time series to that of the sum of high O/C alkane and aromatic SOA components (Figure 6.8a; correlated in time with  $r = 0.69$  shown in Table S6.1), supporting the consistency of Cluster I particles with high O/C components. The centroid for Cluster II particles correlated to that of the low O/C alkane SOA component with an  $r$  of 0.96. The Cluster III centroid correlated to the spectra for COA, PO SOA, and nighttime OA components with  $r$  values of 0.86, 0.76, and 0.70, respectively. Correlation of the Cluster III centroid to the mass-weighted average spectrum for COA, PO SOA and nighttime OA (Figure 6.6b-iii) showed an  $r$  of 0.82. The mass fraction of Cluster III particles and the sum of ensemble-derived Group III components co-varied (Figure 6.8c;  $r = 0.63$  shown in Table S6.1), with low fractions during daytime and increased abundance at night. There were some deviations in magnitude and time series for single-particle clusters and ensemble-derived components, especially for Cluster II particles that only poorly correlated with the low O/C alkane SOA factor ( $r = 0.22$ ). The differences were likely due to 1) measurement and analysis (cluster, PMF, etc.) uncertainties, 2) internally mixed particles that were split between more than one cluster or assigned to one of the minor clusters (IV, V, VI, etc.), or 3) the low detection efficiency of single particles that were smaller than 550 nm  $d_{va}$  (Figure 6.2a). However, the broad match of single-particle clusters and ensemble factors confirmed that the factors reflected organic components of different origins and atmospheric processes.

#### 6.4 Concluding Remarks

The LS-ToF-AMS was valuable for separating single particles with different organic chemical compositions in a 46-day field campaign. 271,641 single particles were optically detected and the chemical mass spectra saved and classified by comparison of the optical and chemical information, with a 46% prompt fraction, a 48% null fraction, and a 6% delayed particle fraction. Thus, the LS-ToF-AMS provided a direct measure of the collection efficiency of ambient particles, resulting in an approximate 50% number-based CE for particles larger than 180 nm  $d_{va}$  (130 nm  $d_g$ ).

Single particles can be consistently represented by several particle types, each of which has distinct chemical compositions formed via different processes. A K-means clustering algorithm was applied to the organic mass spectra for all saved prompt and delayed single particles. We found that ~80% of single particles were dominated by chemical characteristics of one of the three clusters: Cluster I and II particles appeared to be formed from secondary organic components while Cluster III particles suggested a primary origin from fresh urban emissions. Additionally, Cluster I particles likely were more oxidized than particles in Cluster II due to the large contribution of  $m/z$  44 in the Cluster I centroid. Mass spectra and time series of the three particle types broadly matched the organic factors identified from the ensemble-averaged measurements using the LS-ToF-AMS, providing evidence that the factors could represent organic components

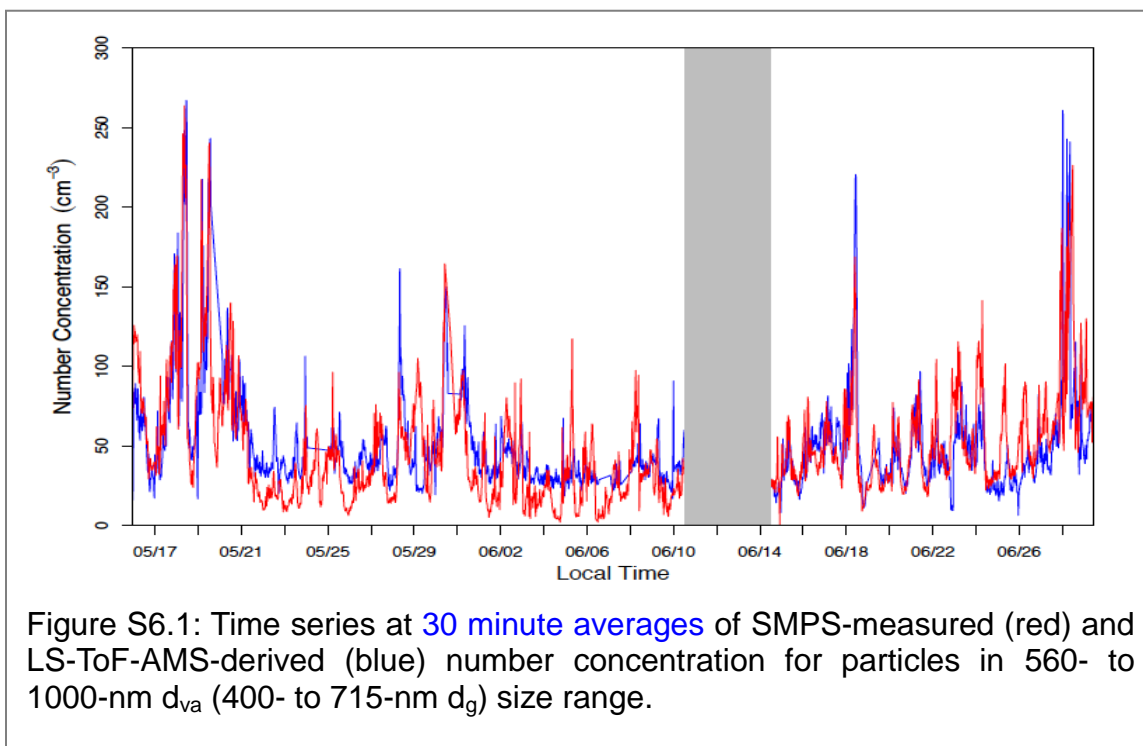
originating from different sources and processes.

Continual developments of LS-ToF-AMS, such as enhancing its ability to detect smaller particles and data transfer and saving efficiency, will result in more detailed information about the origin, transformation, and fate of atmospheric organic particles.

## 6.5 Appendix

### 6.5.1 Comparison of number concentration measured by LS-ToF-AMS and SMPS

Average particle detection rate (particles detected per second) for each saved LSSP mode file (run number) was scaled by the overall duty cycle (for the same file) to calculate total particle number concentration. Time series of LS-ToF-AMS- and SMPS-measured number concentrations were averaged to 30-min intervals for comparison. Total number concentration for 560- to 1000-nm  $d_{va}$  (400- to 715-nm  $d_g$ ) particles compared reasonably well—the linear fit has a slope of 0.89 (the SMPS-measured concentration was 11% higher) and an intercept of 6.3, and the number concentrations correlated with an  $r$  of 0.7 (Figure S6.1).



### 6.5.2 Comparison of ions generated by single particles of different vaporization types

The ions associated with the prompt and delayed, null, and non-particle events were compared using (a) the sum of non-background ions (i.e.,  $m/z$  15, 27, 30, 41, 43, 44, 46, 48, 55, 57, and 64) and (b) all the ions in the mass spectra. The

non-particle events are the noise spikes in the light scattering channel that are characterized by near-zero light scattering signals. In both cases, prompt and delayed particles have significantly higher number of ions than in null- and non-particle events. For the non-particle and null-particle events, there are typically 2-4 ions, which are below the 6-ion detection limit (Figure S6.2).

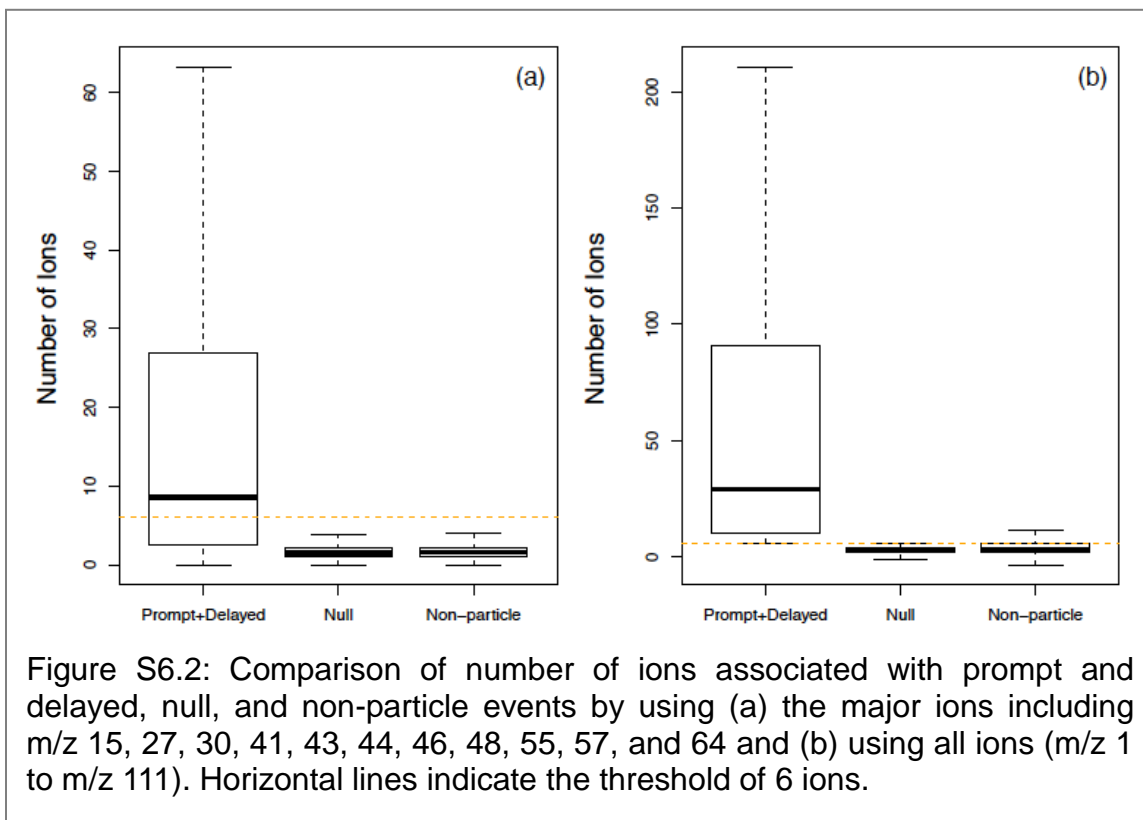


Figure S6.2: Comparison of number of ions associated with prompt and delayed, null, and non-particle events by using (a) the major ions including m/z 15, 27, 30, 41, 43, 44, 46, 48, 55, 57, and 64 and (b) using all ions (m/z 1 to m/z 111). Horizontal lines indicate the threshold of 6 ions.

### 6.5.3 Duty cycle versus particle number concentration

The dependence of duty cycle (data saving duty cycle calculated from the comparator circuit) on particle number concentration (from the SMPS measurement) for particles from 180–1000 nm  $d_{va}$  is shown in Figure S6.3. The duty cycle is weakly, or not at all, dependent on particle number concentration.

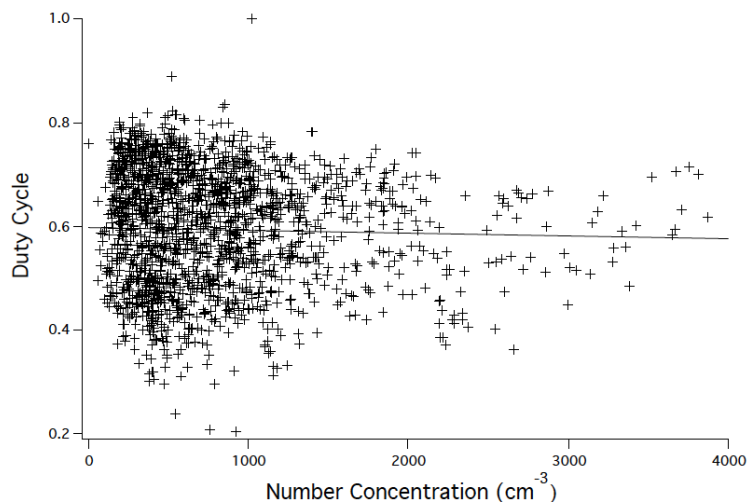


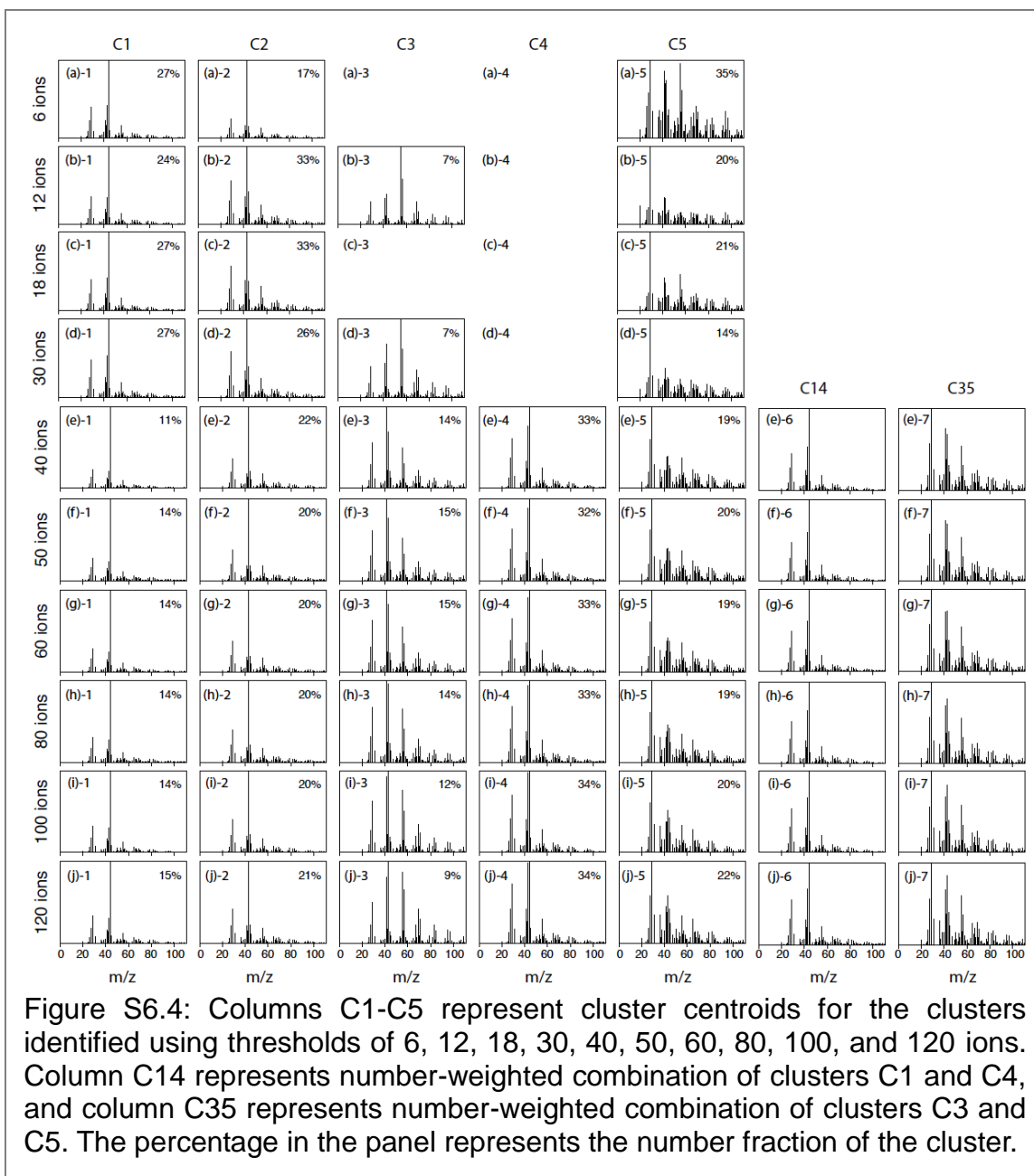
Figure S6.3: Data saving duty cycle (number of particles saved using LSSP over total number of LS-circuit counted particles) versus SMPS measured particle total number concentration (130 to 715 nm  $d_m$ ). The line represents the linear fit of the points with a slope of  $-5.6 \times 10^{-6}$ .

#### 6.5.4 Comparison of mass-based and number-based collection efficiency

The discrepancy of the mass-based and number-based CE may result from the differences of the operation modes. The mass-based CE was derived from the MS mode, whereas the number-based CE was determined using the LSSP mode. On average, the concentration measured by the MS mode was twice the concentration measured by the PToF mode [Liu *et al.*, 2012a] and therefore the LSSP mode (which is in agreement with the PToF mode for particles larger than 600 nm  $d_{va}$  shown in Figure 6.2c), indicates that the null particles, which have chemical signals less than 6 ions per particle, and probably some of the prompt and delayed particles evaporated slower than the LSSP/PToF measurement window ( $\sim 6$  ms) but with sufficient rapidity to be detected in MS mode (10 s). The slowly vaporized particles may result in a higher mass-based CE.

#### 6.5.5 Selecting particles for cluster analysis

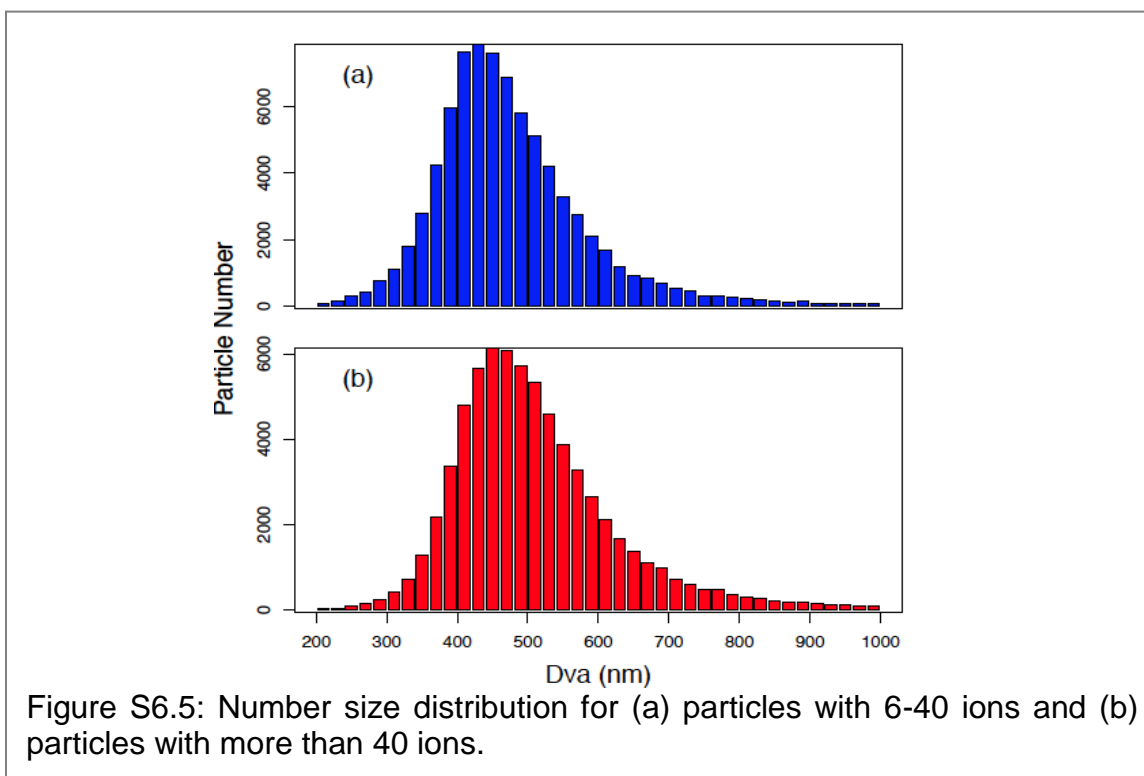
Although the threshold of 6 ions is good for distinguishing particles from background noise, particles with low ions may not have sufficient chemical signatures to be correctly classified. In order to find at what signal level (number of ions) particles can be accurately classified on a single particle basis, we applied the K-means cluster analysis on ten subsets of the prompt and delayed single particle spectra, with each subset containing spectra that have more ions than a threshold. The thresholds include 6, 12, 18, 30, 40, 50, 60, 80, 100, and 120 ions.



The results of the cluster analyses are shown in Figure S6.4. The clusters are labeled as C1, C2, C3, C4, and C5, and similar clusters from different solutions (thresholds) are aligned in the same column for comparison. The blank panels in the results of 6-30 ions indicate that the clusters were not observed in these solutions. Five major clusters were identified.

The clusters identified using different thresholds show differences and similarities. For example, the clusters identified using thresholds of 6-30 ions were not consistent, i.e., C3 only showed up in 12-ion and 30-ion solutions, and the number fractions of C2 and C5 were different among these solutions. It is

likely that a fraction of the particles with low chemical ions were classified inconsistently, resulting in the cluster differences. In contrast, the clusters identified in the 40-120 ion solutions are very consistent in both cluster spectrum and number fraction, suggesting that particles with more than 40 ions likely have enough chemical signals to be accurately categorized so that the results are independent of the threshold values. Therefore, although particles with less than 40 ions and more than 40 ions have similar number size distributions (Figure S6.5), including the low-ion particles in the cluster analysis decreases the robustness of the cluster analysis. Accordingly, we use 40 ions as the threshold for single-particle classification and the clusters identified from particles with more than 40 ions are used in the manuscript.



In order to identify similarities between the single-particle clusters and ensemble PMF factors, we compare their mass spectra and time series. Although the mass spectra of C1-C5 were separately identified as clusters, some of the mass spectra had similar chemical signatures. To simplify the clusters for comparison to the mass-based factors, the clusters with similar chemical signatures were combined, i.e., C1 and C4 were combined because they were both characterized by high-intensity of  $m/z$  44 in their mass spectra, and C3 and C5 were combined because they had significant peaks at  $m/z$  27, 29, 41, 43, and 57 that are characteristic of HOA. C14 (number-weighted combination of C1 and C4), C2, and C35 (number-weighted combination of C3 and C5) are termed as Cluster I, Cluster II, and Cluster III, respectively.



Table S6.1: Cross correlation of the mass fraction time series for the three single-particle clusters (Clusters I, II, and III) and the ensemble-derived factors. Pearson's correlation coefficients are shown.

	High O/C alkane SOA + high O/C aromatic SOA	Low O/C alkane SOA	COA + PO SOA + Nighttime OA
Cluster I	0.69	-0.29	-0.60
Cluster II	0.00	0.23	-0.02
Cluster III	-0.65	0.19	0.60

## 7.0 Implications of Secondary Organic Aerosol Formation<sup>7</sup>

The SOA components, which were derived from factor analysis, differed in mass, chemical composition, and diurnal cycle (summarized in Table 7.1), suggesting they were produced via distinct oxidation processes and likely favored by specific meteorological conditions. In this chapter, we compare the SOA components and discuss the underlying processes that likely led to their formation. Special attention is given to alkane SOA, aromatic SOA, and NOA; the first two prevailed during daytime, and the last was a significant constituent at night. In addition, we discuss size distributions of SOA components, which confirm the source identification and indicate the likely formation process.






### 7.1 Contrasting Formation of Alkane and Aromatic Secondary Organic Aerosol Components

The diurnal cycle for high O/C alkane SOA<sub>AMS</sub> was consistent over the course of the study, with concentrations peaking in the afternoon for 74% of the 45-day campaign (Figure 7.1a). The average diurnal cycle resembled that of the odd oxygen (O<sub>3</sub> + NO<sub>2</sub>), and the factor mass fraction correlated to odd oxygen with an  $r$  of 0.70 (higher temperature associated with larger odd oxygen mixing ratios and greater factor mass fractions) (Figure 7.1b), suggesting O<sub>3</sub> either played an important role in its formation or was coproduced with alkane SOA from similar precursors on similar time scales. Good correlations of alkane SOA to odd oxygen were also found by recent model simulations even without a role for O<sub>3</sub> in the oxidation of alkanes [Pye and Pouliot, 2012]. The alkane SOA<sub>FTIR</sub> factor mole composition (0.11/0.04/0.00/0.86 among carboxylic acid/hydroxyl/non-acid carbonyl/alkane groups) compared well to C<sub>12</sub> alkane oxidation products, with mole fractions of 0.12/0.13/0.02/0.73 for the carboxylic acid/hydroxyl/non-acid carbonyl/alkane groups [Russell *et al.*, 2011]. This composition was inferred from a two-step oxidation pathway: 1) gas-phase alkane oxidation by OH radicals to form particle-phase dihydrofuran; and 2) evaporation of dihydrofuran followed by O<sub>3</sub> oxidation, forming carboxylic acid and alkane group dominated products [Russell *et al.*, 2011]. The products from each step likely represented first and higher generation SOA components, respectively [Lim and Ziemann, 2005; 2009]. Therefore, that the high O/C alkane SOA<sub>AMS</sub> factor correlated with odd oxygen indicated second or higher generation products from alkane oxidation. Neither the low O/C alkane SOA<sub>AMS</sub> factor nor the sum of the high and low O/C alkane SOA<sub>AMS</sub> factors (correlating to the alkane SOA<sub>FTIR</sub> factor,  $r = 0.74$ ) correlated to odd oxygen, indicating that the low O/C alkane SOA<sub>AMS</sub> factor may have been associated with the first step of oxidation which happened faster than O<sub>3</sub> formation or for which O<sub>3</sub> was not required.

---

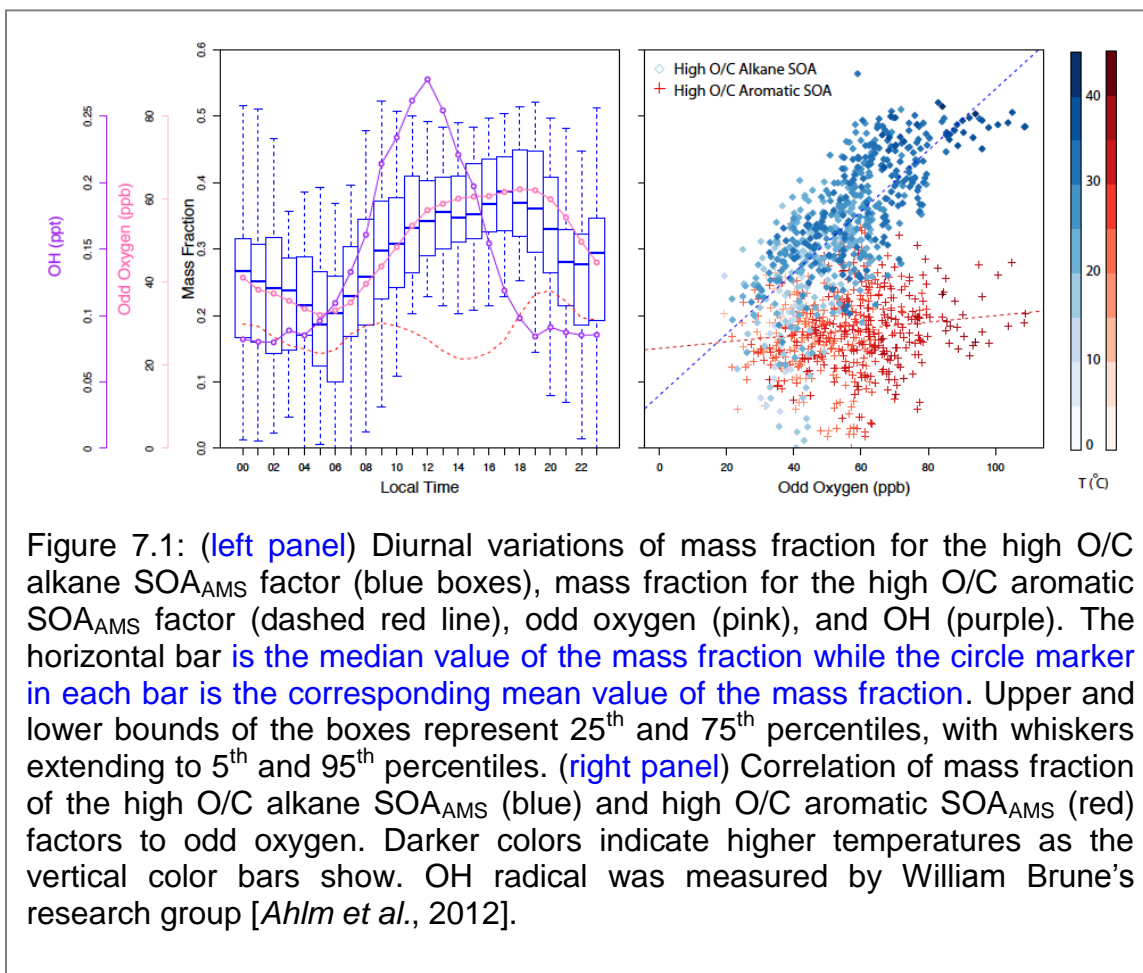
<sup>7</sup> Work in this section is published in Liu *et al.* [2012a].

Table 7.1: Summary of concentration, OM fraction (in parentheses), oxidant, peak time, O/C, organic functional group (OFG) composition, size range, and source of FTIR and the AMS factors.

FTIR			AMS		Oxidant	Peak Time	O/C	OFG <sup>a</sup>	Size (nm)	Source	Primary or secondary
Factor	Conc. in PM <sub>1</sub> (µg m <sup>-3</sup> )	Conc. in PM <sub>2.5</sub> (µg m <sup>-3</sup> )	Factor	Conc. in PM <sub>1</sub> (µg m <sup>-3</sup> )							
Aromatic SOA	0.61 (24%)	0.77 (23%)	Low O/C aromatic SOA	0.35 (9%)	OH	0-6; 12-18	0.36		250-900	Fossil fuel combustion	Secondary
			High O/C aromatic SOA	0.64 (16%)	OH	18-23	0.68		200-500	Fossil fuel combustion	Secondary
Alkane SOA	1.21 (41%)	1.43 (43%)	Low O/C alkane SOA	0.48 (12%)	OH	22-6	0.27		200-500	Fossil fuel combustion	Secondary
			High O/C alkane SOA	1.19 (30%)	O <sub>3</sub>	10-17	0.63		200-500	Fossil fuel combustion	Secondary
NOA	0.30 (10%)	0.25 (8%)	NOA	0.50 (13%)	NO <sub>3</sub>	0-6	0.01		400-700	Fossil fuel combustion/biogenic emissions	Primary and secondary
PO SOA	0.42 (14%)	0.42 (13%)	PO SOA	0.49 (13%)	OH and/or O <sub>3</sub>	10-17	0.20		100-200	Petroleum operations	Secondary
Vegetative detritus	0.29 (10%)	0.45 (14%)	-	-	-	12-18	1.09		-	Resuspended dusts and plant materials	Primary
-	-	-	COA	0.29 (7%)	-	12-18; 20-23	0.05	-	100-200	Cooking activities	Primary

<sup>a</sup>OFG pies are colored for hydroxyl (pink), alkane (blue), amine (orange), carboxylic acid (green), non-acid carbonyl (teal), and organonitrate (beige).

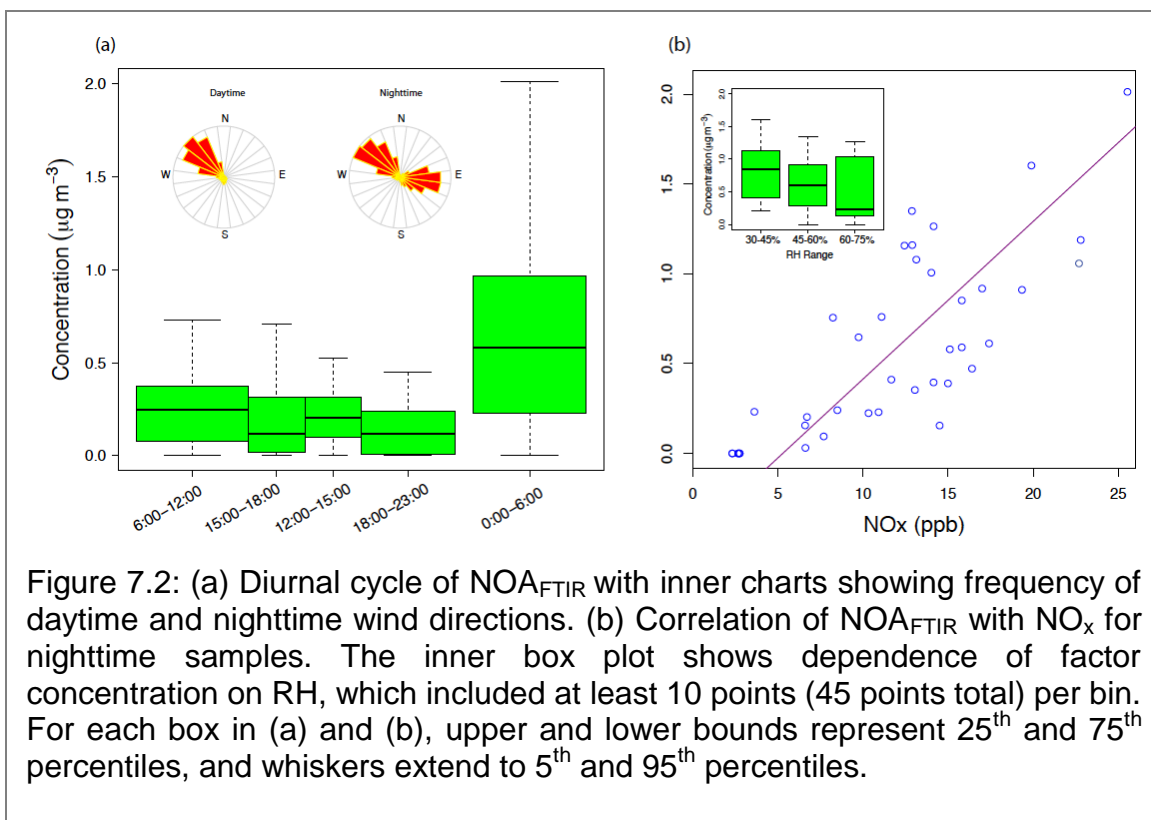
For the diurnal cycle of the high O/C aromatic SOA<sub>AMS</sub> factor, no consistent pattern was identified. Day-to-day variation likely resulted from the variety of the aromatic species emitted from vehicular emissions, including light aromatic hydrocarbons and polycyclic aromatic hydrocarbons (PAHs), the quantities of which are highly dependent on combusted fuels [Richter and Howard, 2000]. In contrast, alkane compounds were relatively simple in their structure and could readily be grouped into linear, branched, and cyclic alkane classes, with SOA products fairly similar among these classes [Lim and Ziemann, 2009]. The mass yield of aromatic compounds may vary significantly as was found in SOA yields from naphthalene, which ranged from 2% to 22% [Shakya and Griffin, 2010] and from 19% to 74% [Chan et al., 2009] under comparable experimental conditions (i.e., OH concentration, initial hydrocarbon concentration, and initial NO<sub>x</sub>-mixing ratio). This indicated that yields of aromatic hydrocarbons were extremely sensitive to environmental conditions. In addition, SOA components from PAH oxidation have been shown to be sensitive to NO<sub>x</sub> mixing ratios, with ring-opening compounds being major products under high NO<sub>x</sub> conditions and ring-retaining compounds formed under low NO<sub>x</sub> conditions [Kautzman et al., 2010].



The variety of the aromatic compounds, sensitivity of their yields to the environmental conditions, and dependence of their oxidation products on  $\text{NO}_x$ , likely contributed to the variability of the diurnal cycle for the high O/C aromatic  $\text{SOA}_{\text{AMS}}$  factor. This factor's mass fraction (or mass concentration) did not correlate to odd oxygen (Figure 7.1), suggesting that  $\text{O}_3$  played a minor role (if any) in its formation. The aromatic  $\text{SOA}_{\text{FTIR}}$  factor, which likely represented the average composition of a variety of aromatic SOA components, was largely composed of non-acid carbonyl groups (59%), which was consistent with the OH radical oxidation products for aromatic precursors, a majority of which contain ketone groups [Esteve *et al.*, 2003; Lee and Lane, 2009; 2010; Wang *et al.*, 2007; Webb *et al.*, 2006]. The similarity of the aromatic  $\text{SOA}_{\text{FTIR}}$  factor to OH oxidation products for aromatic hydrocarbons suggests that OH was the main oxidant that oxidized primary aromatic compounds to their SOA products. This observation is consistent with previous kinetic studies that showed that aromatic hydrocarbons primarily react with OH radicals in the atmosphere [Kwok *et al.*, 1994].

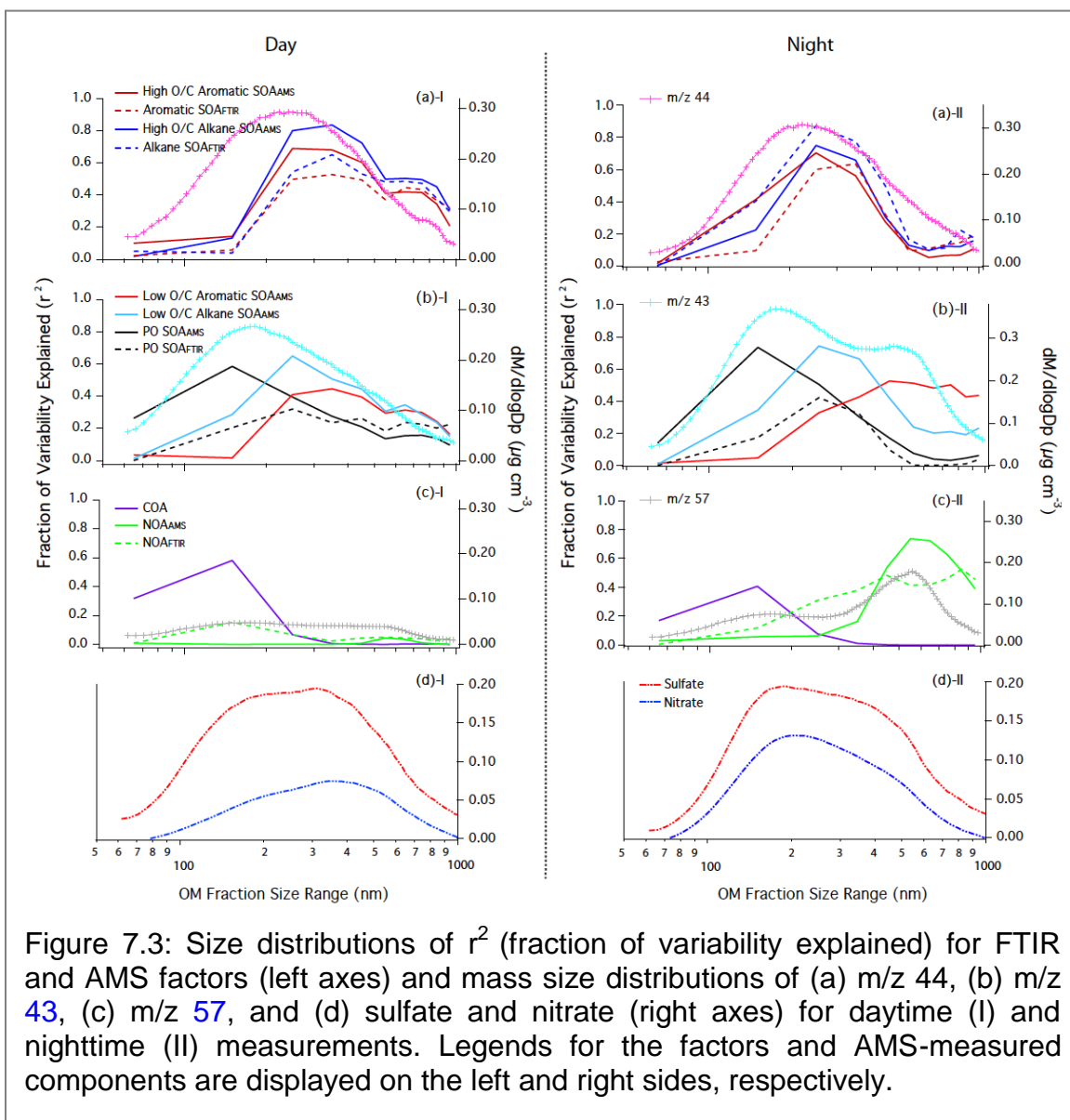
## 7.2 Nighttime Formation of Biogenic Secondary Organic Aerosols

While high O/C alkane and aromatic  $\text{SOA}_{\text{AMS}}$  components peaked during the day, high concentrations (20% to 52% OM) of the NOA factors were observed at night (Figure 7.2a). The  $\text{NOA}_{\text{FTIR}}$  factor, although influenced by primary anthropogenic sources, had significant signatures of biogenic SOA. The factor composition of alkane (57% to 79% OM), organonitrate (8% to 17% OM), and non-acid carbonyl groups (0% to 8% OM) was chemically similar to  $\alpha$ -pinene and  $\beta$ -pinene SOA produced by  $\text{NO}_3$  radical oxidation. These SOA components typically comprise 63% to 68% alkane groups, 8% to 26% organonitrate groups, and 2% to 24% non-acid carbonyl groups [Hallquist *et al.*, 1999; Wangberg *et al.*, 1997]. Therefore, the SOA fraction of the  $\text{NOA}_{\text{FTIR}}$  factor likely formed via  $\text{NO}_3$  radical oxidation. Supporting this argument is the correlation ( $r = 0.5$ ) of  $\text{NOA}_{\text{FTIR}}$  with nitrated organosulfates (e.g.,  $\text{C}_{10}\text{H}_{16}\text{NO}_7\text{S}^-$ ,  $\text{C}_9\text{H}_{14}\text{NO}_8\text{S}^-$ , and  $\text{C}_{10}\text{H}_{16}\text{NO}_{10}\text{S}^-$  ions measured by UPLC/ESI-HR-Q-TOFMS), the most abundant organosulfate compound class (observed at the Bakersfield site) that is likely produced from  $\text{NO}_3$  radical oxidation of  $\alpha$ -pinene and limonene-like monoterpenes (e.g., myrcene) under dark conditions [Surratt *et al.*, 2008].



As described in Section 4.0, easterly downslope winds prevailed at night, which likely carried biogenic VOCs to the sampling site. Biogenic VOCs (e.g., terpenes) typically contain one or more carbon-carbon double bonds, highly chemically active and readily oxidized typically by  $\text{O}_3$  and  $\text{NO}_3$  radicals under nighttime conditions. While some background  $\text{O}_3$  was still detected at night ( $\sim 10$  ppb), no correlation was observed between the  $\text{NOA}_{\text{FTIR}}$  factor and the  $\text{O}_3$  concentration, indicating  $\text{O}_3$  may not play a major role in formation of  $\text{NOA}_{\text{FTIR}}$ . However, background  $\text{O}_3$  could react with  $\text{NO}_2$  to generate  $\text{NO}_3$  radicals and could also convert  $\text{NO}$  to  $\text{NO}_2$  to prevent loss of  $\text{NO}_3$  radicals by reacting with  $\text{NO}$ . The  $\text{NOA}_{\text{FTIR}}$  factor correlated to nighttime  $\text{NO}_x$  (Figure 7.2b), which is the precursor of  $\text{NO}_3$  radicals, confirming that  $\text{NOA}_{\text{FTIR}}$  was likely formed by  $\text{NO}_3$  radical oxidation. *Rollins et al.* [2012] estimated that 1/3 of OM increase at night was accounted for by organonitrate group-containing molecules, which is consistent with the nighttime formation mechanism of the  $\text{NOA}_{\text{FTIR}}$  factor. Moreover, the  $\text{NOA}_{\text{FTIR}}$  factor accounted for 50% to 80% of the observed organonitrate group mass, which is consistent with an expected higher organonitrate group yield from  $\text{NO}_3$  oxidation reactions than that from  $\text{OH}$  radical and  $\text{O}_3$  oxidation processes. Additionally, lower concentrations of  $\text{NOA}_{\text{FTIR}}$  were associated with high RH (Figure 7.2b), which is consistent with the loss of  $\text{NO}_3$  radicals under high RH conditions (shifting the reaction  $\text{NO}_3 + \text{NO}_2 = \text{N}_2\text{O}_5$  to the right through  $\text{N}_2\text{O}_5$  uptake under high RH). Although alkane and aromatic hydrocarbons coexisted with biogenic VOCs at night, their oxidation rate constants for  $\text{NO}_3$  radicals were typically less than  $10^{-16}$  and  $10^{-15} \text{ cm}^3 \text{ molecule}^{-1} \text{ s}^{-1}$ , respectively [*Atkinson and*

Arey, 2003]. These rate constants were  $10^3$  to  $10^6$  times smaller than rate constants of the biogenic hydrocarbons (oxidation by  $\text{NO}_3$  radicals), which typically ranged from  $10^{-10}$  to  $10^{-12}$   $\text{cm}^3 \text{molecule}^{-1} \text{s}^{-1}$  [Atkinson and Arey, 2003]. Therefore,  $\text{NO}_3$  radicals mainly reacted with biogenic VOCs, forming biogenic SOA components with organonitrate functional groups in the nighttime atmosphere.



Compared to the biogenic SOA factors identified at Whistler, British Columbia (at 1020 m above sea level) [Schwartz *et al.*, 2010], the  $\text{NOA}_{\text{FTIR}}$  factor had significantly larger contribution of organonitrate groups. This difference likely arises from distinct oxidation conditions:  $\text{O}_3$  or  $\text{OH}$  radical oxidation under low  $\text{NO}_x$  (1.5 ppb) at Whistler and  $\text{NO}_3$  radical oxidation under high  $\text{NO}_x$  (15 ppb at night) at Bakersfield.

### 7.3 Insights of SOA Formation from Factor Size Distribution

Time series of the OM factors were correlated to time series of OM particle size sections ( $OM_{30-100}$ ,  $OM_{100-200}$ ,  $OM_{200-300}$ ,  $OM_{300-400}$ ,  $OM_{400-500}$ ,  $OM_{500-600}$ ,  $OM_{600-700}$ ,  $OM_{700-800}$ ,  $OM_{800-900}$ ,  $OM_{900-1000}$ ) derived from the AMS TOF mode measurements, resulting in a set of correlation coefficients for each factor. The square of the correlation coefficient ( $r^2$ ) between an OM section and a factor represents the fraction of variability of an OM section that could be explained by variability of the factor [Rogers and Nicewander, 1988]. The mean and variability (standard deviation) for the OM sections were comparable (Table 7.2), suggesting that most of the OM concentration was controlled by OM variability. Similarly, the factor concentration was controlled by variability in the factor concentration. Therefore, high  $r^2$  between an OM section and a factor suggests that the mass of the OM section was likely accounted for by the factor, i.e., a majority of the factor mass likely distributed in the same size range as the OM section. For this reason, the  $r^2$  distribution (versus size) for each factor represents the factor mass size distribution to a great extent. Factor mass size distribution estimated from this approach can be validated by size distribution estimated from a marker-based method (e.g., size distribution of m/z 44 represents size distribution of SOA), which has proven to be approximately accurate [Ulbrich *et al.*, 2012].

Variability of OM in 200- to 500-nm-sized particles was accounted for by the high O/C alkane and aromatic SOA factors (Figure 7.3a), suggesting that the high O/C factors peaked in 200- to 500-nm size range. Mass of fragment  $CO_2^+$  (m/z 44), largely accounted for by high O/C alkane SOA (55%) and high O/C aromatic SOA (30%) factors, peaked in the 150- to 500-nm size range, which agreed well with  $r^2$  distributions for the two high O/C factors. These peak size ranges are comparable to those for the OOA factor identified from Mexico City measurements using 3-D factorization analysis [Ulbrich *et al.*, 2012]. Oxidized components are prevalent in the 200- to 500-nm particle size range because these sizes provide the greatest surface area for condensation of gas-phase secondary organic species [Seinfeld and Pandis, 2006]. In addition, oxidized components in 200- to 500-nm-sized particles are often associated with high  $O_3$  mixing ratios [Alfarra *et al.*, 2004; Liu *et al.*, 2008; Zhang *et al.*, 2005a], suggesting that the high O/C factors were produced during photochemical processes. Note that  $r^2$  size distributions of the high O/C factors shifted 50 nm (daytime) and 20 nm (nighttime) towards larger sized particles compared to the m/z 44 size distribution, a difference likely caused by variation of non-m/z 44 fragments (in the high O/C factors) that underwent different atmospheric processes (compared to m/z 44). Larger daytime shifts reflect more complex processes, which could also explain the shoulder at 600- to 900-nm of daytime  $r^2$  distributions. Low O/C alkane and aromatic SOA factors had similar  $r^2$  size distributions compared to those for the high O/C factors, except the low O/C alkane SOA was broadly distributed (250 to 900 nm) (Figure 7.3b). This likely resulted from the low O/C alkane SOA's temperature-driven condensation at



night [Lanz *et al.*, 2007; Ng *et al.*, 2010], as daily temperatures fluctuated widely (10–20 °C).  $r^2$  of another low O/C factor, PO SOA, peaked in the 100- to 200-nm size range. Fragment m/z 43 (72% C<sub>2</sub>H<sub>3</sub>O<sup>+</sup> and 28% C<sub>3</sub>H<sub>7</sub><sup>+</sup>) was representative of low O/C factors. Daytime size distribution of m/z 43 peaked in the 100- to 600-nm size range, as was consistent with size distributions of low O/C alkane SOA, low O/C aromatic SOA, and PO SOA factors. A distinct mode of m/z 43 at 400- to 700-nm occurred at night, likely a contribution of C<sub>3</sub>H<sub>7</sub><sup>+</sup> from unoxidized primary, hydrocarbon-like vehicle emissions that were emitted at night. The colder nighttime temperatures and the lack of sunlight allowed the hydrocarbon fractions to accumulate in the particle phase more than they did during the daytime hours, when only negligible fractions of hydrocarbon-like fragments were measured.

Table 7.2: Mean concentration, variability, and fraction of variability explained by the AMS factors for the OM sections.

	OM <sub>30-100</sub>	OM <sub>100-200</sub>	OM <sub>200-300</sub>	OM <sub>300-400</sub>	OM <sub>400-500</sub>	OM <sub>500-600</sub>	OM <sub>600-700</sub>	OM <sub>700-800</sub>	OM <sub>800-900</sub>	OM <sub>900-1000</sub>	
Mean concentration (µg m <sup>-3</sup> )	0.12	0.55	0.30	0.20	0.11	0.07	0.04	0.03	0.01	0.01	
Variability (standard deviation) (µg m <sup>-3</sup> )	0.08	0.32	0.22	0.17	0.09	0.06	0.04	0.03	0.02	0.01	
Ratio of variability to mean	0.69	0.58	0.71	0.83	0.83	0.83	0.95	1.05	1.20	1.50	
Fraction of variability explained ( $r^2$ )	Low O/C aromatic SOA	0.03	0.04	0.36	0.44	0.49	0.45	0.43	0.45	0.38	0.35
	High O/C aromatic SOA	0.02	0.28	0.69	0.61	0.35	0.15	0.10	0.12	0.13	0.14
	Low O/C alkane SOA	0.01	0.26	0.60	0.53	0.44	0.30	0.27	0.27	0.24	0.25
	High O/C alkane SOA	0.01	0.16	0.67	0.64	0.31	0.12	0.10	0.13	0.14	0.15
	NOA	0.00	0.04	0.05	0.12	0.45	0.67	0.66	0.56	0.44	0.31
	PO SOA	0.25	0.53	0.33	0.20	0.08	0.02	0.01	0.02	0.03	0.03
	COA	0.21	0.48	0.07	0.01	0.00	0.00	0.00	0.00	0.00	0.00

The size distribution of  $r^2$  of the NOA factor peaked in the 400- to 700-nm size range at night (Figure 7.3c). This size range largely overlapped the larger mode in nighttime size distribution of m/z 57, which was expected because 60% of m/z

57 mass fragment was attributed to the NOA factor. The 400- to 700-nm mode was absent in the size distribution of m/z 44 and the daytime size distribution of the m/z 57 mass fragment, suggesting that nighttime OM<sub>400-700</sub> was likely associated with primary emissions. A likely source of these nighttime emissions was vehicles. Although fresh exhaust particles are typically smaller than 100 nm, a mode at 550 nm was observed from chase studies using AMS [Canagaratna *et al.*, 2004]. In addition, Kleeman *et al.* [2009] attributed a significant mass of particles (560–1000 nm) to diesel fuel and gasoline combustion sources at the same site. Another source of particles in this mode could be vegetative detritus, which likely existed as large particles (Section 4.1). SOA produced at night (e.g., biogenic SOA) could condense on large primary particles to form internal mixtures. Therefore the NOA factor, which included a mixture of primary and secondary signatures, likely represented a mixture of primary hydrocarbons and condensed secondary biogenic SOA components formed by NO<sub>3</sub> oxidation.

The size distribution of  $r^2$  for the COA factor peaked in 100- to 200-nm, a size range consistent with primarily emitted particles from meat charbroiling and frying activities [Allan *et al.*, 2010; Hildemann *et al.*, 1991; Kleeman *et al.*, 2009; Wallace *et al.*, 2004; Zhang *et al.*, 2007], which agreed with the low O/C (0.04) for this factor.

## 7.4 Conclusions

We have studied potential formation mechanisms of the anthropogenic and biogenic SOA components at Bakersfield. Correlation of the alkane SOA factor to O<sub>3</sub> and the similarity of the alkane SOA factor composition to the composition proposed from an O<sub>3</sub>-driven mechanism suggests that O<sub>3</sub> played a major role in formation of this factor; whereas, the aromatic SOA factor was likely formed from OH-driven mechanisms, resulting in large fraction of non-acid carbonyl groups in this component. Both alkane and aromatic SOA components were enriched in 200- to 500-nm-sized particles, suggesting that these components were formed by condensation processes. In contrast, the biogenic SOA component likely originated from oxidation of biogenic VOCs by NO<sub>3</sub> radicals followed by condensation on 400- to 700-nm-sized particles during nighttime hours. The different VOC sources, oxidants, and formation mechanisms identified in this work demonstrate the complexity of emissions and atmospheric processes at Bakersfield.

## 8.0 Formation and Growth of Ultrafine Particles from Secondary Sources in Bakersfield during CalNex<sup>8</sup>

### 8.1 Introduction

There is extensive evidence that aerosol particle pollution has adverse effects on human health [Harrison *et al.*, 2010; Pope and Dockery, 2006]. Aerosols in many locations are regulated by particle mass, for instance PM<sub>2.5</sub> (mass concentration of particles with diameter  $D_p$  lower than 2.5 $\mu$ m). However, urban particle number size distributions are in general observed to have their peak number concentration at a diameter of 20-40 nm [Ketzel *et al.*, 2004; Shi *et al.*, 1999; Stanier *et al.*, 2004b; Woo *et al.*, 2001]. Particles in this size range often make a relatively low contribution to the PM<sub>2.5</sub> aerosol mass. Nevertheless, results from several studies indicate that ultrafine particles ( $D_p < 100$ nm) may cause particularly adverse health effects [Oberdorster *et al.*, 1995; Peters *et al.*, 1997]. Aerosol particles also influence the Earth's climate, and the radiative forcing from anthropogenic particles being activated as cloud condensation nuclei (CCN) in clouds represents one of the largest uncertainties in the climate system [Rosenfeld, 2006].

In urban areas, motor vehicles are a major aerosol source, in particular in the ultrafine size range. Vehicle exhaust can be broadly divided into a nanoparticle mode ( $D_p < 30$ nm), which dominates the exhaust particle number, and an accumulation mode ( $30\text{nm} < D_p < 500$ nm). While nanoparticles from vehicle emissions are composed primarily of semi-volatile organics and sulfur compounds, and are formed by nucleation in the tailpipe or  $\sim 0.1$  s after exiting the tailpipe, the accumulation mode is composed primarily of soot cores coated with sulfate and organic species [Kittelson *et al.*, 2006].

Apart from emissions at the surface, particles may also form in the atmosphere during events of new particle formation [Kulmala *et al.*, 2004]. In general, new particle formation is favored by low concentrations of pre-existing aerosol particles because there is competition between vapor condensation on preexisting particles and new particle formation. Despite this, new particle formation events and subsequent growth have been regularly observed at several polluted urban sites including Leipzig [Birmili and Wiedensohler, 2000], Atlanta [Woo *et al.*, 2001], Pittsburgh [Stanier *et al.*, 2004a], Birmingham, UK [Alam *et al.*, 2003], Mexico City [Dunn *et al.*, 2004] and Beijing [Zhijun *et al.*, 2007]. Newly formed particles can grow in the atmosphere by condensation of low volatility vapors.

In almost all studies, sulfuric acid concentrations were observed to be too low to explain the observed particle growth rates [Alam *et al.*, 2003; Riipinen *et al.*, 2011; Smith *et al.*, 2008]. In those studies, the largest contribution to

---

<sup>8</sup> Work in this section is published by Ahlm *et al.* [2012].

condensational growth came from condensation of organic compounds. Volatile organic compounds (VOCs) can have anthropogenic or biogenic sources and are oxidized in the atmosphere primarily by OH, O<sub>3</sub> and NO<sub>3</sub>. This atmospheric oxidation can lead to a high number of different oxidation products that may have lower volatility than their parent VOCs. Organic vapors with low enough volatility can partition into the particle phase and thereby contribute to condensational growth. However, partly because the number of oxidation products is extremely high, large uncertainties remain in regards to what specific compounds contribute to condensational growth [Hallquist *et al.*, 2009].

In this study we present results from size-resolved measurements of ultrafine aerosol particles at a polluted urban site in Bakersfield, California, where growth events of ultrafine particles were observed on 39 of 45 days. The source of the seed particles, the chemical properties of the ultrafine aerosol, and parameters relevant for the growth are investigated. This study was carried out as part of the CalNex (California Research at the Nexus of Air Quality and Climate Change) campaign at the Bakersfield Supersite in May and June 2010.

## **8.2 Site and Methods**

### **8.2.1 Field Site and Meteorology**

The measurements in this study were performed at the CalNex supersite in Bakersfield, California (35.35°N, 118.97°W). The site is located about 4 km to the southeast of the city center (Figure 8.1). The freeway State Route (SR) 58 passes about 800 m to the north, and the SR 99 passes 7 km to the west. The highway SR 184 is located about 4 km to the east of the site. The average wind direction included in the map over Bakersfield in Figure 8.1 indicates that the air most of the time was not advected from the city center to the sampling site.

Bakersfield was chosen as the site for this project because of its high PM concentrations. The city is located in the southern end of the Central Valley, which stretches 720 km from the Cascade Mountains in the northwest to the Tehachapi Mountains in the southeast. The Central Valley is bordered to the west by the Coastal Ranges and to the east by the Sierra Nevada Mountains. The San Joaquin Valley comprises the southern part of Central Valley and is one of the largest PM<sub>2.5</sub> and PM<sub>10</sub> non-attainment areas in the United States. The geographical boundaries with the surrounding mountains and the meteorology play important roles in accumulating pollutants in the valley, in particular during times of day when the atmospheric boundary layer is shallow and ventilation is limited [Chow *et al.*, 2006b].

Previous studies have shown that the prevailing summertime wind pattern is dominated by marine air that penetrates through the Carquinez Strait and splits into two currents when entering the Central Valley, one flowing northeastwards towards Sacramento and one flowing southeastwards towards San Joaquin

Valley [Moore *et al.*, 1987; Zaremba and Carroll, 1999; Zhong *et al.*, 2004]. Figure 8.1 shows an analysis of back trajectories during the measurements in this study obtained using NOAA's Hybrid Single Particle Lagrangian Integrated Trajectory (HYSPLIT) model with meteorological data sets from Eta Data Assimilation System (EDAS40). The color indicates the number of trajectories that have passed through a certain grid cell. There is a very strong preponderance of trajectories entering Bakersfield from the northwest, consistent with the discussion above, even though most of the trajectories enter the continent at Monterey Bay, south of San Francisco and south of the Carquinez Strait. There are also a relatively large number of trajectories entering Bakersfield from a westerly direction without any northerly component. However, the influence of pollution from Los Angeles in the south should be negligible.

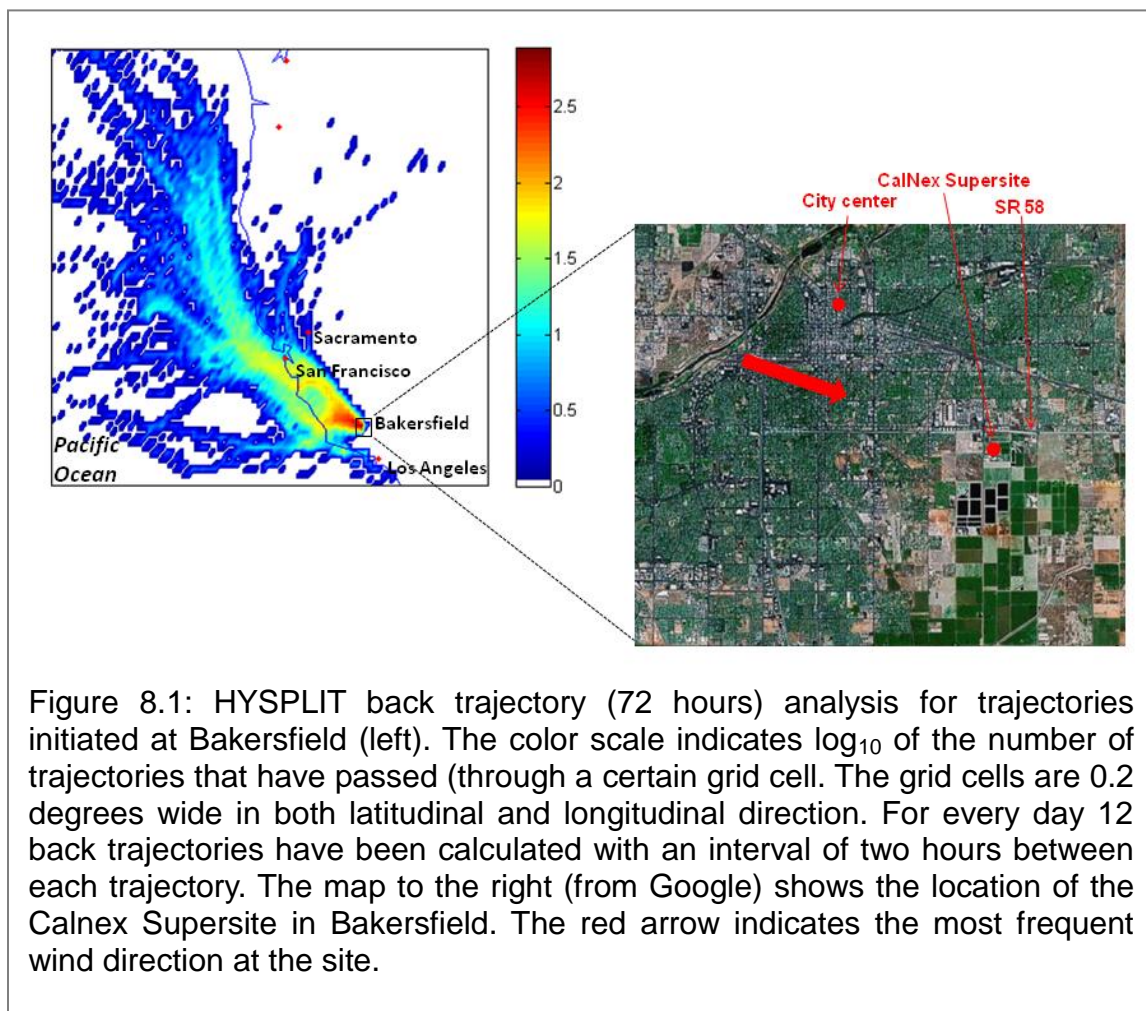


Figure 8.1: HYSPLIT back trajectory (72 hours) analysis for trajectories initiated at Bakersfield (left). The color scale indicates  $\log_{10}$  of the number of trajectories that have passed (through a certain grid cell). The grid cells are 0.2 degrees wide in both latitudinal and longitudinal direction. For every day 12 back trajectories have been calculated with an interval of two hours between each trajectory. The map to the right (from Google) shows the location of the CalNex Supersite in Bakersfield. The red arrow indicates the most frequent wind direction at the site.

The local wind directions were predominantly northwesterly in daytime. However, during some nights the wind direction shifted to the east or south, associated with downslope flows from the surrounding mountains as discussed by Zhong *et al.* [2004]. The median maximum diurnal wind speed was  $\sim 4 \text{ m s}^{-1}$  peaking around 17:00 and the corresponding median minimum value was  $1.5 \text{ m s}^{-1}$ , occurring

around 06:00. The median maximum diurnal temperature during this campaign was 29.5°C peaking around 16:00, the same time as the relative humidity reached its minimum value of ~22%. The median of the diurnal minimum temperature was 16°C, occurring at 05:00, coinciding with a peaking relative humidity of ~60%. The campaign was dominated by cloud free conditions or very low cloudiness, except during a few days in the beginning of the campaign when some rainfall occurred. Apart from the nights on May 18 and May 19, when the relative humidity peaked at 96% and 88%, respectively, the relative humidity never exceeded 82%, indicating mostly dry conditions during the campaign.

*Zhong et al.* [2004] investigated the atmospheric boundary layer in the Central Valley during summertime and found that the afternoon mixed layer was in general deeper than 1000 m, and that the mixed layer depth increased with distance away from the ocean and southwards in the Central Valley. At night, they observed a temperature inversion develop in the lowest few hundred meters.

In this study we have used the HYSPLIT model to get rough estimates of diurnal variations in boundary layer depth during the campaign in Bakersfield. The model indicates that the mixed layer started growing soon after sunrise around 06:00 and often reached its full depth of ~2 km around 17:00. According to the model, the nocturnal boundary layer was about 100 meters deep. Although the depth of the nocturnal inversion from the HYSPLIT model is likely to be associated with large uncertainties, there is a very sharp contrast in boundary layer depth between day and night. The shallowness of the nocturnal boundary layer enhances the impact from surface emissions on local concentrations, which may allow pollutant concentrations to build up at night and in the early morning during rush hour.

### **8.2.2 Experimental**

Particle number size distributions were measured using a scanning Differential Mobility Analyzer (DMA). The DMA is a TSI column with a TSI 3010 CPC running Labview-based software from Collins et al. [2004], modified for negative charging efficiency. Size-resolved number concentrations in 60 size bins from a particle diameter of 10 nm up to 1 µm were collected, and duplicate (upward and downward) mobility scans were completed every 11 min.

Aerosol chemical composition, including all species that are vaporized at a temperature of 600 °C, was measured using an Aerodyne High-Resolution Time-of-Flight Aerosol Mass Spectrometer (HR-ToF-AMS). This instrument provides size-resolved mass concentrations in an approximate vacuum aerodynamic particle diameter range of 0.03 to 1.0 µm. Prior to the start of the campaign, the flow rate of the HR-ToF-AMS was calibrated, and the lens of the AMS was aligned to a position where ~100 % of the 350 nm particles reach the vaporizer of the AMS. Under this configuration particles from ~50-600 nm are expected to be

transmitted with ~100% efficiency. A size/velocity calibration, which relates particle time of flight (ToF) velocity to aerodynamic particle size, was also performed before the campaign started. The ionization efficiency (IE) calibration was performed about twice a week during the campaign. During this calibration, dry ammonium nitrate particles generated by an atomizer with  $D_p = 300\text{-}350$  nm were used to ensure close to 100 % transmission efficiency. The collection efficiency (CE) of the AMS was estimated to be 0.8 based on scaling the AMS mass to the scanning DMA mass (minus the elemental carbon (EC) mass and estimated dust). The vacuum aerodynamic diameter of the AMS has been recalculated to mobility diameter to make it possible to compare with the scanning DMA data in this study. The relation between mobility diameter ( $D_m$ ) measured by the scanning DMA and vacuum aerodynamic diameter ( $D_{va}$ ) measured by the AMS is for spherical particles [Kostenidou *et al.*, 2007]:

$$D_m = \frac{D_{va}}{\rho} \rho_0 \quad (8.1)$$

where  $\rho$  is the effective density and  $\rho_0$  is unity. In this study we found the best agreement in average mass distributions from the scanning DMA and AMS for an average  $\rho$  of  $1.4 \text{ g cm}^{-3}$ .

Gas-phase measurements of  $\text{SO}_2$ , ammonia, formic acid and oxalic acid were made by Ambient Ion Monitor Ion Chromatograph (AIM-IC). The instrument consists of an AIM 9000D air sampler (URG Corp., Chapel Hill, NC), a constantly-generated wet parallel-plate denuder with 5 mM  $\text{H}_2\text{O}_2$  eluent for the collection of gases, and two ICS-2000 ion chromatographs (Dionex Corp., Sunnyvale, CA). The sample collection components of the instrument were located in a separate housing unit, which was specifically built for this study. In this novel instrument configuration gases were stripped into solution in a tower-mounted assembly to minimize sampling inlet losses for soluble gases such as  $\text{NH}_3$  and  $\text{HNO}_3$ .

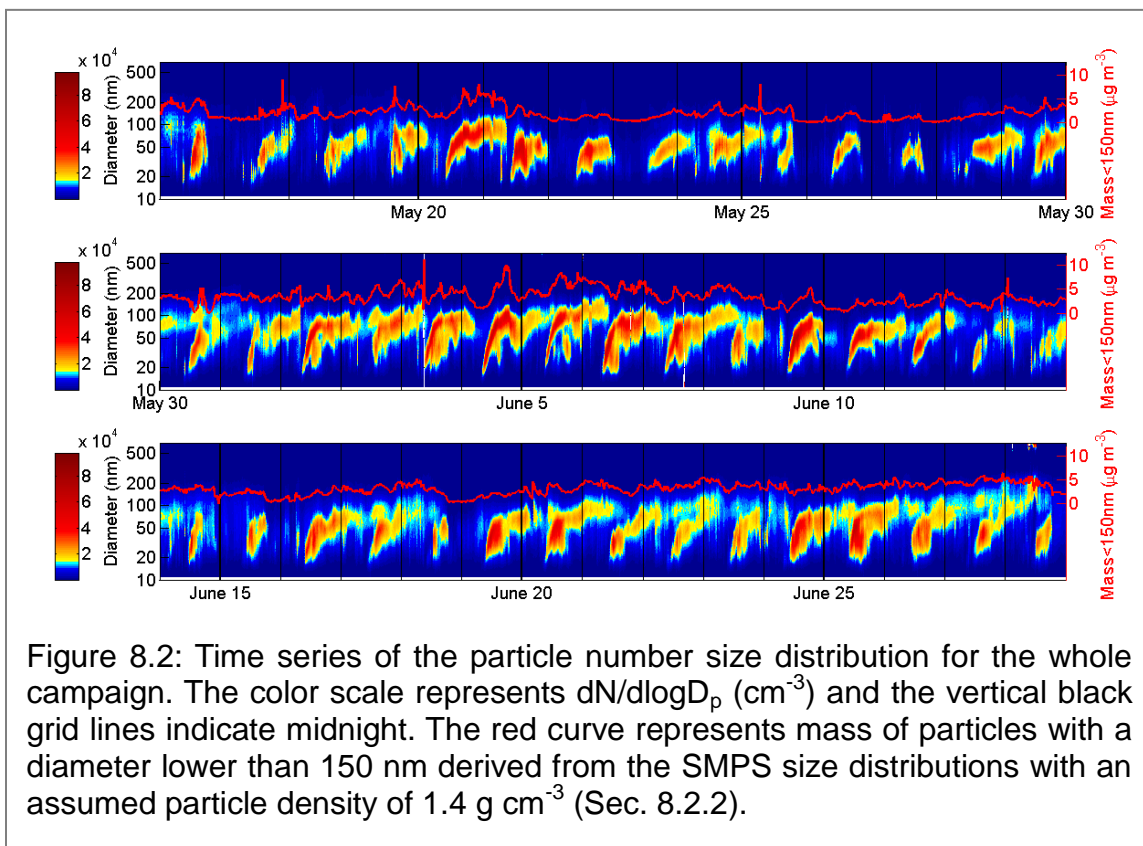
UV radiation was measured by a semiconductor photodiode with a spectral response range from 280 to 360 nm. The sensor was calibrated against a Yankee Environmental Systems' Ultraviolet Pyranometer (Model UVB-1) in natural sunlight. OH concentration was determined using a Ground-based Tropospheric Hydrogen Oxides Sensor (GTHOS) based on laser induced fluorescence, and ozone was measured with a Dasibi 1008 PC monitor. The gas-phase concentration of formaldehyde was determined using Fiber Laser-Induced Fluorescence [DiGangi *et al.*, 2011] and the gas-phase glyoxal concentration was obtained with Laser-Induced Phosphorescence [Huisman *et al.*, 2008]. A broad suite of primary and secondary VOCs were measured with hourly time resolution using a gas chromatograph equipped with both a mass spectrometer and a flame ionization detector. EC was measured with a thermal-optical carbon aerosol analyzer from Sunset Laboratory (Oregon, USA) using a modified IMPROVE-A protocol, operated by the California Air Resource Board.

### 8.3 Results and Discussion

The measurements in this study were performed between 15 May and 29 June, 2010. The average number concentration in the total scanning DMA size range ( $D_p = 0.01\text{-}1\ \mu\text{m}$ ) was  $10300\ \text{cm}^{-3}$ . The average number concentration of ultrafine particles ( $D_p < 100\text{nm}$ ) was  $8600\ \text{cm}^{-3}$ . Hence, the aerosol number population was strongly dominated by ultrafine particles during this campaign.

#### 8.3.1 Ultrafine Particle Growth Events

Figure 8.2 illustrates how the size-resolved number concentration varied throughout the measurement period. In this figure it can be seen that growth of small 15-20 nm particles up to 40-100 nm occurred on almost all days. What is striking is the regularity and the large number of particle growth events for an urban site. Specifically, ultrafine particle growth for at least three hours and at least up to 40 nm could be clearly observed on 39 out of 45 days. It can also be seen in Figure 8.2 that the growth events on many days have a large impact on the aerosol mass, which means that it is possible to investigate the chemical composition of the growing particles. Mass size distributions from the AMS during ultrafine growth events are presented in Section 8.3.2.



Since the growth events varied in mass change, size change, and duration, it is not meaningful to present an average particle number size distribution for the



whole campaign. Rather, it is more interesting to investigate the evolution of the size distributions during different time periods of typical days. Figure 8.3a shows the average particle number size distribution in different two hour intervals throughout the 24 hours of 20 May 2010. This figure illustrates the regular pattern of these growth events. On average, a mode of nanoparticles centered at ~15-20 nm appeared around 09:00 in the morning. In addition to this nanoparticle mode, a pre-existing Aitken mode centered at ~60 nm can be seen. Throughout the morning and most of the afternoon, the number concentration of the nanoparticle mode increases considerably. Meanwhile, the mode shifts to larger diameters when the particles grow, producing an increasingly unimodal size distribution below ~150 nm. Between 13:00 and 15:00, the mode is on average centered at 60 nm. Throughout the evening and night, the growth did often continue, but the number concentration decreased. Since these growth events could be observed clearly for several hours on most days during the campaign, the events must be fairly regionally homogeneous with limited horizontal variability in vapor and particle concentrations. Growth events could be followed from morning until at least 18:00 in the evening for 31 of the 39 observed growth events. For some of the other eight events, growth may have continued until 18:00 but could not be followed all the way because the growing nanoparticle mode and the preexisting Aitken mode could not be separated. A growth event that lasts for about ten hours under an assumed wind speed of  $3 \text{ m s}^{-1}$  gives a horizontal scale of more than 100 km, making these events important regionally for ultrafine particle concentrations.

An interesting question is, from where do the ~15-20 nm particles that appear in the morning (and afternoon) originate? Are they associated with emissions of small particles or do they originate from new particle formation? As mentioned in the introduction, vehicles emit nanoparticles in this size range. However, the fact that the nanoparticle mode was often centered around 15-20 nm when it appeared does not necessarily imply that the particles originate from primary emissions. Brownian diffusion is efficient for 10-20 nm particles, which means that concentrations of the smallest particles are underestimated due to losses in the sampling line. However, the loss by Brownian diffusion in the sampling line was estimated to be less than 10% for 10 nm particles, which is too low to explain the lower concentrations of 10 nm particles relative to the concentrations of ~20 nm particles. Another possibility is that new particle formation occurs before reaching the Bakersfield sampling site but is suppressed in the city where background aerosol concentrations are higher, or that the formation occurs in the residual layer above the growing mixed layer. Then the particles would have some time to grow before being measured by the scanning DMA. Due to the fact that no particle measurements below 10 nm were performed in this field study, there is no direct proof of whether new particle formation or vehicle emission is the mechanism responsible for the production of the observed nanoparticles. However, comparing the diurnal cycle of particle number concentration with that of tracers, it is possible to indirectly show that new particle formation is likely the

most important source for these nanoparticles. This investigation will be presented and discussed in Section 8.3.3.

The growth during the events was in general linear with time until around 13:00, but often decreased in rate throughout the afternoon and evening. Growth rates have been determined by calculating linear fits of the growth of the center of the mode while the growth was linear. The rates varied between 2.9 and 14.9 nm hr<sup>-1</sup> during the campaign. The average growth rate was 7.3 nm hr<sup>-1</sup> with a standard deviation of 2.6 nm hr<sup>-1</sup>. This is within the range of what has been observed at several other urban sites, for instance Atlanta [Stolzenburg *et al.*, 2005], Mexico City [Dunn *et al.*, 2004], Leipzig [Birmili and Wiedensohler, 2000], Budapest [Salma *et al.*, 2011] and Beijing [Zhijun *et al.*, 2007].

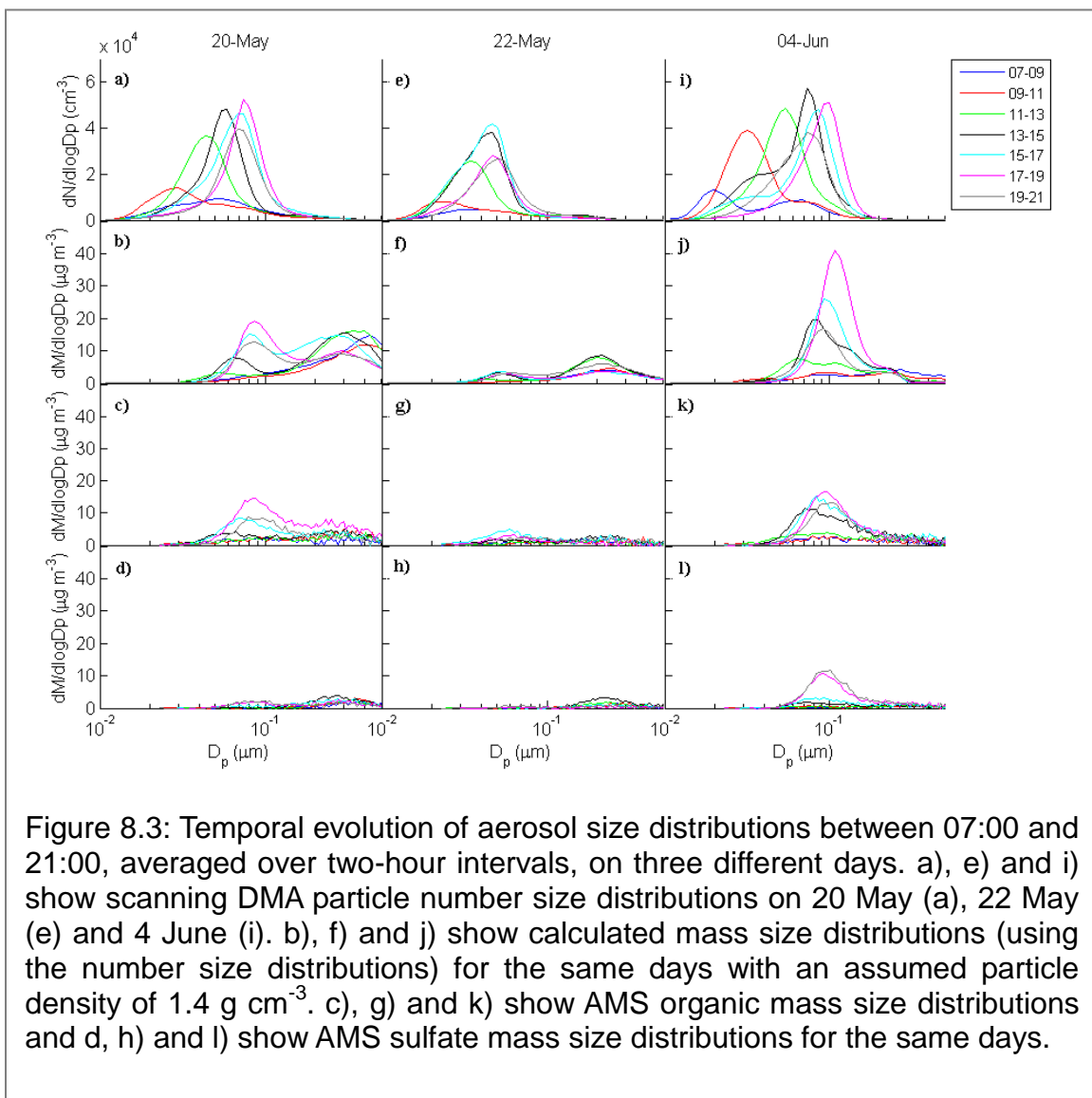


Figure 8.3: Temporal evolution of aerosol size distributions between 07:00 and 21:00, averaged over two-hour intervals, on three different days. a), e) and i) show scanning DMA particle number size distributions on 20 May (a), 22 May (e) and 4 June (i). b), f) and j) show calculated mass size distributions (using the number size distributions) for the same days with an assumed particle density of 1.4 g cm<sup>-3</sup>. c), g) and k) show AMS organic mass size distributions and d), h) and l) show AMS sulfate mass size distributions for the same days.

### **8.3.2 Classification of Growth Events and Chemical Composition of Growing Particles**

The growth events were divided into three classes: High growth (HG) days, low growth (LG) days and non-event (NE) days. HG days were defined as days when the growing mode reached 70 nm before 18:00. LG days were defined as days with growth for at least three hours and up to 40 nm (but less than 70 nm) before 18:00. Remaining days were defined as non-event (NE) days. 11 days fell into the HG class, 28 days fell into the LG class, and 6 days were NE days. Figure 8.3 shows two examples of HG days (20 May and 4 June) and one example of an LG day (22 May) with two-hour averages of scanning DMA and AMS size distributions.

On 20 May a nucleation mode appears in the number size distribution representing 09:00-11:00 (Figure 8.3a), and is followed by growth throughout the day. By 13:00-15:00 the center of the mode has grown to a diameter of 60 nm and at this point the mode starts to make a clear impact also in the mass size distribution (Figure 8.3b). The AMS organic (Figure 8.3c) and sulfate (Figure 8.3d) mass size distributions show that almost all mass in this growing size range consists of organic components. The growth continues until 17:00-19:00 and the center of the mode reaches a final diameter of 80 nm. The mass is still dominated by organics.

Also on 22 May, a nucleation mode appears at 09:00-11:00 followed by growth (Figure 8.3e). However, the growth slows down after 13:00-15:00 and the mode does not reach further than 50 nm. Due to the limited growth on 22 May, the aerosol mass increase caused by the growth is considerably lower than the corresponding mass increase on 20 May (Figure 8.3f). However, also on 22 May almost all the growth seems to have been associated with condensation of organic vapors (Figure 8.3g), and the contribution from sulfate is low (Figure 8.3h).

On 4 June, a nucleation mode appears already at 07:00-09:00 (Figure 8.3i). The growth continues until 17:00-19:00 and the center of the mode reaches a diameter of nearly 100 nm with a large increase in mass as result (Figure 8.3j). From the organic and sulfate mass size distributions (Figure 8.3k, l), it is clear that organics are responsible for almost all growth until 15:00-17:00. At this point the mode has reached a diameter of 80 nm. However, during the next growth phase from 80 to 100 nm sulfate actually makes the largest contribution. The growth event on 4 June was the event with the largest contribution from sulfate of all events during the campaign.

Some of the most distinct growth events with two-hour averaged chemical composition of the aerosol mass below 150 nm can be seen in Figure 8.4. The growth events affected the mass size distributions well above 100 nm on days

with the highest growths. Therefore the size distributions have been cut at 150 nm here to include most of the mass increase during the growth events. The growth events in Figure 8.4 are on most days accompanied by an increase in aerosol mass. The exception to this trend is the relatively high aerosol mass at 06:00-08:00 on some days associated with aerosol mass of the preexisting mode. Organics strongly dominate the addition of mass during most of the growth events in Figure 8.4. Particularly from morning until 12:00-14:00 the growth and mass are nearly exclusively associated with organic components. However, especially on 4 June the contribution from sulfate somewhat increases during late afternoon or early evening (as seen also in Figure 8.3). There was also a tendency of slightly increasing ammonium when sulfate increased, indicating that most of the sulfate was in form of ammonium sulfate and ammonium bisulfate.

### **8.3.3 Diurnal Cycles of Tracers for Primary and Secondary Aerosols**

The composition of the growing particles during the frequent ultrafine growth events in Figure 8.2 indicate that most of the total ultrafine particle mass is organic, and the midday timing of these events (as well as the lack of an afternoon peak in EC) indicates that they are secondary (formed in the atmosphere). This section will focus on the chemical compounds that dominate the ultrafine particle mass, the contribution from primary emissions and secondary aerosol formation to the ultrafine particle mass, and the production mechanism responsible for the frequently observed 15-20 nm particles that provide seeds for the subsequent growth.

The growth events observed in this study are highly regular. They occur almost every day and start in the morning (Figure 8.2 and 8.3). During this campaign, organic components represented 77% of the ultrafine aerosol mass ( $D_p < 100$  nm), thereby strongly dominating the ultrafine mass. Sulfate represented the second largest non-refractory mass contribution with 16%. Ammonium provided a minor contribution (5%) and nitrate was only 2%. In Pittsburgh [Zhang *et al.*, 2004], nitrate was also observed to be a minor component in the ultrafine size range. However, the organic fraction in the ultrafine range is much higher in Bakersfield than what was observed in Pittsburgh where the summertime fraction was 45% [Stanier *et al.*, 2004b]. Accordingly, the sulfate fraction is significantly lower in Bakersfield than what was observed in Pittsburgh, where 40% of the ultrafine mass was salts of ammonium and sulfate.

The AMS mass spectral peak at the mass-to-charge ratio ( $m/z$ ) 57 is often used as a tracer for hydrocarbon-like organic aerosols (HOA), whereas  $m/z$  44 works as a tracer for oxygenated organic aerosols (OOA) [Russell *et al.*, 2009; Zhang *et al.*, 2005b].  $m/z$  57 include the ion peaks of  $C_4H_9^+$  and  $C_3H_5O^+$ , and  $m/z$  44 include the ion peaks of  $CO_2^+$  and  $C_2H_4O^+$ . Here we present the non-oxygenated fragment  $C_4H_9^+$  as a tracer for HOA and the oxygenated fragment  $CO_2^+$  as a tracer for OOA.

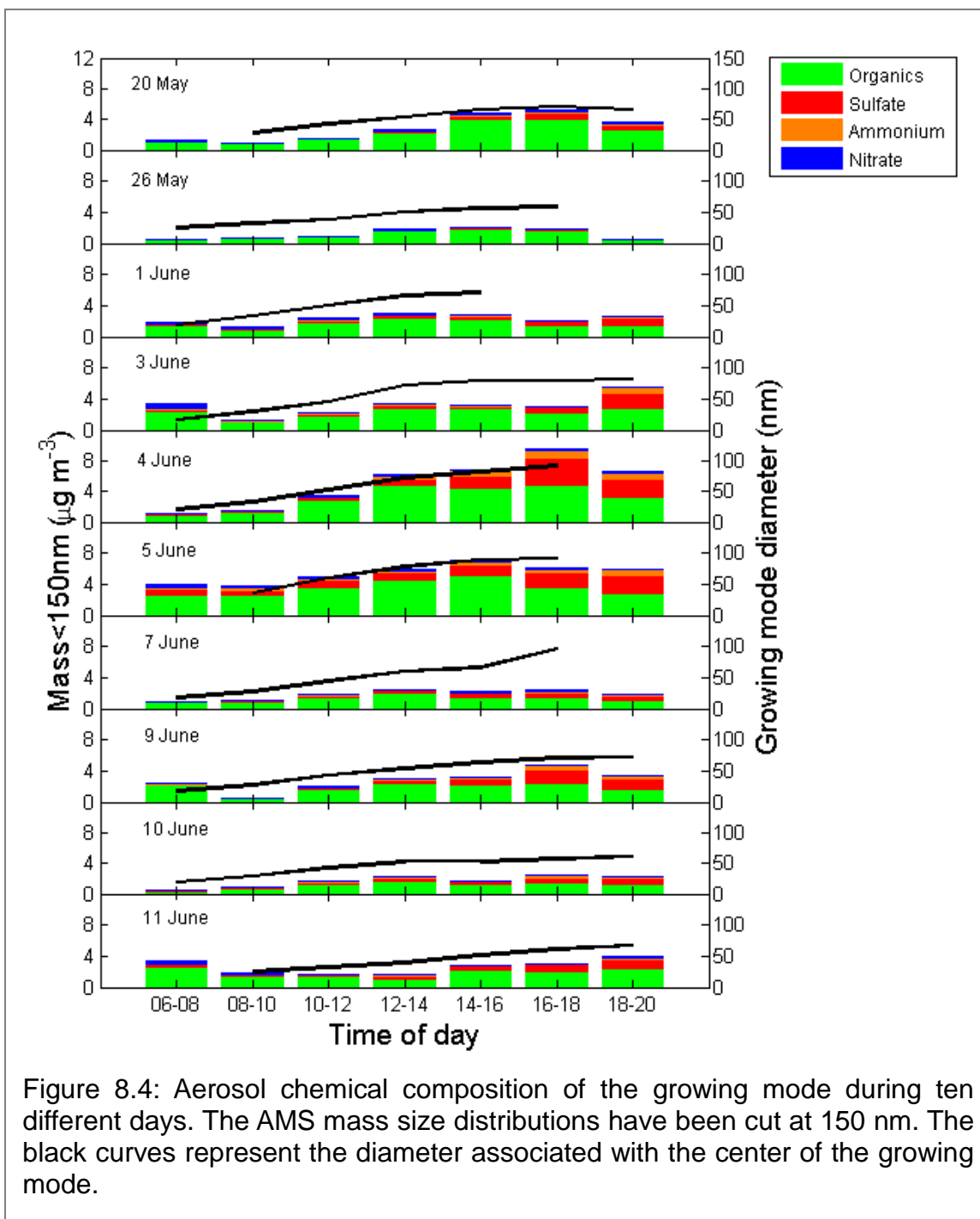


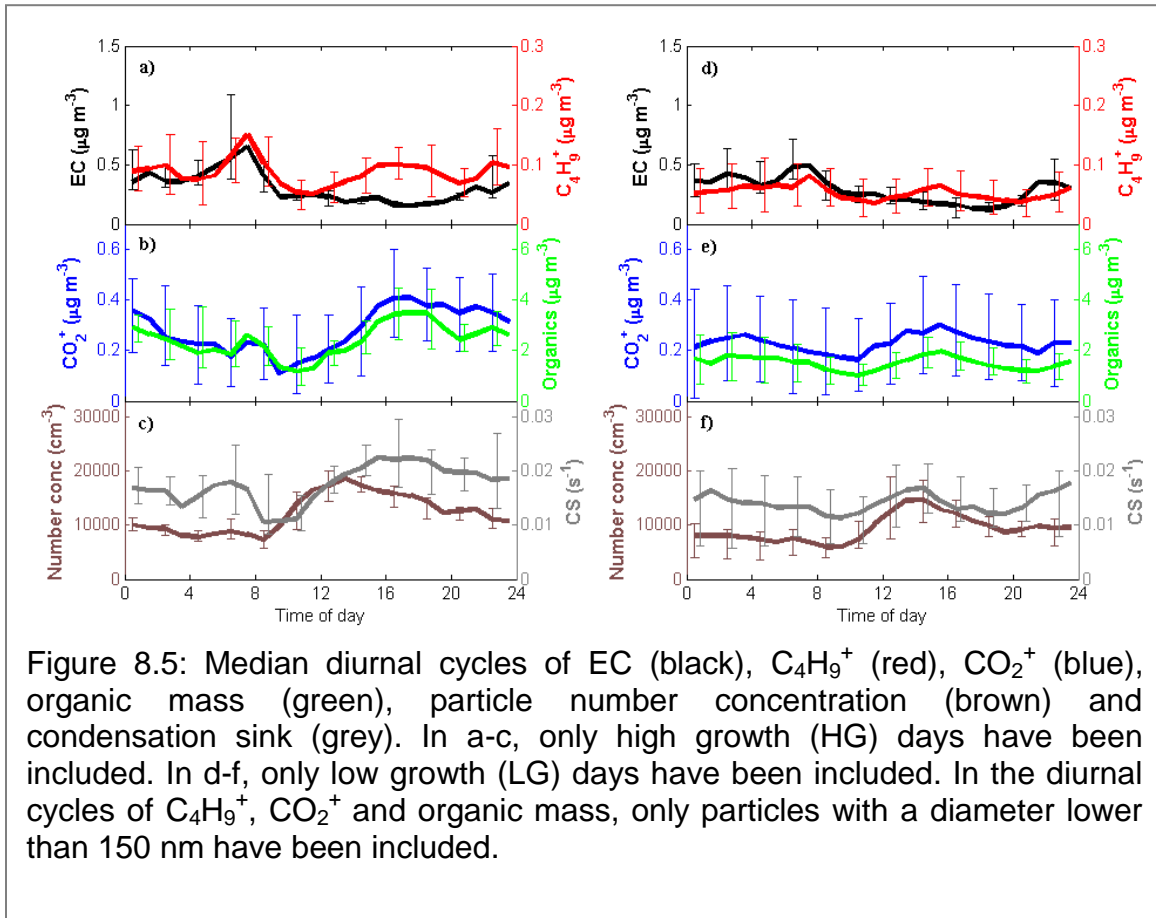
Figure 8.4: Aerosol chemical composition of the growing mode during ten different days. The AMS mass size distributions have been cut at 150 nm. The black curves represent the diameter associated with the center of the growing mode.

Figure 8.5 shows median diurnal cycles of EC, C<sub>4</sub>H<sub>9</sub><sup>+</sup>, CO<sub>2</sub><sup>+</sup>, organic mass, total particle number concentration and vapor condensation sink (CS) for HG (Figure 8.5a-c) and LG (Figure 8.5d-f) days. Only particles with diameters lower than 150 nm have been included in the diurnal cycles of C<sub>4</sub>H<sub>9</sub><sup>+</sup>, CO<sub>2</sub><sup>+</sup> and organic mass. The reason for selecting 150 nm as the cutoff for ultrafine particles was to include most of the mass increase associated with the growth events, as discussed in

Sec. 3.2. The CS determines the rate of condensation of molecules onto pre-existing particles [Kulmala *et al.*, 2001]; it is defined as:

$$CS = 2\pi D \sum_i^n \beta(D_{p,i}) D_{p,i} N_i \quad (8.2)$$

where  $D$  is the diffusion coefficient of the condensing vapor (here as assumed to be  $0.1 \text{ cm}^2 \text{ s}^{-1}$ ),  $D_{p,i}$  is the particle diameter of bin  $i$ ,  $\beta$  is the transition regime correction factor [Fuchs and Sutugin, 1971],  $N_i$  is the number concentration within size bin  $i$ , and  $n$  is the number of size bins. We have assumed the accommodation coefficient to be unity.



In general, the diurnal cycles of EC and  $C_4H_9^+$  are rather similar both on HG (Figure 8.5a) and LG (Figure 8.5d) days. Concentrations are high at nighttime and peak early in the morning around 07:00 during rush hour. A peak in aerosol number concentrations due to primary emissions early in the morning have been observed in several other urban studies, [Harrison and Jones, 2005; Kalafut-Pettibone *et al.*, 2011; Woo *et al.*, 2001]. High traffic in the morning results in high aerosol emissions. Furthermore, the fact that the boundary layer is shallow at this point means that particle emissions will have a large impact on the observed concentration. After ~08:00 both EC and  $C_4H_9^+$  start decreasing to

reach a minimum later in the day. This is likely to a large extent caused by dilution through entrainment when the mixed layer grows. Around 16:00,  $C_4H_9^+$  experiences a second smaller peak concentration, while EC stays low. The rush hour peaks in the morning are somewhat larger in the HG diurnal cycles than in the LG cycles. Higher primary emissions of EC and organic particles on HG days are likely accompanied by higher primary emissions of anthropogenic VOCs that may contribute to more efficient condensational growth on these days.

The median diurnal cycles of  $CO_2^+$  (Figure 8.5b, e), the tracer for OOA, shows a different pattern and shows a second and larger peak concentration in afternoon, which indicates that photochemistry plays an important role in the production of SOA. The relative increase in  $C_4H_9^+$  during afternoon is much lower than the corresponding increase in  $CO_2^+$ , and the ratio between  $CO_2^+$  and  $C_4H_9^+$  is on HG days at maximum around 16:00. Interestingly, the diurnal cycles of organic mass (Figure 8.5b, e) look very similar to the  $CO_2^+$  diurnal cycles, and have their maximum values during the afternoon at the same time as  $CO_2^+$ . The afternoon maxima in  $CO_2^+$  and organic mass concentration are higher on HG days than on LG days, consistent with more SOA formation on HG days. The early morning peak observed in EC and  $C_4H_9^+$  on LG days (Figure 8.5d) is not present in the diurnal cycle of organic mass (Figure 8.5e), indicating that the mass contribution from primary emissions to the organic mass below 150 nm is low on LG days. Also on HG days, the morning peak in organic mass (Figure 8.5b) is small compared to the afternoon peak, indicating that primary emissions make a low relative contribution to the organic mass below 150 nm also on HG days. Instead the organic mass is dominated by photochemically-produced SOA.

The median diurnal cycles of total (0.01-1.0  $\mu m$ ) particle number concentration (Figure 8.5c and 8.5f) also peak in the afternoon, a little earlier than  $CO_2^+$  and the organic mass. This afternoon peak in number concentration occurs when EC reaches its lowest concentrations on both HG and LG days. Also, there is no peak in the multiday-average number concentration during the early morning rush hour on HG or LG days suggesting that primary aerosol emissions do not provide the source of aerosol particles on most days. In fact, a peak in number concentration during rush hour, around 07:00 in the morning, could only be observed on seven days in total. However, on all of those seven days there was an even larger maximum in number concentration during early afternoon. The fact that the peak of the median diurnal cycle for number concentration occurs during afternoon, when EC is at minimum and when the mixed layer is close to fully developed, indicates that new particle formation was likely the most important midday particle number source in Bakersfield during this study and that photochemistry played an important role in the formation.

The number concentration on average increased by over 100% from 10000  $cm^{-3}$  to ~20000  $cm^{-3}$  between 08:00 and 14:00 on HG days, and from 7000  $cm^{-3}$  to ~15000  $cm^{-3}$  between 09:00 and 14:00 on LG days. Figure 8.5c and 8.5f also include the condensation sink, which could be expected to be lower on HG days

than on LG days at the start time of particle formation and growth. There is a small dip in the median condensation sink between 08:00 and 11:00 on HG days. However, the 25-percentile of the CS in Figure 8.5f shows that there were low CS values in the morning also on several LG days, and as will be discussed in Sec 8.3.5, no correlation between low condensation sink in the morning and high particle mass (or number) concentration in the afternoon was found.

New particle formation appears to dominate over primary aerosol emission in producing seed particles for the frequently observed ultrafine growth events in this study. The nucleation mode appeared on most days between 08:00 and 10:00 whereas EC peaked already between 06:00 and 08:00 in the morning. While the EC concentration on most days decreased between 08:00 and 10:00, the particle number concentration rapidly increased in the same time interval. Even on those six days without any clear growth events, the particle number concentration peaked around noon or in early afternoon. These peaks indicate that nucleation events may have occurred also on those days, but that these events must have been local rather than occurring over regional scales.

#### **8.3.4 Sulfuric Acid versus Organics in Contributing to Condensational Growth**

Organics represented 77 % and sulfate only 16 % of the ultrafine particle mass. To estimate what role sulfate may have played in the observed growth events, H<sub>2</sub>SO<sub>4</sub> condensational growth was investigated by using ambient SO<sub>2</sub> and OH concentrations. Interestingly, SO<sub>2</sub> did not peak during rush hour (around 07:00 in the morning) when EC and C<sub>4</sub>H<sub>9</sub><sup>+</sup> were at maximum, indicating that traffic in Bakersfield was not a major source of SO<sub>2</sub>. Actually SO<sub>2</sub> was often at minimum at this time in the morning. This seems to have been a result of the often changing wind direction at night or in early morning (Sec 8.2.1), particularly clear on 25 May, 1 June and 11 June (Figure 8.6). When the wind was blowing from the east or south at night or in early morning, the SO<sub>2</sub> concentration dropped significantly but increased as the wind direction returned to the northwest in daytime. The early morning peaks in EC, however, seemed to be independent of wind direction since these occurred during most mornings of the campaign regardless of wind direction.

To investigate what role H<sub>2</sub>SO<sub>4</sub> played in the observed condensational growth (after new particle formation) a microphysical model was used. The model includes only growth caused by condensation and uses the standard condensation equation [Seinfeld and Pandis, 1998] with the transition regime correction according to [Fuchs and Sutugin, 1971]. The condensational flux of vapor to particles is driven by the difference between the vapor concentration and its saturation concentration over the particle surface. This saturation concentration was set to zero, thereby assuming sulfuric acid to be perfectly non-volatile. The diffusion coefficient for sulfuric acid was assumed to be 0.1 cm<sup>2</sup> s<sup>-1</sup> and the mass accommodation coefficient was assumed to be unity. The model was initiated with a log-normal fit to the 08:00-10:00 average particle number size



distribution from Figure 8.3a, based on three modes. A new nucleation mode was added every hour in order to describe the average increase in particle number concentration observed (as in Figure 8.3a) between 08:00-10:00 and 12:00-14:00. The sulfuric acid concentration was first held constant at a value that could reproduce the growth in Figure 8.3a. This was obtained with a H<sub>2</sub>SO<sub>4</sub> concentration of 1.1·10<sup>8</sup> molec cm<sup>-3</sup>. To investigate whether that concentration was realistic at the site, the model was run with actual SO<sub>2</sub> and OH concentrations from a median diurnal cycle of these parameters. H<sub>2</sub>SO<sub>4</sub> was in the model produced according to the proxy [Petaja *et al.*, 2009]:

$$H_2SO_4 = \frac{k \cdot |SO_2| \cdot |OH|}{CS} \quad (8.3)$$

where CS represents the condensation sink and *k* is defined according to

$$k = 8.6 \cdot 10^{-10} \cdot |OH|^{-0.48} \quad (8.4)$$

where concentrations have units of molec cm<sup>-3</sup>, *k* has the unit cm<sup>3</sup> molec<sup>-1</sup> s<sup>-1</sup> and CS has the unit s<sup>-1</sup>.

Running the model with actual SO<sub>2</sub> and OH concentrations resulted in H<sub>2</sub>SO<sub>4</sub> concentrations around 2·10<sup>6</sup> molec cm<sup>-3</sup>, which is nearly two orders of magnitude lower than what was needed to reproduce the growth. The resulting concentrations of H<sub>2</sub>SO<sub>4</sub> from SO<sub>2</sub> and OH in the model could not grow the nucleation mode significantly. Even when the day with highest SO<sub>2</sub> concentrations was used to initialize the SO<sub>2</sub> concentration (with peak at ~5 ppb) the resulting growth during six hours was lower than 5 nm in the model, which is smaller than the ~40 nm observed growth between the 08:00-10:00 and 14:00-16:00 average size distributions in Figure 8.3a. Thus, SO<sub>2</sub> concentrations were much too low in Bakersfield to explain the observed growth rates in the absence of organics. However, even though organics dominated the ultrafine mass, sulfate still seems to have made a significant contribution on some days, particularly on 4 June (Figure 8.4).

### **8.3.5 Parameters Affecting Condensational Growth and Particle Number Concentration**

Condensational growth of ultrafine particles can be expected to be more efficient when background aerosol concentrations of Aitken and accumulation mode particles are low, since these particles represent a surface for vapors to condense on, thereby reducing the amount of vapor that condenses on the growing ultrafine particles. However, in this study no clear dependence on low submicron condensation sink in the morning, and high mass of particles smaller than 150 nm in the afternoon was observed, indicating that condensation sink was less important than other parameters to be discussed. To analyze what parameters and compounds were important for the growth events, correlations between aerosol mass of particles smaller than 150 nm and several other parameters were investigated. One hour averages of the aerosol mass were calculated for the time period 09:00 to 14:00 for all growth events. During this

time period the aerosol mass was generally increasing. After 14:00 on several days, the aerosol mass was observed to start decreasing as a result of decreasing number concentration despite continued growth.

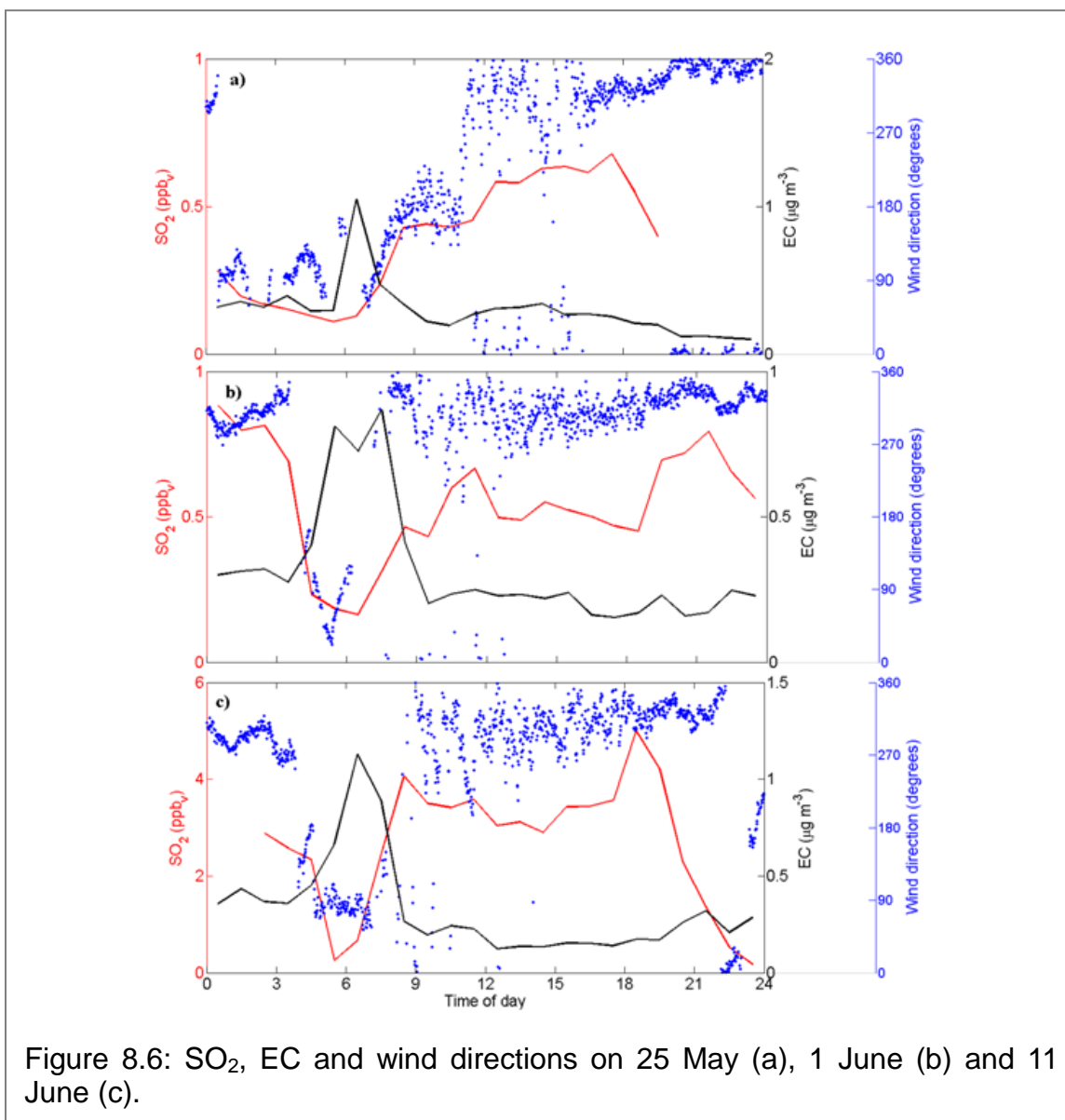


Figure 8.6: SO<sub>2</sub>, EC and wind directions on 25 May (a), 1 June (b) and 11 June (c).

The fact that the peak in the AMS ion CO<sub>2</sub><sup>+</sup> and organic mass below 150 nm often reached maximum in the afternoon (Figure 8.5) indicates that photo-oxidation played an important role in the secondary aerosol formation associated with the growth events. The correlation coefficient ( $r$ ) between aerosol mass and OH concentration was 0.51 and the corresponding coefficient between aerosol mass and ozone was 0.33 suggesting that OH played a more important role than ozone in oxidation of VOCs to organic vapors with low enough volatility to contribute to formation of secondary aerosol. The  $r$  coefficient between aerosol mass and UV radiation was 0.49. Because OH production depends directly on

solar radiation it is logical that the correlation coefficients for OH and UV radiation with aerosol mass have similar values.

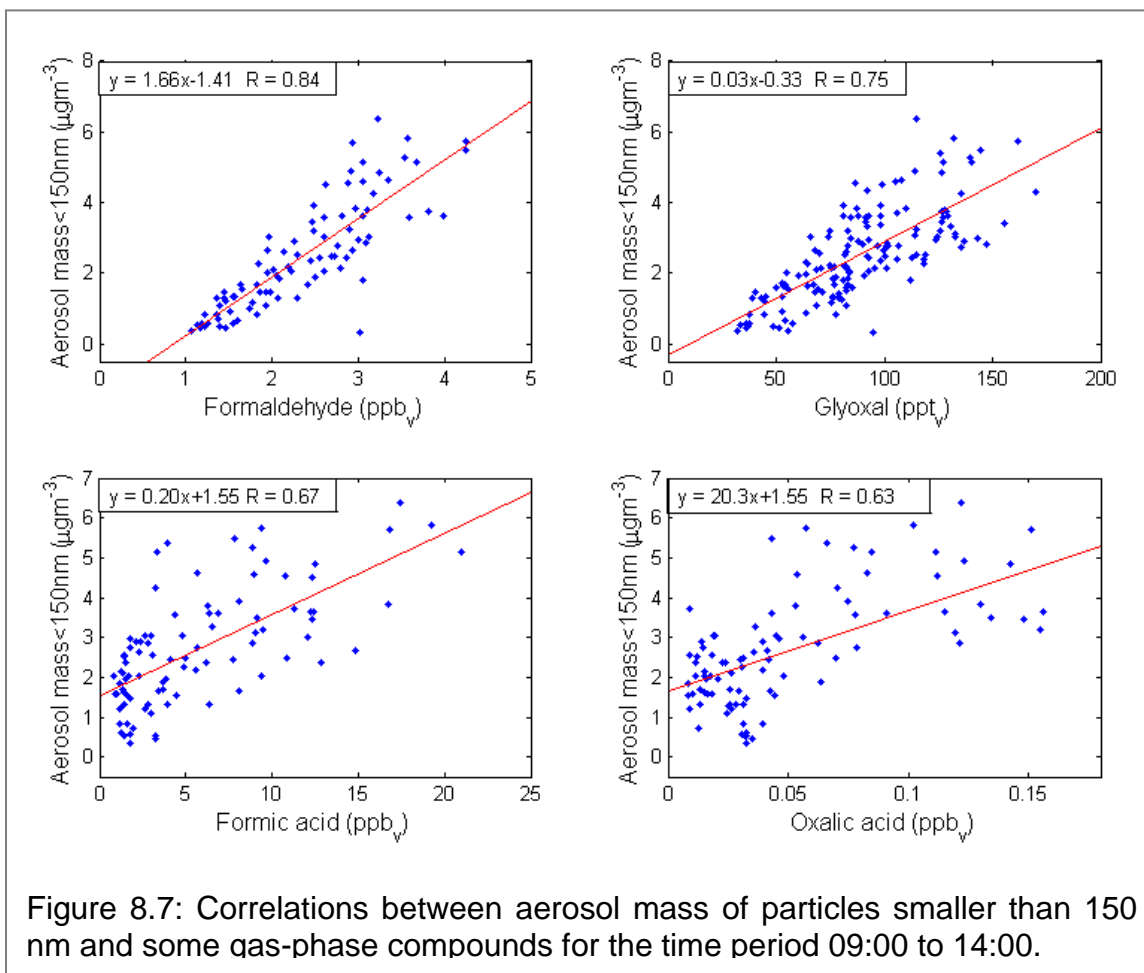
No correlation was observed for SO<sub>2</sub> ( $r = 0.16$ ), consistent with the expectations from the modeling of sulfate condensation (Sec 8.3.4). Acetone, which has a variety of primary (biogenic and anthropogenic) and secondary sources around Bakersfield shows some correlation ( $r = 0.52$ ) with particle mass during growth events suggesting coincident photochemical production of acetone and condensable vapors. The correlation of particle mass during growth events with gas-phase ammonia was similar ( $r = 0.58$ ). However, the strongest correlations were between aerosol mass and gas-phase formaldehyde ( $r = 0.84$ ), glyoxal ( $r = 0.75$ ), formic acid ( $r = 0.67$ ), and oxalic acid ( $r = 0.63$ ), indicating that these vapors may have contributed significantly to condensational growth or at least been co-produced by the chemical reactions that produced condensable vapors. Figure 8.7 shows the dependence of aerosol mass on these vapors with linear fits and associated slopes and intercepts. Formaldehyde was measured between 20 May and 9 June. It is the most abundant aldehyde in the troposphere and can be directly emitted from biomass burning and fossil fuel combustion, or it can be produced by oxidation of both biogenic and anthropogenic hydrocarbons [*Liu et al.*, 2007]. However, there was no indication of any influence from biomass burning during this campaign. Because of its relatively short atmospheric lifetime, typically 2-4 hours during the day [*Fried et al.*, 1997; *Wert et al.*, 2003], formaldehyde is a key indicator of recent atmospheric photochemical activity [*Dasgupta et al.*, 2005]. Therefore, the correlation between aerosol mass and formaldehyde during the growth events does not indicate that formaldehyde has been an important contributor to the growth, but probably instead indicates that photochemical oxidation of VOCs was high during the events. Direct emissions of formaldehyde might have played a role, but these emissions could not have been associated with primary particles (such as EC), since EC did not correlate with particle mass in this study.

Glyoxal forms as a first generation oxidation product from numerous VOCs, including aromatic hydrocarbons in polluted air [*Volkamer et al.*, 2006]. Despite its high volatility, there is growing evidence that glyoxal may also contribute to SOA formation [*Liggio et al.*, 2005; *Volkamer et al.*, 2007].

Oxalic acid is the most abundant dicarboxylic acid in the atmosphere and can be emitted from fossil fuel combustion [*Carlton et al.*, 2007] and formed through gas-phase photo-oxidation of VOCs [*Kerminen et al.*, 2000]. Aqueous-phase photo-oxidation of glyoxal is also a potentially important product of oxalic acid [*Carlton et al.*, 2007], but since relative humidity and cloudiness were low during this campaign in Bakersfield, the latter source was probably not important in this study. Due to the presence of two carboxyl groups, dicarboxylic acids have low volatility and are often found in the particle phase [*Chebbi and Carlier*, 1996]. Oxalic acid has been observed to have the highest particle phase concentration of all dicarboxylic acids in several urban studies [*Kawamura and Ikushima*, 1993;

Sempere and Kawamura, 1994], and may well have contributed to condensational growth in this study.

In addition to the already mentioned gas-phase compounds, potential correlations between particle mass and 16 alkanes, 6 aromatics, 4 halocarbons, 3 CFCs, alpha-pinene, isoprene, limonene, propene, and carbon disulfide were investigated, but all resulted in correlation coefficients lower than 0.45.



Additional parameters that could be important for new particle formation were also investigated. No clear correlation could be found between ultrafine particle number and relevant parameters such as condensation sink and  $\text{O}_3$  concentration between 09:00 and 14:00. However, ultrafine particle number was mildly correlated with UV radiation and OH with  $r$  coefficients of 0.51 and 0.43, respectively.  $\text{SO}_2$  concentrations in this study were in general relatively low, on most days below 1 ppb<sub>v</sub>. This can be compared with  $\text{SO}_2$  concentrations in other urban studies with nucleation and growth events, for instance Pittsburgh where concentrations were often 40-120 ppb<sub>v</sub> [Zhang *et al.*, 2004], Leipzig with daytime peaks around 8ppb<sub>v</sub> [Birmili and Wiedensohler, 2000] and Birmingham with concentrations of 1-21 ppb<sub>v</sub>. No correlation was observed between particle

number and SO<sub>2</sub> concentration ( $r = 0.14$ ), suggesting that the daytime particle number source did not depend critically on SO<sub>2</sub>. This is the third piece of evidence (combined with the sulfate condensation calculations and the composition of the ultrafine particles) that sulfate from SO<sub>2</sub> did not provide most of the particle mass in the high number of particle formation and growth events in this study.

Ammonia concentrations were very high during the campaign, often above 10 ppb<sub>v</sub>. A correlation between ultrafine particle number and ammonia was observed with an  $r$ -coefficient of 0.45, indicating that ammonia might have played a role in new particle formation in this study. *Kirkby et al.* [2011] found that the dependence of nucleation rates on ammonia saturates at ammonia mixing ratios around 100 ppt<sub>v</sub>. The fact that Bakersfield had ammonia concentrations in the ppb-range in this study might explain the relatively low correlation with ammonia.

A higher correlation was observed between ultrafine particle number and formaldehyde ( $r = 0.62$ ). Relatively high correlations were also observed between ultrafine particle number and oxalic acid ( $r = 0.59$ ) and formic acid ( $r = 0.57$ ), whereas the rest of the gas-phase compounds had correlation coefficients lower than 0.4. A high concentration of formaldehyde indicates high VOC oxidation, thereby likely higher concentrations of condensable organic vapors and more efficient condensational growth. More efficient initial growth will reduce particle number sinks like coagulation and Brownian diffusion. Therefore, the correlation between ultrafine particle number and formaldehyde might indicate that the particle number concentration depended more critically on the efficiency of initial growth than on amounts of nucleating vapors in this study in Bakersfield.

#### 8.4 Summary and Conclusion

Physical and chemical properties of ultrafine aerosol particles during the CalNex campaign in Bakersfield from 15 May to 29 June were measured. The focus of this study was on the frequently observed growth events at the site. Condensational growth of small ~20 nm particles up to 40-100 nm occurred on 39 of 45 days. A nucleation mode typically appeared around 09:00 in the morning together with a pre-existing Aitken mode centered around 70-80 nm. Throughout the day the nucleation mode was observed to grow at an average growth rate of 7.3 nm hr<sup>-1</sup>, resulting in a unimodal size distribution in the evening and at night.

Concentrations of EC and a tracer for hydrocarbon-like organic aerosol (C<sub>4</sub>H<sub>9</sub><sup>+</sup>) were in general higher at nighttime and peaked during rush hour in early morning. Throughout the morning and afternoon concentrations decreased as a result of dilution when the mixed layer grew. This is an indication that the impact of primary aerosol emission on local concentrations was at maximum in early morning during rush hour. However, particle number concentration showed a different pattern and peaked in the afternoon when EC was at minimum.

Therefore, new particle formation likely provided the largest contribution to the midday increase in particle number concentration in this study.

Microphysical modeling and size-resolved AMS concentrations showed that organic components dominated the particle growth in the ultrafine mode, and that sulfate on most days only provided a minor contribution to nanoparticle growth. Organic components largely dominated the ultrafine aerosol mass with 77%. The organic mass below 150 nm peaked in the afternoon at the same time as the AMS tracer for oxygenated organic aerosol  $\text{CO}_2^+$ , indicating that most of this organic mass was photochemically produced SOA. Given the complex mixture of anthropogenic and biogenic VOC sources in the Central Valley, there was insufficient information to accurately apportion the sources of the pre-cursor VOCs, but there are likely contributions from both anthropogenic and biogenic sources.

The aerosol mass of particles smaller than 150 nm showed a stronger correlation to OH concentration and UV radiation than to ozone concentration during the growth events. However, the strongest correlations were found between aerosol mass and gas-phase formaldehyde, glyoxal, formic acid and oxalic acid. This is an indication that these compounds may have either contributed to condensational growth or been produced by the same chemical reactions that produced condensable vapors.

## 9.0 Primary and Secondary Organic Aerosols in the CalNex and Cal-Mex Regions and their Fossil Fuel Sources<sup>9</sup>

### 9.1 Introduction

The organic fraction of particles constitutes 10-70% of the mass of fine aerosol [Turpin *et al.*, 2000], but the quantity and composition of the man-made contribution to atmospheric organic particles are not well characterized. Russell *et al.* [2011] used the spectral signatures of FTIR measurements of carbonaceous particle mass to show that fossil fuel combustion accounts for 62% of organic mass but ranges from 35% to 93%, although the sampled locations were biased toward coastal and marine locations. In highly populated urban regions such as southern California, most of the submicron organic mass (OM) is attributable to emissions of fossil fuel combustion, in particular to motor vehicles [Hayes *et al.*, in review; Liu *et al.*, 2012a].

Fossil fuel combustion processes produce organic compounds that can form particles before emission (primary organic aerosol, POA) and after emission (secondary organic aerosol, SOA) into the atmosphere. Models tend to track primary and secondary carbonaceous particles separately because of their different production mechanisms, but observations often have a difficult time separating these components, as some are chemically similar [Cass, 1998]. For example, the loss of some mass of the carbonaceous particles due to increased volatility [Robinson *et al.*, 2007] or reactivity [Molina *et al.*, 2004] in changing ambient conditions means that using tracers will overestimate the OM associated with some sources. Yet, for some sources, carbonaceous particles are accompanied by VOCs that can later add OM to the particle phase as secondary carbonaceous components. SOA has been estimated in several urban, polluted environments [de Gouw *et al.*, 2005; Johnson *et al.*, 2006; Takegawa *et al.*, 2006; Volkamer *et al.*, 2006], but there is significant disparity between laboratory simulations and SOA observations in areas with high anthropogenic activity [Gentner *et al.*, 2012].

Several methods have been used to separate the contributions of POA and SOA to OM [Liu *et al.*, 2011], based on either temporal variation or the oxygenated OM composition. Comparisons of multiple methods have shown good agreement in some regions [Liu *et al.*, 2011; Liu *et al.*, 2012a], but such agreement may depend on local conditions since the types and mixtures of sources are different in each location as is their atmospheric processing.

Characterizing the main sources for POA and SOA in the California region was a major focus of the CalNex and Cal-Mex campaigns at the ground sites at Bakersfield, Pasadena, and Tijuana and the shipboard observations on the R/V *Atlantis* during May and June of 2010. To assess the degree to which this short campaign is representative of the region and the summer season, we consider

---

<sup>9</sup> Work in this section is from a manuscript in preparation by Guzman Morales *et al.* [in prep.].

the OC measurements from the nearby monitoring sites of the IMPROVE and CARB networks. To separate primary and secondary contributions of fossil fuel combustion emissions (primarily from motor vehicles and shipping) to OM, we use organic functional group measurements to provide upper and lower bounds on the uncertainties associated with this separation. The results are compared to other published methods for separating primary and secondary components.

## 9.2 Methods

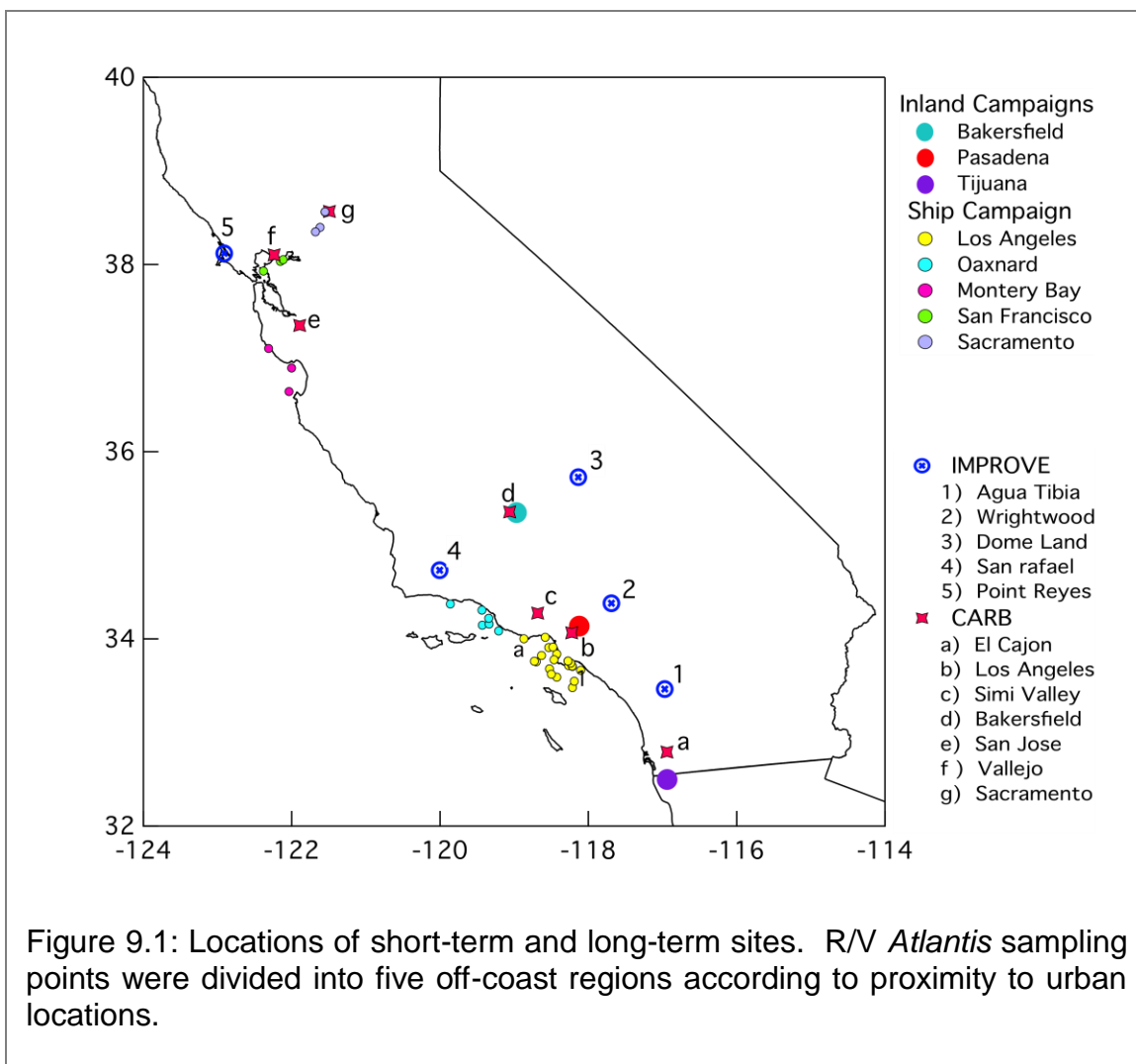
### 9.2.1 OM and CO Measurements

The CalNex and Cal-Mex projects included three ground sites at Bakersfield (35°21'0" N, 118°58'12" W), Pasadena (34° 8'13" N, 118° 7'28" W), and Tijuana (32°29'55" N, 116°56'25" W, US-Mexico border city). The sites are shown in Figure 9.1. Measurements took place on May 15 to June 30, 2010 at Bakersfield and Tijuana, while in the Pasadena location the sampling period was May 15 to June 16 2010. These sites are referred to as inland, due to their distance from the coast. Coastal measurements were collected on board the R/V *Atlantis* during May 15 to June 6, 2010. Ambient particles were sampled at 18 m above sea level through a heated mast that controlled the relative humidity (RH) of the air masses to 60%, which partially dried the aerosol. Sector control for the flow was used to prevent sampling of emissions directly from the R/V *Atlantis*. The cruise track followed the California coastline and the Sacramento-San Joaquin River delta. Sampling was performed in proximity to Los Angeles, Monterey Bay, San Francisco, and Sacramento areas.

For comparison with the CalNex and Cal-Mex sites, we identified seven IMPROVE (Interagency Monitoring of Protected Visual Environments, <http://views.cira.colostate.edu/web/DataWizard/>) and five CARB (California Air Resources Board, <http://www.arb.ca.gov/aqmis2/aqmis2.phpnetwork>) sites with long-term measurements in nearby in both rural and urban locations. These sites, along with the distance to the intensive CalNex and Cal-Mex sites, are listed in Table 9.1 and shown on Figure 9.1. For each intensive site, we identified both a nearby “background” site in a rural location from the IMPROVE network and a nearby “urban” site from the CARB network. At both IMPROVE and CARB sites, 24-hr samples were used to measure OC every 3 days (with one site measuring every 7 days).

For the CalNex and Cal-Mex campaigns, OM was collected through a single 1- $\mu\text{m}$  sharp-cut cyclone (SCC 2.229 PM1, BGI Inc., Waltham, MA) on 37 mm Teflon filters (Pall Corp., Ann Arbor, MI). The filters were loaded at constant air flux between 4 hr and 12hr in a continuous sampling for the corresponding campaign periods. At the Pasadena location, similar sampling was carried out using a 2.5  $\mu\text{m}$  sharp-cut cyclone during 23 hr each day. After particle collection the samples from all of the locations were sealed and stored below 0°C for FTIR and XRF analysis, to avoid evaporative losses.





Filters were scanned before and after aerosol loading by transmission FTIR spectroscopy using a Tensor 27 spectrometer with DTGS detector (Bruker Optics Inc., Billerica, MA; OPUS software). Initial spectra are obtained prior to sampling. After sampling, each ambient spectrum was calculated as the difference of the final and initial scan spectra. The OM and OC concentration of organic functional groups were determined using a previously developed, automated baselining and peak-fitting algorithm [Russell et al., 2009; Takahama et al., 2012] that quantifies alkane, hydroxyl, carboxylic acid, carbonyl, amine and organonitrate functional group concentrations based on the intensity of their characteristic infrared absorption band in the interval between 400 and 4000  $\text{cm}^{-1}$ . Baselining and standard compound calibrations are provided in *Gilardoni et al.* [2007].

Table 9.1: Distances, less than 200km, for each pair of short-term (CalNex/CalMex) and long-term (IMPROVE and CARB) sites. Distances shown for R/V *Atlantis* correspond to the mean value of each sub-region. Minimum and maximum values are also shown in brackets.

Distance (km)	IMPROVE				CARB				
	CalNex Cal-Mex	Wright-wood	San Rafael	Point Reyes	Los Angeles	Simi Valley	San Jose	Vallejo	Sacramento
R/V Atlantis*	Los Angeles	101 (87 - 118)	181 (216 - 133)	-----	45 (65 - 29)	64 (30 - 98)	-----	-----	-----
	Oxnard	162 (144 - 199)	79 (43 - 103)	-----	113 (154 - 91)	71 (53 - 109)	-----	-----	-----
	Monterey Bay	-----	-----	155 (124 - 182)	-----	-----	59 (79 - 47)	-----	-----
	San Francisco	-----	-----	64 (51 - 71)	-----	-----	-----	16 (12 - 23)	-----
	Sacramento	-----	-----	119 (111 - 129)	-----	-----	-----	-----	19 (5 - 29)
Tijuana		Agua Tibia 107				El Cajon 32			
Pasadena		Wrightwood 48				Los Angeles 12			
Bakersfield		San Rafael 117	Dome Land Wilderness 186			Bakersfield 8			

### 9.3 Results and Discussion

#### 9.3.1 Comparison of CalNex and Cal-Mex OC with Monitoring Sites

Figure 9.2 shows the comparison of the OC measurements from the CalNex and Cal-Mex campaigns with the urban and rural monitoring sites. The urban sites typically have OC concentrations higher than the corresponding, nearby rural sites by factors of 2 to 5, annually. Interestingly, the differences in OC concentrations are lower during the summer. This is consistent with a larger

contribution from both biogenic and transported secondary OC and a smaller contribution from residential heating sources, in the summer. At all four CalNex and Cal-Mex campaign sites, the measured OC fell between the nearby rural and urban OC concentrations.

The R/V *Atlantis* measured OC concentrations of  $\sim 1 \mu\text{g C m}^{-3}$ , which is comparable to the Los Angeles and San Francisco sites during the first half of the cruise in early June, when its track was very close to coastal southern California. As the ship moved northward, more offshore winds brought in cleaner air from the northwest, over the ocean. There, the OC concentrations decreased to values below  $0.4 \mu\text{g C m}^{-3}$ , which are more typical of the less polluted Point Reyes site. The R/V *Atlantis* measured particles with an average composition of 16% hydroxyl, 31% carboxylic acid, 51% alkane, and 3% amine. The total ratio of oxygen to carbon was 0.46 indicating oxygenated aerosol. In the southern California samples, the total OM was  $2.11 \mu\text{g m}^{-3}$ , which is higher than the OM measured in Sacramento ( $0.78 \mu\text{g m}^{-3}$ ).

The Agua Tibia and El Cajon sites had very similar OC concentrations during the summer, and both were within 50% of the Cal-Mex measurements at Tijuana in Parque Morelos. This similarity is consistent with the findings of *Takahama et al.* [in press] that the majority of the OM measured at Tijuana during Cal-Mex was transported from the Los Angeles area rather than produced by local sources. The large contribution of transported OC can also explain why the rural site at Agua Tibia and the urban site at El Cajon were so similar. In contrast, the wintertime concentrations at these two sites are very different, with El Cajon OC concentrations of more than  $8 \mu\text{g C m}^{-3}$  exceeding those of Agua Tibia by a factor of 10 or more in December.

The OC concentrations at the CalNex Pasadena site were very similar in magnitude  $3.6 \pm 1.3 \mu\text{g m}^{-3}$  to the measurements at the long-term Los Angeles site. Daytime sea breeze advects emissions from the southwest to the northeast with an average transport time of emissions from LA to Pasadena of 3.25 hrs, making the consistency in OC concentrations between LA and Pasadena reasonable (Hayes et al., Submitted). The emissions in the Basin exit through passes in the San Gabriel (El Cajon Pass) and San Bernardino Mountains (Banning Pass) [Lu and Turco, 1995]. Given that Wrightwood is located in the San Gabriel Mountains and is shielded from the high OC source regions of the LA Basin and its outflow pollution, such low OC concentrations are to be expected. The rural Wrightwood community had considerably lower OC concentrations than either Pasadena or Los Angeles, on average 5-10x lower. Season differences in OC were observed at Pasadena and Wrightwood, with higher concentrations in the winter, as compared to the summer for the LA monitoring site. One would expect similar seasonal differences at Pasadena, given the airflow patterns in the LA Basin. Wrightwood had fairly constant OC throughout the year, indicating no substantial biogenic or urban/agricultural burning sources.

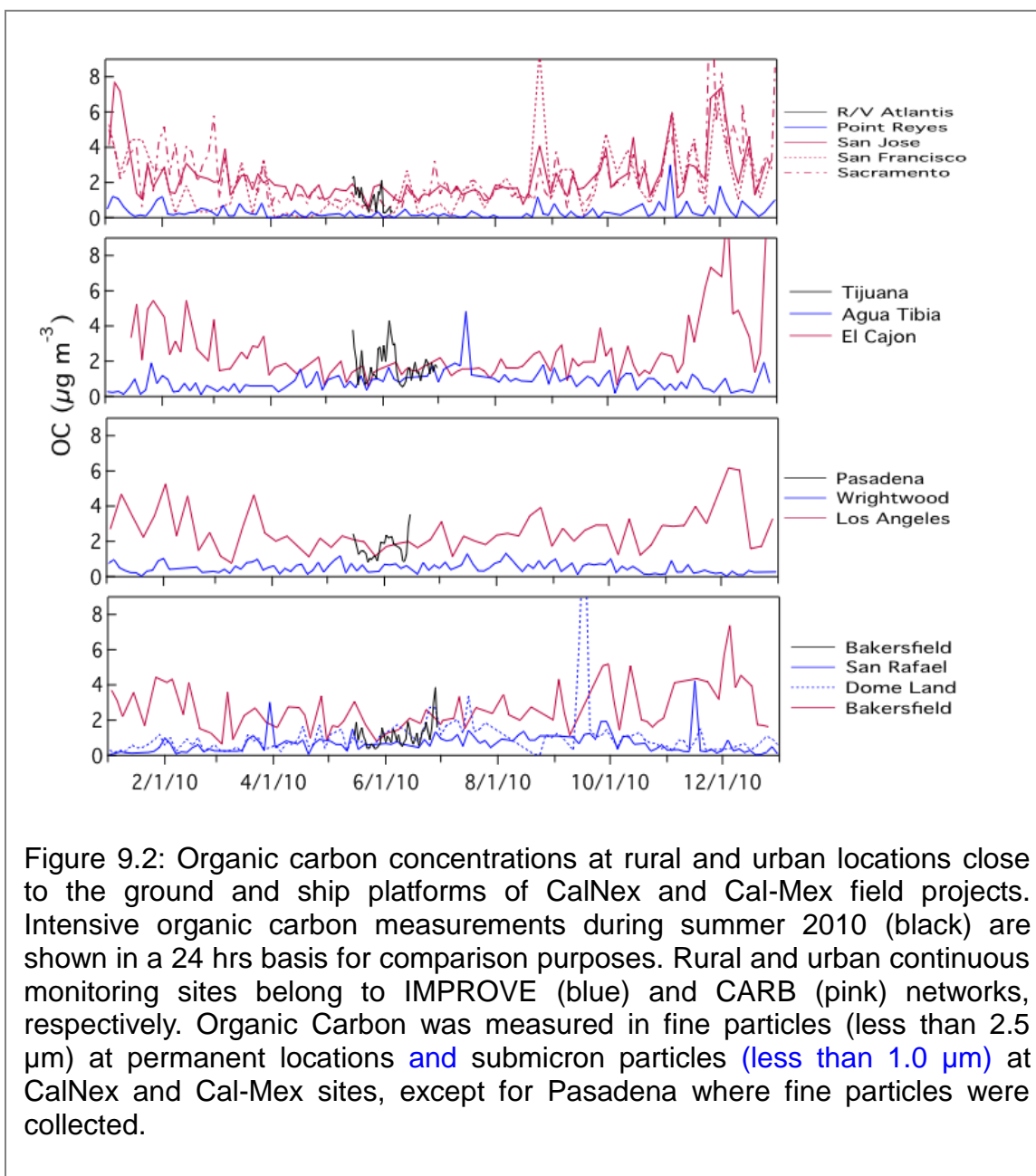


Figure 9.2: Organic carbon concentrations at rural and urban locations close to the ground and ship platforms of CalNex and Cal-Mex field projects. Intensive organic carbon measurements during summer 2010 (black) are shown in a 24 hrs basis for comparison purposes. Rural and urban continuous monitoring sites belong to IMPROVE (blue) and CARB (pink) networks, respectively. Organic Carbon was measured in fine particles (less than 2.5  $\mu\text{m}$ ) at permanent locations and submicron particles (less than 1.0  $\mu\text{m}$ ) at CalNex and Cal-Mex sites, except for Pasadena where fine particles were collected.

The urban and rural OC concentrations near the CalNex Bakersfield site differed by less than a factor of 2 in summer 2010, with Dome Land and San Rafael concentrations of about 1  $\mu\text{g C m}^{-3}$  and those of Bakersfield at 2  $\mu\text{g C m}^{-3}$ . Similar to Tijuana, wintertime OC concentrations showed a larger difference between urban and rural OC, consistent with lower contributions from local sources.

### 9.3.2 Factor Analysis of FTIR Spectra at CalNex and Cal-Mex Sites

To assess the major sources that contribute to the total organic aerosol composition, the apportionment of measured OM using PMF [*Paatero and Tapper, 1994*] was determined for each campaign. This approach provides a framework that separates the organic mass into separate factors with distinctive functional group composition and magnitude.

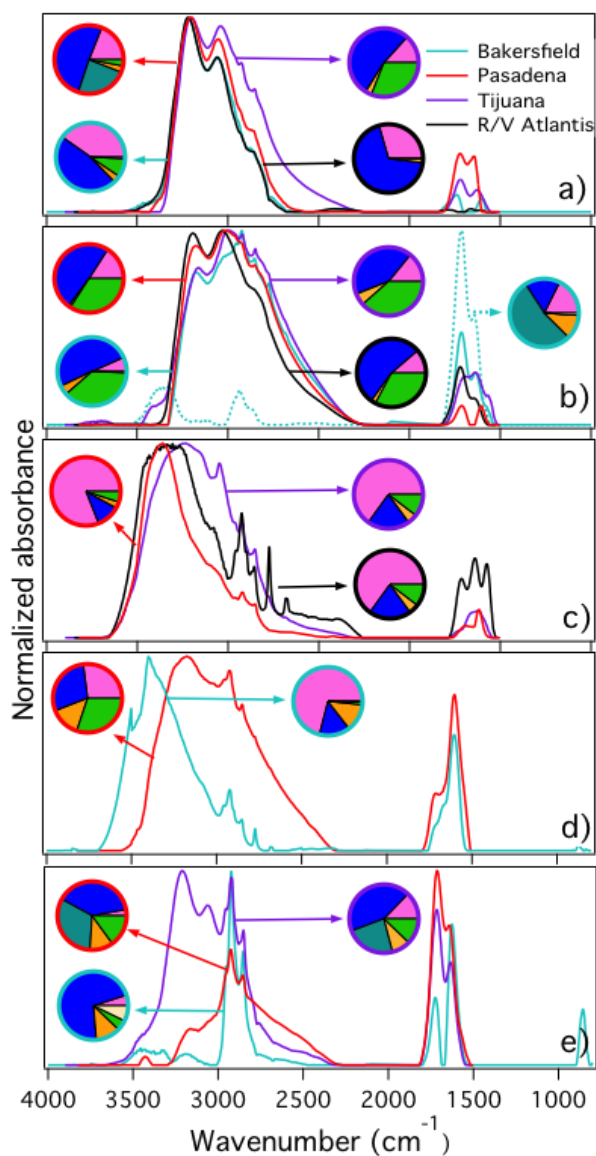


Figure 9.3: Reconstruction of PMF spectra and organic composition for Bakersfield (teal), Pasadena (red), R/V *Atlantis* (black), and Tijuana (purple). Source factors are categorized into five main groups: a) LO fossil fuel combustion, b) MO fossil fuel combustion, c) marine, d) vegetative detritus, and e) biomass burning/polluted biogenic SOA. Pie charts are colored as: hydroxyl (pink), alkane (blue), amine (orange), carboxylic acid (green), non-acid carbonyl (teal), and organonitrate (beige).

Five main source categories were identified based on factor spectra and organic composition similarities: fossil fuel combustion (two), marine, biomass burning/biogenic, and vegetative detritus (Figure 9.3). The factor spectra are shown as the sum of the organic peaks (which excludes ammonium) that were fit

in the original spectra, using the automated peak-fitting algorithm. An additional factor related to biomass burning or processed biogenic emissions was also identified in the inland sites.

Two fossil fuel combustion factors with low covariation in time, and correlated with different fossil fuel combustion markers were identified for each site. The fraction of oxygenated functional groups for each sample were as an indicator of atmospheric processing, with a higher fraction of oxygenated groups resulting from more processing. The first factor was identified as less oxygenated (LO) and is a result of either POA or first generation secondary mass. The second fossil fuel combustion factor, the more oxygenated (MO) factor, is dominated by secondary organic mass. The contribution of organic mass related to total fossil fuel combustion sources accounts for half of the total OM of the inland regions (42% – 58%). Nevertheless, the relative contribution of two types of fossil fuel combustion sources varies considerably among campaigns (less oxygenated fossil fuel combustion factor: 7-40% and more oxygenated fossil fuel combustion factor: 18-82%), indicating that the yields of SOA formation are specific of each location.

The composition of the MO fossil fuel combustion factors are consistent among all of the sites with 50% alkane, 11% alcohol, 36% carboxylic acid, and 4% amine, on average. This suggests that the strong secondary organic mass composition signature is independent of the specific oxidation paths of primary sources. In contrast, there are significant composition differences among LO fossil fuel combustion factors reflecting the different characteristic primary particulate emissions for the different sites.

The Marine factor identified by FTIR PMF is identified as organic mass derived from ocean sources. Both the Marine factor and the Polluted Marine factor are dominated by alcohol functional groups (70%). The Polluted Marine factor correlates well with coarse sea salt particles (Pasadena) and with sodium and chloride in submicron particles measured by XRF (Tijuana, Bakersfield, and R/V *Atlantis*). The alcohol groups found in the Polluted Marine factor are likely derived from polysaccharides concentrated on the ocean's surface [*Aluwihare et al.*, 1997; *Russell et al.*, 2010]. The striking similarity of the OFG composition of the Marine Factor with the vegetative detritus factor found at Bakersfield is consistent with the with saccharide-type compounds also found plant materials [*Bianchi et al.*, 1993].

The final common factor contains a large carbonyl fraction or carboxylic acid fraction and is related to biomass burning (Tijuana) and polluted biogenic SOA mixed (Pasadena and Bakersfield). Despite differences in OFG composition, these factors show spectral characteristics of methylene peaks at 2929 and 2855  $\text{cm}^{-1}$ , which are present from burning of plant materials [*Hawkins and Russell*, 2010].

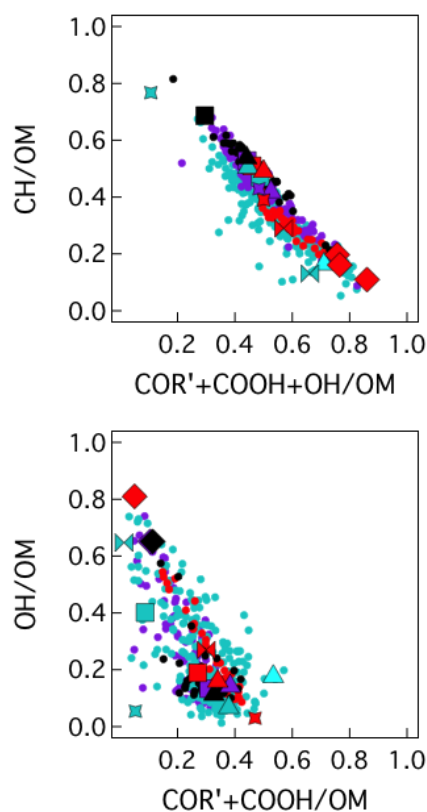


Figure 9.4: Distribution of oxygenated functional groups in ambient samples and PMF factors for each site: Bakersfield (teal), Pasadena (red), R/V Atlantis (black), and Tijuana (purple). Sources, according to PMF solutions, are categorized into five classes, LO fossil fuel combustion (squares), MO fossil fuel combustion (triangles), marine (diamonds), vegetative detritus (wedges), and biomass burning/polluted biogenic (crosses).

### 9.3.3 Comparison of Fuel and Fossil Fuel Factor Organic Functional Groups

*Gentner et al.* [2012] reviewed and quantified the similarities in individual molecular species identified in fuel and OM composition in tunnel studies as well as Bakersfield. Here, we use the alkane absorption region of FTIR spectra (2800-3000  $\text{cm}^{-1}$ ) to look for similarities between the composition of the observed OM and fuel standards. While FTIR spectroscopy cannot resolve the individual compounds, the spectral signature is characteristic of the mixture. Figure 9.5 shows a comparison of each CalNex and Cal-Mex field campaign factors to four fuel standards: gasoline, diesel, and oil purchased from Mobil in southern California in summer 2010 and low-sulfur ship diesel purchased by the R/V *Point Sur* in July 2011.

One interesting aspect of this comparison is that while all of the fossil fuel OM factors at each site have nearly all the same four characteristic peak locations



(2954, 2923, 2869, and 2855  $\text{cm}^{-1}$ ) they differ in the ratio of the four peak heights. These peak heights are summarized for the fuels in Table 9.2.

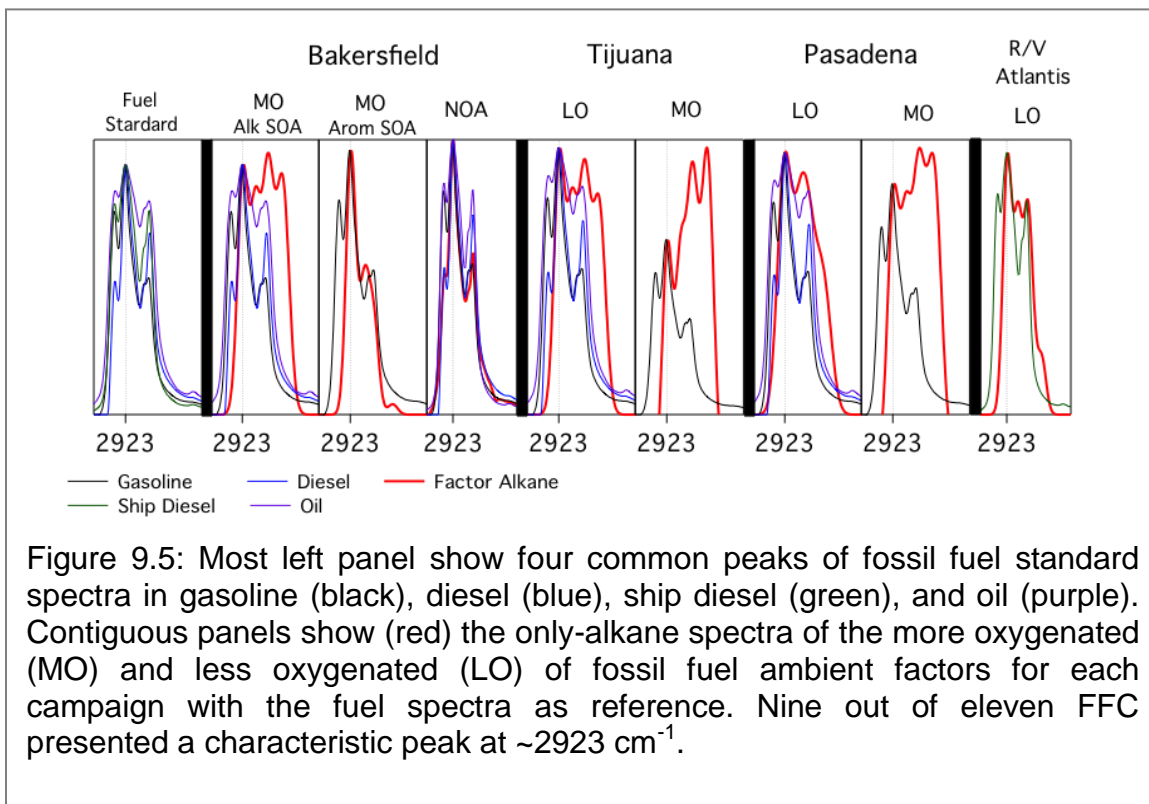


Figure 9.5: Most left panel show four common peaks of fossil fuel standard spectra in gasoline (black), diesel (blue), ship diesel (green), and oil (purple). Contiguous panels show (red) the only-alkane spectra of the more oxygenated (MO) and less oxygenated (LO) of fossil fuel ambient factors for each campaign with the fuel spectra as reference. Nine out of eleven FFC presented a characteristic peak at  $\sim 2923 \text{ cm}^{-1}$ .

Comparing the peak ratios of the factors to the fuels, we see that Tijuana is most similar to the motor oil, which is consistent with the older vehicle fleet in Tijuana than in the U.S. cities [Takahama *et al.*, in prep.]. Bakersfield has the highest  $2850 \text{ cm}^{-1}$  peak, suggesting a larger contribution from diesel. Since the SJV has lower population density than the LA basin but a substantial amount of trans-valley transport of produce and other goods from San Francisco to LA, it is not surprising that diesel is a larger contributor than gasoline in this region. For both the R/V *Atlantis* and the Pasadena measurements, the high peak at  $2860 \text{ cm}^{-1}$  is consistent with a contribution from the ship-type diesel.

Table 9.2: Common peak locations in fossil fuel spectra and their peak heights relative to the highest peak ( $2923 \text{ cm}^{-1}$ ).

Location ( $\text{cm}^{-1}$ )	Height			
	Gasoline	Diesel	Ship Diesel	Oil
2855	0.6	0.7	0.8	0.9
2869	0.5	0.5	0.7	0.8
2923	1	1	1	1
2954	0.8	0.5	0.8	0.9

### 9.3.4 Contributions of POA and SOA

*Liu et al.* [2011] reviewed methods used for attribution of OA as secondary, showing that one of the most prevalent approaches is to define oxygen-containing mass fragments or oxidized functional groups as secondary. For fossil fuel combustion sources, there is little reason to doubt this is true, since partially combusted (oxygen-containing), low-volatility (>C3) hydrocarbons are outnumbered by unburnt hydrocarbons in most engine emissions. However, marine and terrestrial biological sources, as well as biomass burning sources, may have substantial oxygen content [*Jimenez et al.*, 2009; *Russell et al.*, 2010; *Takahama et al.*, 2011]. For this reason, the following method for separation of primary and secondary components has been applied only to the OM associated with the fossil fuel derived sources.

There were nine fossil fuel related factors identified at the four CalNex and Cal-Mex intensive campaigns (shown in Figure 9.3). Only one of these factors had O/C lower than 0.1, a frequently-used cutoff for identification of a purely primary, hydrocarbon-like OA (HOA), meaning that Tijuana, R/V *Atlantis* and Pasadena had negligible POA (below limit for separating by PMF) and Bakersfield had POA that was at most 10% of OM. Since PMF factors are identified by covariation of functional groups with each other, it is not surprising that rapid formation of SOA on time scales faster than captured by PMF of multi-hour filter samples. However, we cannot rule out that some fraction of the factors with O/C between 0.2 and 0.6 was primary. To account for this possibility, we identify only the alkane group fraction of each fossil fuel combustion factor as primary. This calculation represents an upper bound, since most secondary organic products of alkanes contain 70% to 90% (molar) alkane groups, and even aromatic products can retain up to 30% alkane groups. As an initial estimate, we calculate the alkane group mass not associated with SOA. An even more conservative upper bound is provided by POAmax, the sum of the alkane group mass for all of the fossil fuel combustion factors at each site. By the best estimate, POA accounts for 16 to 20% of the OA at the CalNex and Cal-Mex campaigns.

Table 9.3: Summary of the alkane peak locations for the fossil fuel combustion factors.

Peak	Tijuana		Pasadena		Bakersfield			R/V <i>Atlantis</i>	
	LO	MO	LO	MO	LO	MO		LO	MO
						Alkane	PAH		
1	2929	2919	2920	2921	-----	2919	2920	2919	-----
2	-----	-----	-----	-----	-----	-----	-----	-----	-----
3	2884	2880	2884	2867	-----	2883	2879	-----	2885
4	2848	2848	2846	-----	-----	2848	-----	-----	2850
Unidentified	2810	2806	2810	2811	2804	2810	-----	-----	2813

*Bahreini et al.* [2012] used the ratio of  $\Delta\text{OA}/\Delta\text{CO}$  as an indicator of secondary contributions to OA, since CO tracks emissions and so increases in the amount of OA per CO are inferred to be driven by post-emission formation. Figure 9.6 shows the relationship between OA, POA, and SOA with CO. Interestingly, the Tijuana campaign shows no correlation between POA<sub>max</sub> and POA<sub>min</sub> and CO, consistent with the finding that most of the OA is aged and transported. The slopes of POA<sub>max</sub> with CO for Bakersfield and Pasadena are more comparable to those reported in the literature [*De Gouw and Jimenez, 2009*], and their correlation coefficients are slightly higher although still weak ( $0.3 < r < 0.5$ ).

A clear result is that there are significant differences in the estimated  $\Delta\text{POA}/\Delta\text{CO}$  between the three CalNex and Cal-Mex ground sites. Since each site has a different mix of vehicles, and different vehicles have different amounts of POA emitted per CO, this result is not surprising. The wide scatter in  $\Delta\text{OA}/\Delta\text{CO}$  is also consistent with the expected difference in diesel and gasoline usage on weekdays and weekends.

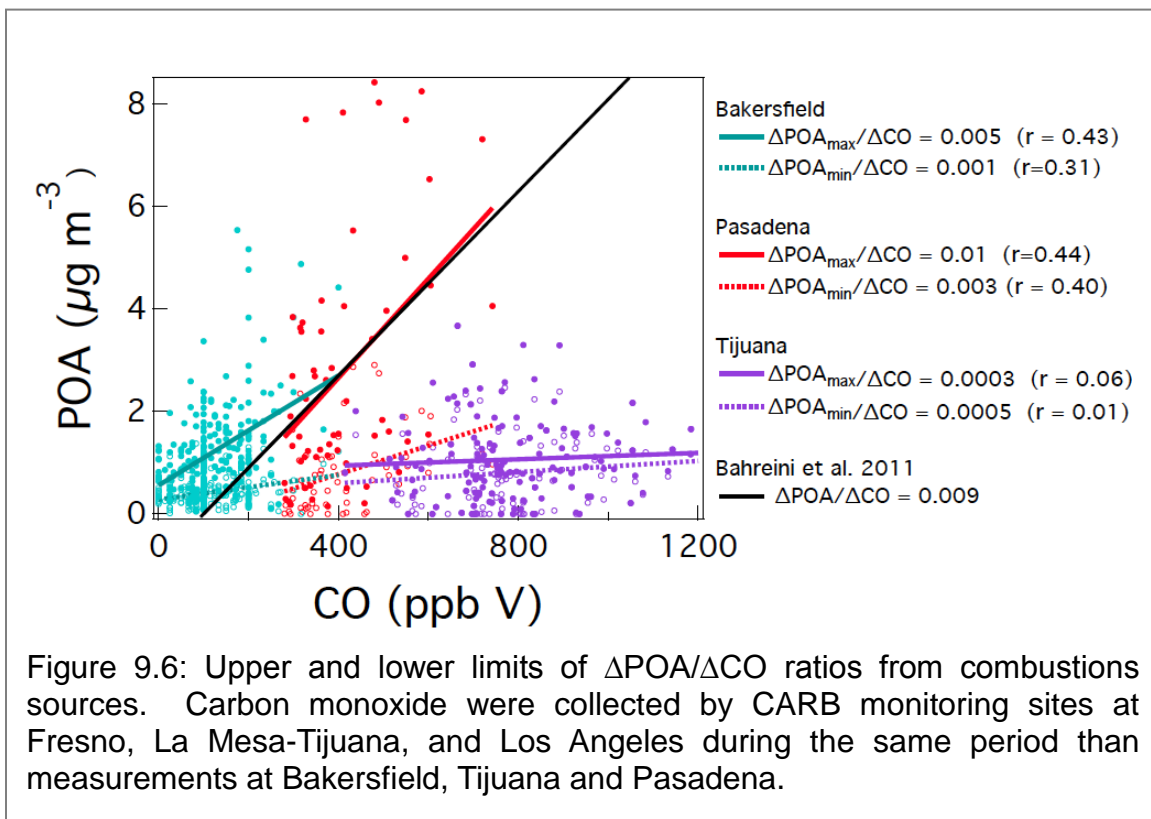


Figure 9.6: Upper and lower limits of  $\Delta\text{POA}/\Delta\text{CO}$  ratios from combustions sources. Carbon monoxide were collected by CARB monitoring sites at Fresno, La Mesa-Tijuana, and Los Angeles during the same period than measurements at Bakersfield, Tijuana and Pasadena.

#### 9.4 Conclusions

The CalNex and Cal-Mex campaigns provided intensive measurements of organic aerosol composition and sources. The OC concentrations were comparable to the measurements at long term monitoring sites during the summer of 2010, which were typically somewhat lower than the wintertime

concentrations due to meteorological differences as well as the lower summertime contributions of biomass burning.

The four CalNex and Cal-Mex campaigns showed similar chemical signatures from fossil fuel combustion sources, with all reflecting contributions with both more and less oxygenated organic components. The coastal measurements on the R/V *Atlantis*, Tijuana, and Pasadena showed primary marine biological contributions, while Bakersfield and Pasadena showed terrestrial biological vegetative detritus. The three land sites also had contributions from cooking (Pasadena, Bakersfield) and biomass burning (Tijuana). The similarity of the factor spectra for each source type across all four sites is striking, indicating that all four sites had similar types of sources, even though they were mixed in different ratios in the ambient OM. The similarities in the fossil fuel combustions factors are interesting in that they clearly separate into more and less oxygenated components at each site – with their similar spectral shapes indicating that the distinction in their chemical formation reflects different functionality in addition to changes in O/C ratios. These differences are reflected in the higher fractions of hydroxyl in the less oxygenated fossil fuel factors, and more carbonyl groups in the more oxygenated fossil fuel combustion factors at all sites. Their nearly linear alignment in the functional group analogy of van Krevelen space may be largely incidental, in that there is no direct evidence for progression from the less oxygenated to the more oxygenated factors.

Comparison of the fossil fuel combustion factors to FTIR spectra of diesel, gasoline, motor oil, and ship diesel shows interesting differences in the alkane group peaks. These differences may reflect either a primary contribution to the factors or the persistent backbone of alkane or aromatic hydrocarbon precursors. In the Bakersfield nighttime factor, the colder temperatures and lack of photochemical degradation led to a strong similarity between the factor's alkane group absorbance and that of diesel fuel, suggesting an important nighttime contribution of primary OM emissions from trucking in the San Joaquin Valley.

Using the functional group composition, we can bound the possible primary contribution to the fossil fuel combustion factors by the alkane group mass contribution. These estimates indicate that at most 34-39% of OM is primary (man-made), although smaller than 16-20% is more likely. However, even these upper bounds show important differences in the  $\Delta POA/\Delta CO$  at the CalNex and Cal-Mex sites. While it is not surprising that this ratio differs substantially at locations with different source emissions and vehicle fleets, we note that this has important implications for using variations this ratio to identify sources.

## 9.5 Appendix

### 9.5.1 Factor extraction for FTIR $PM_{10}$ samples onboard R/V *Atlantis*

PMF was used to identify source factors of the organic mass for the 40 ambient R/V *Atlantis* samples. The standard deviation for each wavenumber for the back

filters was used as the uncertainty for PMF. The results from 2 through 6 factor solutions were calculated. The  $f_{\text{peak}}$  (rotation) value was varied from -1.2 to 1.2 in steps of 0.6. The seed value was varied for each number of factors and  $f_{\text{peak}}$  values using 1, 10, and 100 and did not significantly change the solution. For factor solutions of 3 to 6 factors, the  $f_{\text{peak}}$  of 0 showed the lowest value of  $Q/Q_{\text{expected}}$ , although it did not change significantly between  $f_{\text{peak}}$  values. A four factor solution, recombined to three factors, was determined to best represent the OM ( $r = 0.98$ , factor OM =  $0.89 \times$  original OM). The recombined factors correlated in time with  $r = 0.78$ . Solutions with more factors created unrealistic splitting of the factors.

### **9.5.2 Factor extraction for FTIR $PM_{2.5}$ samples at Pasadena**






Positive matrix factorization [Paatero and Tapper, 1994] was calculated using 60 spectra from Fourier transform infrared (FTIR) filter samples to identify robust, linearly independent components. Both long (23 hr filter resolution) and short samples (3-6 hr resolution taken during 9 intensive days) were used for PMF analysis. The portion of the spectra with quantifiable peaks ( $3800\text{-}1500\text{ cm}^{-1}$ , with the exclusion of the Teflon interference) was used for the analysis. The standard deviation of each wavenumber for the back filters was used as the uncertainty for PMF. Evaluated solutions included factors 2-6 that were calculated by varying the FPEAK (rotation) from -1.2 to 1.2, by increments of 0.2. Altering the seed value by 1, 10, and 100 for each combination of FPEAK and number of factors did not significantly change spectral features of the factors or correlations with tracers. The sensitivity to rotation was negligible for FPEAK=-0.2, 0, and 0.2, with FPEAK=0 giving the lowest Q value. FPEAK=0 was chosen to represent the solution due to both low residuals and co-linearity amongst the factors.

Two and three-factor solutions underrepresented total OM and four-factor solutions indicated one factor was not robust amongst rotations. Therefore, a five-factor solution was chosen to best represent the OM, resulting in the reconstruction of 90% of the mass and representing 95% of the variance. The organic functional group reconstruction for the solution was near 95% for all groups. Six-factor solutions resulted in over-splitting, producing unrealistic spectral features. Additionally the five-factor solution had similar spectral structures ( $r > 0.85$ ) with previously identified factors [Russell *et al.*, 2011].

The five-factor PMF solution was found to contain 5 unique sources of  $PM_{2.5}$  OM in Pasadena: Alkane SOA (32%), Mixed SOA (20%), Aromatic SOA (15%), Marine (15%), and Vegetative Detritus (17%) (Figure 9.3, Table S9.1). Classification of the five unique sources was determined by their correlations with independent tracer species and similarities with robust solutions from previous campaigns [Russell *et al.*, 2011]. The five factors showed little correlation amongst each other ( $r < 0.3$ ), with the exception of Alkane SOA and the Mixed SOA components ( $r = 0.55$ ), which appear to arrive from similar source regions.

Two fossil fuel combustion SOA factors, that had low correlation ( $r=0.37$ ) in time, were found at Pasadena. The Alkane SOA factor had spectral similarities to previously identified fossil fuel combustion sources (Russell et al., 2011). Particularly, the Alkane SOA factor is characterized by a large fraction of alkane (53%) and carboxylic acid (31%) (Table S9.1). Additionally the Alkane SOA factor correlated moderately to fossil fuel tracers and products of SOA formation: Sulfate (0.66), Ammonium (0.55), Benzene (0.51), and Acetone (0.71) (Table S9.2). The Alkane SOA factor also correlated to AMS PMF factors, HOA (0.66) and SV-OOA (0.50) [Hayes et al., in review]. Excluding the long filters (23 hr resolution) from analysis, the concentration and mass fraction of the Alkane SOA factor increases from  $1.86 \mu\text{g m}^{-3}$  (32%) to  $5.83 \mu\text{g m}^{-3}$  (52%). Filters with 23 hr resolution exhibited lower OM, presumably from evaporated losses of semi-volatiles due to daytime heating. The Alkane SOA factor had the most dramatic change in concentration and mass fraction when comparing all filters to the higher resolution, short filters. Suggesting that of the five factors identified, Alkane SOA is the most susceptible to evaporative losses of organics. Additionally the correlations to tracers also increased for this factor when daily, 23 hr samples were excluded (Table S9.2).

Table S9.1: Concentration, mass fraction, and composition of PMF factors identified from the FTIR measurements. Colors in pie charts indicate alcohol (pink), alkane (blue), carboxylic acid (green), non-acid carbonyl (teal), and primary amine (orange) organic functional groups. Concentrations and mass fractions listed in parentheses indicate short filters only (3-6 hr resolution). Values not in parentheses were calculated for both long and short filters.

FTIR Factor	Concentration ( $\mu\text{g m}^{-3}$ )	Mass Fraction	Composition
<b>Alkane SOA</b>	1.86 (5.83)	32% (52%)	
<b>Mixed SOA</b>	1.16 (1.71)	20% (15%)	
<b>Aromatic SOA</b>	0.90 (1.94)	15% (17%)	
<b>Marine</b>	0.90 (1.34)	15% (12%)	
<b>Vegetative Detritus</b>	1.01 (0.38)	17% (3%)	

A second fossil fuel combustion source was identified as Aromatic SOA due to the predominant ammonium peaks and a high fraction of carbonyl organic

functional groups (21%). Previous aromatic oxidation studies have found aromatic SOA products to be dominated by carbonyl and carboxylic acid groups in FTIR spectra [Saathoff *et al.*, 2003]. In addition, this factor correlated moderately to LV-OOA (0.53) [Hayes *et al.*, in review], non-refractory chloride (0.52), and a series of Hopanes (0.30-0.61) (Table S9.2).

A third factor was classified as Mixed SOA. The factor was highly oxidized and contained substantial amounts of carbonyl (35%) and carboxylic acid (13%) functional groups. The SOA mixture peaked during the afternoon and correlated strongly to secondary tracers: Acetaldehyde (0.84), Acetone (0.80), and Ox (0.79), suggesting photochemical production. The factor also had strong correlations to both biogenic- and anthropogenic-like tracers; including biogenic-like tracers MVK/MACR (0.86), Isoprene (0.82), and anthropogenic-like Sulfate (0.70), Benzene (0.69), and refractory Black Carbon (rBC) (0.64). The factor correlated to AMS factors: HOA (0.75) and SV-OOA (0.86) [Hayes *et al.*, in review]. PMF would not be able to separate the anthropogenic factor from the biogenic factor, if the emissions from the different sources co-varied, which is highly probable.

Table S9.2: Correlations (r values) of FTIR PMF components with gas phase and aerosol tracers measured at the Pasadena ground site during CalNex. The highest correlation for each tracer is underlined. Correlations in parentheses indicate those for short samples only

Tracer	Alkane SOA	Mixed SOA	Aromatic SOA	Marine	Vegetative Detritus	
HOA	0.66 (0.75)	<u>0.75</u>	0.29	0.02	-0.26	AMS - Factor
LV-OOA	0.36	0.51	<u>0.53</u>	0.01	-0.01	AMS - Factor
SV-OOA	0.50	<u>0.86</u>	0.27	0.32	-0.24	AMS - Factor
LOA	0.37	<u>0.47</u>	0.17	-0.07	0.04	AMS - Factor
CIOA	-0.17	-0.06	-0.29	0.16	0.14	AMS - Factor
SO <sub>4</sub>	0.66 (0.89)	<u>0.70</u>	0.32	-0.27	-0.06	AMS
NO <sub>3</sub>	0.43 (0.79)	<u>0.49</u>	0.37	-0.39	0.16	AMS
NH <sub>4</sub>	0.55 (0.91)	<u>0.59</u>	0.36	-0.40	0.10	AMS
Benzene	0.51 (0.63)	<u>0.69</u>	0.18	-0.12	0.00	Primary
CO	0.47	<u>0.69</u>	0.18	-0.02	0.00	Primary
nr-Cl	0.10	0.12	<u>0.52</u>	0.23	-0.04	Primary
rBC	0.62 (0.75)	<u>0.64</u>	0.17	-0.28	-0.01	Primary
Dust	0.04	0.25	-0.20	-0.47	<u>0.41</u>	Primary
O <sub>x</sub>	0.48	<u>0.79</u>	-0.01	0.05	-0.03	Secondary
Acetaldehyde	0.63 (0.70)	<u>0.84</u>	0.28	0.00	-0.06	Secondary
Acetone	0.71 (0.80)	<u>0.80</u>	0.13	-0.19	-0.11	Secondary
Isoprene	0.44	<u>0.82</u>	0.17	0.21	-0.21	Biogenic
MVK/MACR	0.47	<u>0.86</u>	0.18	0.20	-0.17	Biogenic
Na (PM <sub>1.15</sub> )	-0.10	-0.04	-0.04	<u>0.69</u>	-0.09	Marine
Na (PM <sub>2.5</sub> )	-0.23	0.04	0.17	<u>0.46</u>	0.19	Marine

Two additional factors were identified by FTIR PMF and are believed to occur on refractory material: mineral dust and sea salt, and therefore not measurable by AMS. These two factors have been identified as Marine and Vegetative Detritus. The Marine factor is dominated by alcohol functional groups (84%), correlates well with the FTIR Alcohol Fraction (0.65) and PM<sub>1</sub> and PM<sub>2.5</sub> Na<sup>2+</sup> measured by XRF (0.69 and 0.46 respectively) (Table S9.2). The alcohol groups found in the Marine factor are likely derived from polysaccharides concentrated on the ocean's surface [Aluwihare *et al.*, 1997; Russell *et al.*, 2010]. In addition, the Marine factor contains strong spectral signatures of methylene peaks (2929 and 2855 cm<sup>-1</sup>), consistent with either long-chain fatty acids or potentially anthropogenic influences. The factor correlates with C<sub>27</sub> and C<sub>28</sub> alkanes, heptacosane (0.46) and octacosane (0.48), two dominant alkanes found in shipping emissions [Agrawal *et al.*, 2008]. Additionally, the Marine factor correlates strongly to PM<sub>1</sub> Ni (0.74), Cu (0.74), and Pb (0.67), which are often found in shipping emissions [Isakson *et al.*, 2001]. Correlations to Ni, Pb, C<sub>27</sub> and C<sub>28</sub> alkanes, and presence of methylene peaks could indicate influence of shipping emissions from the Port of Long Beach in the Marine factor.

The fifth factor contained a high fraction of amine (14%) and strong spectral characteristics of methylene peaks (Figure 9.3). This factor, identified as Vegetative Detritus, had strong correlation to FTIR Amine Fraction (0.73), presumably from amino acids in plant material, and mild correlation to Dust Particles (0.41). However, no other strong correlations were found for this factor. The factor was episodic and did not occur as frequently during the intensive sampling periods, thus the difference in mass fractions between all periods and intensive periods (17% vs. 3%). In the LA Basin, roughly 47% of the region is covered by vegetation and some studies have suggested that 6-20% of the organics from PM<sub>2.5</sub> in the LA Basin has a vegetative origin [Miller and Winer, 1984; Simoneit, 1986] and a substantial portion of the OM from vegetation is believed to be from the re-suspension of dust [Simoneit, 1986].

Factors identified from AMS and FTIR measurements compare well, despite their different size cuts, PM<sub>1</sub> and PM<sub>2.5</sub> respectively. Due to the similar arrival times at Pasadena and strong correlation to HOA and SV-OOA [Hayes *et al.*, in review], Alkane SOA and Mixed SOA are grouped together for the comparison. Combined Alkane SOA + Mixed SOA was found to compare well (r=0.87) to the sum of HOA + SV-OOA. Since both Alkane SOA and Mixed SOA are expected to be submicron, it is not unexpected that these factors would compare so well. Additionally, AMS did not identify Marine or Vegetative Detritus factors [Hayes *et al.*, in review]. Two reasons can explain this discrepancy. First, both Marine and Vegetative Detritus aerosol is expected to be in the supermicron aerosol mode, which due to size cuts would not be measured by the AMS. Second, the aerosol is presumed to contain organics on refractory particles, sea salt and dust, which too would not be measured by the AMS [Russell *et al.*, 2011]. In addition, two factors identified by AMS were absent in factor components separated by FTIR:



local organic aerosol (LOA) and cooking-influenced organic aerosol (CIOA) [Hayes *et al.*, in review]. The LOA component was highly variable and accounted for a small fraction of OM (5%) [Hayes *et al.*, in review]. Therefore, due to the low sample number (n=60) and lower resolution of FTIR, factor analysis was unable to separate this component. Liu *et al.* [2012a] also identified a CIOA in AMS factor analysis, but failed to find a similar component in the FTIR factor analysis, despite having higher resolution filters. It is believed that CIOA is predominantly in particles < 200nm and therefore below the detection limit of FTIR spectroscopy. Although AMS and FTIR measure different sizes and types of organic aerosol, comparison of PMF results indicates a good agreement for aerosol in the overlap region of these independent techniques.

## 10.0 Summary of Contributions to Other Completed Papers

The sections below summarize the findings of other completed papers that used the measurements and analyses performed as part of this project.

### 10.1 NO<sub>x</sub> control of nighttime SOA formation

*Rollins et al.* [2012] reports NO<sub>x</sub> controls the nighttime formation of organic nitrates, as seen by an increase in particulate alkyl and multifunctional nitrates ( $p\Sigma\text{AN}$ ) after sunset, which coincides with the onset of NO<sub>3</sub> production. This SOA enriched in organic nitrates accounts for a third of the nighttime increase in OA in Bakersfield and is consistent with unique nighttime factors identified by AMS and FTIR measurements, described in detail in Section 4.1. This work implies reductions in NO<sub>x</sub> emissions will reduce OA concentrations in Bakersfield and nearby regions.

### 10.2 SOA formation from diesel and gasoline vehicles

The chemical composition and SOA formation potential of gasoline and diesel fuel emissions were investigated by *Gentner et al.* [2012] and compared to field data collected downwind of urban regions. A chemical mass balance model was used to predict daytime SOA concentrations at Bakersfield from diesel and gasoline, which compared well to AMS and FTIR derived SOA factors from fossil fuel combustion, described in Section 4.1. Results indicate diesel exhaust is seven times more efficient in aerosol formation than gasoline exhaust, which will help guide future control policies and fuel regulations to improve regional pollution in the San Joaquin Valley.

### 10.3 Sources of OA using speciated organic compounds as tracers

*Zhao et al.* [submitted] investigated source classes of OA in Bakersfield by applying PMF to organic tracer compounds measured by Thermal desorption Aerosol Gas chromatography (TAG). Six OA source factors were identified, including four types of SOA. On average, SOA contributed to 72% of OA and formed primarily through condensation of gas-phase oxidation products. The contribution of daytime SOA showed nearly identical diurnal patterns when compared to the sum of SOA (alkane, aromatic, and petroleum) derived from AMS measurements, described in Section 4.1.

### 10.4 Nanospray desorption/electrospray ionization mass spectrometry to characterize OA

*O'Brien et al.* [2012] measured oxygen (CHO) and nitrogen-containing organic compounds (NOC) by nanospray desorption/electrospray ionization mass spectrometry (nano-DESI-MS). CHO compounds were primarily identified during the day, while NOC compounds were dominant at nighttime. It is hypothesized

that NOC compounds form from the imidization of carbonyl groups, suggesting the important role ammonia plays in nighttime OA formation and oligomerization.

### **10.5 Molecular associations with field and lab-generated SOA**

O'Brien et al. [Accepted 2012] generated SOA from photooxidation of diesel and isoprene was analyzed by nano-DESI-MS and compared to ambient aerosol collected in Bakersfield and Pasadena. Ambient SOA at Bakersfield compared better to diesel SOA, than isoprene and was found to be more oxidized and contain more organic nitrogen than ambient aerosol at Pasadena. Ammonia was added to the diesel SOA experiment to generate the 2N compounds frequently seen in Bakersfield, suggesting  $\text{NH}_3$  chemistry is important for the formation of nitrogen-rich SOA in the San Joaquin Valley.

## 11.0 Conclusions and Findings

### 11.1 Primary Conclusions

To study the sources and formation of SOA in the San Joaquin Valley, we have conducted field measurements at Bakersfield during 15 May – 29 June 2010. The measurements suggested that organic mass comprised the major component of fine aerosol particles at Bakersfield. On average, OM in PM<sub>1</sub> and PM<sub>2.5</sub> was 2.42 and 3.23 μg m<sup>-3</sup>, respectively. PMF analysis was applied to the FTIR and AMS measurements, resulting in very high agreement between the two sets of independently-derived factors, both of which suggested that SOA components accounted for 80% to 90% of fine particle OM. The high O/C AMS factors were chemically similar, so that external source marker were needed to link them to specific sources; whereas the FTIR factors had distinct infrared spectra that could be used as references for future studies when source marker measurements are not available. Among the PMF-derived components, vehicular emission oxidation products (the alkane and aromatic SOA factors) constituted 65% OM, whereas nighttime organic aerosols (the NOA factor), a mixture of POA and SOA that likely originated from biogenic emissions, accounted for a relatively small fraction on average (10% OM), although it was higher at night (20% OM).

Potential formation mechanisms of the SOA components were discussed. Anthropogenic SOA components mainly formed during daytime. The alkane SOA consisted of alkane and carboxylic acid groups, consistent with the composition expected for oxidation products of C<sub>12</sub>-C<sub>25</sub> alkanes. Furthermore, organic mass fraction of alkane SOA covaried and correlated with odd oxygen, providing evidence for the ozone-driven formation of alkane SOA, a mechanism derived from laboratory studies. In contrast, aromatic SOA did not correlate with ozone. This component was largely composed of non-acid carbonyl groups, which is consistent with oxidation products formed from OH radical-driven reactions for aromatic hydrocarbons and, therefore, indicates formation by this process. The nighttime organic aerosol component, NOA, accounted for 50% to 80% of organonitrate group mass during the project; the secondary fraction of NOA likely formed from oxidation of biogenic precursors (e.g., terpenes) by nitrate radicals during nighttime hours.

Not only did anthropogenic and biogenic SOA components differ in composition, they also differed in size: namely, oxidized alkane and aromatic SOA components was largely distributed in 200- to 500-nm-sized particles, suggesting that they were formed from condensation of gas-phase oxidation products, while biogenic SOA was in 400- to 700-nm-sized particles at night, likely due to condensation of biogenic SOA on large primary particles.

We also identified aerosols likely emitted from local petroleum operations and cooking activities, which were likely in particles smaller than 200 nm. Though

these sources were negligibly small in the emission inventory for the Bakersfield site, they accounted for 13% and 7% of the PM<sub>1</sub> organic mass, respectively.

Overall, this work demonstrates that OOA components identified from factor analysis can be linked to SOA formed by different oxidants mainly from gasoline and diesel fuel combustion emissions with minor contributions from petroleum operation and biogenic sources. In addition, these SOA components were enriched at particular sizes. We conclude that SOA accounts for a major fraction of summertime OM, even in areas close to urban sources. This result provides a benefit to the SJV community because it identifies the need for regulating vehicular emissions as the largest source of PM<sub>1</sub> in summertime.

## 11.2 Research highlights

1. We have conducted an intensive field campaign using a set of complementary ensemble and single-particle measurement techniques, which enabled us to derive a comprehensive picture of particle properties at Bakersfield.
2. We have identified a number of sources that contributed to organic mass, from which fossil fuel combustion is the largest source at Bakersfield.
3. The PMF factors derived from independent techniques were compared. Good agreement confirms the robustness of the measurements and the identified sources.
4. Each factor identified from the FTIR-PMF analysis was associated with distinct IR spectrum and functional group compositions, which can be used as references for future studies where source markers are not available.
5. We have linked the PMF factors to specific sources as well as specific precursor VOC compound classes based on molecular source markers.
6. Our measurements suggest that the SOA from alkane hydrocarbons were likely driven by ozone, consistent with a mechanism proposed by *Russell et al.* [2011]
7. We have observed formation of SOA from oxidation of biogenic hydrocarbons by NO<sub>3</sub> radical at night.
8. The PMF analysis suggested that secondary organic aerosols from petroleum operation sources accounted for 10% of OM, which was likely underestimated in current source inventories.
9. We have derived size distributions of the SOA components, which suggest that the SOA components were formed by condensation processes.
10. The measurements suggested that SOA could account for 60-90% of summertime OM even in regions close to source emissions.
11. Ensemble and single particles were grouped into clusters, each of which was likely associated with a specific source type or atmospheric process.
12. We have applied the single-particle mass spectrum measurement using the high-resolution time-of-flight aerosol mass spectrometer coupled with a light scattering module for the first time.
13. Consistency of the single-particle mass spectral clusters with the source types identified from the ensemble measurements supports the connection

between ensemble-based factors and atmospheric particle sources and processes.

14. The CalNex and Cal-Mex campaigns provided intensive measurements of organic aerosol composition and sources that were comparable to the measurements at long term monitoring sites during the summer of 2010.
15. The four CalNex and Cal-Mex campaigns showed similar chemical signatures from fossil fuel combustion sources, with both more and less oxygenated components at each site – with their similar spectral shapes indicating that the distinction in their chemical formation reflects different functionality in addition to changes in O/C ratios. These differences are reflected in the higher fractions of hydroxyl in the less oxygenated fossil fuel factors, and more carbonyl groups in the more oxygenated fossil fuel combustion factors at all sites.
16. Using the functional group composition, we can bound the possible primary contribution to the fossil fuel combustion factors by the alkane group mass contribution. These estimates indicate that the  $\Delta POA/\Delta CO$  at the CalNex and Cal-Mex sites differs substantially at locations with different source emissions and vehicle fleets, and this has important implications for using variations in this ratio to identify sources.

## References

- Agrawal, H., W. A. Welch, J. W. Miller, and D. R. Cocker (2008), Emission Measurements from a Crude Oil Tanker at Sea, *Environmental Science & Technology*, 42(19), 10.1021/es703102y.
- Ahlm, L., S. Liu, D. A. Day, L. M. Russell, R. Weber, et al. (2012), Formation and Growth of Ultrafine Particles from Secondary Sources in Bakersfield, California, *Journal of Geophysical Research-Atmospheres*, 117
- Aiken, A. C., P. F. DeCarlo, and J. L. Jimenez (2007), Elemental Analysis of Organic Species with Electron Ionization High-Resolution Mass Spectrometry, *Analytical Chemistry*, 79(21), 8350-8358, 10.1021/ac071150w.
- Aiken, A. C., P. F. Decarlo, J. H. Kroll, D. R. Worsnop, J. A. Huffman, et al. (2008), O/C and Om/Oc Ratios of Primary, Secondary, and Ambient Organic Aerosols with High-Resolution Time-of-Flight Aerosol Mass Spectrometry, *Environmental Science & Technology*, 42(12), 4478-4485, 10.1021/es703009q.
- Alam, A., J. P. Shi, and R. M. Harrison (2003), Observations of New Particle Formation in Urban Air, *Journal of Geophysical Research-Atmospheres*, 108(D3), 10.1029/2001jd001417.
- Alfarra, M. R., H. Coe, J. D. Allan, K. N. Bower, H. Boudries, et al. (2004), Characterization of Urban and Rural Organic Particulate in the Lower Fraser Valley Using Two Aerodyne Aerosol Mass Spectrometers, *Atmospheric Environment*, 38(34), 5745-5758
- Allan, J. D., P. I. Williams, W. T. Morgan, C. L. Martin, M. J. Flynn, et al. (2010), Contributions from Transport, Solid Fuel Burning and Cooking to Primary Organic Aerosols in Two Uk Cities, *Atmospheric Chemistry and Physics*, 10(2), 647-668
- Aluwihare, L. I., D. J. Repeta, and R. F. Chen (1997), A Major Biopolymeric Component to Dissolved Organic Carbon in Surface Sea Water, *Nature*, 387(6629), 166-169
- American Lung Association (2011), *State of the Air*, New York, NY.
- Atkinson, R., and J. Arey (2003), Atmospheric Degradation of Volatile Organic Compounds, *Chemical Reviews*, 103(12), 4605-4638
- Bahreini, R., A. M. Middlebrook, J. A. de Gouw, C. Warneke, M. Trainer, et al. (2012), Gasoline Emissions Dominate over Diesel in Formation of Secondary Organic Aerosol Mass, *Geophysical Research Letters*, 39, 10.1029/2011gl050718.
- Bianchi, G., A. Gamba, R. Limiroli, N. Pozzi, R. Elster, et al. (1993), The Unusual Sugar Composition in the Leaves of the Resurrection Plant *Myrothamnus-Flabellifolia*, *Physiologia Plantarum*, 87(2), 223-226
- Birmili, W., and A. Wiedensohler (2000), New Particle Formation in the Continental Boundary Layer: Meteorological and Gas Phase

- Parameter Influence, *Geophysical Research Letters*, 27(20), 10.1029/1999gl011221.
- Braun, A. (2005), Carbon Speciation in Airborne Particulate Matter with C (1s) Nexafs Spectroscopy, *Journal of Environmental Monitoring*, 7(11), 1059
- Canagaratna, M. R., J. T. Jayne, D. A. Ghertner, S. Herndon, Q. Shi, et al. (2004), Chase Studies of Particulate Emissions from in-Use New York City Vehicles, *Aerosol Science and Technology*, 38(6), 555-573, 10.1080/02786820490465504.
- Canagaratna, M. R., J. T. Jayne, J. L. Jimenez, J. D. Allan, M. R. Alfarra, et al. (2007), Chemical and Microphysical Characterization of Ambient Aerosols with the Aerodyne Aerosol Mass Spectrometer, *Mass Spectrometry Reviews*, 26(2), 185-222, 10.1002/mas.20115.
- Carlton, A. G., B. J. Turpin, K. E. Altieri, S. Seitzinger, A. Reff, et al. (2007), Atmospheric Oxalic Acid and Soa Production from Glyoxal: Results of Aqueous Photooxidation Experiments, *Atmospheric Environment*, 41(35), 10.1016/j.atmosenv.2007.05.035.
- Cass, G. R. (1998), Organic Molecular Tracers for Particulate Air Pollution Sources, *Trac-Trends in Analytical Chemistry*, 17(6), 356-366
- Chan, A. W. H., K. E. Kautzman, P. S. Chhabra, J. D. Surratt, M. N. Chan, et al. (2009), Secondary Organic Aerosol Formation from Photooxidation of Naphthalene and Alkyl-naphthalenes: Implications for Oxidation of Intermediate Volatility Organic Compounds (Ivoc), *Atmospheric Chemistry and Physics*, 9(9), 3049-3060
- Chebbi, A., and P. Carlier (1996), Carboxylic Acids in the Troposphere, Occurrence, Sources, and Sinks: A Review, *Atmospheric Environment*, 30(24), 10.1016/1352-2310(96)00102-1.
- Chow, J. C., J. G. Watson, L. L. Ashbaugh, and K. L. Magliano (2003), Similarities and Differences in Pm10 Chemical Source Profiles for Geological Dust from the San Joaquin Valley, California, *Atmospheric Environment*, 37(9-10), 1317-1340
- Chow, J. C., L. W. A. Chen, J. G. Watson, D. H. Lowenthal, K. A. Magliano, et al. (2006a), Pm2.5 Chemical Composition and Spatiotemporal Variability During the California Regional Pm10/Pm2.5 Air Quality Study (Crpaqs), *Journal of Geophysical Research-Atmospheres*, 111(D10)
- Chow, J. C., J. G. Watson, D. H. Lowenthal, L. W. A. Chen, and K. L. Magliano (2006b), Particulate Carbon Measurements in California's San Joaquin Valley, *Chemosphere*, 62(3), 337-348
- Claeys, M., R. Szmigielski, I. Kourtev, P. Van der Veken, R. Vermeylen, et al. (2007), Hydroxydicarboxylic Acids: Markers for Secondary Organic Aerosol from the Photooxidation of Alpha-Pinene, *Environmental Science & Technology*, 41(5), 1628-1634
- Collins, D. R., D. R. Cocker, R. C. Flagan, and J. H. Seinfeld (2004), The Scanning Dma Transfer Function, *Aerosol Science and Technology*, 38(8), 10.1080/027868290503082.



- Cross, E. S., J. G. Slowik, P. Davidovits, J. D. Allan, D. R. Worsnop, et al. (2007), Laboratory and Ambient Particle Density Determinations Using Light Scattering in Conjunction with Aerosol Mass Spectrometry, *Aerosol Science and Technology*, 41(4), 343-359
- Cross, E. S., T. B. Onasch, M. Canagaratna, J. T. Jayne, J. Kimmel, et al. (2009), Single Particle Characterization Using a Light Scattering Module Coupled to a Time-of-Flight Aerosol Mass Spectrometer, *Atmospheric Chemistry and Physics*, 9(20)
- Dasgupta, P. K., J. Z. Li, G. F. Zhang, W. T. Luke, W. A. McClenny, et al. (2005), Summertime Ambient Formaldehyde in Five Us Metropolitan Areas: Nashville, Atlanta, Houston, Philadelphia, and Tampa, *Environmental Science & Technology*, 39(13), 10.1021/es048327d.
- De Gouw, J., and J. L. Jimenez (2009), Organic Aerosols in the Earth's Atmosphere, *Environmental Science & Technology*, 43(20), 7614-7618, 10.1021/es9006004.
- de Gouw, J. A., A. M. Middlebrook, C. Warneke, P. D. Goldan, W. C. Kuster, et al. (2005), Budget of Organic Carbon in a Polluted Atmosphere: Results from the New England Air Quality Study in 2002, *Journal of Geophysical Research-Atmospheres*, 110(D16), D16305  
10.1029/2004jd005623.
- DeCarlo, P. F., J. R. Kimmel, A. Trimborn, M. J. Northway, J. T. Jayne, et al. (2006), Field-Deployable, High-Resolution, Time-of-Flight Aerosol Mass Spectrometer, *Analytical Chemistry*, 78(24), 8281-8289, 10.1021/ac061249n.
- DeCarlo, P. F., I. M. Ulbrich, J. Crouse, B. de Foy, E. J. Dunlea, et al. (2010), Investigation of the Sources and Processing of Organic Aerosol over the Central Mexican Plateau from Aircraft Measurements During Milagro, *Atmospheric Chemistry and Physics*, 10(12), 5257-5280
- DiGangi, J. P., E. S. Boyle, T. Karl, P. Harley, A. Turnipseed, et al. (2011), First Direct Measurements of Formaldehyde Flux Via Eddy Covariance: Implications for Missing in-Canopy Formaldehyde Sources, *Atmospheric Chemistry and Physics*, 11(20), 10.5194/acp-11-10565-2011.
- Drewnick, F., S. S. Hings, P. DeCarlo, J. T. Jayne, M. Gonin, et al. (2005), A New Time-of-Flight Aerosol Mass Spectrometer (ToF-Ams) - Instrument Description and First Field Deployment, *Aerosol Science and Technology*, 39(7), 637-658
- Dunn, M. J., J. L. Jimenez, D. Baumgardner, T. Castro, P. H. McMurry, et al. (2004), Measurements of Mexico City Nanoparticle Size Distributions: Observations of New Particle Formation and Growth, *Geophysical Research Letters*, 31(10), 10.1029/2004gl019483.
- Esteve, W., H. Budzinski, and E. Villenave (2003), Heterogeneous Reactivity of Oh Radicals with Phenanthrene, Polycyclic Aromatic Compounds, 23(5), 441-456

- Fatemi, S. M., and B. Y. Jamaloei (2011), Preliminary Considerations on the Application of Toe-to-Heel Steam Flooding (Thsf): Injection Well-Producer Well Configurations, *Chemical Engineering Research & Design*, 89(11A), 2365-2379
- Fried, A., S. McKeen, S. Sewell, J. Harder, B. Henry, et al. (1997), Photochemistry of Formaldehyde During the 1993 Tropospheric Oh Photochemistry Experiment, *Journal of Geophysical Research-Atmospheres*, 102(D5), 10.1029/96jd03249.
- Fuchs, N. A., and A. G. Sutugin (1971), Highly Dispersed Aerosols, *Topics in Current Aerosol Research, Part II*
- Gentner, D. R., G. Isaacman, D. R. Worton, A. W. H. Chan, T. R. Dallmann, et al. (2012), Elucidating Secondary Organic Aerosol from Diesel and Gasoline Vehicles through Detailed Characterization of Organic Carbon Emissions, *Proceedings of the National Academy of Sciences of the United States of America*, 109(45), 10.1073/pnas.1212272109.
- Gilardoni, S., L. M. Russell, A. Sorooshian, R. C. Flagan, J. H. Seinfeld, et al. (2007), Regional Variation of Organic Functional Groups in Aerosol Particles on Four US East Coast Platforms During the International Consortium for Atmospheric Research on Transport and Transformation 2004 Campaign, *Journal of Geophysical Research-Atmospheres*, 112(D10), 10.1029/2006jd007737.
- Gilardoni, S., S. Liu, S. Takahama, L. M. Russell, J. D. Allan, et al. (2009), Characterization of Organic Ambient Aerosol During Mirage 2006 on Three Platforms, *Atmospheric Chemistry and Physics*, 9(15), 5417-5432
- Goldstein, A. H., and I. E. Galbally (2007), Known and Unexplored Organic Constituents in the Earth's Atmosphere, *Environmental Science & Technology*, 41(5), 1514-1521
- Goldstein, A. H., C. D. Koven, C. L. Heald, and I. Y. Fung (2009), Biogenic Carbon and Anthropogenic Pollutants Combine to Form a Cooling Haze over the Southeastern United States, *Proceedings of the National Academy of Sciences of the United States of America*, 106(22), 8835-8840
- Gray, H. A., G. R. Cass, J. J. Huntzicker, E. K. Heyerdahl, and J. A. Rau (1986), Characteristics of Atmospheric Organic and Elemental Carbon Particle Concentrations in Los-Angeles, *Environmental Science & Technology*, 20(6), 580-589
- Grosjean, D. (1984), Particulate Carbon in Los Angeles Air, *Science of the Total Environment*, 32(2), 133-145
- Guzman Morales, J., A. A. Frossard, A. L. Corrigan, S. Liu, S. Takahama, et al. (in prep.), Primary and Secondary Organic Aerosols in the Calnex and Cal-Mex Regions and Their Fossil Fuel Sources
- Hallquist, M., I. Wangberg, E. Ljungstrom, I. Barnes, and K. H. Becker (1999), Aerosol and Product Yields from No3 Radical-Initiated Oxidation of

- Selected Monoterpenes, *Environmental Science & Technology*, 33(4), 553-559
- Hallquist, M., J. C. Wenger, U. Baltensperger, Y. Rudich, D. Simpson, et al. (2009), The Formation, Properties and Impact of Secondary Organic Aerosol: Current and Emerging Issues, *Atmospheric Chemistry and Physics*, 9(14), 5155-5236
- Hamilton, J. F., P. J. Webb, A. C. Lewis, J. R. Hopkins, S. Smith, et al. (2004), Partially Oxidised Organic Components in Urban Aerosol Using Gcxcg-Tof/Ms, *Atmospheric Chemistry and Physics*, 4, 1279-1290
- Harrison, R. M., and A. M. Jones (2005), Multisite Study of Particle Number Concentrations in Urban Air, *Environmental Science & Technology*, 39(16), 10.1021/es040541e.
- Harrison, R. M., C. Giorio, D. C. S. Beddows, and M. Dall'Osto (2010), Size Distribution of Airborne Particles Controls Outcome of Epidemiological Studies, *Science of the Total Environment*, 409(2), 10.1016/j.scitotenv.2010.09.043.
- Hartigan, J. A., and M. A. Wong (1979), A K-Means Clustering Algorithm, *Applied Statistics*, 28(1)
- Hatakeyama, S., T. Tanonaka, J. H. Weng, H. Bandow, H. Takagi, et al. (1985), Ozone Cyclohexene Reaction in Air - Quantitative-Analysis of Particulate Products and the Reaction-Mechanism, *Environmental Science & Technology*, 19(10), 935-942
- Hatakeyama, S., M. Ohno, J. H. Weng, H. Takagi, and H. Akimoto (1987), Mechanism for the Formation of Gaseous and Particulate Products from Ozone-Cycloalkene Reactions in Air, *Environmental Science & Technology*, 21(1), 52-57
- Hawkins, L. N., and L. M. Russell (2010), Oxidation of Ketone Groups in Transported Biomass Burning Aerosol from the 2008 Northern California Lightning Series Fires, *Atmospheric Environment*, 44(34), 4142-4154, 10.1016/j.atmosenv.2010.07.036.
- Hayes, P. L., A. M. Ortega, and e. al. (in review), Organic Aerosol Composition and Sources in Pasadena, California During the 2010 Calnex Campaign
- He, L. Y., M. Hu, X. F. Huang, B. D. Yu, Y. H. Zhang, et al. (2004), Measurement of Emissions of Fine Particulate Organic Matter from Chinese Cooking, *Atmospheric Environment*, 38(38), 6557-6564
- He, L. Y., Y. Lin, X. F. Huang, S. Guo, L. Xue, et al. (2010), Characterization of High-Resolution Aerosol Mass Spectra of Primary Organic Aerosol Emissions from Chinese Cooking and Biomass Burning, *Atmospheric Chemistry and Physics*, 10(23), 11535-11543
- Heald, C. L., D. A. Ridley, S. M. Kreidenweis, and E. E. Drury (2010), Satellite Observations Cap the Atmospheric Organic Aerosol Budget, *Geophysical Research Letters*, 37
- Heintzenberg, J. (1989), Fine Particles in the Global Troposphere a Review, *Tellus Series B-Chemical and Physical Meteorology*, 41(2), 149-160, 10.1111/j.1600-0889.1989.tb00132.x.

- Hildemann, L. M., G. R. Markowski, M. C. Jones, and G. R. Cass (1991), Submicrometer Aerosol Mass Distributions of Emissions from Boilers, Fireplaces, Automobiles, Diesel Trucks, and Meat-Cooking Operations, *Aerosol Science and Technology*, 14(1), 138-152
- Hopke, P. K., and L. Kaufman (1990), The Use of Sampling to Cluster Large Data Sets, *Chemometrics and Intelligent Laboratory Systems*, 8(2), 195-204, 10.1016/0169-7439(90)80135-s.
- Huisman, A. J., J. R. Hottle, K. L. Coens, J. P. DiGangi, M. M. Galloway, et al. (2008), Laser-Induced Phosphorescence for the in Situ Detection of Glyoxal at Part Per Trillion Mixing Ratios, *Analytical Chemistry*, 80(15), 10.1021/ac800407b.
- IPCC (2007), *Climate Change 2007: The Physical Science Basis. Contribution of Working Group I to the Fourth Assessment Report of the Intergovernmental Panel on Climate Change*, Cambridge University Press, New York, NY, USA.
- Isakson, J., T. A. Persson, and E. S. Lindgren (2001), Identification and Assessment of Ship Emissions and Their Effects in the Harbour of Goteborg, Sweden, *Atmospheric Environment*, 35(21), 3659-3666
- Jakober, C. A., M. A. Robert, S. G. Riddle, H. Destailats, M. J. Charles, et al. (2008), Carbonyl Emissions from Gasoline and Diesel Motor Vehicles, *Environmental Science & Technology*, 42(13), 4697-4703, 10.1021/es7029174.
- Jaoui, M., E. O. Edney, T. E. Kleindienst, M. Lewandowski, J. H. Offenberg, et al. (2008), Formation of Secondary Organic Aerosol from Irradiated Alpha-Pinene/Toluene/No(X) Mixtures and the Effect of Isoprene and Sulfur Dioxide, *Journal of Geophysical Research-Atmospheres*, 113(D9)
- Jayne, J. T., D. C. Leard, X. F. Zhang, P. Davidovits, K. A. Smith, et al. (2000), Development of an Aerosol Mass Spectrometer for Size and Composition Analysis of Submicron Particles, *Aerosol Science and Technology*, 33(1-2), 49-70
- Jimenez, J. L., M. R. Canagaratna, N. M. Donahue, A. S. H. Prevot, Q. Zhang, et al. (2009), Evolution of Organic Aerosols in the Atmosphere, *Science*, 326(5959), 1525-1529, 10.1126/science.1180353.
- Johnson, D., S. R. Utembe, M. E. Jenkin, R. G. Derwent, G. D. Hayman, et al. (2006), Simulating Regional Scale Secondary Organic Aerosol Formation During the Torch 2003 Campaign in the Southern UK, *Atmospheric Chemistry and Physics*, 6, 403-418
- Kalafut-Pettibone, A. J., J. Wang, W. E. Eichinger, A. Clarke, S. A. Vay, et al. (2011), Size-Resolved Aerosol Emission Factors and New Particle Formation/Growth Activity Occurring in Mexico City During the Milagro 2006 Campaign, *Atmospheric Chemistry and Physics*, 11(17), 10.5194/acp-11-8861-2011.
- Kautzman, K. E., J. D. Surratt, M. N. Chan, A. W. H. Chan, S. P. Hersey, et al. (2010), Chemical Composition of Gas- and Aerosol-Phase Products

- from the Photooxidation of Naphthalene, *Journal of Physical Chemistry A*, 114(2), 913-934
- Kawamura, K., and K. Ikushima (1993), Seasonal-Changes in the Distribution of Dicarboxylic-Acids in the Urban Atmosphere, *Environmental Science & Technology*, 27(10), 2227-2235
- Kerminen, V. M., C. Ojanen, T. Pakkanen, R. Hillamo, M. Aurela, et al. (2000), Low-Molecular-Weight Dicarboxylic Acids in an Urban and Rural Atmosphere, *Journal of Aerosol Science*, 31(3), 10.1016/s0021-8502(99)00063-4.
- Ketzel, M., P. Wahlin, A. Kristensson, E. Swietlicki, R. Berkowicz, et al. (2004), Particle Size Distribution and Particle Mass Measurements at Urban, near-City and Rural Level in the Copenhagen Area and Southern Sweden, *Atmospheric Chemistry and Physics*, 4
- Khalaf, F., P. Literathy, and V. Anderlini (1982), Vanadium as a Tracer of Oil Pollution in the Sediments of Kuwait, *Hydrobiologia*, 91-2(JUL), 147-154
- Kimmel, J. R., D. K. Farmer, M. J. Cubison, D. Sueper, C. Tanner, et al. (2011), Real-Time Aerosol Mass Spectrometry with Millisecond Resolution, *International Journal of Mass Spectrometry*, 303(1), 10.1016/j.ijms.2010.12.004.
- Kirchstetter, T. W., B. C. Singer, R. A. Harley, G. R. Kendall, and J. M. Hesson (1999), Impact of California Reformulated Gasoline on Motor Vehicle Emissions. 2. Volatile Organic Compound Speciation and Reactivity, *Environmental Science & Technology*, 33(2), 329-336
- Kirkby, J., J. Curtius, J. Almeida, E. Dunne, J. Duplissy, et al. (2011), Role of Sulphuric Acid, Ammonia and Galactic Cosmic Rays in Atmospheric Aerosol Nucleation, *Nature*, 476(7361), 10.1038/nature10343.
- Kittelson, D. B., W. F. Watts, and J. P. Johnson (2006), On-Road and Laboratory Evaluation of Combustion Aerosols - Part 1: Summary of Diesel Engine Results, *Journal of Aerosol Science*, 37(8), 10.1016/j.jaerosci.2005.08.005.
- Kleeman, M. J., L. S. Hughes, J. O. Allen, and G. R. Cass (1999), Source Contributions to the Size and Composition Distribution of Atmospheric Particles: Southern California in September 1996, *Environmental Science & Technology*, 33(23), 4331-4341
- Kleeman, M. J., S. G. Riddle, M. A. Robert, C. A. Jakober, P. M. Fine, et al. (2009), Source Apportionment of Fine (Pm(1.8)) and Ultrafine (Pm(0.1)) Airborne Particulate Matter During a Severe Winter Pollution Episode, *Environmental Science & Technology*, 43(2), 272-279
- Kostenidou, E., R. K. Pathak, and S. N. Pandis (2007), An Algorithm for the Calculation of Secondary Organic Aerosol Density Combining Ams and Smps Data, *Aerosol Science and Technology*, 41(11), 10.1080/02786820701666270.
- Kulmala, M., K. Hameri, P. P. Aalto, J. M. Makela, L. Pirjola, et al. (2001), Overview of the International Project on Biogenic Aerosol

- Formation in the Boreal Forest (Biofor), *Tellus Series B-Chemical and Physical Meteorology*, 53(4), 324-343
- Kulmala, M., H. Vehkamäki, T. Petaja, M. Dal Maso, A. Lauri, et al. (2004), Formation and Growth Rates of Ultrafine Atmospheric Particles: A Review of Observations, *Journal of Aerosol Science*, 35(2), 10.1016/j.jaerosci.2003.10.003.
- Kwok, E. S. C., W. P. Harger, J. Arey, and R. Atkinson (1994), Reactions of Gas-Phase Phenanthrene under Simulated Atmospheric Conditions, *Environmental Science & Technology*, 28(3), 521-527
- Lanz, V. A., M. R. Alfarra, U. Baltensperger, B. Buchmann, C. Hueglin, et al. (2007), Source Apportionment of Submicron Organic Aerosols at an Urban Site by Factor Analytical Modelling of Aerosol Mass Spectra, *Atmospheric Chemistry and Physics*, 7(6), 1503-1522
- Lee, J., and D. A. Lane (2009), Unique Products from the Reaction of Naphthalene with the Hydroxyl Radical, *Atmospheric Environment*, 43(32), 4886-4893
- Lee, J., and D. A. Lane (2010), Formation of Oxidized Products from the Reaction of Gaseous Phenanthrene with the OH Radical in a Reaction Chamber, *Atmospheric Environment*, 44(20), 2469-2477
- Liggio, J., S. M. Li, and R. McLaren (2005), Heterogeneous Reactions of Glyoxal on Particulate Matter: Identification of Acetals and Sulfate Esters, *Environmental Science & Technology*, 39(6), 1532-1541
- Lim, Y. B., and P. J. Ziemann (2005), Products and Mechanism of Secondary Organic Aerosol Formation from Reactions of N-Alkanes with OH Radicals in the Presence of NO<sub>x</sub>, *Environmental Science & Technology*, 39(23), 9229-9236, 10.1021/es051447g.
- Lim, Y. B., and P. J. Ziemann (2009), Chemistry of Secondary Organic Aerosol Formation from OH Radical-Initiated Reactions of Linear, Branched, and Cyclic Alkanes in the Presence of NO<sub>x</sub>, *Aerosol Science and Technology*, 43(6), 604-619, 10.1080/02786820902802567.
- Liu, B. Y. H., and K. W. Lee (1976), Efficiency of Membrane and Nuclepore Filters for Submicrometer Aerosols, *Environmental Science & Technology*, 10(4), 345-350
- Liu, P. S. K., R. Deng, K. A. Smith, L. R. Williams, J. T. Jayne, et al. (2007), Transmission Efficiency of an Aerodynamic Focusing Lens System: Comparison of Model Calculations and Laboratory Measurements for the Aerodyne Aerosol Mass Spectrometer, *Aerosol Science and Technology*, 41(8), 10.1080/02786820701422278.
- Liu, S., M. Hu, S. Slanina, L.-Y. He, Y.-W. Niu, et al. (2008), Size Distribution and Source Analysis of Ionic Compositions of Aerosols in Polluted Periods at Xinken in Pearl River Delta (Prd) of China, *Atmospheric Environment*, 42(25), 6284-6295
- Liu, S., S. Takahama, L. M. Russell, S. Gilardoni, and D. Baumgardner (2009), Oxygenated Organic Functional Groups and Their Sources in Single and Submicron Organic Particles in Milagro 2006 Campaign, *Atmospheric Chemistry and Physics*, 9(18), 6849-6863

- Liu, S., D. A. Day, J. E. Shields, and L. M. Russell (2011), Ozone-Driven Daytime Formation of Secondary Organic Aerosol Containing Carboxylic Acid Groups and Alkane Groups, *Atmospheric Chemistry and Physics*, 11(16), 8321-8341, 10.5194/acp-11-8321-2011.
- Liu, S., L. Ahlm, D. Day, L. Russell, Y. Zhao, et al. (2012a), Secondary Organic Aerosol Formation from Fossil Fuel Sources Contribute Majority of Summertime Organic Mass at Bakersfield, *Journal of Geophysical Research*, 117(D00V26), doi:10.1029/2012JD018170.
- Liu, S., L. M. Russell, D. T. Sueper, and T. B. Onasch (2012b), Organic Particle Types by Single-Particle Measurements Using a Time-of-Flight Aerosol Mass Spectrometer Coupled with a Light Scattering Module, *Atmospheric Measurements Techniques Discussions*, 5, 3047-3077
- Lohmann, U., and J. Feichter (2005), Global Indirect Aerosol Effects: A Review, *Atmospheric Chemistry and Physics*, 5, 715-737
- Lu, R., and R. P. Turco (1995), Air Pollution Transport in a Coastal Environment .2. 3-Dimensional Simulations over Los Angeles Basin, *Atmospheric Environment*, 29(13), 10.1016/1352-2310(95)00015-q.
- Mader, B. T., R. C. Flagan, and J. H. Seinfeld (2001), Sampling Atmospheric Carbonaceous Aerosols Using a Particle Trap Impactor/Denuder Sampler, *Environmental Science & Technology*, 35(24), 4857-4867
- Maria, S. F., L. M. Russell, B. J. Turpin, and R. J. Porcja (2002), Field Measurements of Functional Groups and Organic Mass in Aerosol Samples over the Caribbean, *Atmospheric Environment*, 36(33), 5185-5196
- Maria, S. F., L. M. Russell, B. J. Turpin, R. J. Porcja, T. L. Campos, et al. (2003), Source Signatures of Carbon Monoxide and Organic Functional Groups in Asian Pacific Regional Aerosol Characterization Experiment (Ace-Asia) Submicron Aerosol Types, *Journal of Geophysical Research-Atmospheres*, 108(D23), 10.1029/2003jd003703.
- Matthew, B. M., A. M. Middlebrook, and T. B. Onasch (2008), Collection Efficiencies in an Aerodyne Aerosol Mass Spectrometer as a Function of Particle Phase for Laboratory Generated Aerosols, *Aerosol Science and Technology*, 42(11), 884-898, 10.1080/02786820802356797.
- Middlebrook, A. M., D. M. Murphy, and D. S. Thomson (1998), Observations of Organic Material in Individual Marine Particles at Cape Grim During the First Aerosol Characterization Experiment (Ace 1), *Journal of Geophysical Research-Atmospheres*, 103(D13), 16475-16483
- Middlebrook, A. M., R. Bahreini, J. L. Jimenez, and M. R. Canagaratna (2012), Evaluation of Composition-Dependent Collection Efficiencies for the Aerodyne Aerosol Mass Spectrometer Using Field Data, *Aerosol Science and Technology*, 46(3), 10.1080/02786826.2011.620041.
- Miller, P. R., and A. M. Winer (1984), Composition and Dominance in Los Angeles Basin Urban Vegetation, *Urban Ecology*, 8(1-2), 10.1016/0304-4009(84)90005-6.

- Minguillon, M. C., M. Arhami, J. J. Schauer, and C. Sioutas (2008), Seasonal and Spatial Variations of Sources of Fine and Quasi-Ultrafine Particulate Matter in Neighborhoods near the Los Angeles-Long Beach Harbor, *Atmospheric Environment*, 42(32), 7317-7328, 10.1016/j.atmosenv.2008.07.036.
- Mohr, C., J. A. Huffman, M. J. Cubison, A. C. Aiken, K. S. Docherty, et al. (2009), Characterization of Primary Organic Aerosol Emissions from Meat Cooking, Trash Burning, and Motor Vehicles with High-Resolution Aerosol Mass Spectrometry and Comparison with Ambient and Chamber Observations, *Environmental Science & Technology*, 43(7), 2443-2449, 10.1021/es8011518.
- Mohr, C., P. F. DeCarlo, M. F. Heringa, R. Chirico, J. G. Slowik, et al. (2012), Identification and Quantification of Organic Aerosol from Cooking and Other Sources in Barcelona Using Aerosol Mass Spectrometer Data, *Atmospheric Chemistry and Physics*, 12(4), 10.5194/acp-12-1649-2012.
- Molina, M. J., A. V. Ivanov, S. Trakhtenberg, and L. T. Molina (2004), Atmospheric Evolution of Organic Aerosol, *Geophys Res Lett*, 31(22), 10.1029/2004gl020910.
- Moore, G. E., C. Daly, M. K. Liu, and S. J. Huang (1987), Modeling of Mountain-Valley Wind Fields in the Southern San Joaquin Valley, California, *Journal of Climate and Applied Meteorology*, 26(9), 10.1175/1520-0450(1987)026<1230:momvwf>2.0.co;2.
- Myers, C. O. (1986), Kern River Cogeneration Project, *IEEE ElectroTechnology Review*, 2, 113-114
- Nakao, S., M. Shrivastava, N. Anh, H. Jung, and D. Cocker, III (2011), Interpretation of Secondary Organic Aerosol Formation from Diesel Exhaust Photooxidation in an Environmental Chamber, *Aerosol Science and Technology*, 45(8)
- National Research Council (NRC) (1996), *A Plan for a Research Program on Aerosol Radiative Forcing and Climate Change*, National Academy Press, Washington, D.C.
- Ng, N. L., M. R. Canagaratna, Q. Zhang, J. L. Jimenez, J. Tian, et al. (2010), Organic Aerosol Components Observed in Northern Hemispheric Datasets from Aerosol Mass Spectrometry, *Atmospheric Chemistry and Physics*, 10(10), 4625-4641
- Ng, N. L., M. R. Canagaratna, J. L. Jimenez, P. S. Chhabra, J. H. Seinfeld, et al. (2011), Changes in Organic Aerosol Composition with Aging Inferred from Aerosol Mass Spectra, *Atmospheric Chemistry and Physics*, 11(13), 6465-6474
- O'Brien, R. E., A. Laskin, J. Laskin, S. Liu, R. Weber, et al. (2012), Molecular Characterization of Organic Aerosol Using Nanospray Desorption/Electrospray Ionization Mass Spectrometry: Calnex 2010 Field Study, *Atmospheric Environment*, 10.1016/j.atmosenv.2012.11.056.



- O'Brien, R. E., T. B. Nguyen, L. Laskin, J. Laskin, P. L. Hayes, et al. (Accepted 2012), Probing Molecular Associations of Field-Collected and Laboratory-Generated Soa with Nano-Desi High-Resolution Mass Spectrometry, *Journal of Geophysical Research - Atmospheres*
- Oberdorster, G., R. M. Gelein, J. Ferin, and B. Weiss (1995), Association of Particulate Air-Pollution and Acute Mortality - Involvement of Ultrafine Particles, *Inhalation Toxicology*, 7(1), 10.3109/08958379509014275.
- Paatero, P., and U. Tapper (1994), Positive Matrix Factorization- a Nonnegative Factor Model with Optimal Utilization of Error-Estimates of Data Values, *Environmetrics*, 5(2), 111-126
- Paatero, P., P. K. Hopke, X. H. Song, and Z. Ramadan (2002), Understanding and Controlling Rotations in Factor Analytic Models, *Chemometrics and Intelligent Laboratory Systems*, 60(1-2), 253-264
- Paatero, P., and P. K. Hopke (2003), Discarding or Downweighting High-Noise Variables in Factor Analytic Models, *Analytica Chimica Acta*, 490(1-2), 277-289
- Petaja, T., R. L. Mauldin, III, E. Kosciuch, J. McGrath, T. Nieminen, et al. (2009), Sulfuric Acid and Oh Concentrations in a Boreal Forest Site, *Atmospheric Chemistry and Physics*, 9(19)
- Peters, A., H. E. Wichmann, T. Tuch, J. Heinrich, and J. Heyder (1997), Respiratory Effects Are Associated with the Number of Ultrafine Particles, *American Journal of Respiratory and Critical Care Medicine*, 155(4)
- Pope, C. A., and D. W. Dockery (2006), Health Effects of Fine Particulate Air Pollution: Lines That Connect, *Journal of the Air & Waste Management Association*, 56(6), 709-742
- Pye, H. O. T., and G. A. Pouliot (2012), Modeling the Role of Alkanes, Polycyclic Aromatic Hydrocarbons, and Their Oligomers in Secondary Organic Aerosol Formation, *Environmental Science & Technology*, doi: 10.1021/es300409w
- Quinn, P. K., T. S. Bates, D. Coffman, T. B. Onasch, D. Worsnop, et al. (2006), Impacts of Sources and Aging on Submicrometer Aerosol Properties in the Marine Boundary Layer across the Gulf of Maine, *Journal of Geophysical Research-Part D-Atmospheres*, 1-20, 10.1029/2006jd007582.
- Ramanathan, V., P. J. Crutzen, J. Lelieveld, A. P. Mitra, D. Althausen, et al. (2001), Indian Ocean Experiment: An Integrated Analysis of the Climate Forcing and Effects of the Great Indo-Asian Haze, *Journal of Geophysical Research-Atmospheres*, 106(D22), 28371-28398
- Richter, H., and J. B. Howard (2000), Formation of Polycyclic Aromatic Hydrocarbons and Their Growth to Soot - a Review of Chemical Reaction Pathways, *Progress in Energy and Combustion Science*, 26(4-6), 565-608
- Riipinen, I., J. R. Pierce, T. Yli-Juuti, T. Nieminen, S. Hakkinen, et al. (2011), Organic Condensation: A Vital Link Connecting Aerosol Formation

- to Cloud Condensation Nuclei (Ccn) Concentrations, *Atmospheric Chemistry and Physics*, 11(8), 10.5194/acp-11-3865-2011.
- Robinson, A. L., N. M. Donahue, M. K. Shrivastava, E. A. Weitkamp, A. M. Sage, et al. (2007), Rethinking Organic Aerosols: Semivolatile Emissions and Photochemical Aging, *Science*, 315(5816), 1259-1262, 10.1126/science.1133061.
- Rodgers, J. L., and W. A. Nicewander (1988), 13 Ways to Look at the Correlation-Coefficient, *American Statistician*, 42(1), 59-66
- Rollins, A. W., E. C. Browne, K. E. Min, S. E. Pusede, P. J. Wooldridge, et al. (2012), Evidence for Nox Control over Nighttime Soa Formation, *Science*, 337(6099), 10.1126/science.1221520.
- Rosenfeld, D. (2006), Atmosphere - Aerosols, Clouds, and Climate, *Science*, 312(5778), 10.1126/science.1128972.
- Russell, L. M., S. F. Maria, and S. C. B. Myneni (2002), Mapping Organic Coatings on Atmospheric Particles, *Geophysical Research Letters*, 29(16)
- Russell, L. M. (2003), Aerosol Organic-Mass-to-Organic-Carbon Ratio Measurements, *Environmental Science & Technology*, 37(13), 2982-2987, 10.1021/es026123w.
- Russell, L. M., S. Takahama, S. Liu, L. N. Hawkins, D. S. Covert, et al. (2009), Oxygenated Fraction and Mass of Organic Aerosol from Direct Emission and Atmospheric Processing Measured on the R/V Ronald Brown During Texaqs/Gomaccs 2006, *Journal of Geophysical Research-Atmospheres*, 114, 10.1029/2008jd011275.
- Russell, L. M., L. N. Hawkins, A. A. Frossard, P. K. Quinn, and T. S. Bates (2010), Carbohydrate-Like Composition of Submicron Atmospheric Particles and Their Production from Ocean Bubble Bursting, *Proceedings of the National Academy of Sciences of the United States of America*, 107(15), 6652-6657, 10.1073/pnas.0908905107.
- Russell, L. M., R. Bahadur, and P. J. Ziemann (2011), Identifying Organic Aerosol Sources by Comparing Functional Group Composition in Chamber and Atmospheric Particles, *Proceedings of the National Academy of Sciences of the United States of America*, 108(9), 3516-3521, 10.1073/pnas.1006461108.
- Saathoff, H., K. H. Naumann, M. Schnaiter, W. Schock, E. Weingartner, et al. (2003), Carbon Mass Determinations During the Aida Soot Aerosol Campaign 1999, *Journal of Aerosol Science*, 34(10), 10.1016/s0021-8502(03)00365-3.
- Salma, I., T. Borsos, T. Weidinger, P. Aalto, T. Hussein, et al. (2011), Production, Growth and Properties of Ultrafine Atmospheric Aerosol Particles in an Urban Environment, *Atmospheric Chemistry and Physics*, 11(3), 10.5194/acp-11-1339-2011.
- Schade, G. W., and P. J. Crutzen (1995), Emission of Aliphatic-Amines from Animal Husbandry and Their Reactions - Potential Source of N<sub>2</sub>O and Hcn, *Journal of Atmospheric Chemistry*, 22(3), 319-346

- Schauer, J. J., W. F. Rogge, L. M. Hildemann, M. A. Mazurek, G. R. Cass, et al. (1996), Source Apportionment of Airborne Particulate Matter Using Organic Compounds as Tracers, *Atmospheric Environment*, 30(22), 3837-3855
- Schauer, J. J., M. J. Kleeman, G. R. Cass, and B. R. T. Simoneit (1999), Measurement of Emissions from Air Pollution Sources. 2. C-1 through C-30 Organic Compounds from Medium Duty Diesel Trucks, *Environmental Science & Technology*, 33(10), 1578-1587
- Schauer, J. J., and G. R. Cass (2000), Source Apportionment of Wintertime Gas-Phase and Particle-Phase Air Pollutants Using Organic Compounds as Tracers, *Environmental Science & Technology*, 34(9), 1821-1832
- Schauer, J. J., M. P. Fraser, G. R. Cass, and B. R. T. Simoneit (2002a), Source Reconciliation of Atmospheric Gas-Phase and Particle-Phase Pollutants During a Severe Photochemical Smog Episode, *Environmental Science & Technology*, 36(17), 3806-3814
- Schauer, J. J., M. J. Kleeman, G. R. Cass, and B. R. T. Simoneit (2002b), Measurement of Emissions from Air Pollution Sources. 5. C-1-C-32 Organic Compounds from Gasoline-Powered Motor Vehicles, *Environmental Science & Technology*, 36(6), 1169-1180
- Schwartz, R. E., L. M. Russell, S. J. Sjostedt, A. Vlasenko, J. G. Slowik, et al. (2010), Biogenic Oxidized Organic Functional Groups in Aerosol Particles from a Mountain Forest Site and Their Similarities to Laboratory Chamber Products, *Atmospheric Chemistry and Physics*, 10(11), 5075-5088, 10.5194/acp-10-5075-2010.
- Seinfeld, J. H., and S. N. Pandis (1998), *Atmospheric Chemistry and Physics: From Air Pollution to Climate Change*, Hoboken, NJ.
- Seinfeld, J. H., and S. N. Pandis (2006), *Atmospheric Chemistry and Physics: From Air Pollution to Climate Change*, J. Wiley, New York.
- Sempere, R., and K. Kawamura (1994), Comparative Distributions of Dicarboxylic-Acids and Related Polar Compounds in Snow Rain and Aerosols from Urban Atmosphere, *Atmospheric Environment*, 28(3), 10.1016/1352-2310(94)90123-6.
- Shakya, K. M., and R. J. Griffin (2010), Secondary Organic Aerosol from Photooxidation of Polycyclic Aromatic Hydrocarbons, *Environmental Science & Technology*, 44(21), 8134-8139
- Shi, J. P., A. A. Khan, and R. M. Harrison (1999), Measurements of Ultrafine Particle Concentration and Size Distribution in the Urban Atmosphere, *Science of the Total Environment*, 235(1-3), 10.1016/s0048-9697(99)00189-8.
- Silva, P. J., and K. A. Prather (2000), Interpretation of Mass Spectra from Organic Compounds in Aerosol Time-of-Flight Mass Spectrometry, *Analytical Chemistry*, 72(15), 3553-3562
- Simoneit, B. R. T. (1986), Characterization of Organic-Constituents in Aerosols in Relation to Their Origin and Transport - a Review, *International Journal of Environmental Analytical Chemistry*, 23(3), 10.1080/03067318608076446.

- Smith, J. N., M. J. Dunn, T. M. VanReken, K. Iida, M. R. Stolzenburg, et al. (2008), Chemical Composition of Atmospheric Nanoparticles Formed from Nucleation in Tecamac, Mexico: Evidence for an Important Role for Organic Species in Nanoparticle Growth, *Geophysical Research Letters*, 35(4), 10.1029/2007gl032523.
- Sorooshian, A., S. N. Murphy, S. Hersey, H. Gates, L. T. Padro, et al. (2008), Comprehensive Airborne Characterization of Aerosol from a Major Bovine Source, *Atmospheric Chemistry and Physics*, 8(17), 5489-5520
- Stanier, C. O., A. Y. Khlystov, and S. N. Pandis (2004a), Nucleation Events During the Pittsburgh Air Quality Study: Description and Relation to Key Meteorological, Gas Phase, and Aerosol Parameters, *Aerosol Science and Technology*, 38, 10.1080/02786820390229570.
- Stanier, C. O., A. Y. Khlystov, and S. N. Pandis (2004b), Ambient Aerosol Size Distributions and Number Concentrations Measured During the Pittsburgh Air Quality Study (Paqs), *Atmospheric Environment*, 38(20), 10.1016/j.atmosenv.2004.03.020.
- Stein, S. E., and D. R. Scott (1994), Optimization and Testing of Mass Spectral Library Search Algorithms for Compound Identification, *Journal of the American Society for Mass Spectrometry*, 5(9), 859-866
- Stolzenburg, M. R., P. H. McMurry, H. Sakurai, J. N. Smith, R. L. Mauldin, et al. (2005), Growth Rates of Freshly Nucleated Atmospheric Particles in Atlanta, *Journal of Geophysical Research-Atmospheres*, 110(D22), 10.1029/2005jd005935.
- Sun, Y. L., Q. Zhang, J. J. Schwab, K. L. Demerjian, W. N. Chen, et al. (2011), Characterization of the Sources and Processes of Organic and Inorganic Aerosols in New York City with a High-Resolution Time-of-Flight Aerosol Mass Spectrometer, *Atmospheric Chemistry and Physics*, 11(4), 1581-1602
- Surratt, J. D., Y. Gomez-Gonzalez, A. W. H. Chan, R. Vermeylen, M. Shahgholi, et al. (2008), Organosulfate Formation in Biogenic Secondary Organic Aerosol, *Journal of Physical Chemistry A*, 112(36), 8345-8378, 10.1021/jp802310p.
- Takahama, S., S. Gilardoni, L. M. Russell, and A. L. D. Kilcoyne (2007), Classification of Multiple Types of Organic Carbon Composition in Atmospheric Particles by Scanning Transmission X-Ray Microscopy Analysis, *Atmospheric Environment*, 41(40), 9435-9451, 10.1016/j.atmosenv.2007.08.051.
- Takahama, S., S. Liu, and L. M. Russell (2010), Coatings and Clusters of Carboxylic Acids in Carbon-Containing Atmospheric Particles from Spectromicroscopy and Their Implications for Cloud-Nucleating and Optical Properties, *Journal of Geophysical Research-Atmospheres*, 115, 21, D01202  
10.1029/2009jd012622.
- Takahama, S., R. E. Schwartz, L. M. Russell, A. M. Macdonald, S. Sharma, et al. (2011), Organic Functional Groups in Aerosol Particles from

- Burning and Non-Burning Forest Emissions at a High-Elevation Mountain Site, *Atmospheric Chemistry and Physics*, 11(13), 6367-6386, 10.5194/acp-11-6367-2011.
- Takahama, S., A. Johnson, and L. M. Russell (2012), Quantification of Carboxylic and Carbonyl Functional Groups in Organic Aerosol Infrared Absorbance Spectra, *Aerosol Science and Technology*, 10.1080/02786826.2012.752065.
- Takahama, S., L. M. Russell, J. Zheng, R. Zhang, and W. R. Leitch (in prep.), Sources and Sizes of Black Carbon During Cal-Mex 2010
- Takahama, S., A. Johnson, J. Guzman Morales, L. M. Russell, R. Duran, et al. (in press), Submicron Organic Aerosol in Tijuana, Mexico, from Local and Southern California Sources During the Calmex Campaign, *Atmospheric Environment*
- Takegawa, N., T. Miyakawa, Y. Kondo, D. R. Blake, Y. Kanaya, et al. (2006), Evolution of Submicron Organic Aerosol in Polluted Air Exported from Tokyo, *Geophysical Research Letters*, 33(15), Artn L15814  
Doi 10.1029/2006gl025815.
- Tanner, R. L., and B. Zielinska (1994), Determination of the Biogenic Emission Rates of Species Contributing to Voc in the San Joaquin Valley of California, *Atmospheric Environment*, 28(6), 1113-1120
- Tivanski, A. V., R. J. Hopkins, T. Tyliczszak, and M. K. Gilles (2007), Oxygenated Interface on Biomass Burn Tar Balls Determined by Single Particle Scanning Transmission X-Ray Microscopy, *Journal of Physical Chemistry A*, 111(25), 5448-5458
- Turpin, B. J., J. J. Huntzicker, S. M. Larson, and G. R. Cass (1991), Los Angeles Summer Midday Particulate Carbon - Primary and Secondary Aerosol, *Environmental Science & Technology*, 25(10), 1788-1793
- Turpin, B. J., P. Saxena, and E. Andrews (2000), Measuring and Simulating Particulate Organics in the Atmosphere: Problems and Prospects, *Atmospheric Environment*, 34(18), 2983-3013
- Ulbrich, I. M., M. Lechner, and J. L. Jimenez (2007), Ams Spectral Database, [Http://Cires.Colorado.Edu/Jimenez-Group/Amssd](http://Cires.Colorado.Edu/Jimenez-Group/Amssd)
- Ulbrich, I. M., M. R. Canagaratna, Q. Zhang, D. R. Worsnop, and J. L. Jimenez (2009), Interpretation of Organic Components from Positive Matrix Factorization of Aerosol Mass Spectrometric Data, *Atmospheric Chemistry and Physics*, 9(9), 2891-2918
- Ulbrich, I. M., M. R. Canagaratna, M. J. Cubison, Q. Zhang, N. L. Ng, et al. (2012), Three-Dimensional Factorization of Size-Resolved Organic Aerosol Mass Spectra from Mexico City, *Atmos. Meas. Tech.*, 5, 195-224
- Usher, C. R., A. E. Michel, and V. H. Grassian (2003), Reactions on Mineral Dust, *Chemical Reviews*, 103(12), 4883-4939
- Volkamer, R., J. L. Jimenez, F. San Martini, K. Dzepina, Q. Zhang, et al. (2006), Secondary Organic Aerosol Formation from Anthropogenic Air Pollution: Rapid and Higher Than Expected, *Geophysical Research Letters*, 33(17)

- Volkamer, R., F. S. Martini, L. T. Molina, D. Salcedo, J. L. Jimenez, et al. (2007), A Missing Sink for Gas-Phase Glyoxal in Mexico City: Formation of Secondary Organic Aerosol, *Geophysical Research Letters*, 34(19), 10.1029/2007gl030752.
- Wallace, L. A., S. J. Emmerich, and C. Howard-Reed (2004), Source Strengths of Ultrafine and Fine Particles Due to Cooking with a Gas Stove, *Environmental Science & Technology*, 38(8), 2304-2311
- Wang, L., R. Atkinson, and J. Arey (2007), Dicarbonyl Products of the Oh Radical-Initiated Reactions of Naphthalene and the C-1- and C-2-Alkylnaphthalenes, *Environmental Science & Technology*, 41(8), 2803-2810
- Wangberg, I., I. Barnes, and K. H. Becker (1997), Product and Mechanistic Study of the Reaction of No<sub>3</sub> Radicals with Alpha-Pinene, *Environmental Science & Technology*, 31(7), 2130-2135
- Ward, J. H. (1963), Hierarchical Grouping to Optimize an Objective Function, *Journal of the American Statistical Association*, 58(301), 10.2307/2282967.
- Webb, P. J., J. F. Hamilton, A. C. Lewis, and K. Wirtz (2006), Formation of Oxygenated-Polycyclic Aromatic Compounds in Aerosol from the Photo-Oxidation of O-Tolualdehyde, *Polycyclic Aromatic Compounds*, 26(4), 237-252
- Wert, B. P., M. Trainer, A. Fried, T. B. Ryerson, B. Henry, et al. (2003), Signatures of Terminal Alkene Oxidation in Airborne Formaldehyde Measurements During Texaqs 2000, *Journal of Geophysical Research-Atmospheres*, 108(D3), 10.1029/2002jd002502.
- Woo, K. S., D. R. Chen, D. Y. H. Pui, and P. H. McMurry (2001), Measurement of Atlanta Aerosol Size Distributions: Observations of Ultrafine Particle Events, *Aerosol Science and Technology*, 34(1), 10.1080/027868201300082049.
- Yee, L. D., J. S. Craven, C. L. Loza, K. A. Schilling, N. L. Ng, et al. (2012), Secondary Organic Aerosol Formation from Low-Nox Photooxidation of Dodecane: Evolution of Multi-Generation Gas-Phase Chemistry and Aerosol Composition, *Journal of Physical Chemistry A*, DOI: 10.1021/jp211531h
- Zaremba, L. L., and J. J. Carroll (1999), Summer Wind Flow Regimes over the Sacramento Valley, *Journal of Applied Meteorology*, 38(10), 10.1175/1520-0450(1999)038<1463:swfrot>2.0.co;2.
- Zhang, Q., C. O. Stanier, M. R. Canagaratna, J. T. Jayne, D. R. Worsnop, et al. (2004), Insights into the Chemistry of New Particle Formation and Growth Events in Pittsburgh Based on Aerosol Mass Spectrometry, *Environmental Science & Technology*, 38(18), 10.1021/es035417u.
- Zhang, Q., M. R. Alfarra, D. R. Worsnop, J. D. Allan, H. Coe, et al. (2005a), Deconvolution and Quantification of Hydrocarbon-Like and Oxygenated Organic Aerosols Based on Aerosol Mass Spectrometry, *Environmental Science & Technology*, 39(13), 4938-4952, 10.1021/es048568l.

- Zhang, Q., M. R. Canagaratna, J. T. Jayne, D. R. Worsnop, and J. L. Jimenez (2005b), Time- and Size-Resolved Chemical Composition of Submicron Particles in Pittsburgh: Implications for Aerosol Sources and Processes, *Journal of Geophysical Research-Atmospheres*, 110(D7)
- Zhang, Q., J. L. Jimenez, M. R. Canagaratna, J. D. Allan, H. Coe, et al. (2007), Ubiquity and Dominance of Oxygenated Species in Organic Aerosols in Anthropogenically-Influenced Northern Hemisphere Midlatitudes, *Geophysical Research Letters*, 34(13)
- Zhao, Y., N. M. Kreisberg, D. R. Worton, G. Issacman, D. R. Gentner, et al. (submitted), Sources of Organic Aerosol Investigated Using Organic Compounds as Tracers Measured During Calnex in Bakersfield, *Journal of Geophysical Research - Atmospheres*
- Zheng, M., G. R. Cass, J. J. Schauer, and E. S. Edgerton (2002), Source Apportionment of Pm<sub>2.5</sub> in the Southeastern United States Using Solvent-Extractable Organic Compounds as Tracers, *Environmental Science & Technology*, 36(11), 2361-2371
- Zhijun, W., H. Min, L. Shang, B. Wehner, S. Bauer, et al. (2007), New Particle Formation in Beijing, China: Statistical Analysis of a 1-Year Data Set, *Journal of Geophysical Research-Part D-Atmospheres*, 112(9), 10.1029/2006jd007406.
- Zhong, S. Y., C. D. Whiteman, and X. D. Bian (2004), Diurnal Evolution of Three-Dimensional Wind and Temperature Structure in California's Central Valley, *Journal of Applied Meteorology*, 43(11), 1679-1699